

Molecularly Engineered Hole Transporting Materials for High Performance Perovskite Solar Cells

THÈSE N° 8264 (2018)

PRÉSENTÉE LE 26 JANVIER 2018
À LA FACULTÉ DES SCIENCES DE BASE
LABORATOIRE DE PHOTONIQUE ET INTERFACES
ET

GROUPE SCI-SB-MN
PROGRAMME DOCTORAL EN CHIMIE ET GÉNIE CHIMIQUE

ÉCOLE POLYTECHNIQUE FÉDÉRALE DE LAUSANNE

POUR L'OBTENTION DU GRADE DE DOCTEUR ÈS SCIENCES

PAR

Kasparas RAKSTYS

acceptée sur proposition du jury:

Prof. H. Girault, président du jury
Prof. M. K. Nazeeruddin, Prof. M. Graetzel, directeurs de thèse
Prof. T. Torres, rapporteur
Prof. G. Pozzi, rapporteur
Prof. A. Hagfeldt, rapporteur



ÉCOLE POLYTECHNIQUE
FÉDÉRALE DE LAUSANNE

Suisse
2018

Abstract

Perovskite solar cells have rapidly revolutionized the photovoltaic research showing an impressively dynamic progress on power conversion efficiency from 3.8 to 22% in only several years, a record for a nascent technology. Furthermore, inexpensive precursors and simple fabrication methods of perovskite materials hold a great potential for future low-cost energy generation enabling the global transition to a low-carbon society. The best performing device configuration of perovskite solar cell is composed of an electron transporting material, typically a mesoporous layer of titanium dioxide, which is infiltrated with perovskite material and coated with a hole transporting material. However, although perovskite solar cells have achieved high power conversion efficiency values, there are several challenges limiting the industrial realization of low-cost, stable, and high-efficiency photovoltaic devices.

To date, spiro-OMeTAD and PTAA are hole transporting materials of choice in order to maintain the highest efficiency, however, the prohibitively high price hinders progress towards cheap perovskite solar cell manufacturing and may contribute to more than 30% of the overall module cost. Additionally, such wide bandgap hole transporting materials typically require doping in order to match necessary electrical conductivity and the use of additives is problematic, since hygroscopic nature of doping makes the hole transporting layer highly hydrophilic leading to rapid degradation, negatively influencing the stability of the entire device.

In order to overcome these problems, the rational design, synthesis, and characterization of a variety of small molecule-based hole transporting materials have been on a focus of this thesis. Through judicious molecular engineering four innovative hole transporting materials KR131, KR216, KR374, and DDOF were developed via alternative synthetic schemes with the minimized number of steps and simple workup procedures allowing cost-effective upscale. Employing various characterization methods, the relationship between the molecular structure of the novel hole transporting materials and performance of perovskite solar cells was investigated, leading to a fundamental understanding of the requirements of the hole transporting materials and further improvement of the photovoltaic performance.

Furthermore, the synthesis of the dopant-free hole transporting materials based on push-pull architecture is presented. Highly ordered characteristic face-on organization of KR321 hole transporting molecules benefits to increased vertical charge carrier transport within a perovskite solar cell, leading to a power conversion efficiency over 19% with improved durability. The obtained result using pristine hole transporting material is the highest and outperforms most of the other dopant-free hole transporting materials reported to date. Highly hydrophobic nature of KR321 may serve as a protection of perovskite layer from the moisture and prevent the diffusion of external moieties, showing a promising avenue to stabilize perovskite solar cells.

Keywords: photovoltaic, perovskite solar cell, molecular engineering, hole transporting material, organic semiconductor, triazatruxene, bifuorenylidene, dispiro-oxepine, bistricyclic aromatic ene, organic synthesis.

Résumé

Les cellules solaires à base de pérovskite ont rapidement révolutionné la recherche photovoltaïque montrant un impressionnant progrès au niveau du rendement de conversion passant de 3,8 à 22% en seulement quelques années, un record pour une technologie naissante. En effet, les précurseurs peu coûteux et les méthodes de fabrication simples de matériaux de pérovskite présentent un énorme potentiel pour la génération future d'énergie à faible coût permettant la transition vers une société à faible émission de carbone. L'architecture de cellule solaire de pérovskite est généralement constituée d'un matériau de transport d'électrons, typiquement une couche mésoporeuse d'oxyde de titane, qui est infiltrée par le matériau pérovskite en question et revêtue d'un matériau de transport de trous. Cependant, bien que les cellules solaires de la pérovskite aient atteint des valeurs d'efficacité de conversion élevées, plusieurs défis limitent la réalisation industrielle de dispositifs photovoltaïques peu coûteux, stables et à haut rendement.

À ce jour, spiro-OMeTAD et PTAA sont les matériaux de transport de trous de référence afin d'obtenir le meilleur rendement, mais le prix prohibitif empêche de progresser vers la fabrication de cellules solaires à pérovskite bon marché et pourrait contribuer à plus de 30% du coût global du module. De plus, de tels matériaux de transport de trous à large bande nécessitent généralement d'être dopés pour correspondre à la conductivité électrique nécessaire et l'utilisation d'additifs est problématique, car la nature hygroscopique du dopage rend la couche de transport de trous hautement hydrophile entraînant une dégradation rapide, influençant négativement la stabilité de tout l'appareil.

Afin de surmonter ces problèmes, la conception rationnelle, la synthèse et la caractérisation de plusieurs matériaux de transport de trous à base de petites molécules ont fait l'objet de cette thèse. A travers une judicieuse ingénierie moléculaire quatre matériaux de transport de trous innovants KR131, KR216, KR374, et DDOF ont été développés à partir d'autres schémas synthétiques avec le minimum nombre d'étapes et de procédures de traitement simples permettant un haut rapport qualité-prix. En utilisant diverses méthodes de caractérisation, j'ai étudié la relation entre la structure moléculaire des nouveaux matériaux de transport des trous et la

performance des cellules solaires de la pérovskite, ce qui a permis de mieux comprendre les exigences des matériaux de transport des trous et d'améliorer la performance photovoltaïque.

Par ailleurs, la synthèse des matériaux de transport de trous non-dopés basés sur une architecture attraction-répulsion est ici présentée. L'organisation caractéristique hautement ordonnée des molécules de transport de trous KR321 permet un transport de charge verticale supérieur, ce qui mène à un rendement supérieur à 19%, tout en améliorant la durabilité. Le résultat obtenu en utilisant ce matériau de transport de trous pur (sans additifs) est le plus élevé et surpasse la plupart des autres matériaux de transport de trous non dopés rapportés à ce jour. La nature hautement hydrophobe du KR321 peut servir de protection à la couche de pérovskite contre l'humidité, ce qui est très prometteur pour stabiliser les cellules solaires en pérovskite.

Mots clés: photovoltaïque, pérovskite cellules solaires, ingénierie moléculaire, matériau de transport des trous, semi-conducteur organique, triazatruxène, bifluorénylidène, dispiro-oxépine, arôme bistricyclique, synthèse organico-chimique.

Symbols and Abbreviations

Å	Angstrom
Δ	Heat
Ω	Ohm
η	Solar energy-to-electricity conversion efficiency
λ	Wavelength
$h\nu$	Photon
σ	Electrical conductivity
μ	Hole-drift mobility
τ	Lifetime
2D	Two-dimensional
3D	Three-dimensional
A	Electron acceptor
aq.	Aqueous solution
a.u.	Arbitrary unit
AM1.5G	Reference solar spectral irradiance according to ASTM G173-03
ATT	Anthra[1,2- <i>b</i> :4,3- <i>b'</i> :5,6- <i>b''</i> :8,7- <i>b'''</i>]tetrathiophene
BA	<i>n</i> -Butylammonium
BAE	Bistricyclic aromatic ene
BT	Benzothiadiazole
BTT	Benzotrithiophene
Bu	Butyl
CB	Conduction band
CCD	Charge-coupled device
CHF	Swiss franc
cm	Centimeter
CT	Charge transfer
CV	Cyclic voltammetry
CWPL	Continuous wave photoluminescence
D	Electron donor
DBU	1,8-Diazabicyclo[5.4.0]undec-7-ene
DCE	1,2-Dichloroethane
DCM	Dichloromethane
DMF	<i>N,N</i> -dimethylformamide
DMSO	Dimethylsulfoxide
DSC	Differential scanning calorimetry

DSSC	Dye-sensitized solar cell
e	Elementary charge
e.g.	Exempli gratia (for example)
eq.	Equivalent
E_g	Electronic/optical bandgap
E_{HOMO}	Ground-state oxidation potential
E_{LUMO}	Excited-state redox potential
ESI	Electrospray ionization
et al.	Et alia (and others)
Et	Ethyl
ETL	Electron transporting layer
ETM	Electron transporting material
eV	Electronvolt
EXO	Exothermic process
F4TCNQ	2,3,5,6-Tetrafluoro-7,7,8,8-tetracyanoquinodimethane
FA	Formamidinium
FB	Forward bias
Fc	Ferrocene
FF	Fill factor
FK209	tris(2-(1 <i>H</i> -pyrazol-1-yl)-4- <i>tert</i> -butylpyridine)cobalt(III) tri[bis(trifluoromethane)sulfonimide]
FTO	Fluorine-doped tin oxide
g	Gram
GIWAXS	Grazing-incidence wide-angle X-ray scattering
h	Hour
Hex	Hexane
HOMO	Highest occupied molecular orbital
HTL	Hole transporting layer
HTM	Hole transporting material
Hz	Hertz
i	Intrinsic
<i>i</i> -	Iso
ICT	Intramolecular charge transfer
I_p	Ionization potential
IPCE	Incident photon-to-current conversion efficiency
ITO	Tin-doped indium oxide
J - V	Photocurrent-voltage
J_{max}	Maximum photocurrent
J_{sc}	Short-circuit photocurrent density
K	Kelvin
LDA	Lithium diisopropylamide
LiTFSI	Lithium bis(trifluoromethanesulfonyl)imide

M	Molar
m-TiO ₂	Mesoporous titanium dioxide
MA	Methylammonium
mA	Milliampere
MALDI	Matrix-assisted laser desorption/ionization
Me	Methyl
MS	Mass spectrometry
MO	Molecular orbital
mol%	Molar percentage
mW	Milliwatt
<i>n</i> -	Normal
n	Negative
NBS	<i>N</i> -bromosuccinimide
NHE	Normal hydrogen electrode
nm	Nanometer
NMR	Nuclear magnetic resonance
OFET	Organic field-effect transistor
<i>p</i> -	<i>para</i> -
p	Positive
PCBM	[6,6]-Phenyl-C ₆₁ -butyric acid methyl ester
PC ₇₁ BM	[6,6]-Phenyl-C ₇₁ -butyric acid methyl ester
PCE	Power conversion efficiency
PEDOT:PSS	Poly(3,4-ethylenedioxythiophene) polystyrene sulfonate
PESA	Photoelectron spectroscopy in air
P_{in}	Power of the incident light
P_{max}	Maximum power
PL	Photoluminescence
PMMA	Poly(methyl methacrylate)
ppm	Parts per million
Pr	Propyl
PSC	Perovskite solar cell
PTAA	Poly[bis(4-phenyl)(2,4,6-trimethylphenyl)amine]
PV	Photovoltaic
PW	Petawatt
rpm	Revolutions per minute
RT	Room temperature
s	Second
S	Siemens
SC	Short-circuit
SCLC	Space-charge limited current
SEM	Scanning electron microscope
SFX	Spiro[fluorene-9,9'-xanthene]
Spiro-OMeTAD	2,2',7,7'-Tetrakis-(<i>N,N'</i> -di- <i>p</i> -methoxyphenylamine)-9,9'-spirobifluorene

ssDSSC	Solid-state dye-sensitized solar cell
<i>t</i> -	Tertiary
T_{cr}	Crystallization temperature
T_{dec}	Decomposition temperature
T_g	Glass transition temperature
T_m	Melting point
TAA	Titanium diisopropoxide bis(acetylacetonate)
tBP	4- <i>t</i> -butylpyridine
TCO	Transparent conducting oxide
TCSPC	Time-correlated single photon counting
TD-DFT	Time-dependent density functional theory
TGA	Thermogravimetric analysis
THF	Tetrahydrofuran
TIPL	Time-integrated photoluminescence
TLC	Thin layer chromatography
TMS	Trimethylsilyl
Tol	Toluene
TPA	Triphenylamine
TRPL	Time-resolved photoluminescence
TW	Terawatt
UV	Ultraviolet
V	Volt
V_{max}	Maximum voltage
V_{oc}	Open-circuit voltage
VB	Valence band
Vis	Visible
vs.	Versus (against)
XPhos	2-Dicyclohexylphosphino-2',4',6'-triisopropylbiphenyl
XTOF	Xerographic time of flight

Contents

ABSTRACT	1
RÉSUMÉ	3
SYMBOLS AND ABBREVIATIONS	5
CONTENTS	9
CHAPTER 1 INTRODUCTION	13
1.1 PEROVSKITE SOLAR CELLS	14
1.1.1 <i>Organic-Inorganic Hybrid Perovskites</i>	14
1.1.2 <i>Architectures and Operating Mechanism</i>	15
1.1.3 <i>Components</i>	17
1.1.3.1 Working Electrode	17
1.1.3.2 Electron Transporting Material.....	17
1.1.3.3 Perovskite Absorber	18
1.1.3.4 Hole Transporting Material.....	18
1.1.3.5 Back Contact.....	20
1.1.4 <i>Photovoltaic Parameters</i>	21
1.1.4.1 Current-Voltage Curve	21
1.1.4.2 Incident Photon-to-Current Conversion Efficiency	22
1.2 ORGANIC SEMICONDUCTORS	23
1.2.1 <i>π-Conjugation</i>	23
1.2.2 <i>Charge Transport</i>	24
1.2.3 <i>HOMO-LUMO Tuning</i>	25
1.2.3.1 Donor-Donor (D-D) Type.....	27
1.2.3.2 Donor-Acceptor (D-A) Type	28
1.2.4 <i>Chemical Doping</i>	28
1.2.5 <i>Molecular Engineering of Hole Transporting Materials</i>	30
1.3 MOTIVATION AND OUTLINE OF THE THESIS.....	38
CHAPTER 2 TRIAZATRUXENE DERIVATIVES AS HOLE TRANSPORTING MATERIALS	41
2.1 INTRODUCTION	41
2.2 RESULTS AND DISCUSSION.....	42

2.2.1	<i>Design and Synthesis</i>	42
2.2.2	<i>Thermal, Optical, Electrochemical, and Photophysical Properties</i>	43
2.2.3	<i>Spectroscopy and Photovoltaic Properties of Perovskite-Based Devices</i>	45
2.3	CONCLUSIONS	49
2.4	SYNTHETIC METHODS AND PROCEDURES	50
CHAPTER 3	DOPANT-FREE HOLE TRANSPORTING MATERIALS BASED ON D-π-A ARCHITECTURE	55
3.1	INTRODUCTION	55
3.2	RESULTS AND DISCUSSION	56
3.2.1	<i>Design, Synthesis and Structure</i>	56
3.2.2	<i>Optical, Thermal, and Electrochemical Properties</i>	58
3.2.3	<i>Surface Geometry Investigation</i>	60
3.2.4	<i>Photophysical Properties</i>	61
3.2.5	<i>Photovoltaic Performance and Dopant-Free HTM-Based Device Stability</i>	62
3.3	CONCLUSIONS	64
3.4	SYNTHETIC METHODS AND PROCEDURES	65
CHAPTER 4	BIFLUORENYLIDENE-BASED HOLE TRANSPORTING MATERIAL	73
4.1	INTRODUCTION	73
4.2	RESULTS AND DISCUSSION	74
4.2.1	<i>Synthesis and Structure Optimization</i>	74
4.2.2	<i>Crystal Structure</i>	75
4.2.3	<i>Thermal, Optical, and Electrochemical Properties</i>	77
4.2.4	<i>Photoelectric Properties</i>	78
4.2.5	<i>Photovoltaic Performance</i>	80
4.3	CONCLUSIONS	81
4.4	SYNTHETIC METHODS AND PROCEDURES	81
4.4.1	<i>Synthesis Cost Analysis</i>	83
CHAPTER 5	HETEROMEROUS BISTRICYCLIC AROMATIC ENES AS HOLE TRANSPORTERS	85
5.1	INTRODUCTION	85
5.2	RESULTS AND DISCUSSION	86
5.2.1	<i>Design and Synthesis</i>	86
5.2.2	<i>Structure, Optical, and Electrochemical Properties</i>	87
5.2.3	<i>Photoelectrical and Photophysical Properties</i>	89
5.2.4	<i>Photovoltaic Properties</i>	91
5.3	CONCLUSIONS	92
5.4	SYNTHETIC METHODS AND PROCEDURES	93

5.4.1	<i>Synthesis Cost Analysis</i>	97
CHAPTER 6	DISPIRO-OXEPINE-BASED HOLE TRANSPORTING MATERIAL	99
6.1	INTRODUCTION	99
6.2	RESULTS AND DISCUSSION.....	100
6.2.1	<i>Synthesis and Crystal Structure</i>	100
6.2.2	<i>Structure Optimization</i>	102
6.2.3	<i>Thermal, Optical, and Electrochemical Characterization</i>	103
6.2.4	<i>Photophysical Properties</i>	105
6.2.5	<i>Photovoltaic Properties and Device Stability</i>	106
6.3	CONCLUSIONS.....	108
6.4	SYNTHETIC METHODS AND PROCEDURES	108
	SUMMARY	111
	EXPERIMENTAL PART	115
	GENERAL METHODS FOR SYNTHESIS.....	115
	STRUCTURAL CHARACTERIZATION	115
	COMPUTATIONAL DETAILS.....	116
	THERMAL MEASUREMENTS	116
	OPTICAL CHARACTERIZATION	116
	ELECTROCHEMICAL CHARACTERIZATION	116
	X-RAY MEASUREMENTS.....	117
	PHOTOELECTRICAL MEASUREMENTS	117
	SCANNING ELECTRON MICROSCOPY	118
	PHOTOPHYSICAL MEASUREMENTS	119
	FABRICATION AND CHARACTERIZATION OF PSCS.....	119
	APPENDIX	121
	¹ H/ ¹³ C NMR SPECTRA	121
	MS SPECTRA	134
	CRYSTALLOGRAPHIC PARAMETERS	147
	ACKNOWLEDGEMENTS	149
	REFERENCES	151
	CURRICULUM VITAE	163

Chapter 1 Introduction

In recent decades, depletion of fossil fuel reserves and increasing environmental pollution has urged attention toward renewable energy sources. Over 85% of the global energy requirements are satisfied by burning fossil fuels, which are the largest source of emission of carbon dioxide and other detrimental gasses, with devastating consequences on health and environment. Solar radiation is the largest reliable, sustainable, and long-term supply of carbon-free energy source that can be converted into other forms, such as heat and electricity. Conversion of sunlight directly into electricity using solar cells is one of the most promising approaches. However, efficient and inexpensive energy conversion by photovoltaic (PV) devices is a great challenge in the field of renewable energy. The annual predicted power potential for solar energy is 23 PW, while the projected total worldwide energy consumption in 2050 reaches only 27 TW.¹ Therefore, the solar energy is capable enough to fully cover the electricity demand around the globe and represents an ideal solution to supply sustainable, environmentally friendly and grid-free electricity.

First generation conventional silicon-based PV technology has been developed and commercialized many years ago and still remains the key player in the field for large area static solar harvesting, despite the fact that silicon is indirect bandgap semiconductor and has a low absorption coefficient. However, silicon-based solar panels are not always economically viable due to the cost-intensive manufacturing process required to make the necessarily pure material. Moreover, they are rigid, fragile and bulky limiting the mass production spread of lightweight integrated technologies.^{2,3}

Over the last three decades, many types of emerging PV technologies towards thin and flexible devices have attracted notable attention and are being developed. The potential advantages of emerging photovoltaic technologies are abundant and cheap materials, which can be solution processable reducing the fabrication costs of large-area printed applications for future low-cost energy generation enabling the global transition to carbon-free society.

In 1991, dye-sensitized solar cell (DSSC) was invented, using nanocrystalline mesoporous titanium dioxide (TiO₂) film, light-absorbing dye as the sensitizer, redox electrolyte, and the counter electrode.⁴ Sunlight power conversion efficiency (PCE) over 13% has been reached by

DSSC using a liquid electrolyte.^{5,6} Nevertheless, leakage and corrosion issues due to the redox electrolyte have caused instability problems influencing the commercialization of DSSCs. In order to accelerate the rate of market penetration of DSSCs, the focus has shifted toward solid-state devices in which the liquid electrolyte is replaced by a solid hole transporting material (HTM), obtaining all solid-state DSSC that is currently reported to reach an efficiency of 7.2%.⁷

Most recently, a breakthrough in PCE has been achieved by replacing traditional dyes with organic-inorganic hybrid perovskite material. Since the first report in 2009, perovskite-based solar cells (PSCs) have rapidly become the hottest topic in photovoltaics due to their unique optical and electrical properties.⁸ Fast development of device engineering allowed to prepare solar cells with PCE from 9% to over 22% within five years, already exceeding those of commercialized polycrystalline silicon solar cells.⁹⁻¹³

1.1 Perovskite Solar Cells

1.1.1 Organic-Inorganic Hybrid Perovskites

The term “perovskite” was attributed to the crystal structure of calcium titanate (CaTiO_3), which was discovered by the German mineralogist Gustav Rose in 1839 and named in honor of the Russian mineralogist Lev Perovski. The organic-inorganic hybrid halide perovskites were widely studied in the 1990s for the application in transistor technology and light emitting diodes, due to their suitable optoelectronic properties and solution processability.¹⁴⁻¹⁷ Organic-inorganic hybrid halide perovskites are a group of materials represented by the general formula ABX_3 , where A is a small monovalent organic methylammonium (CH_3NH_3^+) or formamidinium ($\text{NH}_2=\text{CH}_2\text{NH}_2^+$) cation, B is a divalent cation (Pb^{2+} or Sn^{2+}) and X stands for halide anion (I⁻, Br⁻, or Cl⁻).^{18,19} The ideal perovskite structure has cubic-symmetry (Figure 1.1a), where the A cation is 12-fold coordinated by the X anion in a cuboctahedral arrangement and the B cation is 6-fold coordinated by X in an octahedral configuration.

Although organolead halide perovskites have been known to have a good charge transporting properties for over a decade,²⁰ the first work, with the perovskite as absorbing material in DSSC architecture was published only in 2009, where methylammonium lead triiodide (MAPbI_3) and methylammonium lead tribromide (MAPbBr_3) were used as sensitizers replacing organic dyes.⁸ Particularly, MAPbI_3 exhibits excellent optoelectronic properties covering

almost the whole visible region with a direct bandgap of 1.54 eV, corresponding to an absorption onset of about 800 nm (Figure 1.1b).²¹

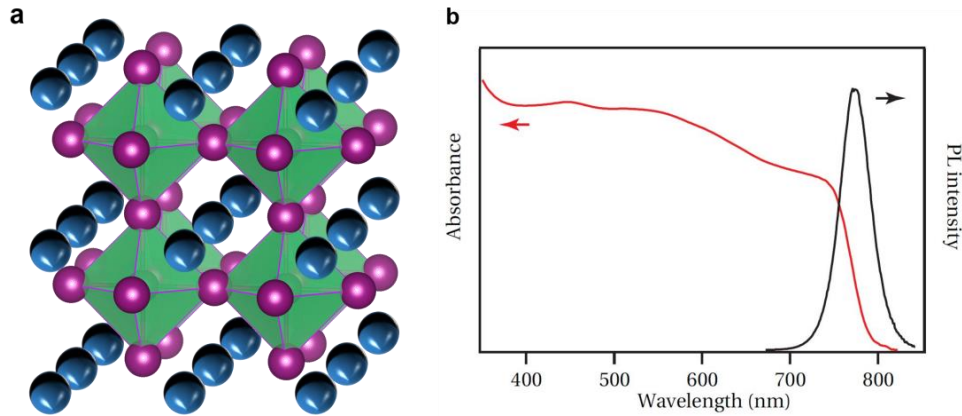


Figure 1.1 a) Projected view of the 3D ABX₃ perovskite crystal structure (A cations represented in blue, B cations in green and X anions in violet, respectively); b) absorption and photoluminescence (PL) spectra of a thin film of CH₃NH₃PbI₃.

With the further development of the PSCs, more complex multi-cation and mixed-anion compositions of the perovskite absorber layer were being used. The first changes were made mostly to improve light harvesting properties and get closer to the optimum bandgap by incorporation of the formamidinium (FA) cation and Br⁻/I⁻ anion mixture.^{22,23} Later on, modifications in composition were made in order to stabilize the perovskite: great improvement in reproducibility and stability was achieved by incorporation of the cesium cation. The Cs_{0.1}(MA_{0.15}FA_{0.85})_{0.9}Pb(I_{0.85}Br_{0.15})₃ composition became standard for the further development of the PSCs.²⁴

1.1.2 Architectures and Operating Mechanism

Hybrid lead halide perovskites can cumulate the function of light absorption with n- and p-type conduction.^{25,26} This ambipolar charge transport property of perovskite makes the design of PSCs quite versatile. The common device architecture is composed of five layers, which allow several combinations of materials: transparent electrode, n-type semiconducting electron transporting material (ETM), photoactive perovskite, p-type semiconducting hole transporting material (HTM) and metallic electrode. Depending on the structure of the n-type layer, PSCs can be cataloged into mesoscopic or planar heterojunction structures,^{27,28} where both can be further divided into two categories varying on the position of the p-type and n-type

selective contact materials. The solar cells could thus be considered n-i-p (conventional) and p-i-n (inverted) structures,²⁹⁻³¹ where the perovskite is an intrinsic semiconductor, and light enters through the n-type or the p-type layer, resulting in four different device architectures. Moreover, since the perovskites have been proved to be ambipolar semiconductors, device architectures of PSCs that employ only one of the two selective contacts, such as ETM-free or HTM-free have been demonstrated.³²⁻³⁵ However, these typically fail to produce high PCE, therefore it is generally agreed with the view that both the electron and hole selective contact materials are vital to reach high performance in PSCs.

To date, the mesoscopic n-i-p PSC device configuration shows the highest PCE reaching 22.1%.³⁶ Typically, the glassy transparent electrode fluorine-doped tin oxide (FTO) is coated with the compact electron transporting layer (ETL) made from TiO_2 and the additional mesoscopic TiO_2 scaffold is used on top, following by infiltration with photoactive perovskite material. A hole transporting layer (HTL) is deposited on top of the perovskite, followed by the evaporation of a metallic top electrode, usually made of a high work function metal, such as gold, as shown in Figure 1.2a.³⁷⁻⁴¹

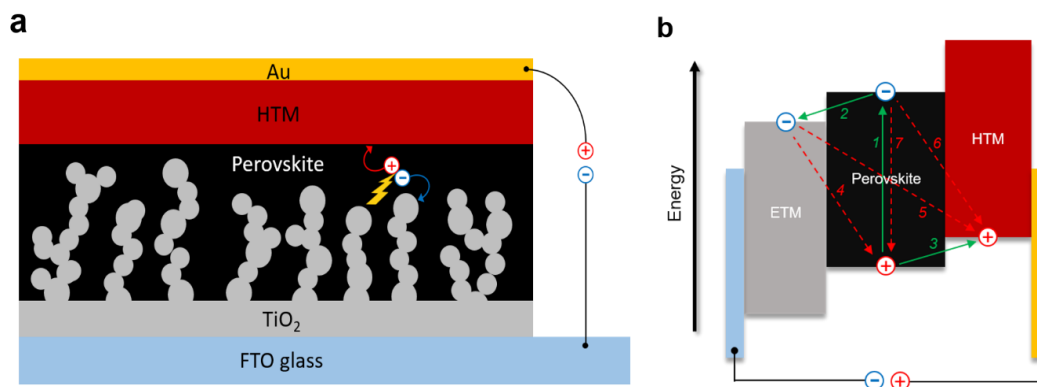


Figure 1.2 a) Structure of typical mesoscopic n-i-p device configuration perovskite solar cell; b) schematic illustration of energy levels and charge-transfer processes in PSC.

The simplified operating mechanism and key charge-transfer processes of the typical PSC are shown in Figure 1.2b. Incident photons excite the perovskite light harvesting layer through the transparent electrode, leading to the photogeneration of electron-hole pairs in the material. Electrons are separated (1) from the holes and injected (2) into the conduction band (CB) of the electron transporting material before migrating to the anode. Meanwhile, the holes generated in the perovskite are transferred (3) to the HOMO level of the hole transporting mate-

rial, before injection of the hole into the cathode. Electron and hole injections occur quite efficient due to the high diffusion lengths of charge carriers. Undesirable charge transfer (CT) processes such as back CT recombination of the charge carriers at three ETM/perovskite/HTM interfaces also occur (4-6), including non-radiative recombination (7). The kinetics of these processes are largely expected to control the overall photovoltaic conversion efficiency.

1.1.3 Components

1.1.3.1 Working Electrode

The cells generally consist of a transparent conducting oxide (TCO) as working electrode: fluorine-doped tin oxide $\text{SnO}_2:\text{F}$ (FTO) or tin-doped indium oxide (ITO), which is coated on glass or plastic substrate to provide electrical conductivity. FTO has been recognized as a very promising material because it is relatively stable under atmospheric conditions, chemically inert, mechanically hard, high-temperature resistant, has a high tolerance to physical abrasion, high transparency, low reflection and absorption, low sheet resistance and is less expensive than ITO. In this work, all substrates used for PSCs fabrication were FTO glass from Nippon Sheet Glass with a sheet resistance of $10 \Omega/\text{square}$.

1.1.3.2 Electron Transporting Material

The most important characteristic of an ETM is to satisfy band alignment with the perovskite layer, having conduction band (CB) or lowest unoccupied molecular orbital (LUMO) higher than that of the perovskite active layer. The purpose of the ETM is to prevent the photoinjected electrons in the conductive substrate from direct recombination with the holes. It must have high transmittance in the UV-Vis region so that a photon can pass through easily and be absorbed by the perovskite absorber. The ETM layer, which acts as a hole blocking layer is directly deposited onto the conductive glass substrate and should form a compact, continuous n-type contact intending to provide electron selectivity.

A number of metal oxides as TiO_2 , ZnO , SnO_2 , etc. have been demonstrated to be useful as ETMs for planar and mesoscopic PSCs.⁴²⁻⁴⁴ In latter, it is common to use the same material for the mesoscopic scaffold. TiO_2 has been proved to be leading ETM in PSCs, with a conduction band (CB) of 4.4 eV and the wide bandgap of approximately 3.2 eV.⁴⁵ Having CB slightly lower than that of perovskite it guarantees electron injection through direct contact, and its very low-lying valence band (VB) provides outstanding hole blocking properties. Furthermore, it is low-

cost and non-toxic material. In this work, as well as the most frequently using in different research groups worldwide, the TiO₂ blocking layer was deposited by aerosol spray pyrolysis technique,⁴⁶ followed by mesoporous TiO₂ scaffold deposition by spin coating. The TiO₂ framework facilitates the crystallization of the perovskite with enhanced nucleation at the surface and enlarges the contact area between the perovskite and the ETM to efficiently collect photogenerated electrons.

In case of inverted configuration, organic semiconductors have been successfully employed as ETMs. To the contrary, LUMO must be lower than that of the perovskite layer and many organics, including fullerene-based PCBM and PC₇₁BM, satisfy the criteria, allowing device structures on flexible substrates.⁴⁷⁻⁵⁰

1.1.3.3 Perovskite Absorber

Organolead halide perovskite layer is the key component in all possible device configurations and is crucial for light absorption and photogeneration of free carriers. It has received the huge attention for solar cell applications, mainly due to its fascinating optoelectronic properties, inexpensive precursors, and simple fabrication methods. In particular, CH₃NH₃PbI₃ has a wide bandgap of 1.54 eV, with CB and VB positioned at about 3.9 eV and 5.4 eV vs. vacuum, respectively, showing the excellent driving forces for the electron injection into the TiO₂ CB and the hole injection into the HOMO level of the HTM. Methylammonium lead iodide has a very strong tendency to form and crystallize, even at room temperature, enabling the convenient solution processable deposition techniques, simply using solutions of low-cost PbI₂ and CH₃NH₃I precursors in common organic solvents as *N,N*-dimethylformamide (DMF) or dimethylsulfoxide (DMSO). During the solution process, the perovskite crystallizes on the substrate due to the evaporation of the organic solvent. Various deposition protocols of perovskite films such as sequential solution deposition, spin coating, vapor-assisted deposition, thermal evaporation, and vacuum flash-assisted have been intensively studied.⁵¹⁻⁵⁷

1.1.3.4 Hole Transporting Material

HTM is important active material in PSC, responsible for efficient hole extraction at the perovskite/HTM interface and preventing undesirable charge transfer processes, leading to improvement in the performance of the device. For efficient device operation, well-aligned energy levels with perovskite are crucial: HOMO level must be less negative than that of perovskite for efficient hole injection, while the high-lying LUMO level will ensure low electron affinity enabling beneficial electron blocking properties. An ideal HTM candidate should also

have high hole mobility to reduce losses during hole transport to the contact, as well as sufficient conductivity. HTM has to be well soluble and should not require strong polar and protic solvents, as such solvents may dissolve the perovskite layer. Furthermore, since perovskites are known to be sensitive to moisture and oxygen, the hole transporting layer should act as protection from the air and prevent the diffusion of external moieties, therefore high thermal and photochemical stability, as well as high hydrophobicity, are desirable properties of HTM to resist from degradation factors and ensure long-term durable PV operation. On the other hand, to ensure low-cost PSC manufacturing, an ideal HTM candidate has to be easily affordable for the reasonable cost.

A huge research interest directed into new HTM candidates has been raised to find a better understanding in relationship between the HTM and PSC performance. A large number and different types of HTMs have been reported so far, based on organic⁵⁸⁻⁶⁹ and inorganic⁷⁰⁻⁷² nature, where organic HTMs can further be divided into small-molecules and conducting polymers.

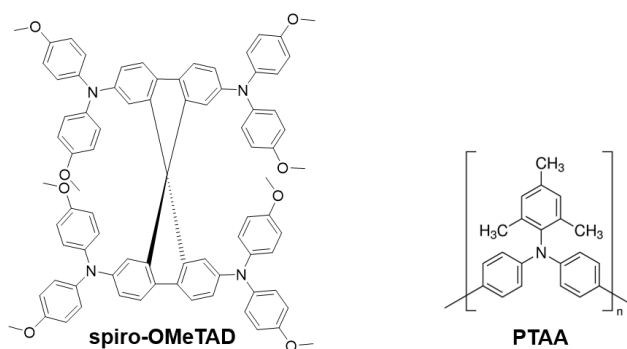


Figure 1.3 Chemical structures of 2,2',7,7'-tetrakis-(*N,N*-di-*p*-methoxyphenylamine)-9,9'-spirobifluorene (spiro-OMeTAD) and poly[bis(4-phenyl)(2,4,6-trimethylphenyl)amine] (PTAA).

Since the first report as HTM in ssDSSC two decades ago,⁷³ organic p-type semiconductor 2,2',7,7'-tetrakis-(*N,N*-di-*p*-methoxyphenylamine)-9,9'-spirobifluorene (spiro-OMeTAD) is still dominating the field and has been selected as the benchmark HTM to achieve high PCE values for PSCs (Figure 1.3). Spiro-MeOTAD has a HOMO level around -5.1 eV, exhibits a hole mobility in the range of 10^{-5} to 10^{-4} $\text{cm}^2 \text{V}^{-1} \text{s}^{-1}$ and has high solubility in organic solvents such as toluene or chlorobenzene, giving almost colorless thin films. However, the tedious multi-step synthesis of spiro-OMeTAD makes it prohibitively expensive and cost-ineffective. Typically, high-purity sublimation-grade spiro-OMeTAD is required to obtain high-performance devices. Moreover, it has been demonstrated as a limiting factor for the long-term stability of the device.⁷⁴

Among the polymers, triphenylamine-based poly[bis(4-phenyl)(2,4,6-trimethylphenyl)amine] (PTAA) is the most efficient and holds the world record so far.^{36,75} The superior performance of PTAA arises from the exceptional hole mobility ($10^{-3} - 10^{-2} \text{ cm}^2 \text{ V}^{-1} \text{ s}^{-1}$). However, it is extremely expensive reaching the price of $\sim 2000 \text{ CHF/g}$.

Among the inorganic hole conductors, only very few examples reaching high efficiency have been shown in the literature. Due to the limited choice of suitable materials, inorganic HTMs remain a quite unexplored alternative to the organic ones. Two most interesting examples of this class are copper thiocyanate (CuSCN) and delafossite phase copper gallium oxide (CuGaO₂). These wide bandgap semiconductors have high conductivity, suitable energy levels and good transparency. CuSCN has been studied by several research groups allowing to improve device performance from 12.4% to the recent achievement of 18%.⁷⁶⁻⁷⁸ CuSCN-based devices also demonstrate improved stability under the dry air and thermal annealing. Very recently, solution-processed CuGaO₂ nanoplates were employed as the hole transporting layer yielding the devices with the efficiency of 18.5% and significantly improved long-term ambient stability.⁷⁹

In this work, organic small molecule-based HTMs have been employed in the PSCs with optimized perovskite compositions of (MAPbBr₃)_{0.15}(FAPbI₃)_{0.85} and Cs_{0.1}(MA_{0.15}FA_{0.85})_{0.9}Pb(I_{0.85}Br_{0.15})₃ to investigate the influence of different hole transporting layers on device performance and other properties. Spiro-OMeTAD was used as a reference HTM.

1.1.3.5 Back Contact

Counter-electrode as the back contact is required to complete the internal circuit and to function as an electrode providing current and voltage for the external electrical work. Traditionally, the back contact of PSC is formed by thermal evaporation of a noble metal with high work function, required to reach high open-circuit voltage of the devices, such as gold or silver, but both have limitations: Au is expensive and migrates through the HTM once exposed to higher temperatures, where Ag is unstable due to the oxidation. In case of HTM-free PSCs, the carbon composites were demonstrated to be a promising replacement for Au back contact electrodes, allowing simple deposition methods as screen-printing or drop-casting.^{80,81}

1.1.4 Photovoltaic Parameters

The performance of PSC is characterized by photocurrent-voltage (J - V) curve (open-circuit voltage (V_{oc}), short-circuit photocurrent density (J_{sc}), fill factor (FF)) and incident photon-to-current conversion efficiency (IPCE).

1.1.4.1 Current-Voltage Curve

The J - V measurement is the most important technique for the evaluation of the photovoltaic performance of the perovskite solar cell. The following photovoltaic parameters such as short-circuit current, open-circuit potential, fill factor and power conversion efficiency are obtained from a J - V curve. Typically the measurement under 1 sun intensity at standard AM1.5G illumination ($P_{in} = 100 \text{ mW cm}^{-2}$) is used to classify the solar cell photovoltaic performance and it is done by applying an external potential bias to the cell while measuring the current response. As shown in Figure 1.4, the current density is recorded along the scan of linearly-varying voltage in the direction from V_{oc} to 0 V to provide a J - V curve, where the V_{oc} is determined as the measured potential at open-circuit condition when the current density equals to 0 mA cm^{-2} and the J_{sc} is determined monitoring current density at short-circuit when the photovoltage equals to 0 V. Therefore, the V_{oc} (V) is the difference in electrical potential between two terminals of a cell, when no current is flowing and the J_{sc} (mA cm^{-2}) is the photocurrent per unit area when device is short-circuited.

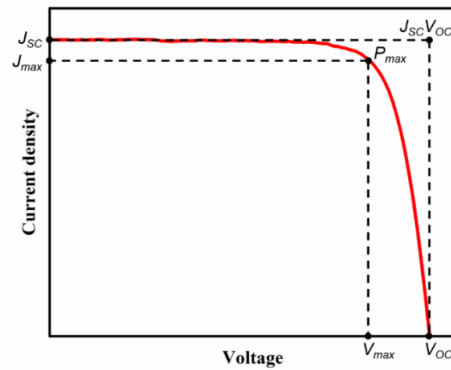


Figure 1.4 Illustration of typical current-voltage (J - V) characteristics of perovskite solar cell under illumination and its important parameters.

The maximum power (P_{max}) point then can be found as the product of the photocurrent and voltage reaching maximum values (J_{max} and V_{max}). The overall power conversion efficiency (η) of a device is therefore defined by the ratio of the maximum power to the power of the incident light (P_{in}) as the following equation:

$$\eta = \frac{P_{max}}{P_{in}} = \frac{J_{sc} V_{oc} FF}{P_{in}}$$

For PSCs, the J - V curves are often highly dependent on the scan direction, which is called hysteresis behavior.⁸² Therefore, the scan direction and the scan rate are important for obtaining reliable photovoltaic parameters. That is because higher efficiency may be obtained holding a perovskite device at a forward bias voltage before measurement than that found when the device has been reverse biased or when the device is held at the maximum power point or at short-circuit. In addition, measuring the device at the rate faster than its response time may also result in varying efficiency measurements.⁸³ Although the origins causing hysteresis remain controversial, possible reasons have been proposed such as ion migration, unbalanced charge collection rates, and ferroelectricity.^{84–86}

The fill factor (FF) is a parameter to evaluate the deviation of the measured solar cell efficiency from the theoretical maximum power output of the cell and is defined as the ratio of the maximum power (P_{max}) to the external short- and open-circuit values:

$$FF = \frac{J_{max} V_{max}}{J_{sc} V_{oc}}$$

1.1.4.2 Incident Photon-to-Current Conversion Efficiency

IPCE indicates how efficiently the incoming photons at a specific wavelength are converted into electrons by the PSC device. The IPCE spectrum is obtained when the device is exposed to illumination and scanning through each monochromatic light wavelength while recording the photocurrent output simultaneously.

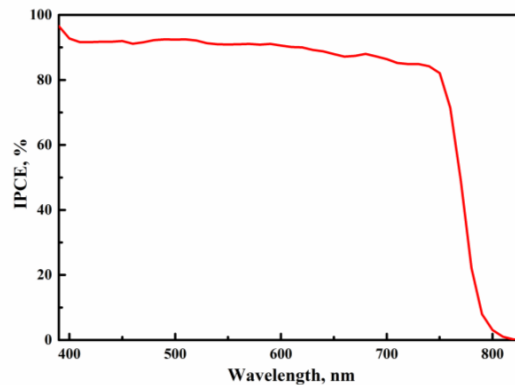


Figure 1.5 Typical IPCE spectrum of perovskite device as a function of wavelength.

Figure 1.5 shows an example of IPCE spectrum of a typical PSC, calculated by the following equation:

$$IPCE(\lambda) = \frac{n_{electrons}(\lambda)}{n_{photons}(\lambda)} = \frac{J_{sc}(\lambda)}{e P_{in}(\lambda)}$$

Where the $J_{sc}(\lambda)$ is the short-circuit photocurrent density under monochromatic irradiation, $P_{in}(\lambda)$ is the input optical power, and e stands for an elementary charge. Integration of the product of IPCE and $J_{sc}(\lambda)$ over the wavelength of the incoming light yields the total short-circuit photocurrent density that is expected to be generated by the solar cell.

1.2 Organic Semiconductors

Organic semiconductors have gained much interest and have been studied for over five decades, resulting in thousands of materials designed and synthesized. As a class, organic semiconductors have very different electrical properties when compared to traditional, inorganic semiconductors, where atoms are held together with strong covalent or ionic bonds forming highly crystalline solids. Organic semiconductors are composed of individual molecules that are weakly bound together by van der Waals forces, hydrogen bonding, and π - π interactions, resulting in relatively disordered systems. All organic semiconducting materials, whether they are small molecules or polymers, rely on conjugated π -electron systems for conduction. Holes and electrons in π orbitals are the typical charge carriers in organic semiconductors, where charge transport typically depends on the ability of the charge carriers to move from one molecule to another. Changing the degree of π -conjugation within an organic solid has a large impact on electrical properties. Increased conjugation length causes a greater degree of electron delocalization, increasing the mobility of charges through the π -bonding system.^{87,88} Although organic materials suffer from comparably low charge carrier mobilities due to weak intermolecular interactions, the main advantages include wide synthetic variety, tunable properties, high purity and simple solution-based processability (compatible with the large area, low temperature, and structural flexibility).

1.2.1 π -Conjugation

Systems are considered π -conjugated when alternating carbon-containing single and double bonds are present in their molecular structure. The sp^2 hybridization is the condition to have

double bonds: three electrons per carbon atom are employed to form strong C-C σ bond, by creating an orbital overlap of two sp^2 orbitals, while the leftover non-hybridized fourth is employed to give an additional C-C π bond, having weak interaction due to small electron cloud overlap above and below the molecular plane, leading to semiconducting properties (Figure 1.6a).

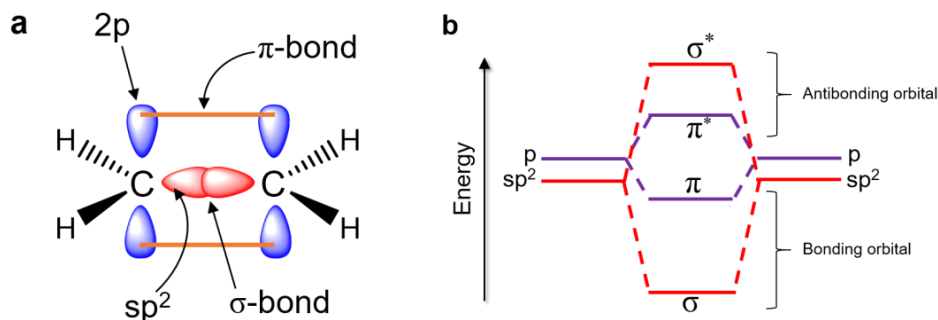


Figure 1.6 a) Orbital structure of σ - and π -bonding in ethylene molecule, b) schematic HOMO-LUMO energy level diagram, taken as the π - π^* gap.

The strength of the overlapping σ -bonds leads to strong bonding (σ) and antibonding (σ^*) molecular orbitals (MO). The weaker interactions of the parallel non-hybridized orbitals give correspondingly weaker bonding (π) and antibonding (π^*) MO energy levels, making the π - π^* transition the smallest possible electronic excitation within the molecule, thus the lowest-energy option in a π -conjugated system (Figure 1.6b). The π -bonding MO is called the highest occupied molecular orbital (HOMO) and the π^* -antibonding MO is the lowest unoccupied molecular orbital (LUMO), respectively, being analogous to the valence and conduction bands. The separation of these energy levels is then defined as the bandgap E_g of the organic material and indicates the minimum energy required to promote an electron from the HOMO to the LUMO of the molecule.

1.2.2 Charge Transport

Organic semiconductors are commonly classified as p-type (hole transporting) or n-type (electron transporting) depending on which type of charge carrier is more efficiently transferred through the material. Theoretically, all organic semiconductors should be able to conduct both charge carriers, but the differences in internal reorganization energies or Fermi level of the electrodes relative to the HOMO and LUMO energies of the material can favor one type of

charge transport.^{89,90} Generally, molecules having high HOMO levels exhibit electron-donating properties, therefore they are good candidates for hole transport, while electron-accepting molecules with low HOMO levels act as electron transporters.

In organic materials, the charge is localized within single molecules, therefore MOs of each molecule play the role of the HOMO and LUMO. Extended delocalized π -electron systems enable to transport charge carriers in the optoelectronic devices. Typically, charge transport within organic materials occurs via charge hopping from localized states and can be described as a charge carrier transfer between charged and neighboring neutral molecules, overcoming an energy barrier to move from one molecule to the next (Figure 1.7). Efficient charge transport requires that the charges be able to move from molecule to the adjacent one without being trapped or scattered, therefore factors like molecular packing, disorder, the presence of impurities or molecular weight are very important for the design of new semiconductors.^{91,92}

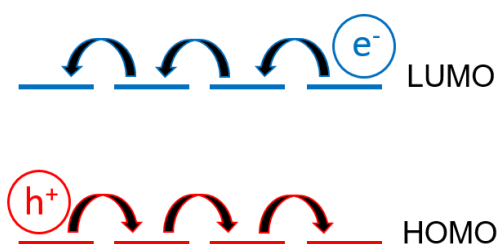


Figure 1.7 Schematic illustration of electron and hole hopping transport within organic molecules.

1.2.3 HOMO-LUMO Tuning

A fine tuning of the electronic properties of organic molecular semiconductors allows the tailoring of the HOMO-LUMO levels as well as the bandgap. This is crucial for optoelectronic devices such as perovskite solar cells since the mismatch between the charge transporting materials, photoactive perovskite, and the electrodes could lead to large injection barriers or contact resistances. Therefore, it is of great importance to optimize the positions of the energy levels of the electron and hole transporting materials leading to the most efficient injection at the interfaces. In Figure 1.8, it is shown the typical ranges of HOMO and LUMO levels of p-type and n-type semiconductors, respectively, and compared with energy levels of methylammonium lead triiodide perovskite and contact materials (FTO and Au).

The stable hole transporting materials generally have HOMO levels between -4.9 and -5.5 eV, resulting in ohmic contact with high work function metals such as gold (5.1 eV). Higher HOMO

values than -4.9 eV typically lead to the instability of semiconductor due to the oxidation in air. This can be easily tuned by changing the electron-donating groups, in other words pushing the π -orbital selectively, because HOMO largely contributes from the donors on the molecule. On the other hand, a stable electron transporting materials generally have LUMO levels between -3.5 and -4.5 eV. In this case, molecules with strong electron-withdrawing groups in the periphery are typically used to increase the electron affinity and stabilize the anionic form of the molecule. A minimum offset of approximately 0.1-0.2 eV between the LUMO of the ETM and the HOMO of the HTM with respective perovskite LUMO and HOMO levels is typically necessary to ensure efficient electron and hole injection at the interfaces. This leads to the conclusion that the ideal LUMO energy level of ETM should have a value of around -4.0 to -4.1 eV, while the HOMO of HTM should lie at -5.2 to -5.3 eV, respectively, in case of $\text{CH}_3\text{NH}_3\text{PbI}_3$ perovskite.

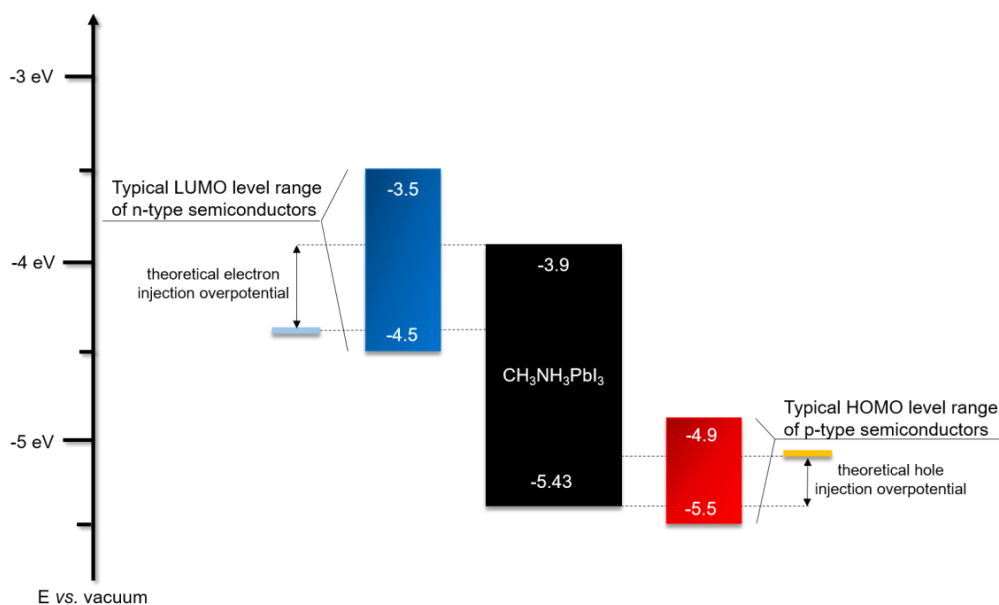


Figure 1.8 Energy level diagram of organic semiconductors, $\text{CH}_3\text{NH}_3\text{PbI}_3$ perovskite and typical contact materials FTO and gold, showing general range of HOMO and LUMO levels of different type semiconducting materials and theoretical injection overpotentials.

In this work, the main focus was on the synthesis of a novel organic hole transporting materials possessing suitable HOMO level for efficient hole extraction from perovskite as well as an efficient electron blocking properties resulted from high-lying LUMO level. A vast variety of organic HTMs has been studied and could be classified as donor-donor (D-D or D- π -D) or donor-acceptor (D-A or D- π -A) systems depending on the molecular architecture. This leads to very different fundamental aspects for tuning the electronic properties.

1.2.3.1 Donor-Donor (D-D) Type

Typical electron donors D are obtained by substituting functional groups like $-NH_2$, $-OH$ or $-SH$. Therefore, generally attaching one electron donor moiety with another of various electron-donating nature leads to the selective HOMO tuning. However, finding the donor partners can be tricky. Simply attaching the donors with HOMO of interest will not necessarily lead to the good HTM with suitable HOMO level with perovskite. Moreover, having an extra π -bridge conjugation between two donors can also significantly change the electronic properties as well as steric geometry. Therefore, a rational design has to be taken while changing the electron-donating groups, in order to push the π -orbital to match with perovskite.

The majority of HTM molecules for PSC are prepared by the cross-coupling reaction between the corresponding core component, which generally has weak electron-donating properties, and another donating moiety, which is usually responsible for HOMO tuning. General principle for molecular design strategy of energy level engineering using different strength donors of D-D type HTMs is shown in Figure 1.9.

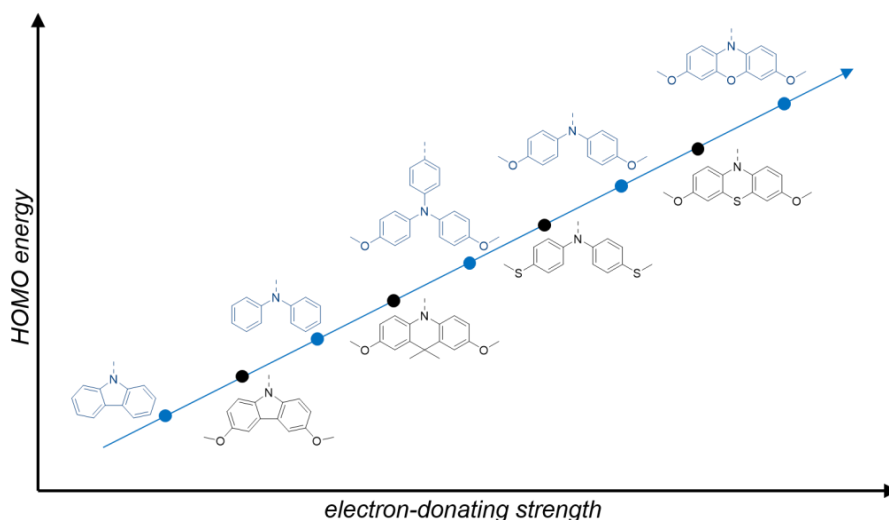


Figure 1.9 Schematic illustration of molecular design strategy of energy level engineering with different strength electron-donating units.

The most widely employed electron donors are diphenylamine, carbazole or triphenylamine moieties with or without alkoxy groups (typically methoxy) as auxiliary electron donors. The HOMO level then may be easily tailored knowing the trend of common donor strength: carbazole < dimethoxycarbazole < diphenylamine < dimethoxyacridine < dimethoxythiophenylamine < dimethylthiodiphenylamine < dimethoxydiphenylamine < dimethoxyphenothiazine < dimethoxyphenoxazine, while the LUMO level remains almost unaltered.

Due to the very weak interaction between two donating moieties, this type of molecules typically exhibits almost no visible absorption yielding colorless to pale colored solids, which is advantageous since it does not interfere with perovskite in the absorption of light. On the other hand, such a wide bandgap organic semiconductors suffer from relatively low conductivity. To overcome this problem, typically they are doped with external additives to generate additional charge carriers.

1.2.3.2 Donor-Acceptor (D-A) Type

Organic D-A systems, also widely known as push-pull systems, possess intramolecular charge transfer (ICT) and generates a molecular dipole between donor and acceptor parts, generally leading to deeply colored chromophores. Due to strong ICT, this type of molecules have a great potential to show high charge carrier mobility, therefore are very promising candidates as dopant-free HTMs. Most of the electron acceptors involve substituents featuring $-NO_2$, $-CN$, or $-CHO$ groups as well as electron deficient heterocyclic compounds as triazines, benzoxadiazoles or benzothiadiazoles,⁹³⁻⁹⁵ while the π -linker is most commonly constructed by a combination of multiple bonds and aromatic units and may act as auxiliary electron donor or acceptor. Push-pull molecules may adopt several arrangements including linear (D- π -A), quadrupolar (D- π -A- π -D or A- π -D- π -A) and tripodal ((D- π)₃-A or (A- π)₃-D) systems.⁹⁶

The electronic properties of D-A molecules can be engineered according to the each part of the system. The same as for D-D type, the donor moiety is mainly responsible for HOMO tuning, therefore replacing the weaker donor with stronger one, will lead to selective HOMO destabilization, in other words, will shorten the bandgap. In contrary, the LUMO level can be selectively tuned engineering the electron-accepting moiety in the system. In general, the LUMO level can be lowered by increasing the strength of the electron-acceptor, leading to the lower bandgaps due to the stronger ICT and red-shift response in absorption spectrum.

1.2.4 Chemical Doping

Chemical doping is an important method in organic electronics to enhance device efficiency by controlling the energy levels, increasing the conductivity, and reducing ohmic losses in charge transport layers and injection barriers at the interface with the electrodes.^{97,98} The basic principle of doping in organic semiconductors is that additional mobile charge carriers are generated by electron donors or acceptors, which either donate electrons to the LUMO (n-

type doping) or remove electrons from the HOMO to generate holes (p-type doping) of an intrinsic semiconductor (Figure 1.10).^{99,100}

The introduction of additional charge carriers, holes or electrons, leads to an increased charge carrier density in the organic semiconductor, resulting in a higher conductivity. The key requirement for efficient doping process is the suitable electron affinity of the dopant with respect to the energy levels of an organic semiconductor.

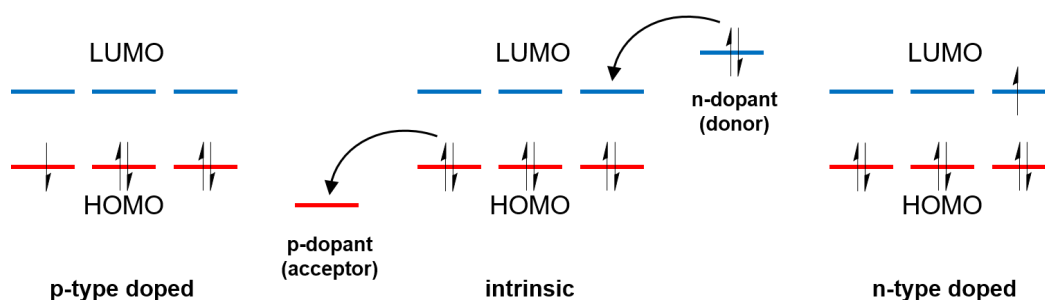


Figure 1.10 Schematic illustration of the doping mechanisms for molecular p-type (left) and n-type (right) doping. In p-type doping, the dopant is an acceptor, where in n-type it is a donor, respectively.

Traditionally, the hole transporting layer of PSCs is heavily doped with p-type dopants to provide the necessary electrical conductivity for the state-of-art spiro-OMeTAD and other wide bandgap HTMs. Numerous p-type dopants have been developed and realized including 2,3,5,6-tetrafluoro-7,7,8,8-tetracyanoquinodimethane (F4TCNQ),^{101–103} benzoyl peroxide,¹⁰⁴ copper(II),¹⁰⁵ and cobalt(III)^{7,106} complexes (Figure 1.11). To date, the combination of second generation cobalt complex-based tris(2-(1*H*-pyrazol-1-yl)-4-*tert*-butylpyridine)cobalt(III) tri[bis(trifluoromethane)sulfonimide] (FK209)¹⁰⁷ and lithium bis(trifluoromethanesulfonyl)imide (LiTFSI) is routinely employed as p-type dopant in PSCs.^{108–111}

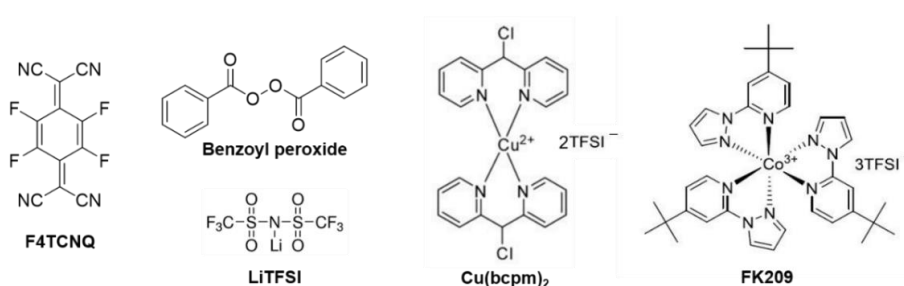


Figure 1.11 Chemical structures of different p-type dopants for HTMs employed in PSCs.

On the other hand, the use of dopants is problematic, since the hygroscopic nature of the lithium salt makes the HTL highly hydrophilic and the Co(III) dopant shows a tendency towards

chemical degradation, negatively influencing the stability of the entire device.^{112,113} Therefore, a promising solution for stabilizing PSCs may be the appropriate choice of dopant-free HTMs.

1.2.5 Molecular Engineering of Hole Transporting Materials

Organic chemistry literally offers an infinite number of well-defined structural possibilities enabling the rational tuning for electronic properties, molecular functionality, and intermolecular interactions. This allows to achieve plenty of desirable characteristics that are necessary for high performance hole transporting materials in perovskite solar cells such as high mobility, well-aligned energy levels, material stability, and hydrophobicity. On the other hand, to ensure low-cost perovskite solar cell manufacturing, an ideal HTM candidate has to be easily affordable by simple synthetic schemes with a minimized number of steps and easy workup and purification procedures for cost-effective upscale.

Triphenylamine is known to be a parent building block for HTMs.¹¹⁴ The gradual rise in understanding of the electronic properties of triphenylamine-based materials led to the discovery of amazing electronic properties and applications of triphenylamine compounds. Exhibiting a remarkable charge transporting properties, good thermal and morphological stability phenylamines have been of great interest as HTMs in optoelectronic devices.^{115,116} Being a good electron donor it possesses two basic properties: easy oxidizability of the amine nitrogen atom and the ability to transport positive charge efficiently. Many of the aromatic amines are HTMs, where the electron donating amine nitrogen atom is responsible for the hole transporting behavior.¹¹⁷ Functionalization of triphenylamine generally leads to the electron-rich star-shaped molecular glasses. Fused ring systems, especially with the introduction of heteroatoms (e.g. sulfur, nitrogen or oxygen), are known to maximize the π -orbital overlap, inducing face-to-face π -stacking and facilitating charge transport through intermolecular hopping.⁸⁷ Also, fused aromatic rings increase rigidity and coplanarity, enhancing effective π -conjugation, therefore fluorene, carbazole, indolocarbazole, benzotrithiophene, and other fused-ring building blocks have been of large interest for molecular engineering of HTMs.¹¹⁸ On the other hand, a huge focus is dedicated to spiro-type linking units containing spirobifluorene, spirofluorenexanthene, spirobicyclopentadithiophene and other cores.¹¹⁹⁻¹²¹ These molecules are based on a very interesting concept of connecting two molecular π -systems via sp^3 -hybridized atom, resulting in symmetric round structure and small intermolecular linkage. Although the chances of intermolecular π - π interactions become very low due to the highly sterically demanding

perpendicular arrangement of both units, it was observed that it leads to a high stability of the amorphous state.¹²²

It is worth noticing that the first novel hole transporting materials for perovskite solar cells have started to be published at 2014, about a year after perovskite photovoltaic topic has started. One has to understand, that the knowledge at that time was completely different from the one of present time at the end of 2017, resulting in sluggish progress at the beginning. However, during the time span of three years, around 300 HTM-based articles were reported, including inorganic, organic molecular and polymeric materials. It would be futile to list all the compounds individually because the new ones are being published each month and only a fraction shows the promising performance of at least 18%. Therefore, in this section only the flagship HTMs will be reviewed, which exhibit the highest performance so far. Summarized photovoltaic parameters are listed in Table 1.1.

As mentioned in the section 1.1.3.4, spiro-OMeTAD is still dominating the field and despite the high price (~350 CHF/g) routinely employed as highly efficient reference material for the research interests. This comes mainly because it is widely available and well-studied since it was commercialized decades ago. However, the cost-effective industrial potential for practical applications is hardly probable. Therefore, huge research interest directed into new HTM candidates has been raised to find an ideal HTM, which would be easily scalable for reasonable cost as well as for a better understanding between the HTM structure and PSC performance relationship.

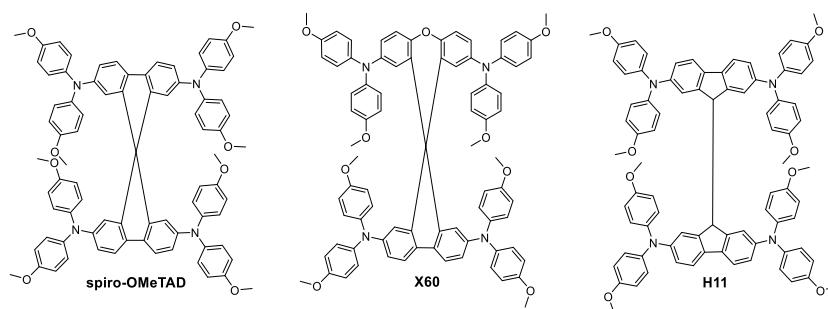


Figure 1.12 Chemical structures of spiro-OMeTAD, X60 and H11.

As a result of spiro-OMeTAD, many research groups have been focused on spiro-type compounds and tried to improve the PCE with slight structural modifications. Some representative examples of these modifications are shown in Figure 1.12 and Figure 1.13. Xu et al. have reported X60, where the spirobifluorene central core is replaced by spiro[fluorene-9,9'-xanthene] (SFX), which is synthesized by a one-pot approach condensing 4-bromophenol and 2,7-

dibromo-9-fluorenone as the starting materials. This allowed to reduce the price of the final product by thirty times comparing with that of spiro-OMeTAD. Moreover, the insert of oxygen bridge into the structure leads to improved hole mobility and device performance of 19.8%.¹²³ The same device performance was achieved employing another spiro-OMeTAD analog H11, where spiro linkage between the two planar fluorene halves is replaced by the single C-C bond.¹²⁴ This novel design also offers a facile two-step synthesis process. Remarkable performance and simplified synthetic schemes make X60 and H11 as very promising HTM candidates for large-scale industrial production.

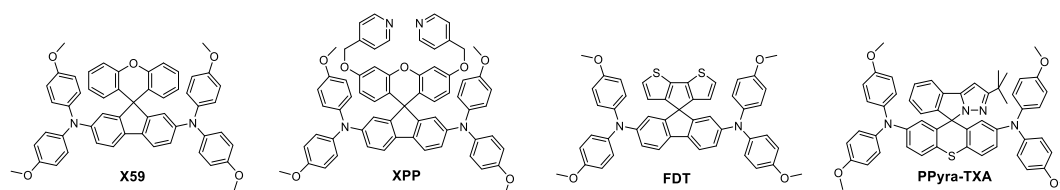


Figure 1.13 Chemical structures of X59, XPP, FDT and PPyra-TXA.

Two-fold dimethoxydiphenylamine-substituted X59 was reported a few months later, with an identical device performance as predecessor X60 and almost no hysteric behavior,¹²⁵ showing that diphenylamine units on the xanthene do not play a major role, therefore it was further functionalized with covalently linked differently substituted pyridine groups. This allowed to realize 4-*t*-butylpyridine (tBP)-free PSCs with improved stability compared with that of spiro-OMeTAD-based solar cell that contained tBP as an additive.¹²⁶ *Para*-position substituted pyridine-based XPP showed the highest performance of 19.5% among the series, due to the fact that both nitrogen atoms in XPP can easily form a strong chemical bonding with the Pb atoms, while the *ortho*- and *meta*-anchored molecules can only contribute with one nitrogen atom binding to the Pb. However, the pyridine anchors slightly lowered the performance once compared with X59.

Another interesting strategy how to improve the hole transfer at the HTM/perovskite interface was demonstrated employing FDT as HTM, where the cyclopenta[2,1-*b*:3,4-*b'*]dithiophene moiety acts as an anchor to reveal the additional thiophene-iodine interaction.¹²⁷ This led to one of the highest reported device performance so far of 20.2% with J_{sc} of 22.4 mA cm⁻², V_{oc} of 1.15 V and FF of 0.76. C-N linked spiro structures were reported in order to investigate unsymmetrical spiro configurations, consisting of phenylpyrazole and different heteroaromatic fragments.¹²⁸ S-bridged PPyra-TXA showed the highest PCE of 18% among the reported series, however, the role of *t*-Bu antenna on the pyrazole remains unclear.

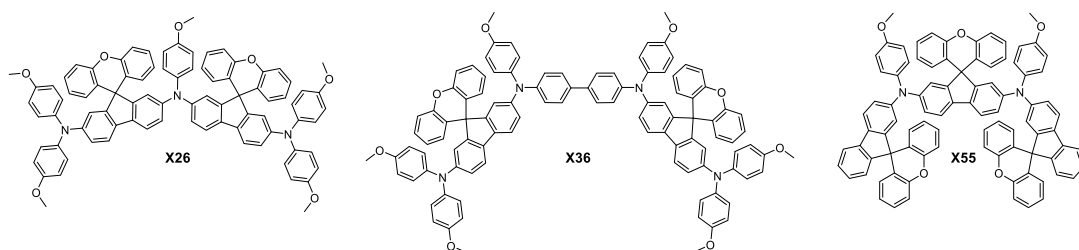


Figure 1.14 Chemical structures of SFX-based HTMs X26, X36 and X55.

Zhang et al. were further studied X-series molecules based on SFX core (Figure 1.14). Very recently, they reported X26 and X36 molecules, which could be considered as differently connected dimers of X59. Connection through the one of the nitrogen atom in diphenylamine unit led to X26, meanwhile connecting through the one of phenyl ring in diphenylamine yielded X36. The PSCs based on X26 showed a remarkable power conversion efficiency of 20.2% in comparison to 18.9% for X36-based devices, respectively. It was found that X26 forms a homogeneous capping layer, with efficient interfacial hole transfer and fast charge collection, leading to the improved V_{oc} and J_{sc} of the device, once compared with X36.¹²⁹ Furthermore, replacing one of phenyl rings in both diphenylamine arms by SFX core gave trimer X55 with excellent 3D structured configuration.¹³⁰ PSC devices with X55 as the HTM show an impressive PCE of 20.8%, with J_{sc} of 23.4 mA cm⁻², V_{oc} of 1.15 V and FF of 0.77, which is currently the highest result among the alternative HTM candidates. Correspondingly, the efficient charge collection in X55-based devices can be related to fast hole transport and interfacial hole transfer, which also explains their high FF and J_{sc} .

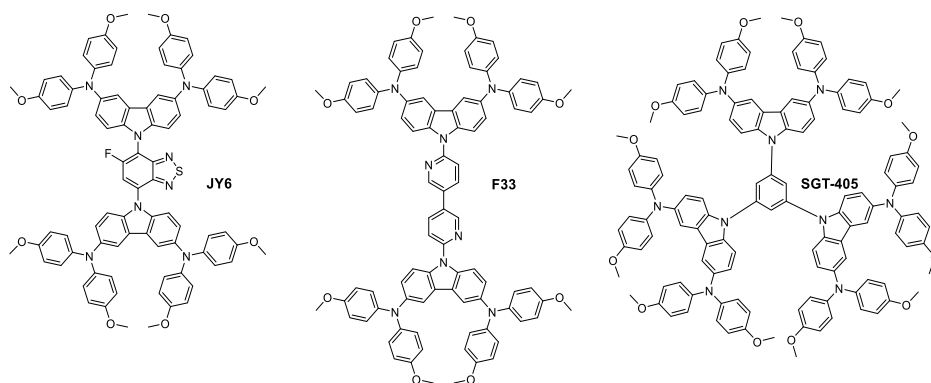


Figure 1.15 Chemical structures of JY6, F33 and SGT-405.

Carbazole derivatives have been intensively studied since it has interesting features such as the low-cost of the 9H-carbazole starting material, good chemical and environmental stability provided by the fully aromatic unit, as well as easy incorporation of a wide variety of functional

groups into the nitrogen atom that allow better solubility and fine tuning of the electronic and optical properties.¹³¹ 3,6-Dimethoxydiphenylamine-substituted carbazoles as donor units in the periphery were widely used to tune the HOMO level of the final molecule. Some representative examples of such systems are shown in Figure 1.15. Wu and co-workers reported benzothiadiazole (BT)-based HTM series.⁹³ The monofluorinated BT in JY6 increases its hole mobility, hole extraction, and hole transporting ability, and thus significantly enhances the photovoltaic performance ($\eta = 18.5\%$) comparing with non-fluorinated ($\eta = 16.9\%$) and difluorinated ($\eta = 15.7\%$) analogs. The same photovoltaic performance was recently obtained with F33, where BT is replaced by 3,3'-bipyridine.¹³² Lu et al. reported carbazole-based starburst HTMs via tuning the carbazole substitution position from 2,7- to 3,6-, respectively. 3,6-substituted SGT-405 showed slightly improved device performance of 18.9%, compared with that of 18% in case of 2,7- substitution.¹³³

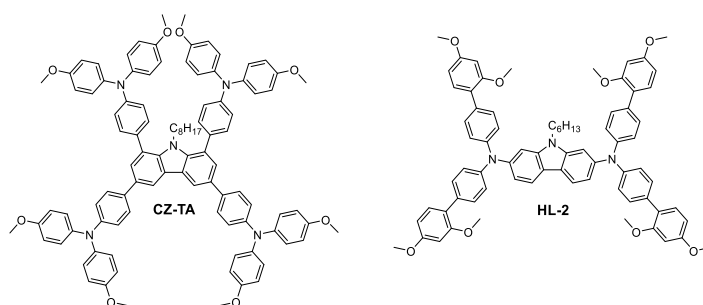


Figure 1.16 Chemical structures of carbazole-based HTMs CZ-TA and HL-2.

In Figure 1.16, most efficient central carbazole-based HTMs are shown. CZ-TA¹³⁴ and HL-2¹³⁵ showed the identical photovoltaic performance of 18.3%. From a structural point of view, both have long alkyl chain for solubility improvement, octyl and hexyl, respectively, whereas periphery donors are completely different. CZ-TA possesses 1,3,6,8-substituted *p*-dimethoxytriphenylamine units, while HL-2 is 2,7-substituted with *o,p*-dimethoxyphenyl-extended diphenylamine units.

HTMs based on sulfur-rich benzotrithiophene (BTT) core was intensively studied as such fused systems are known to maximize the π -orbital overlap, inducing face-to-face π -stacking and facilitating charge transport through intermolecular hopping. Star-shaped BTT-3 was firstly reported with optimized HOMO level, showing an excellent band alignment with the perovskite, leading to the PCE of 18.2%.¹³⁶ Encouraged by this result, Garcia-Benito et al. have further studied the impact of isomerism on BTT-based HTMs.¹³⁷ It was found that *cis* arrange-

ment of the sulfur atoms facing each other in the core of BTT-4 may further benefit the interaction with the perovskite, leading to impressive PCE of 19%, while the 4-fold isomeric form of BTT-5 showed 18.2%, respectively. Another more extended sulfur-rich core anthra[1,2-*b*:4,3-*b'*:5,6-*b''*:8,7-*b'''*]tetrathiophene (ATT) was used as scaffold for novel HTMs. Devices prepared with ATT-OMe showed the highest efficiency of 18.1% among the series of different alkoxy length HTMs, showing that longer alkoxy chains are not beneficial.¹³⁸

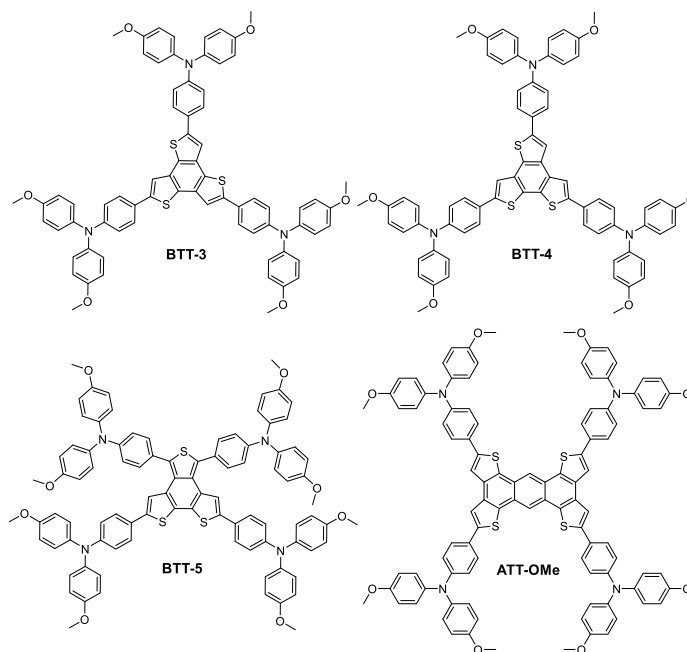


Figure 1.17 Chemical structures of sulfur-rich BTT and ATT-based HTMs.

Very recently, Zhang and co-workers reported thiophene-based HTM coded Z26, exhibiting an impressive PCE of 20.1%.¹³⁹ Due to the introduction of double bonds, Z26 presents a more homogeneous surface, higher hole mobility, and higher conductivity than its analog, where *p*-dimethoxytriphenylamine units are connected directly to the thiophene. Another very interesting branched molecules V862 and V859, bearing *p*-dimethoxydiphenylamine-substituted fluorene fragments were reported by Malinauskas et al. and are presented in Figure 1.18.¹⁴⁰ They can be produced in a two-step procedure from cheap, commercially available starting reagents, therefore, are very promising for large-scale production. Furthermore, V862 yielded a maximum PCE up to 20%, where V859 showed a slightly lower value of 19.5%.

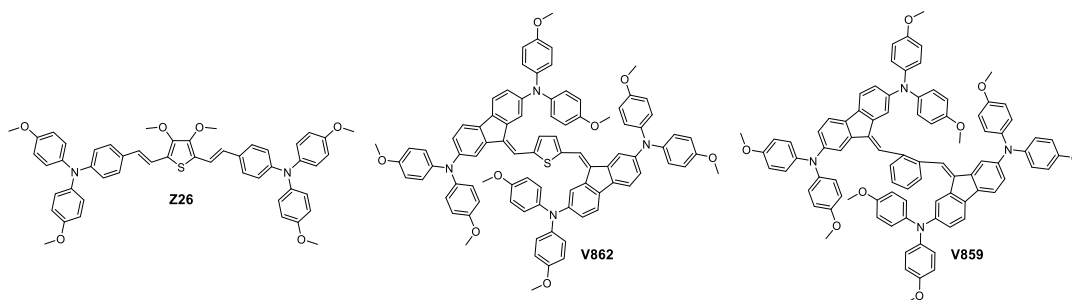


Figure 1.18 Chemical structures of Z26, V862 and V859 HTMs.

Cho and co-workers reported fluorinated indolo[3,2-*b*]indole-based derivative IDIDF (Figure 1.19).¹⁴¹ A planar π -conjugated backbone linked with a flexible alkyl chain enabled a formation of molecular stacked arrangement by strong π - π interaction, leading to improved hole mobility, and PCE of 19.8%. Phthalocyanine derivatives have been also successfully applied as an HTMs, owing to its specific molecular ordering, thereby giving rise to build a highly crystalline and robust stack with high hole mobility. To date, the most successful example of this class is CuPc, which resulted in the highest PCE of 18.8% with an outstanding long-term stability to thermal stress under air atmosphere.¹⁴²

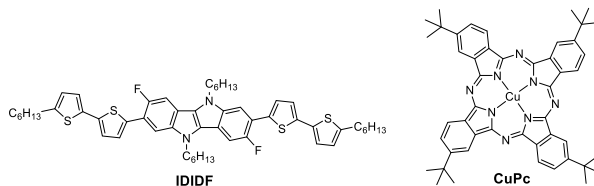


Figure 1.19 Chemical structures of IDIDF and CuPc.

A promising solution for stabilizing PSCs is the appropriate choice of dopant-free HTMs. However, the PCE of pristine HTL devices are consistently lying around 15% with only very few examples over 18% (Figure 1.20). Huang et al. presented dopant-free truxene-based HTM decorated with three arylamine groups, and six hexyl side chains, adapting a planar, rigid, and fully conjugated molecular geometry. PSCs fabricated under p-i-n architecture using Trux-OMeTAD showed a high PCE of 18.6% with minimal hysteresis.¹⁴³ Very recently, D- π -A-type HTM coded as FA-CN was reported, incorporating a rigid quinolizino acridine donor with alkyl-substituted terthiophenes and malononitriles as acceptors. Optimized devices with dopant-free FA-CN showed an impressive PCE of 18.9% with improved long-term stability under full illumination.¹⁴⁴

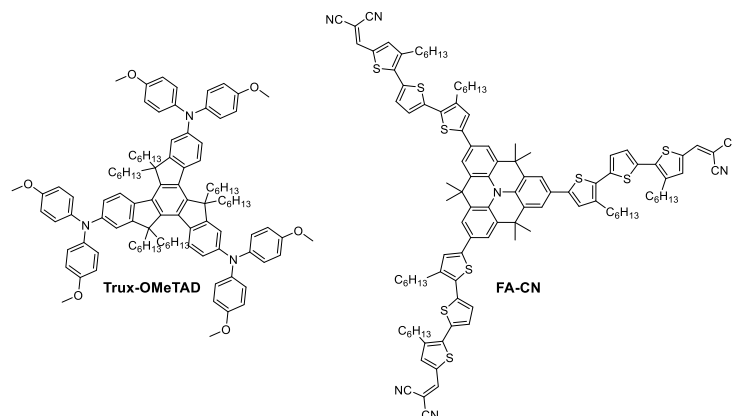


Figure 1.20 Chemical structures of star-shaped dopant-free Trux-OMeTAD and FA-CN HTMs.

ID	J_{sc} (mA cm ⁻²)	V_{oc} (V)	FF	PCE (%)	Ref. PCE (%) ^a
KR216 ^f	22.3	1.023	0.77	17.8	18.4
PPyra-TXA ^e	20.6	1.10	0.797	18.06	16.15
ATT-OMe	21.75	1.07	0.781	18.13	17.80
BTT-5	22.50	1.10	0.733	18.17	18.9
BTT-3	21.9	1.065	0.767	18.2	18.1
KR131 ^f	20.7	1.145	0.77	18.3	17.9
CZ-TA ^e	21.66	1.044	0.81	18.32	18.28
HL-2	21.30	1.09	0.79	18.34	18.77
F33 ^e	21.01	1.11	0.79	18.48	16.26
JY6 ^e	21.39	1.066	0.81	18.54	16.24
Trux-OMeTAD ^{b,c}	23.2	1.02	0.79	18.6	16.3
CuPc	22.6	1.07	0.775	18.8	20.5
SGT-405	22.93	1.046	0.786	18.87	17.71
X36	23.7	1.06	0.76	18.9	18.34
FA-CN ^b	21.71	1.13	0.77	18.9	19.2
BTT-4	23.04	1.090	0.753	18.97	18.9
KR321 ^{b,f}	21.70	1.13	0.78	19.03	19.01
KR374 ^f	23.15	1.092	0.762	19.26	19.54
DDOF ^f	22.37	1.101	0.79	19.4	18.8
V859	23.3	1.120	0.75	19.47	18.25
XPP ^{d,e}	23.18	1.12	0.75	19.5	16.5
H11	24.2	1.150	0.71	19.8	18.9
X59	23.4	1.13	0.73	19.8	20.8
IDIDF	23.6	1.06	0.792	19.8	16.8
X60	24.2	1.14	0.71	19.84	-
V862	22.5	1.139	0.77	19.96	18.25
Z26	23.59	1.132	0.75	20.1	20.6
FDT	22.7	1.148	0.76	20.2	19.7
X26	24.3	1.11	0.75	20.2	18.34
X55	23.4	1.15	0.77	20.8	18.8

Table 1.1 Photovoltaic performance of the perovskite devices employed with best performing small molecule-based HTMs. ^aSpiro-OMeTAD and PTAA were used as the reference in most of the cases; ^bdopant-free composition; ^cp-i-n device architecture; ^dtBP-free composition; ^eplanar device architecture; ^fpresented in this work.

1.3 Motivation and Outline of the Thesis

Research in renewable energy is moving to the forefront and becoming indisputably relevant for the future security of energy needs. Among various renewable energy technologies, solar energy is an incredibly abundant and extremely clean source, which remains underexploited to date. Perovskite solar cells are considered a promising and burgeoning technology for solar energy conversion with the power conversion efficiency, currently exceeding 22%. Efficient and inexpensive energy conversion by perovskite solar cells is vital for the global transition to a low-carbon society. However, although perovskite solar cells have reached high power conversion efficiency, there are still several challenges limiting the industrial realization. The actual bottleneck for real uptake in the market still remains the cost-ineffective components and instability, where doping-induced degradation of charge selective layers may contribute significantly.

Spiro-OMeTAD is the hole transporting material routinely employed in order to maintain the highest efficiency, however, its prohibitively high price hinders progress towards low-cost perovskite solar cell manufacturing. The price of the spiro-OMeTAD may contribute to more than 30% of the overall module price. The reason resides in the complicated multi-step synthetic procedure, which is affordable in small quantities but is hardly scalable. Therefore, it is important to find alternative synthetic schemes for cost-effective hole transporting materials with the minimized number of steps and simple workup procedures.

Another key factor that plays a major role in the commercialization potential is the stability of the device. Wide bandgap hole transporting materials as spiro-OMeTAD typically require to be heavily doped by external chemical doping and the use of additives may be problematic, since hygroscopic nature of doping makes the hole transporting layer highly hydrophilic leading to chemical degradation and negatively influences the stability of the entire device. One promising avenue to stabilize perovskite solar cells could be the appropriate choice of the dopant-free and the highly hydrophobic hole transporting materials, acting as a protection layer from the moisture and prevent the diffusion of external moieties.

In order to solve these problems, the bulk of the work described in a thesis is focused on the design, synthesis, and characterization of a variety of small molecule-based hole transporting materials. The general aim is to investigate the relation between the molecular structure of the novel hole transporting materials and performance of perovskite solar cells, leading to a fundamental understanding of the requirements of the hole transporting materials and further improvement of the photovoltaic performance.

In the second chapter, a rapid and efficient synthesis of a series of novel triazatruxene-based two-dimensional HTMs comprising electron-rich methoxy-engineered substituents is reported. HTMs are obtained from simple and inexpensive starting materials, offering potentially much lower production costs in comparison with the most widely used spiro-OMeTAD. Molecularly engineered triazatruxene derivatives exhibited surface interaction with perovskite material resulting efficient hole injection from the valence band of perovskite into the HOMO of HTM. Remarkable power conversion efficiency of 18.3% was realized using KR131, showing a potential of 2D materials like triazatruxene-derivatives as an alternative low-cost HTMs. The trend, showing that deeper HOMO level of the HTM correlates with the larger V_{oc} was indicated.

Chapter 3 presents the synthesis of the dopant-free hole transporting materials based on D- π -A type architecture. For the first time, it is shown that the highly ordered characteristic face-on organization of hole transporting molecules is benefiting to increased vertical charge carrier transport within a perovskite solar cell, leading to a power conversion efficiency over 19% with improved stability. The result obtained employing KR321 is the highest so far in the field of a pristine hole transporting materials without any chemical additives or doping.

In chapter 4, an easily attainable 9,9'-bifluorenylidene-based HTM named KR216 was obtained by a straightforward and elegant two-step synthetic route. The estimated price of KR216 is around 50 times lower than that of commercial spiro-OMeTAD. PCE of 17.8% was obtained for PSC using KR216, which is on par with the PCE of the commercial spiro-OMeTAD reference. In chapter 5, the bistricyclic aromatic ene (BAE)-based HTMs are explored further. The impact on different atoms in the heteromeric BAE structure was revealed through the various characterization techniques. Replacement of the oxygen atom by sulfur showed a significantly improved hole-drift mobility leading to enhanced photovoltaic performance and reduced hysteresis, most likely owing to the improved interface between the perovskite and HTM caused by stronger Pb-S interaction, whereas oxidation of sulfur to sulfone has a negative effect on the device performance. S-bridged KR374 exhibited a PCE of 19.2%, which is on par with the widely researched spiro-OMeTAD reference.

In chapter 6, dispiro-oxepine derivative, obtained by facile 3-step synthetic route has been reported. PSCs employed DDOF as HTM showed one of the highest power conversion efficiency of 19.4% reported to date. Moreover, improved long-term stability over 250 h has been demonstrated.

Chapter 2 Triazatruxene Derivatives as Hole Transporting Materials

Four center symmetrical star-shaped hole transporting materials comprising a planar triazatruxene core and electron-rich methoxy-engineered side arms have been synthesized and successfully employed in $(\text{FAPbI}_3)_{0.85}(\text{MAPbBr}_3)_{0.15}$ perovskite solar cells. These HTMs are obtained from relatively cheap starting materials by adopting facile preparation procedure, without using expensive and complicated purification techniques. Developed compounds have suitable highest occupied molecular orbitals with respect to the valence band level of the mixed perovskite, and time-resolved photoluminescence indicates that hole injection from the valence band of perovskite into the HOMO of triazatruxene-based HTM is relatively more efficient as compared to that of well-studied spiro-OMeTAD. Remarkable power conversion efficiency over 18% was achieved using 5,10,15-trihexyl-3,8,13-tris(4-methoxyphenyl)-10,15-dihydro-5*H*-diindolo[3,2-*a*:3',2'-*c*]carbazole (**KR131**) with composite perovskite absorber. This result demonstrates triazatruxene-based compounds as a new class of HTMs for the fabrication of highly efficient PSCs.

This chapter is based on published work: *Rakstys et al. J. Am. Chem. Soc., 2015, 137 (51), 16172–16178. DOI: 10.1021/jacs.5b11076.*¹⁴⁵

2.1 Introduction

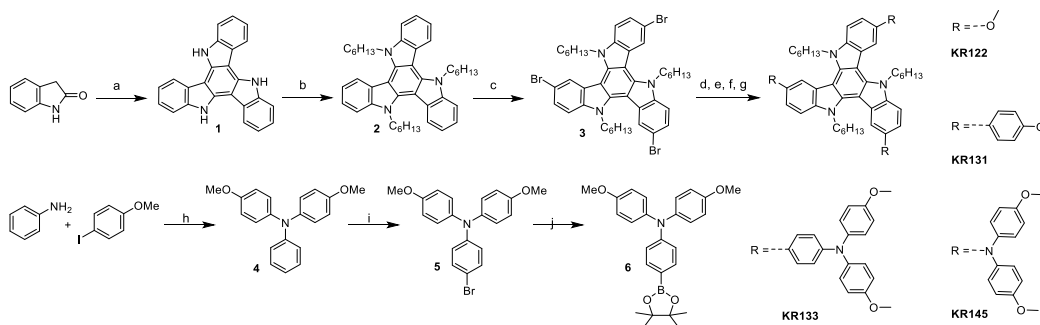
Star-shaped triazatruxene derivatives are potential new HTMs for PSCs, since they have been known as hole selective layers for organic solar cells.¹⁴⁶ Triazatruxene core being structured from three indole units combined by one benzene ring can be considered as a two-dimensional π -system, which provides a large aromatic surface to overlap with each other for efficient intermolecular charge transfer. In addition, it offers large chemical versatility to tune electronic and morphological properties. Considering these advantages and high hole mobility values that have been reported in the literature,^{147,148} triazatruxene derivatives were prepared to serve as potential HTMs for PSC. By adopting a facile synthetic strategy, four novel derivatives

have been synthesized from inexpensive precursor materials and characterized to reveal their electrochemical and optoelectronic properties and are demonstrated as HTMs in highly efficient PSCs.

2.2 Results and Discussion

2.2.1 Design and Synthesis

The general synthesis procedure for the preparation of 5,10,15-trihexyl-3,8,13-trimethoxy-10,15-dihydro-5*H*-diindolo[3,2-*a*:3',2'-*c*]carbazole **KR122**, 5,10,15-trihexyl-3,8,13-tris(4-methoxyphenyl)-10,15-dihydro-5*H*-diindolo[3,2-*a*:3',2'-*c*]carbazole **KR131**, 4,4',4''-(5,10,15-trihexyl-10,15-dihydro-5*H*-diindolo[3,2-*a*:3',2'-*c*]carbazole-3,8,13-triyl)tris(*N,N*-bis(4-methoxyphenyl)aniline) **KR133**, and 5,10,15-trihexyl-*N*³,*N*³,*N*⁸,*N*⁸,*N*¹³,*N*¹³-hexakis(4-methoxyphenyl)-10,15-dihydro-5*H*-diindolo[3,2-*a*:3',2'-*c*]carbazole-3,8,13-triamine **KR145** is shown in Scheme 2.1. Triazatruxene core **1** was prepared by intermolecular condensation of commercially available 2-indolinone via one-step procedure. Obtained planar aromatic core was then attached with *n*-hexyl chains to make it soluble in common organic solvents. Furthermore, hydrophobic chains may prevent the perovskite surface from the moisture¹⁴⁹ and suppress crystal growth in the HTM layer.¹⁵⁰ After that, **2** was brominated using *N*-bromosuccinimide (NBS) to get **3**, which is ready for further Ullmann, Suzuki, and Buchwald coupling reactions to yield final HTMs containing methoxy-engineered donor moieties. To obtain **KR133**, 4-(4,4,5,5-tetramethyl-1,3,2-dioxaborolan-2-yl)-*N,N*-bis(4-methoxyphenyl)aniline **6** was synthesized from 4-iodoanisole and aniline in three steps. The methoxy groups have been demonstrated in literature as effective anchors for the interface between perovskite/HTM.¹⁵¹ The chemical structures of the synthesized products were verified by ¹H/¹³C NMR spectroscopy and mass spectrometry. Detailed synthetic procedures are fully described in section 2.4 Synthetic Methods and Procedures. All final compounds are soluble in common organic solvents such as THF, chloroform, toluene, or chlorobenzene, which are typically used for deposition of hole transporting layer in PSCs.



Scheme 2.1 Synthesis of one-step triazatruxene core and its-based HTMs. (a) POCl_3 , 100 °C; (b) 1-iodododecane, NaH, DMF, 25–120 °C; (c) NBS in DMF, CHCl_3 , 0–25 °C; (d) NaOMe 5.4 M in MeOH, CuI, DMF, 120 °C; (e) *p*-methoxybenzene boronic acid, $\text{Pd}(\text{dppf})\text{Cl}_2$, K_2CO_3 , toluene/MeOH, 80 °C; (f) 4,4'-dimethoxydiphenylamine, *t*-BuONa, $\text{Pd}_2(\text{OAc})_2$, (*t*-Bu) $_3\text{P}$ 1 M in Tol, toluene, 100 °C; (g) 4-(4,4,5,5-tetramethyl-1,3,2-dioxaborolan-2-yl)-*N,N*-bis(4-methoxyphenyl)aniline (6), $\text{Pd}(\text{PPh}_3)_4$, 2 M aqueous K_2CO_3 , THF, 80 °C; (h) CuI, 1,10-phenanthroline, KOH, toluene, 100 °C; (i) NBS, THF, 0 °C; (j) bis(pinacolato)diboron, CH_3COOK , $\text{Pd}(\text{dppf})\text{Cl}_2$, DMSO, 80 °C.

2.2.2 Thermal, Optical, Electrochemical, and Photophysical Properties

To determine thermal properties of the synthesized HTMs, thermogravimetric analysis (TGA) was carried out (Figure 2.1a). It was found that all HTMs show good thermal stability up to ~440 °C, except that **KR122** starts to decompose at the lowest temperature of 439 °C, indicating that addition of more aromatic substitution increases thermal stability. The normalized UV-Vis absorption and photoluminescence (PL) spectra of **KR122**, **KR131**, **KR133**, and **KR145** in THF solution are shown in Figure 2.1b. Absorption bands appear in the spectral region between 300 and 400 nm, which are assigned to the π - π^* transitions of the conjugated system. The maxima and the line width of the absorption bands increase with the addition of more aromatic substitutions, moving from **KR122** ($\lambda_{\text{max}} = 322$ nm) to **KR133** ($\lambda_{\text{max}} = 368$ nm). An additional shoulder is noticed for **KR145** ($\lambda_{\text{max}} = 378$ nm), which makes the absorption of this derivative particularly broad. PL spectra show that all molecules have relatively large Stokes shifts of around 50–70 nm suggesting significant changes in geometrical configuration of the molecules upon excitation. The optical bandgap (E_g) is estimated from the intersection of the corresponding normalized absorbance and PL spectra. The intersection wavelengths for **KR122**, **KR131**, **KR133**, and **KR145** are 354, 380, 401, and 395 nm, which corresponds to E_g of 3.50, 3.26, 3.09, and 3.14 eV, respectively. The experimental HOMO energy levels of all the triazatruxene derivatives were derived from the ground-state oxidation potential E_{HOMO} estimated from cyclic voltammogram shown in Figure 2.1c. The pair of redox peaks of all the HTMs is highly reversible, indicating an excellent electrochemical stability. Expectedly, an additional

phenyl ring between triazatruxene core and electron donating moiety stabilized the oxidation potential by 130 and 200 mV, moving from **KR122** to **KR131** and from **KR145** to **KR133**, respectively. The E_{HOMO} values were calculated as -5.18, -5.30, -5.26, and -5.06 eV vs. vacuum for **KR122**, **KR131**, **KR133**, and **KR145**, respectively.

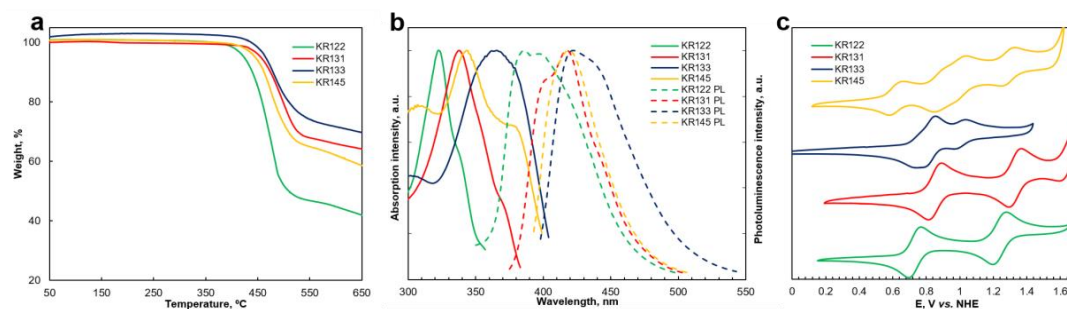


Figure 2.1 a) Thermogravimetric analysis (TGA) with scan rate of 20 °C/min; N₂ atmosphere; b) UV-Vis absorption (solid line) and photoluminescence (dashed line) spectra normalized at the peak value; and c) cyclic voltammograms of triazatruxene-based HTMs.

Ground- and excited-state time-dependent DFT (TD-DFT) calculations were done at B3LYP/6-31G(d) level to predict the electronic properties of new triazatruxene-based materials. It was found that the calculated HOMO and LUMO levels coincide well with the trends of experimental data. HOMOs of the triazatruxene-based materials delocalize over the whole molecule, while the LUMOs are largely localized on the linking groups (Figure 2.2a).

ID	λ_{abs} (nm) ^a	λ_{em} (nm) ^a	E_{HOMO} (eV) ^b	E_g (eV) ^c	E_{LUMO} (eV) ^d	I_p (eV) ^e	E_{HOMO} (eV) ^f	E_{LUMO} (eV) ^f	μ_0 (cm ² V ⁻¹ s ⁻¹) ^g
KR122	323	388	-5.18	3.50	-1.68	-5.09	-4.60	-0.46	5·10 ⁻⁴
KR131	340	419	-5.30	3.26	-2.04	-5.22	-4.76	-0.61	2.8·10 ⁻⁵
KR133	368	422	-5.26	3.09	-2.17	-5.14	-4.46	-0.61	2·10 ⁻⁵
KR145	346, 378	419	-5.06	3.14	-1.92	-4.96	-4.31	-0.57	6·10 ⁻⁴

Table 2.1 Optical and electrochemical properties of synthesized HTMs. ^aMeasured in THF solution; ^bmeasured in DCM/tetra-*n*-butylammonium hexafluorophosphate (0.1 M) solution, using glassy carbon working electrode, Pt reference electrode and Pt counter electrode with Fc/Fc⁺ as an internal standard. Potentials were converted to the normal hydrogen electrode (NHE) by addition of +0.624 V and -4.44 eV to the vacuum, respectively; ^cestimated from the intersection of the normalized absorbance and emission spectra; ^dcalculated from $E_{LUMO} = E_{HOMO} + E_g$; ^eionization potential was measured by the photo-emission in air method from films; ^fground and excited state time dependent DFT (TD-DFT) calculations were done at B3LYP/6-31G(d) level; ^ghole mobility value at zero field strength.

To have a better understanding in energy level matching of the HTMs in PSC, solid-state ionization potential (I_p) was measured by the electron photoemission in air on the thin films (Figure 2.2b), the measured I_p values are fully in agreement with the HOMO levels investigated in

the cyclic voltammetry (CV) experiments. The ~ 0.1 eV difference can be explained by solvent effect during the CV measurements. All optical and electrochemical properties are summarized in Table 2.1. Charge transport properties (Figure 2.2c) of the synthesized triazatruxene derivatives were studied by the xerographic time of flight (XTOF) technique. The room-temperature hole-drift mobility of **KR122** and **KR145** was approximately one order of magnitude higher compared to spiro-OMeTAD ($\mu_0 = 4.1 \times 10^{-5} \text{ cm}^2 \text{ V}^{-1} \text{ s}^{-1}$),¹⁵⁰ whereas **KR131** and **KR133** showed hole mobility in the same level of spiro-OMeTAD, indicating similar charge hopping properties.

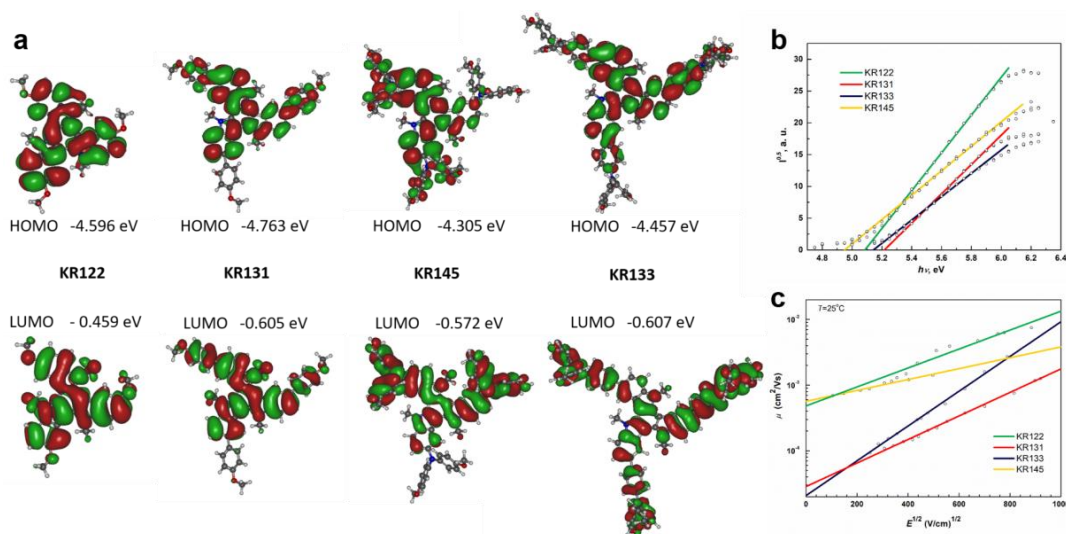


Figure 2.2 a) Electron distribution of HOMO and LUMO. Fully optimized at B3LYP/6-31G(d) level; b) photoemission in air spectra; c) electric field dependencies of hole-drift mobility.

2.2.3 Spectroscopy and Photovoltaic Properties of Perovskite-Based Devices

The energy level diagram of the $\text{TiO}_2/(\text{FAPbI}_3)_{0.85}(\text{MAPbBr}_3)_{0.15}/\text{HTM}/\text{Au}$ devices is shown in Figure 2.3b. Considering the valence band of double-mixed perovskite is at -5.65 eV (vs. vacuum),¹⁵² all triazatruxene derivatives showed enough over potential leading to efficient charge transfer at the interfaces. Moreover, the HOMO levels of **KR131** and **KR133** are more stabilized comparing with that of spiro-OMeTAD ($E_{\text{HOMO}} = -5.22$ eV vs. vacuum),¹⁵³ thus higher open circuit voltages (V_{OC}) are expected, especially for **KR131**. To demonstrate the functioning of triazatruxene derivatives as HTMs, composite perovskite absorber based solar cells were prepared.²³ The perovskite films were deposited from a precursor solution containing FAI (1 M), PbI_2 (1.1 M), MABr (0.2 M), and PbBr_2 (0.2 M) in anhydrous DMF:DMSO 4:1 (volume ratio) following by HTM layer prepared from 70 mM solution in chlorobenzene. All HTMs were

doped with bis(trifluoromethylsulfonyl)imide lithium salt (LiTFSI),^{154,155} tris(2-(1*H*-pyrazol-1-yl)-4-*tert*-butylpyridine)cobalt(III)-tris(bis(trifluoro-methylsulfonyl)imide)⁷ (FK209) and 4-*tert*-butylpyridine (tBP). The molar ratio of additives for HTMs was: 0.5, 0.03 and 3.3 for LiTFSI, FK209 and tBP, respectively, following the method that has been previously optimized for the spiro-OMeTAD. The device is made by ~490 nm perovskite atop 150 nm thick mesoporous TiO₂ layer, which was deposited on FTO glass coated with ~50 nm compact TiO₂. Device is completed by ~190 nm thick HTM and 80 nm gold as back contact. Figure 2.3c displays the cross-section images of the PSCs analyzed by field-emission scanning electron microscope.

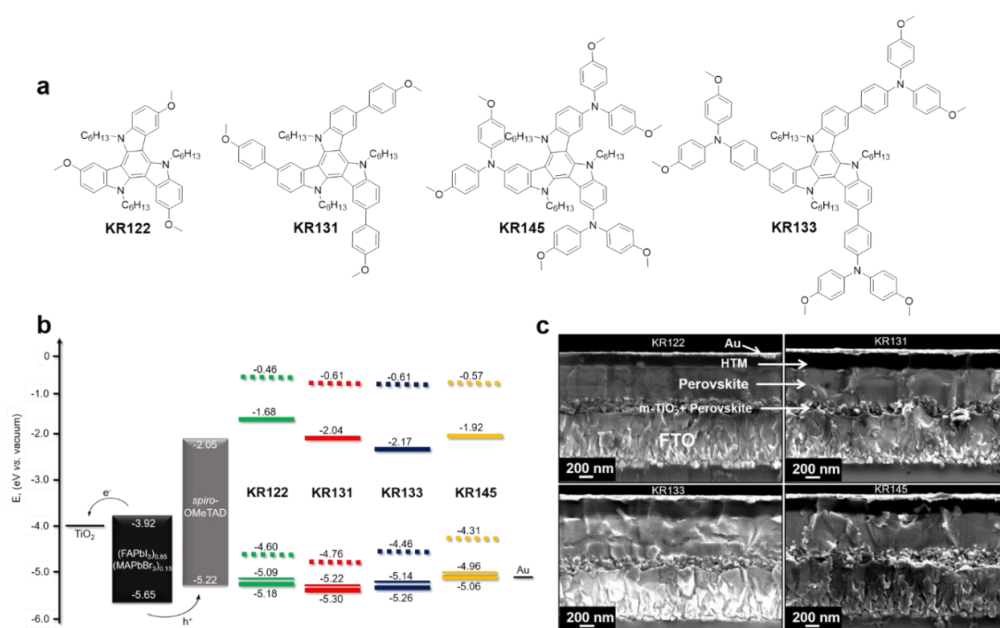


Figure 2.3 a) Chemical structures of synthesized HTMs; b) energy level diagram for the corresponding materials and HTMs used in TiO₂/mixed-perovskite/HTM/Au devices. Calculated HOMO and LUMO values are presented as dashed lines, solid-state ionization energies as narrow solid lines, E_{HOMO} and E_{LUMO}^* values as wide solids, respectively; c) cross-sectional SEM micrographs of perovskite devices containing different HTMs.

In order to determine the capability of new HTMs in acting as hole acceptors within the perovskite-based devices, time-integrated photoluminescence (TIPL) quenching of the perovskite emission in bilayer films was estimated (Figure 2.4a). Upon exciting the perovskite films at 420 nm, strong TIPL spectra appear in between 1.63 and 1.59 eV. The TIPL spectra of perovskite films containing different HTMs revealed a blue shift, which in addition to the optical properties of the interface e.g. perovskite/HTM, could be attributed to the strong chemical interaction between flat HTM and perovskite surface. Furthermore, the relative diminution of TIPL intensity in the perovskite films containing HTMs confirms the injection of hole from the

valence band of perovskite into the HOMO of HTM.¹⁵⁶ To illustrate the injection rate of holes further, decay kinetics of emission through time-resolved photoluminescence (TRPL) were investigated. Figure 2.4b shows TRPL spectra acquired from various perovskite films deposited on nonconducting glass containing different HTMs atop. Emission lifetime for various perovskite films containing different HTMs was fitted with a two-component exponential decay model. The kinetics of second-order bimolecular recombination occurring within the perovskite layer increases in the presence of HTM. The pristine perovskite films showed the longest charge carrier lifetime ($\tau_2 = 69$ ns), whereas the perovskite film containing **KR122**, **KR131**, **KR133**, and **KR145** as HTM showed the fastest decay of 7, 8, 4, and 8 ns, respectively. On the contrary, excited states in the perovskite films containing spiro-OMeTAD are relatively long lasting and exhibit lifetime of 18 ns. From these observations, we conclude that hole injection from the valence band of perovskite into the HOMO of triazatruxene-based HTMs is relatively more efficient as compared to that of well-studied spiro-OMeTAD.

Figure 2.4c illustrates the current-voltage (J - V) traces collected under simulated solar illumination (AM1.5G, 100 mW cm⁻²) for the best PSCs, prepared using mixed perovskite absorber (FAPbI₃)_{0.85}(MAPbBr₃)_{0.15} (MA: CH₃NH₃⁺, FA: NH=CHNH₃⁺), synthesized derivatives as HTM candidates, and spiro-OMeTAD as the reference. It is well-known that the J - V characteristic of PSCs may show hysteretic behavior, which makes it ambiguous to calculate the actual PCE.^{82,157} To estimate the impact of the hysteresis on the calculated PCE, the J - V curves were collected by scanning the applied voltage at 0.01 V s⁻¹ from forward bias (FB) to short-circuit (SC) and the other way around. Summarized device performance parameters are reported in Table 2.2. Solar cell performance parameters extracted from the data in Figure 2.4c. The PCE of the prepared devices with the triazatruxene derivatives varies from 8.8% for **KR122** to 18.3% for **KR131**. The significantly lower performances shown by **KR122** and **KR145** are mainly related to the lower V_{oc} due to the relatively higher HOMO level. Although **KR122** and **KR145** showed high hole-drift mobility and relatively short PL lifetime, the lower PCE may be induced by the high roughness of the HTM surface resulting in poor contact with the gold electrode. The cells fabricated with **KR131** and **KR133** exhibited significantly higher values of $V_{oc} = 1.145$ V for **KR131** and 1.133 V for **KR133** in comparison to that of spiro-OMeTAD (1.087 V), respectively. Notably, the J_{sc} is significantly higher for the spiro-OMeTAD than **KR131** and **KR133**. Previous works demonstrated that the J_{sc} has a superlinear increase as HTM oxidation potential decreases (HOMO level closer to vacuum).¹⁵⁸ Spiro-Ome-TAD has slightly lower redox potential than **KR131** and **KR133** and thus is expected to induce a larger J_{sc} , as the data in Table 2.2 show. Nevertheless, it is worth noticing that the difference in J_{sc} between Spiro-OMeTAD and **KR131** and **KR133** is ~ 1 mA cm⁻², which is close to the measurement error. Furthermore,

although there is marginal difference in the V_{oc} and J_{sc} between the devices with **KR131** and **KR133**, the FF of the former HTM based device (0.77) is significantly higher than that of the later (0.72) meaning better film quality with **KR131**.

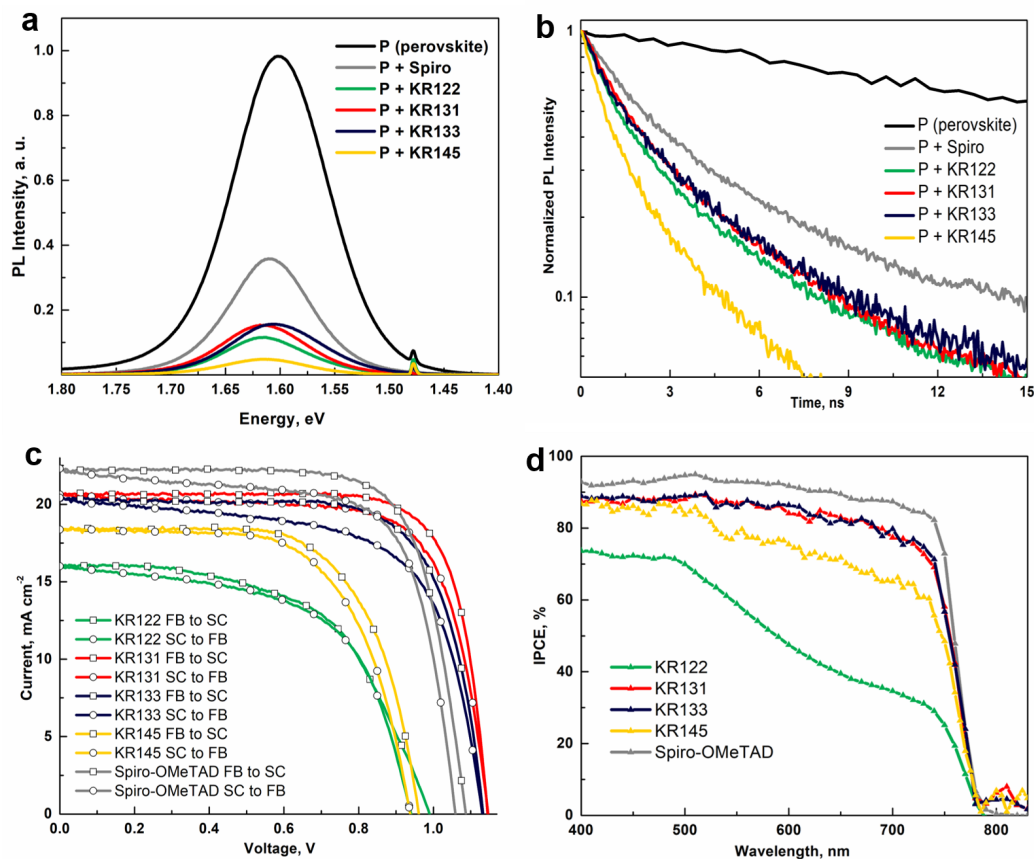


Figure 2.4 a) Time-integrated photoluminescence spectra of perovskite films containing different HTMs; b) time-resolved photoluminescence spectra measured at a wavelength near bandgap that yields maximum photoluminescence signal upon exciting various perovskite films containing different HTMs at 420 nm; c) J - V curves of best performing PSCs prepared with new HTMs and spiro-OMeTAD reference. Devices were masked with a black metal aperture of 0.16 cm^2 to define the active area. The curves were recorded scanning at 0.01 V s^{-1} from forward bias to short circuit condition and *vice versa* with no device preconditioning such as light soaking or holding at forward voltage bias; d) IPCE spectra as a function of the wavelength of monochromatic light for perovskite devices.

Devices fabricated using spiro-OMeTAD as HTM exhibited PCE of 17.9% as extracted from the backward and 16.3% for the forward scan, which is comparable with the state-of-the-art spiro-OMeTAD devices prepared under similar perovskite composition and device architecture.⁹⁻¹² Under the same conditions, both **KR131** and **KR133** showed performances with PCE of 18.3% and 16.8% for the forward and 17.0% and 14.8% in the backward scan, respectively. The PCE of **KR131** is on par with that of spiro-OMeTAD underlining new promising HTM family for

PSCs. The incident photon-to-current efficiency (IPCE) (Figure 2.4d) of the perovskite devices as a function of wavelength obtained after depositing different HTMs shows that the generation of photocurrent begins at ~ 770 nm, and the photocurrents obtained from the IPCE data are in close agreement with those of current-voltage measurements and show similar trends.

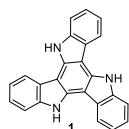
ID	Scan direction	V_{oc} (mV)	J_{sc} (mA cm ⁻²)	FF	PCE (%)	Light int. (mW cm ⁻²)
KR122	FB to SC	990	16.0	0.57	9.0	99.6
	SC to FB	940	16.0	0.58	8.8	
KR131	FB to SC	1145	20.7	0.77	18.3	99.3
	SC to FB	1147	20.6	0.72	17.0	
KR133	FB to SC	1133	20.4	0.72	16.8	99.2
	SC to FB	1132	20.4	0.64	14.8	
KR145	FB to SC	961	18.4	0.67	11.9	98.3
	SC to FB	940	18.4	0.64	11.1	
spiro-OMeTAD	FB to SC	1087	22.3	0.74	17.9	97.8
	SC to FB	1059	22.3	0.69	16.3	

Table 2.2 Solar cell performance parameters extracted from the data in Figure 2.4c.

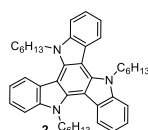
2.3 Conclusions

In summary, a rapid and efficient synthesis of a series of novel triazatruxene-based two-dimensional HTMs comprising electron-rich methoxy-engineered substituents is reported. HTMs are obtained from simple and inexpensive starting materials merely in four scalable synthetic steps, offering potentially much lower production costs in comparison with the most widely used spiro-OMeTAD. On the basis of the CV measurements, UV-Vis, and PL spectra, the HOMO and LUMO energy levels of each compound were found to be in good alignment with the energy levels of perovskite material. Molecularly engineered triazatruxene derivatives exhibit surface interaction with perovskite material resulting efficient hole injection from the valence band of perovskite into the HOMO of HTM. Remarkable power conversion efficiency of 18.3% was realized using **KR131** as HTM and compositive perovskite as absorber, which is on par with that of spiro-OMeTAD (17.9%). This study demonstrates a potential of 2D materials like triazatruxene derivatives as an alternative for the existing cost ineffective and synthetically challenging spiro-OMeTAD and PTAA HTMs in PSCs. Expectedly, further modification of the triazatruxene core by molecular engineering of functional groups not only improves interfacial properties and efficiency but also protects from humidity and UV induced degradation of PSCs.

2.4 Synthetic Methods and Procedures

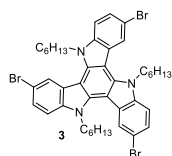


10,15-dihydro-5H-diindolo[3,2-a:3',2'-c]carbazole (1).¹⁵⁹ A mixture of 2-indolinone (10 g, 75 mmol) and POCl₃ (50 mL) was heated at 100 °C for 8 h. Then, the reaction mixture was poured into ice and neutralized carefully with NaOH. After neutralization, the precipitate was filtered to give the crude product as a brown solid. The crude solution in MeOH was absorbed on silica-gel, dried, loaded, and eluated through a thick silica-gel pad with a DCM as a mobile phase. After evaporation of eluate at reduced pressure and recrystallization from acetone, pure pale yellow solid was obtained. (5.5 g, 63%). ¹H NMR (400 MHz, DMSO-d₆) δ 11.86 (s, 3H), 8.66 (d, J = 7.4 Hz, 3H), 7.71 (d, J = 7.9 Hz, 3H), 7.41 – 7.28 (m, 6H). ¹³C NMR (100 MHz, Acetone-d₆) δ 141.0, 136.4, 124.8, 124.5, 121.5, 121.4, 112.9, 103.3. C₂₄H₁₅N₃[M⁺] Exact Mass = 345.1266, MS (ESI-TOF) = 345.1034.



5,10,15-trihexyl-10,15-dihydro-5H-diindolo[3,2-a:3',2'-c]carbazole (2).¹⁶⁰

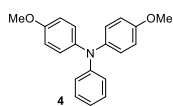
To a solution of (1) (500 mg, 1.45 mmol, 1 eq.) in DMF (10 mL), NaH (0.1 g, 5.1 mmol, 3.5 eq.) was added at room temperature and stirred for half hour, then 1-iodohexane (1.23 g, 5.8 mmol, 4 eq.) was added via syringe and the mixture was then refluxed for 2 h. The cooled mixture was poured into water and extracted with DCM. The organic phase was dried over MgSO₄. The product was isolated off on a silica gel column with 20% DCM in hexane to give a product as a pale yellow solid (650 mg, 75%). ¹H NMR (400 MHz, Chloroform-d) δ 8.29 (d, J = 8.0 Hz, 3H), 7.64 (d, J = 8.0 Hz, 3H), 7.45 (t, J = 7.4 Hz, 3H), 7.34 (t, J = 7.6 Hz, 3H), 4.92 (m, 6H), 1.99 (p, J = 7.9 Hz, 6H), 1.38 – 1.16 (m, 18H), 0.81 (t, J = 7.1 Hz, 9H). ¹³C NMR (100 MHz, Chloroform-d) δ 13.80, 21.56, 25.70, 29.17, 31.15, 44.76, 107.14, 110.30, 118.79, 119.80, 120.96, 127.47, 137.25, 138.29. C₄₂H₅₁N₃[M⁺] Exact Mass = 597.4083, MS (ESI-QTOF) = 597.4080.



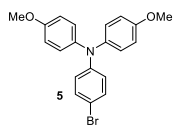
3,8,13-tribromo-5,10,15-trihexyl-10,15-dihydro-5H-diindolo[3,2-a:3',2'-c]carbazole (3).¹⁶¹

To a solution of (2) (350 mg, 0.58 mmol, 1 eq.) in 30 mL CHCl₃, (320 mg, 1.8 mmol, 3.1 eq.) of NBS in 5 mL DMF was added dropwise via syringe at 0 °C. After addition reaction mixture was stirred for 1 h at room temperature. The mixture was extracted with DCM and organic phase was dried over MgSO₄. The product was isolated off on a silica gel column with 10% DCM in hexane to give a product as a pale-yellow solid (400 mg, 82%). ¹H NMR (400 MHz, Chloroform-d) δ 8.03 (d, J = 8.6 Hz, 3H), 7.71 (s, 3H), 7.42 (d, J = 8.6 Hz, 3H), 4.81 – 4.70 (m, 6H), 1.96 – 1.76 (m, 6H), 1.12 – 1.28 (m, 18H), 0.80 (t, J = 7.0 Hz, 9H). ¹³C NMR (100 Hz, Chloroform-d) δ 125.9, 124.9, 124.2, 124.0,

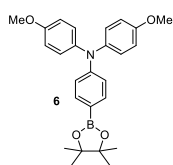
123.1, 122.7, 113.4, 112.2, 53.7, 47.4, 31.8, 30.4, 26.5, 22.8, 14.2. $C_{42}H_{48}Br_3N_3[M^+]$ Exact Mass = 831.1398, MS (ESI-QTOF) = 831.1389.



4-methoxy-N-(4-methoxyphenyl)-N-phenylaniline (4).¹⁶² 4-iodoanisole (78 g, 205 mmol, 2.3 eq.), aniline (8 mL, 87.5 mmol, 1 eq.), and 1,10-phenanthroline (3 g, 16.5 mmol, 0.2 eq.) were dissolved in toluene (200 mL). After the solution was heated to 100 °C, CuI (3.23 g, 16.5 mmol, 0.2 eq.) and KOH (37 g, 0.66 mol, 7.5 eq.) were added under nitrogen atmosphere. The mixture was heated at 100 °C overnight. After cooling to room temperature, the mixture was washed with water three times, and the organic phase was dried over $MgSO_4$. After removal of the solvent, the residual was purified on a silica gel column (hexane/DCM: 4/1). (13.9 g, 57% yield). 1H NMR (400 MHz, Chloroform-d) δ 7.19 (t, J = 7.6 Hz, 2H), 7.07 (d, J = 6.9 Hz, 4H), 6.96 (d, J = 7.1 Hz, 2H), 6.89 (d, J = 7.1 Hz, 1H), 6.84 (d, J = 8.9 Hz, 4H), 3.82 (s, 6H). ^{13}C NMR (100 MHz, Chloroform-d) δ 155.9, 148.9, 141.2, 128.7, 126.2, 120.9, 119.9, 114.2, 55.5. $C_{20}H_{19}NO_2[M^+]$ Exact Mass = 305.1416, MS (ESI-QTOF) = 305.1543.

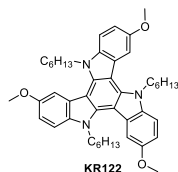


4-bromo-N,N-bis(4-methoxyphenyl)aniline (5).¹⁶³ A solution of 4-methoxy-N-(4-methoxyphenyl)-N-phenylaniline (4) (11 g, 36 mmol, 1 eq.) in THF (35 mL) was cooled to 0 °C. NBS (6.5 g, 36 mmol, 1 eq.) was added in one portion. The reaction mixture was stirred at 0 °C for 3 h. The reaction was quenched by addition of water and extracted with dichloromethane. The organic phase was dried over anhydrous magnesium sulfate. The solvent was removed by rotary evaporation, and the residue was purified on a silica gel column using 20% of DCM in hexane. Yield 10.9 g, 91%. 1H NMR (400 MHz, Chloroform-d) δ 7.26 (d, J = 8.8 Hz, 2H), 7.05 (d, J = 8.5 Hz, 4H), 6.85 (d, J = 8.9 Hz, 4H), 6.82 (d, J = 8.9 Hz, 2H), 3.82 (s, 6H). ^{13}C NMR (100 MHz, Chloroform-d) δ 59.36, 115.07, 124.48, 133.97, 134.58, 138.27, 146.19, 147.41, 152.63. $C_{20}H_{18}BrNO_2[M^+]$ Exact Mass = 383.0521, MS (ESI-QTOF) = 383.0528.



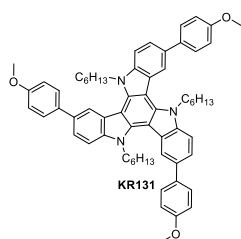
4-methoxy-N-(4-methoxyphenyl)-N-(4-(4,4,5,5-tetramethyl-1,3,2-dioxaborolan-2-yl)phenyl)aniline (6).¹⁶⁴ Compound (5) (6.9 g, 17.9 mmol, 1 eq.) was dissolved in dry DMSO (100 mL) along with bis(pinacolato)diboron (6.8 g, 26.9 mmol, 1.5 eq.), $PdCl_2(dppf)$ (1.46 g, 1.8 mmol, 0.1 eq.), and potassium acetate (5.3 g, 54 mmol, 3 eq.). After stirring the reaction mixture at 80 °C overnight, water was added, and the cooled solution was extracted with DCM. The crude product was purified by column chromatography on silica gel using a 35% to 60% DCM in hexane. Yield 6.1 g, (72%). 1H NMR (400 MHz, Chloroform-d) δ 7.63 (d, J = 8.6 Hz, 2H), 7.10 (d, J = 8.9 Hz, 4H), 6.90 (d, J = 8.6 Hz, 2H), 6.86 (d, J = 8.9 Hz, 4H), 3.83 (s, 6H), 1.35 (s, 12H). ^{13}C NMR (100 MHz, Chloroform-

d) δ 24.83, 55.46, 83.38, 114.72, 118.65, 127.10, 135.74, 140.43, 156.20. $C_{26}H_{30}BNO_4[M^+]$ Exact Mass = 431.2268, MS (ESI-QTOF) = 431.2314.



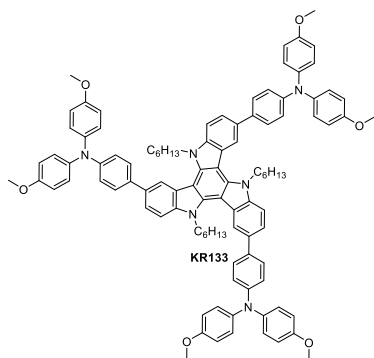
5,10,15-trihexyl-3,8,13-trimethoxy-10,15-dihydro-5H-diindolo[3,2-*a*:3',2'-*c*]carbazole (KR122). In a 50 mL three-necked flask, a solution of 1.95 mL (10.5 mmol, 15 eq.) of sodium methoxide 5.4 M in methanol, dry DMF (15 mL), copper(I) iodide (810 mg, 4.3 mmol, 6 eq.), (3) (0.6 g, 0.72

mmol, 1 eq.) was heated to reflux for 3 h under a N₂ atmosphere. After that, solution was filtered while hot through the celite to remove copper(I) iodide and washed with water. The mixture was extracted with DCM and organic phase was dried over MgSO₄. The product was isolated off on a silica gel column with 50% DCM in hexane to give a product as a pale yellow solid (300 mg, 55%). ¹H NMR (400 MHz, Acetone-d₆) δ 8.17 (d, J = 8.8 Hz, 3H), 7.27 (s, 3H), 6.95 (d, J = 8.7 Hz, 3H), 5.01 – 4.83 (m, 6H), 3.96 (s, 9H), 1.94 – 1.73 (m, 6H), 1.27 – 1.05 (m, 18H), 0.73 (t, J = 7.0 Hz, 9H). ¹³C NMR (100 MHz, Benzene-d₆) δ 157.31, 143.12, 138.04, 122.55, 118.14, 107.27, 104.20, 95.97, 55.02, 46.71, 31.23, 29.28, 26.23, 22.35, 13.71. $C_{45}H_{57}N_3O_3[M^+]$ Exact Mass = 687.4400, MS (MALDI-TOF) = 687.443.



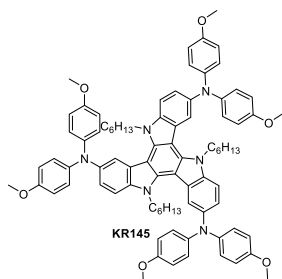
5,10,15-trihexyl-3,8,13-tris(4-methoxyphenyl)-10,15-dihydro-5H-diindolo[3,2-*a*:3',2'-*c*]carbazole (KR131). In a 50 mL single-neck round-bottom flask, (3) (600 mg, 0.72 mmol, 1 eq.), *p*-methoxybenzene boronic acid (440 mg, 2.88 mmol, 4 eq.) and K₂CO₃ (500 mg, 3.6 mmol, 5 eq.) were dissolved in 10 mL of toluene and 5 mL of methanol. This solution was degassed for 20 minutes with a stream of N₂, after which

time (100 mg, 10%) of Pd(dppf)Cl₂ was added. The reaction was then brought to 80 °C overnight. After that, reaction was washed with water. The mixture was extracted with DCM and organic phase was dried over MgSO₄. A gradient eluent of 35:65% DCM:Hex to 50:50% DCM:Hex was used to purify the compound. 500 mg (76% yield) of a white solid was obtained. ¹H NMR (400 MHz, Benzene-d₆) δ 8.52 (d, J = 8.5 Hz, 3H), 7.95 (s, 3H), 7.85 (d, J = 8.6 Hz, 6H), 7.80 (d, J = 8.3 Hz, 6H), 7.03 (d, J = 8.6 Hz, 3H), 4.96 – 4.80 (m, 6H), 3.42 (s, 9H), 2.02 – 1.81 (m, 6H), 1.24 – 0.85 (m, 18H), 0.70 (t, J = 5.6 Hz, 9H). ¹³C NMR (100 MHz, Benzene-d₆) δ 159.69, 142.48, 139.80, 136.56, 135.30, 128.88, 123.05, 122.52, 119.61, 114.88, 114.75, 109.16, 104.11, 54.96, 47.09, 31.63, 30.06, 26.67, 22.76, 14.10. $C_{63}H_{69}N_3O_3[M^+]$ Exact Mass = 915.5339, MS (MALDI-TOF) = 915.536.



4,4',4''-(5,10,15-trihexyl-10,15-dihydro-5H-diindolo[3,2-a:3',2'-c]carbazole-3,8,13-triyl)tris(*N,N*-bis(4-methoxyphenyl)aniline) (KR133). To a degassed mixture of (3) (300 mg, 0.36 mmol, 1 eq.), 4-(4,4,5,5-tetramethyl-1,3,2-dioxaborolan-2-yl)-*N,N*-bis(4-methoxyphenyl)aniline (540 mg, 1.3 mmol, 3.5 eq.) in THF (10 mL) and 2 M aqueous K_2CO_3 (2 mL), $Pd(PPh_3)_4$ (90 mg, 20%) was added under N_2 , the resulting solution was heated to 80 °C overnight. After

cooling to room temperature, the mixture was poured into water and extracted with DCM. The organic layer was concentrated and the residue was purified by column chromatography on silica gel with 60% DCM in hexane gradiently increasing polarity to pure DCM. 240 mg of yellow solid was obtained (45%). 1H NMR (400 MHz, Benzene- d_6) δ 8.52 (d, J = 8.5 Hz, 3H), 7.99 (s, 3H), 7.85 (d, J = 8.6 Hz, 9H), 7.35 (d, J = 8.6 Hz, 6H), 7.20 (d, J = 8.9 Hz, 12H), 6.79 (d, J = 9.0 Hz, 12H), 4.97 – 4.79 (m, 6H), 3.33 (s, 18H), 2.00 – 1.83 (m, 12H), 1.21 – 0.81 (m, 12H), 0.67 (t, J = 6.7 Hz, 9H). ^{13}C NMR (100 MHz, Benzene- d_6) δ 156.15, 148.22, 142.23, 141.36, 139.52, 136.31, 134.87, 126.53, 122.75, 122.24, 121.85, 119.18, 114.87, 108.71, 103.86, 54.71, 46.81, 31.24, 29.66, 26.29, 22.37, 13.71. $C_{102}H_{102}N_6O_6[M^+]$ Exact Mass = 1506.7861, MS (MALDI-TOF) = 1506.805.



5,10,15-trihexyl-*N^3,N^3,N^8,N^8,N^{13},N^{13}*-hexakis(4-methoxyphenyl)-10,15-dihydro-5H-diindolo[3,2-a:3',2'-c]carbazole-3,8,13-tri-amine (KR145). In a 50 mL Schlenk-tube, 500 mg of (3) (0.6 mmol,

1 eq.), 550 mg commercially available 4,4'-dimethoxydiphenylamine (2.4 mmol, 4 eq.) and 290 mg *t*-BuONa (3 mmol, 5 eq.) were dissolved in 10 mL dry toluene and degassed for 20 minutes with N_2 . After the addition of 70 mg $Pd(OAc)_2$ and 0.15 mL of (*t*-Bu) $_3P$ 1 M in toluene, the reaction was heated to 100 °C overnight. The reaction was then diluted with DCM and flashed through a plug of $MgSO_4$ to remove inorganic salts and metallic palladium. This crude residue was purified by flash chromatography with 10% acetone in hexane. 600 mg (78% yield) of yellow solid was obtained. 1H NMR (400 MHz, Benzene- d_6) δ 8.26 (d, J = 8.8 Hz, 3H), 7.51 (s, 3H), 7.40 (d, J = 8.7 Hz, 3H), 7.33 (d, J = 8.9 Hz, 12H), 6.81 (d, J = 8.8 Hz, 12H), 4.65 – 4.52 (m, 6H), 3.33 (s, 18H), 1.82 – 1.66 (m, 6H), 1.09 – 0.80 (m, 18H), 0.68 (t, J = 5.5 Hz, 9H). ^{13}C NMR (100 MHz, Benzene- d_6) δ 155.71, 154.94, 145.12, 143.21, 142.80, 142.33, 138.45, 125.85, 124.27, 122.44, 118.89, 115.90, 114.81, 105.12, 104.20, 54.68, 46.50, 31.21, 29.46, 26.00, 22.26, 13.73. $C_{84}H_{90}N_6O_6[M^+]$ Exact Mass = 1278.6922, MS (MALDI-TOF) = 1278.705.

Chapter 3 Dopant-Free Hole Transporting Materials Based on D- π -A Architecture

Through judicious molecular engineering, novel dopant-free star-shaped D- π -A type hole transporting materials coded **KR355**, **KR321**, and **KR353** were systematically designed, synthesized and characterized. **KR321** has been revealed to form a particular face-on organization on perovskite films favoring vertical charge carrier transport and for the first time, it is shown that this particular molecular stacking feature resulted in a power conversion efficiency over 19% in combination with mixed-perovskite (FAPbI₃)_{0.85}(MAPbBr₃)_{0.15}. The obtained 19% efficiency using a pristine hole transporting layer without any chemical additives or doping is the highest, establishing that the molecular engineering of a planar donor core, π -spacer and periphery acceptors leads to high mobility, and the design provides useful insight into the synthesis of next-generation HTMs for perovskite solar cells and optoelectronic applications.

This chapter is based on published work: *Rakstys et al. J. Mater. Chem. A, 2017, 5, 7811–7815. DOI: 10.1039/C7TA01718A.*¹⁶⁵

3.1 Introduction

Traditionally, the hole transporting layer (HTL) of PSCs is heavily doped with the bis(trifluoromethane)sulfonimide lithium salt (LiTFSI), 4-*tert*-butylpyridine (tBP), and tris(2-(1*H*-pyrazol-1-yl)-4-*tert*-butylpyridine)cobalt(III) tri[hexafluorophosphate] (FK209). tBP is commonly used as the HTL morphology controller, while LiTFSI and FK209 provide the necessary electrical conductivity.^{110,166} However, the use of additives is problematic, since the hygroscopic nature of the lithium salt makes the HTL highly hydrophilic and the Co(III) dopant shows a tendency towards chemical degradation, negatively influencing the stability of the entire device.^{112,113} Therefore, a promising solution for stabilizing PSCs is the appropriate choice of dopant-free HTMs. However, the PCE of pristine HTL based devices are consistently lying around 10%, with only very few examples over 15%.^{167–173} Therefore, development of dopant-free

HTMs with both enhanced moisture resistance and charge transport properties is desired to probe their structure-performance correlations towards the realization of stable and high efficiency PSCs.

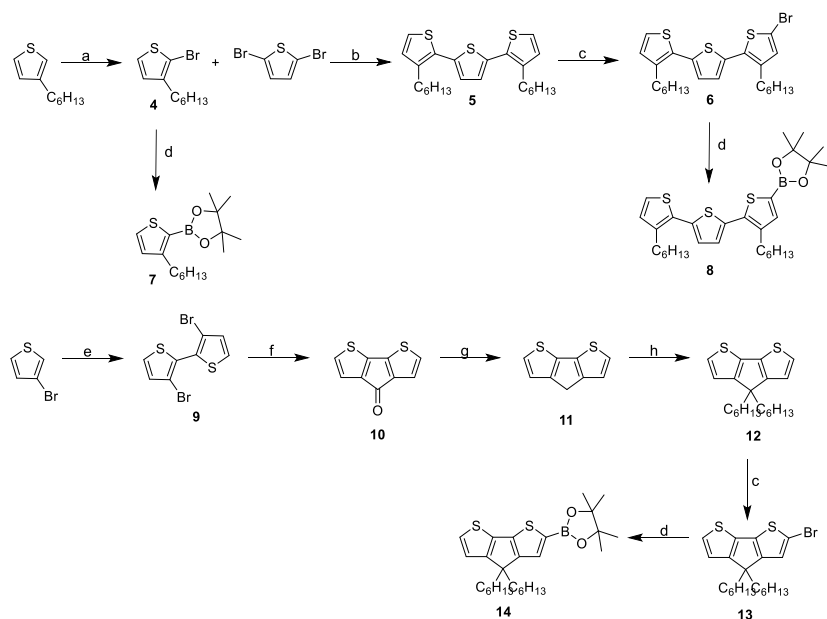
In this work, three novel dopant-free star-shaped donor- π -bridge-acceptor (D- π -A) type HTMs have been systematically engineered. Such molecules feature a planar triazatruxene central core (D), inducing π -stacking for vertical hole conduction, thiophene-based multiple conjugated arms (π) and malononitrile (A). Due to strong intermolecular interaction, these molecules have great potential to show high charge carrier mobility, minimizing ohmic losses of the contact. Moreover, they combine the advantages of both small molecules, e.g. well-defined structures, and polymers, like good thermal, electrochemical and photochemical stability, together with high solubility and suitable wetting on the perovskite.¹⁷⁴ All three molecularly engineered HTMs have been applied in PSCs and for the first time, we show that a highly ordered characteristic face-on organization could favor vertical charge carrier transport in the perovskite solar cell and a PCE over 19% with improved stability was achieved using **KR321**.

3.2 Results and Discussion

3.2.1 Design, Synthesis and Structure

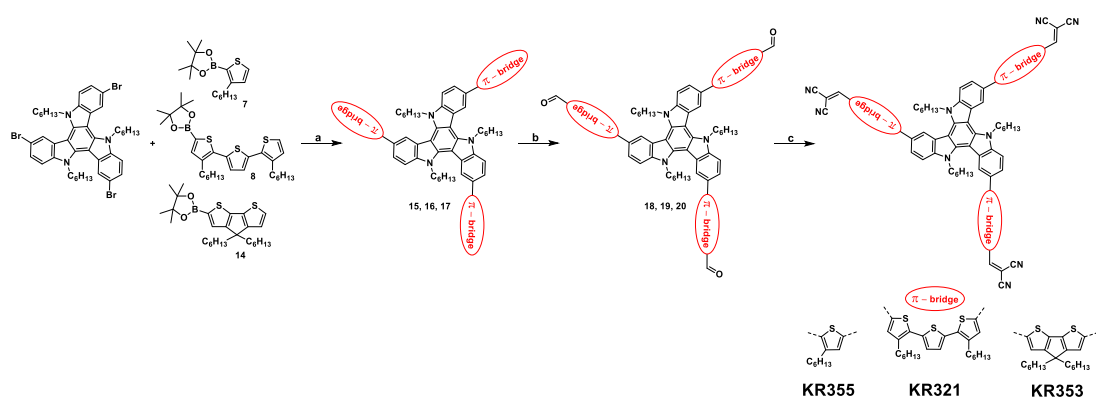
The triazatruxene donor and malononitrile acceptor groups were preserved throughout the series, while the π -bridge was modulated with 3-hexylthiophene, 3,3''-dihexyl-2,2':5',2''-terthiophene and 4,4-dihexyl-4*H*-cyclopenta[2,1-*b*:3,4-*b'*]dithiophene, respectively. The preparation of different π -bridges is presented in Scheme 3.1.

The general synthesis scheme for the preparation of 2,2',2''-(((5,10,15-trihexyl-10,15-dihydro-5*H*-diindolo[3,2-*a*:3',2'-*c*]carbazole-3,8,13-triyl)tris(4-hexylthiophene-5,2-diyl))tris(methanylylidene))trimalononitrile **KR355**, 2,2',2''-(((5,10,15-trihexyl-10,15-dihydro-5*H*-diindolo[3,2-*a*:3',2'-*c*]carbazole-3,8,13-triyl)tris(3,3''-dihexyl-[2,2':5',2''-terthiophene]-5'',5-diyl))tris(methanylylidene))trimalononitrile **KR321** and 2,2',2''-(((5,10,15-trihexyl-10,15-dihydro-5*H*-diindolo[3,2-*a*:3',2'-*c*]carbazole-3,8,13-triyl)tris(4,4-dihexyl-4*H*-cyclopenta[2,1-*b*:3,4-*b'*]dithiophene-6,2-diyl))tris(methanylylidene))trimalononitrile **KR353** is shown in Scheme 3.2.



Scheme 3.1 (a) NBS, CH_3COOH , RT; (b) Mg, $\text{Ni}(\text{dppp})\text{Cl}_2$, $(\text{C}_2\text{H}_5)_2\text{O}$, THF, RT-reflux; (c) NBS, DMF, -40°C -RT; (d) *n*-BuLi, 2-isopropoxy-4,4,5,5-tetramethyl-1,3,2-dioxaborolane, THF, -78°C -RT; (e) LDA, CuCl_2 , THF, -78°C -RT; (f) *n*-BuLi, dimethyl carbamoyl chloride, Et_2O , -78°C -RT; (g) KOH, $\text{NH}_2\text{NH}_2\cdot\text{H}_2\text{O}$, ethylene glycol, 180°C ; (h) $\text{C}_6\text{H}_{13}\text{Br}$, KOH, KI, DMSO, -78°C -RT.

The synthesis begins with the construction of functional conjugated arms on the triazatruxene core by the Suzuki cross-coupling reaction of desired building blocks. After formylation with the Vilsmeier complex, the aldehyde-terminated derivatives were converted into final low bandgap chromophoric HTMs with malononitrile through the Knoevenagel condensation reaction, successfully forming electron accepting moieties.



Scheme 3.2 Synthesis route for star-shaped D- π -A HTMs. (a) $\text{Pd}(\text{PPh}_3)_4$, 2 M aq. K_2CO_3 , THF, 80°C ; (b) POCl_3/DMF , DCE, 0°C -reflux; (c) $\text{CH}_2(\text{CN})_2$, Et_3N , DCM, RT.

The optimized geometries of the new HTMs, along with the HOMO and LUMO pictograms are presented in Figure 3.1. In all three molecules, the HOMO orbitals are mostly developed in the central triazatruxene core along with some thiophene substituents. After three thiophene rings, the space extension of the total HOMO is almost negligible. The extension of the LUMO orbitals is mainly in the arms and localized around the 2-methylenemalononitrile. All calculated energy level values are in close agreement with those obtained experimentally.

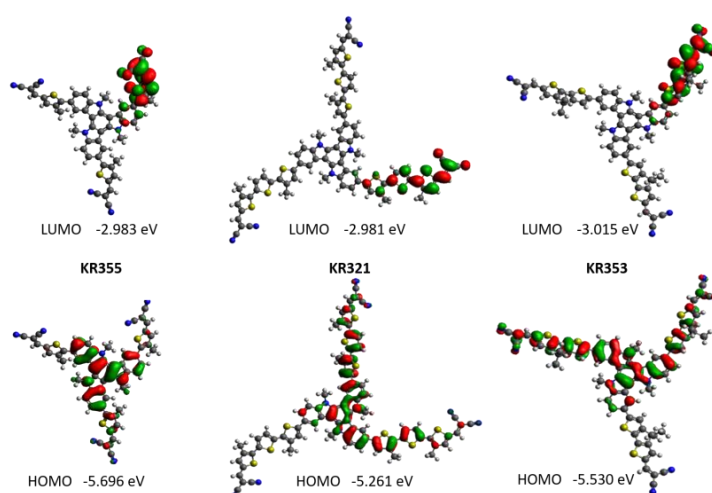


Figure 3.1 Isodensity surface plots (isovalue of 0.025) and energies calculated for the frontier orbitals of the molecules.

3.2.2 Optical, Thermal, and Electrochemical Properties

The normalized UV-vis absorption and photoluminescence (PL) spectra of the new compounds in DCM solutions are shown in Figure 3.2b. Typically, for the dipolar D- π -A type molecules, sharp charge-transfer absorption bands were found in the visible region, with the peak maxima centered at 487, 515 and 569 nm for **KR355**, **KR321**, and **KR353**, respectively. As expected, **KR355** and **KR321** have an extra π - π^* transition induced absorption band in the UV region. Photoluminescence spectra show that all molecules have very large Stokes shifts of around 200 nm suggesting significant changes in the geometrical configuration of the molecules upon excitation.

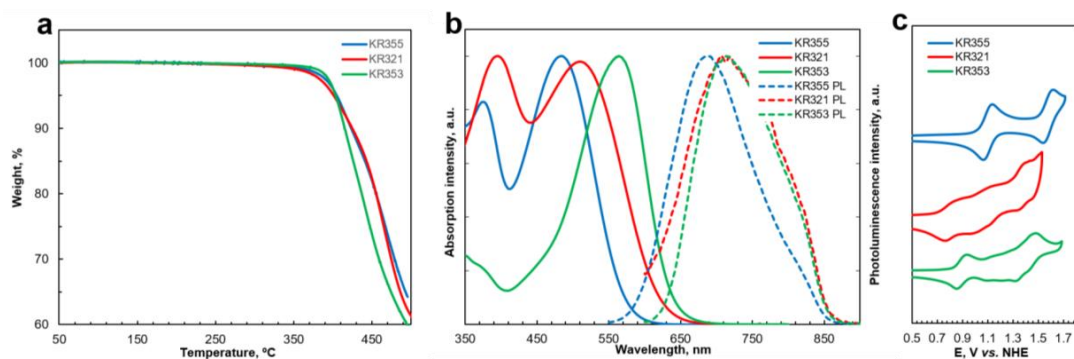


Figure 3.2 a) Thermogravimetric analysis (TGA) data of HTMs, heating rate of 10 °C min⁻¹, N₂ atmosphere; b) UV-Vis absorption (solid line) and photoluminescence (dashed line) spectra normalized at the peak value; and c) cyclic voltammograms of triazatruxene-based HTMs.

The optical bandgap (E_g) is estimated from the intersection of the corresponding normalized absorbance and photoluminescence spectra. It is known that reducing the bandgap of a semiconductor can enhance the intrinsic electrical conductivity by increasing the carrier concentration.¹⁷⁵ E_g values of 2.13, 2.05 and 1.96 eV were determined for **KR355**, **KR321**, and **KR353**, respectively. The HOMO energies of **KR355**, **KR321** and **KR353** were measured to lie at -5.55, -5.24 and -5.34 eV, respectively, by cyclic voltammetry (CV) in Figure 3.2c. The solid-state ionization potential (I_p) was measured by electron photoemission in air on the thin films (Figure 3.4a), and the measured I_p values are fully in agreement with the HOMO levels, -5.52, -5.18 and -5.38 eV, respectively. The oxidation potential variation can be attributed to the changes in the length of the π -bridge moiety. These values are in alignment with those of the photoactive perovskite layer (FAPbI₃)_{0.85}(MAPbBr₃)_{0.15} having a valence band at -5.65 eV and should favor efficient photogenerated charge transfer at the interface. Also, the determined LUMO values below -4 eV should effectively block electron transfer from perovskite to the HTMs (Figure 3.3a). All optical and electrochemical properties are summarized in Table 3.1.

ID	λ_{abs} (nm) ^a	λ_{em} (nm) ^a	E_{HOMO} (eV) ^b	E_g (eV) ^c	E_{LUMO} (eV) ^d	μ_0 (cm ² V ⁻¹ s ⁻¹) ^e
KR355	365, 487	688	-5.55	2.13	-3.42	5.0×10^{-7}
KR321	401, 515	710	-5.24	2.05	-3.19	2.6×10^{-4}
KR353	569	721	-5.34	1.96	-3.38	1.1×10^{-5}

Table 3.1 Optical and electrochemical properties of synthesized HTMs. ^aMeasured in DCM solution; ^bmeasured in DCM/tetra-*n*-butylammonium hexafluorophosphate (0.1 M) solution, using glassy carbon working electrode, Pt reference electrode and Pt counter electrode with Fc/Fc⁺ as an internal standard. Potentials were converted to the normal hydrogen electrode (NHE) by addition of +0.624 V and -4.44 eV to the vacuum, respectively; ^cestimated from the intersection of the normalized absorbance and emission spectra; ^dcalculated from $E_{LUMO} = E_{HOMO} + E_g$; ^emeasured by space-charge limited current (SCLC) regime and fitted using Mott-Gurney law.

3.2.3 Surface Geometry Investigation

It is known that the charge within the active layers of a thin film solar cell will preferentially transfer through the vertical direction. At the same time, C_{3h} symmetrical molecules have the advantage of forming face-on stacking and columnar geometry on the surface, which will favor vertical charge transport along the π - π stacking direction. To prove the concept, the supramolecular organization of the new HTMs on the silica substrate surface was determined by grazing-incidence wide-angle X-ray scattering (GIWAXS). The corresponding patterns in Figure 3.3b indicate significant differences in self-assembly between the compounds. The highest order of the series and a distinct surface arrangement has been found only for **KR321**. Interestingly, **KR321** shows an ideally characteristic face-on organization with columnar stacks standing on the surface as illustrated. For this molecular arrangement, an intense π -stacking reflection appears out-of-plane of the pattern and is related to a d -spacing of 0.38 nm. Furthermore, in-plane scattering intensities correspond to the rectangular lattice of the intercolumnar organization of **KR321** (lattice parameters of $a = 6.04$ nm and $c = 1.46$ nm). The narrow azimuthal intensity distribution of these reflections suggests a pronounced out-of-plane surface alignment of the columnar stacks (Figure 3.3c). The observed face-on orientation is expected to favor the vertical charge carrier transport and improve the solar cell efficiency in comparison to those of **KR353** and **KR355**. An identical enhancement in solar cell performance was observed for face-on arranged donor-acceptor polymers.¹⁷⁶ However, the alignment mechanisms of organic semiconductors during solution deposition are still under discussion. One hypothesis is that low aggregation and the existence of monomeric species in the solution result in a face-on organization, while aggregates are arranged edge-on in the film.^{177,178} The molecular structure plays a fundamental role in the solution aggregation and hence for the surface ordering. Normally a face-on orientation was achieved for various small molecular weight disc-shaped liquid crystalline molecules by cooling from their isotropic melt between two surfaces.¹⁷⁹⁻¹⁸¹ In contrast to **KR321**, **KR353** and **KR355** are poorly ordered leading to patterns with only one isotropic intercolumnar peak (the d -spacing of the first peak is 2.27 nm for **KR353** and 2.02 nm for **KR355**). The decrease in order and lack of vertical surface alignment of **KR353** and **KR355** could lead to the decline of their device performance.

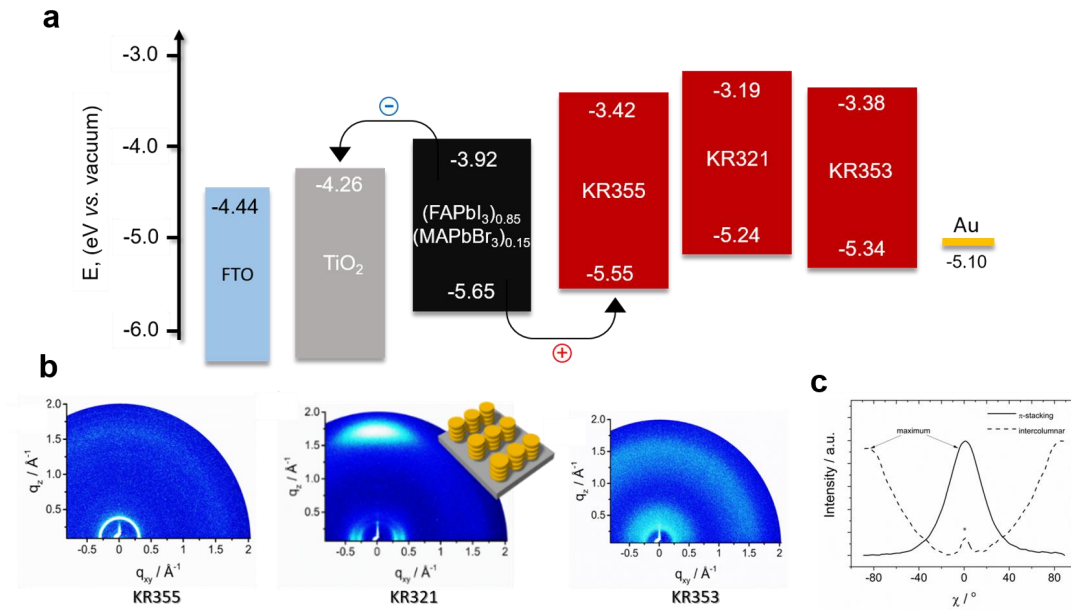


Figure 3.3 a) Energy level comparison in FTO/TiO₂/mixed-perovskite/HTMs/Au stack; b) GIWAXS patterns of the HTM films coated from tetrachloroethane on a silica wafer (schematic illustration of the molecular surface arrangement of KR321); and c) azimuthal integration of the π -stacking and intercolumnar reflections (the star indicates scattering at the beam stop).

3.2.4 Photophysical Properties

To gain insight into the interface processes and in particular on the hole transfer at the perovskite/HTM interface, the steady-state photoluminescence (PL) was monitored. Figure 3.4b shows the comparison of the PL spectra between the pristine perovskite and the perovskite interfaced with spiro-OMeTAD as well as with the series of new molecules presented. The perovskite samples have a comparable thickness of 300 nm. This enables to retain a constant density of absorbed photons for all the samples investigated. The CWPL spectra have been registered upon excitation at 650 nm; this enabled to selectively excite the perovskite and not the HTM. The perovskite/HTMs show a reduction of the PL signal with respect to the pristine perovskite film. This suggests that interfacial hole transfer happens and quenches the PL signal. In particular, **KR321** shows a similar quenching to that observed for spiro-OMeTAD. The charge transport properties (Figure 3.4c, Table 3.1) of the novel derivatives were studied using the space-charge limited current (SCLC) regime by fabricating hole-only devices on an ITO/PEDOT:PSS/HTM/Au architecture. The calculated vertical hole mobility value of **KR321** is $2.6 \times 10^{-4} \text{ cm}^2 \text{ V}^{-1} \text{ s}^{-1}$, which is one order of magnitude higher than that of **KR353** ($\mu_0 = 1.1 \times 10^{-5} \text{ cm}^2 \text{ V}^{-1} \text{ s}^{-1}$) and three orders of magnitude higher than that of **KR355** ($\mu_0 = 5.0 \times 10^{-7} \text{ cm}^2 \text{ V}^{-1} \text{ s}^{-1}$).

$V^{-1} s^{-1}$), indicating improved charge hopping properties through face-on oriented columnar stacks.

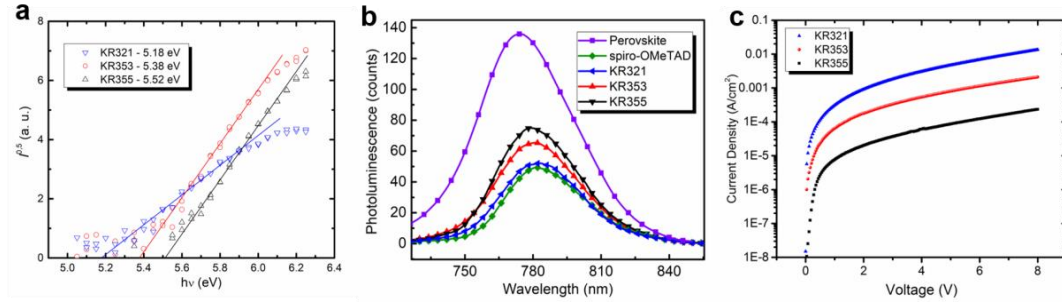


Figure 3.4 a) Photoemission in air spectra of the synthesized HTMs; b) CW photoluminescence spectra, excited at 650 nm for the pristine perovskite film and perovskite/HTM. All the samples have been encapsulated with a PMMA layer to prevent degradation or any oxygen/moisture induced effects; and c) SCLC measurement of the HTMs films.

3.2.5 Photovoltaic Performance and Dopant-Free HTM-Based Device Stability

To demonstrate the function of the novel compounds as dopant-free HTMs, PSCs with mixed perovskite absorber $(FAPbI_3)_{0.85}(MAPbBr_3)_{0.15}$ (MA: $CH_3NH_3^+$, FA: $NH=CHNH_3^+$) were prepared. Perovskite precursor solution was prepared by dissolving PbI_2 (1.15 M), FAI (1.10 M), $PbBr_2$ (0.2 M), and MABr (0.2 M) in an anhydrous solvent DMF:DMSO = 4:1 (volume ratio). 15 mM HTM solutions in tetrachloroethane at 70°C, was spin-coated on the top of the perovskite layer. For comparison, the devices using Spiro-OMeTAD as HTM were prepared from chlorobenzene solutions consisting of 60 mM spiro-OMeTAD, 30 mM LiTFSI, 198 mM tBP, and 1.8 mM of tris(2-(1H-pyrazol-1-yl)-4-tert-butylpyridine)cobalt(III)tris(bis(trifluoromethylsulfonyl)imide) (FK209). Figure 3.5a displays the cross-sectional image of the PSC containing **KR321**, analyzed using a field-emission scanning electron microscope. The device is made using 700 nm thick perovskite atop a 200 nm thick mesoporous TiO_2 layer, which was deposited on FTO glass coated with 50 nm of compact TiO_2 . The device is completed by depositing a 70 nm thick HTM layer and 80 nm of gold as the back contact.

The current density-voltage ($J-V$) characteristics of the champion PSCs using the dopant-free HTMs under AM1.5G irradiation at 100 mW cm^{-2} are shown in Figure 3.5b, and the corresponding device output parameters are summarized in Table 3.2. The device with dopant-free **KR321** as the HTM, which was determined to have ideal columnar stacks standing on the surface showed an excellent PCE of 19%. The device exhibited an open-circuit voltage (V_{oc}) of

1.13 V, a short-circuit current density (J_{sc}) of 21.7 mA cm⁻², and a fill factor (FF) of 0.78, indicating its identical photovoltaic performance to the heavily doped spiro-OMeTAD reference. In contrast, devices using dopant-free **KR353** and **KR355** only yield very low PCEs of 14.87% and 8.8%, respectively, which is attributed to the significantly decreased J_{sc} and FF, most likely due to the lower lying LUMO level leading to poor electron blocking and greater charge recombination. This is also fully in agreement with the result of GIWAXS measurement, proving the advantage of ordered face-on stacking on the charge transport and hence the device performance. The incident photon-to-electron conversion efficiency (IPCE) spectra with integrated J_{sc} values are shown in Figure 3.5c. The integrated photocurrents calculated from the overlap integral of the IPCE spectra are 21.2, 18.4, 16.6, and 22.4 mA cm⁻² for **KR321**, **KR353**, **KR355**, and spiro-OMeTAD, respectively, and are consistent with those obtained from the experimental J - V measurements.

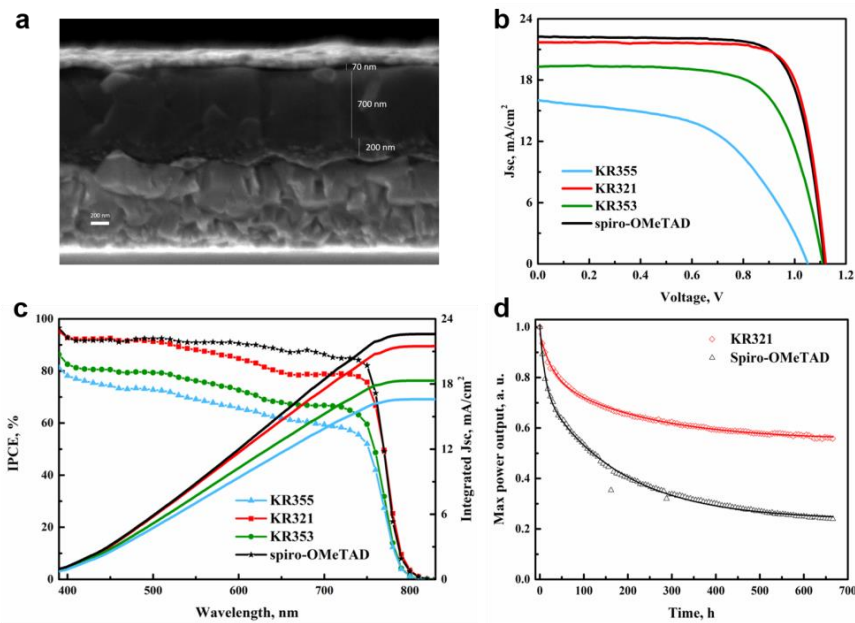


Figure 3.5 a) Cross-sectional SEM micrograph of perovskite device containing KR321; b) current-voltage curves of the novel dopant-free HTMs and doped spiro-OMeTAD as the reference; c) IPCE spectra of the devices; and d) normalized maximum power point tracking of perovskite solar cells prepared in a single experiment, using KR321 and spiro-OMeTAD as HTMs. The measurement was performed under UV-filtered simulated sunlight in an argon atmosphere without any encapsulation for 650 h.

ID	J_{sc} (mA/cm ²)	V_{oc} (V)	FF	PCE (%)
KR355	16.01	1.05	0.53	8.88
KR321	21.70	1.13	0.78	19.03
KR353	19.31	1.11	0.69	14.87
spiro-OMeTAD	22.25	1.12	0.76	19.01

Table 3.2 Photovoltaic performance of the devices based on KR321, KR353, KR355 and spiro-OMeTAD under AM1.5G illumination (100 mW cm⁻²).

In Figure 3.5d, the maximum power point tracking of perovskite devices containing pristine **KR321** and doped spiro-OMeTAD layers is shown. During the measurement, unsealed devices were kept in argon ambience under a constant illumination of 100 mW cm⁻². The devices were maintained at the maximum power point during aging and the current-voltage curve was recorded automatically every 2 h. The efficiency of the devices initially decreased in early time decay. Similar dynamics have recently been observed demonstrating that a rapid degradation mechanism is activated by metal electrode migration through HTMs and contact with the perovskite layer.^{182,183} The general trend showed significantly improved durability of the device prepared with dopant-free **KR321**, which maintained 60% of its initial PCE after 650 h, while the PCE of devices with doped spiro-OMeTAD dropped by 80% under identical conditions.

3.3 Conclusions

To conclude, three symmetrical dopant-free hole transporting materials based on the D- π -A type architecture have successfully synthesized. For the first time, we show that face-on formed columnar stacks of HTM molecules are beneficial for charge transfer within a perovskite solar cell. The optimized structure of **KR321** showed a highly ordered characteristic face-on organization leading to increased vertical charge carrier transport and a power conversion efficiency over 19% with improved stability. This result is on par with the heavily doped spiro-OMeTAD reference, clearly showing the importance of appropriate molecular engineering and the great prospects of dopant-free HTMs for perovskite solar cells, and outperforms most of the other dopant-free HTMs reported to date.

3.4 Synthetic Methods and Procedures

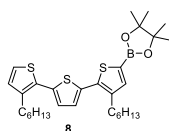
2-bromo-3-hexylthiophene (4).¹⁸⁴ To a solution of 3-hexylthiophene (7.66 g, 45.5 mmol, 1 eq.) in glacial acetic acid (25 mL) was added *N*-bromosuccinimide (8.02 g, 45.5 mmol, 1 eq.) in one portion under nitrogen at room temperature. The mixture was left to stir at RT for 24 h and was washed with water three times, extracted with hexane and the organic phase was dried over MgSO₄. After removal of the solvent, the residual was purified on a silica gel column using hexane as eluent. (10.7 g, 95% yield). ¹H NMR (400 MHz, Chloroform-d) δ 7.18 (d, *J* = 5.6 Hz, 1H), 6.79 (d, *J* = 5.6 Hz, 1H), 2.62-2.49 (m, 2H), 1.60-1.54 (m, 2H), 1.36-1.26 (m, 6H), 0.91-0.86 (m, 3H). ¹³C NMR (100 MHz, Chloroform-d) δ 142.1, 128.4, 125.3, 108.9, 77.4, 77.2, 76.9, 31.8, 29.9, 29.5, 29.0, 22.8, 14.2. C₁₀H₁₅BrS[M⁺] Exact Mass = 246.0078, MS (ESI-QTOF) = 246.01.

3,3''-dihexyl-2,2':5,2''-terthiophene (5).¹⁸⁵ Mg turnings (0.89 g, 36.6 mmol, 3.8 eq.) were suspended in 30 mL of diethyl ether. A solution of (4) (7 g, 28.3 mmol, 2.9 eq.) in 20 mL of diethyl ether was added dropwise to the reaction vessel and the mixture was refluxed for 1 h. The solution was cannulated into a second flask, which contained a solution of 2,5-dibromothiophene (2.35 g, 9.7 mmol, 1 eq.) and Ni(dppp)Cl₂ (65 mg, 0.12 mmol, 12%) in 30 mL of diethyl ether and was refluxed for 1.5 h. The organic layer was washed with water three times and extracted with DCM. The solvent was removed via rotary evaporation to yield a brown oil which was purified on a silica gel column using hexane as eluent to yield 3.5 g (86%). ¹H NMR (400 MHz, Chloroform-d) δ 7.21 (d, 2H), 7.09 (s, 2H), 6.98 (d, 2H), 2.82 (t, 4H), 1.71-0.91 (m, 22H). ¹³C NMR (100 MHz, Chloroform-d) δ 139.72, 136.09, 130.07, 126.08, 123.76, 31.72, 30.76, 29.34, 29.28, 22.67, 14.12. C₂₄H₃₂S₃[M⁺] Exact Mass = 416.1666, MS (ESI-QTOF) = 416.1668.

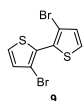
5-bromo-3,3''-dihexyl-2,2':5,2''-terthiophene (6). Compound (5) (3 g, 7.2 mmol, 1 eq.) was dissolved in DMF (40 mL) and cooled to -40 °C. NBS (1.28 g, 7.2 mmol, 1 eq.) was added in small portions during the period of 4 h. After stirring the reaction mixture at RT overnight, water was added, and the solution was extracted with DCM. The crude product was purified by column chromatography on silica gel using hexane. Yield 2.4 g of yellow oil (67%). ¹H NMR (400 MHz, Chloroform-d) δ 7.06 (d, *J* = 5.2, 2H), 7.01 (d, *J* = 3.6, 2H), 6.89 (s, 1H), 2.74 (t, *J* = 8.0, 4H), 1.58 (m, 4H), 1.31 (m, 12H), 0.90 (t, *J* = 6.6, 6H). C₂₄H₃₁BrS₃[M⁺] Exact Mass = 494.0771, MS (ESI-QTOF) = 494.068.

2-(3-hexylthiophen-2-yl)-4,4,5,5-tetramethyl-1,3,2-dioxaborolane (7). Compound (4) (3.8 g, 15 mmol, 1 eq.) was dissolved in 50 mL THF. The solution was

cooled to $-78\text{ }^{\circ}\text{C}$. *n*-Butyllithium (2.5 M in hexane, 7 mL, 16.5 mmol, 1.1 eq.) was added dropwise by syringe and the solution was stirred for 1 h at $-78\text{ }^{\circ}\text{C}$. 2-Isopropoxy-4,4,5,5-tetramethyl-1,3,2-dioxaborolane (3.14 g, 16.5 mmol, 1.1 eq.) was added dropwise by syringe. The solution was allowed to warm to room temperature and stirred overnight. The reaction was quenched by adding 30 mL of water. The organic layer was extracted with DCM ($2 \times 40\text{ mL}$), washed with water (50 mL) and brine (50 mL) and dried over magnesium sulfate. After filtration, the organic layer was concentrated under reduced pressure. The crude product was purified by column chromatography on silica gel using 40% DCM in hexane. Yield 2.7 g of yellow oil (71%). $^1\text{H NMR}$ (400 MHz, Dichloromethane- d_2) δ 7.43 (s, 1H), 7.21 (d, $J = 5.2\text{ Hz}$, 1H), 7.14 (d, $J = 3.7\text{ Hz}$, 1H), 7.08 (d, $J = 3.8\text{ Hz}$, 1H), 6.97 (d, $J = 5.2\text{ Hz}$, 1H), 2.80 (t, $J = 7.6\text{ Hz}$, 4H), 1.78 – 1.55 (m, 4H), 1.34 (s, 24H), 0.88 (t, $J = 6.1\text{ Hz}$, 6H). $\text{C}_{30}\text{H}_{43}\text{BO}_2\text{S}_3[\text{M}^+]$ Exact Mass = 542.2518, MS (ESI-QTOF) = 542.252.



2-(3,3'-dihexyl-[2,2':5,2''-terthiophen]-5-yl)-4,4,5,5-tetramethyl-1,3,2-dioxaborolane (8). Compound (6) (2.2 g, 4.4 mmol, 1 eq.) was dissolved in 30 mL THF. The solution was cooled to $-78\text{ }^{\circ}\text{C}$. *n*-Butyllithium (2.5 M in hexane, 2 mL, 4.9 mmol, 1.1 eq.) was added dropwise by syringe and the solution was stirred for 1 h at $-78\text{ }^{\circ}\text{C}$. 2-Isopropoxy-4,4,5,5-tetramethyl-1,3,2-dioxaborolane (0.9 g, 4.9 mmol, 1.1 eq.) was added dropwise by syringe. The solution was allowed to warm to room temperature and stirred overnight. The reaction was quenched by adding 30 mL of water. The organic layer was extracted with DCM ($2 \times 40\text{ mL}$), washed with water (50 mL) and brine (50 mL) and dried over magnesium sulfate. After filtration, the organic layer was concentrated under reduced pressure. The crude product was purified by column chromatography on silica gel using 20-50% DCM in hexane. Yield 1.2 g (50%). $^1\text{H NMR}$ (400 MHz, Chloroform- d) δ 7.47 (d, $J = 4.6\text{ Hz}$, 1H), 7.01 (d, $J = 4.7\text{ Hz}$, 1H), 2.89 (t, $J = 7.7\text{ Hz}$, 2H), 1.65-1.57 (m, 2H), 1.33 (s, 12H), 1.29 (m, 6H), 0.91-0.89 (t, 3H). $^{13}\text{C NMR}$ (101 MHz, CDCl_3) δ 154.83, 148.34, 131.39, 130.42, 83.65, 31.91, 31.81, 30.26, 29.11, 24.93, 22.76, 14.26. $\text{C}_{16}\text{H}_{27}\text{BO}_2\text{S}[\text{M}^+]$ Exact Mass = 294.1825, MS (ESI-QTOF) = 294.203.



3,3'-dibromo-2,2'-bithiophene (9).¹⁸⁶ To a solution of 3-bromothiophene (32 g, 100 mmol, 1 eq.) in freshly distilled THF (240 mL) at $-78\text{ }^{\circ}\text{C}$ was added with lithium diisopropylamide (LDA) (50 mL, 100 mmol, 1 eq.) over 30 min. After 1 h stirring at $-78\text{ }^{\circ}\text{C}$, the reaction solution was added with anhydrous CuCl_2 (52.8 g, 400 mmol, 4 eq.) in portions. After another 1 h stirring at $-78\text{ }^{\circ}\text{C}$, the reaction mixture was warmed to room temperature and stirred overnight. Quenched with saturated aqueous NH_4Cl , the organic layer was separated and the aqueous layer was extracted with DCM. The combined organic layers were

washed with water and brine, dried over MgSO_4 , and concentrated via rotary evaporation. The pure compound was obtained as a pale yellow solid (24 g, 74%) with flash chromatography over silica gel column using hexane as eluent. ^1H NMR (400 MHz, Chloroform- d) δ 7.08 (d, J = 5.4 Hz, 2H), 7.41 (d, J = 5.4 Hz, 2H). ^{13}C NMR (100 MHz, Chloroform- d) δ 112.65, 127.53, 128.89, 130.81. $\text{C}_8\text{H}_4\text{Br}_2\text{S}_2[\text{M}^+]$ Exact Mass = 321.8121, MS (ESI-QTOF) = 321.824.



4H-cyclopenta[2,1-b:3,4-b']dithiophen-4-one (10).¹⁸⁷ To a solution of (9) (24 g, 46 mmol, 1 eq.) in Et_2O (350 mL), n -BuLi 2.5 M in hexane (41 mL, 102 mmol, 2.2 eq.) was added dropwise at -78°C . After keeping at -78°C for 2 h, dimethyl carbamoyl chloride (5.66 mL, 46 mmol, 1 eq.) was added, then the reaction mixture warmed slowly to RT overnight. The reaction mixture was quenched with water at 0°C , extracted with Et_2O and then washed with saturated ammonium chloride and water. After drying over MgSO_4 , the solvent was removed by rotary evaporation. The residue was purified by column chromatography (DCM:hexane, 1:1) as eluent to yield 7 g of purple solid (79%). ^1H NMR (400 MHz, Chloroform- d) δ 6.99 (d, J = 4.8 Hz, 2H), 7.04 (d, J = 4.8 Hz, 2H). ^{13}C NMR (100 MHz, Chloroform- d) δ 121.7, 127.1, 142.4, 149.2, 182.7. $\text{C}_9\text{H}_4\text{BOS}_2[\text{M}^+]$ Exact Mass = 191.9704, MS (ESI-QTOF) = 191.982.

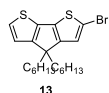


4H-cyclopenta[2,1-b:3,4-b']dithiophene (11).¹⁸⁸ KOH (6 g, 107 mmol, 3.5 eq.) and hydrazine hydrate (12.15 mL) were added to a suspension of compound (10) (6 g, 31 mmol, 1 eq.) in ethylene glycol (200 mL). Reaction mixture was refluxed at 180°C during 8 h under argon. After cooling down, water (100 mL) with HCl and 300 mL DCM was added. Organic layer was isolated, washed with water (2×200 mL) and dried over anhydrous MgSO_4 . After removing the solvent by rotary evaporation and purification by column chromatography, using hexane as an eluent, pure product was obtained (3.3 g, 60% yield). ^1H NMR (400 MHz, Chloroform- d) δ 7.19 (d, J = 4 Hz, 2H), 7.10 (d, J = 4 Hz, 2H), 3.56 (s, 2H). ^{13}C NMR (100 MHz, Chloroform- d) δ 149.9, 138.9, 124.7, 123.2, 31.8. $\text{C}_9\text{H}_6\text{S}_2[\text{M}^+]$ Exact Mass = 177.9911, MS (ESI-QTOF) = 177.991.

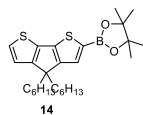


4,4-dihexyl-4H-cyclopenta[2,1-b:3,4-b']dithiophene (12).¹⁸⁹ To a solution of (11) (1.5 g, 8.4 mmol, 1 eq.) in dimethyl sulfoxide (100 mL) was added hexyl bromide (3.5 g, 21.2 mmol, 2.5 eq.) and a catalytic amount of potassium iodide (50 mg). The mixture was cooled to 0°C , followed by the slow addition of solid potassium hydroxide (1.5 g). The mixture was stirred at room temperature overnight. The mixture was then poured into water and the organic phase extracted with DCM and dried over MgSO_4 , filtered, and concentrated to give the crude product as yellow oil. Purification via flash chromatography with hexane gave pure product as colorless oil. Yield 2.4 g (82%). ^1H NMR (400 MHz, Chloroform- d) δ 7.14 (d, J = 4.8 Hz, 2H), 6.92 (d, J = 4.8 Hz, 2H), 1.81 (m, 4H), 1.13 (m, 12H), 0.94 (m, 4H), 0.81 (t, J = 7.0 Hz,

6H). ^{13}C NMR (100 MHz, Chloroform- d) δ 158.08, 136.43, 124.38, 121.59, 53.22, 37.75, 31.60, 29.68, 24.47, 22.58, 14.01. $\text{C}_{21}\text{H}_{30}\text{S}_2[\text{M}^+]$ Exact Mass = 346.1789, MS (ESI-QTOF) = 346.192.



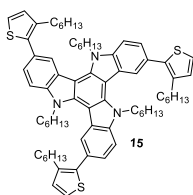
2-bromo-4,4-dihexyl-4H-cyclopenta[2,1-b:3,4-b']dithiophene (13). Compound (12) (2.4 g, 6.9 mmol, 1 eq.) was dissolved in DMF (30 mL) and cooled to $-40\text{ }^\circ\text{C}$. NBS (1.23 g, 6.9 mmol, 1 eq.) was added in small portions during the period of 4 h. After stirring the reaction mixture at RT overnight, water was added, and the solution was extracted with DCM. The crude product was purified by column chromatography on silica gel using hexane. Yield 2.3 g (78%). ^1H NMR (400 MHz, Chloroform- d) δ 7.16 (d, $J = 4.8$ Hz, 1H), 6.94 (s, 1H), 6.91 (d, $J = 4.8$ Hz, 1H), 1.79 (m, 4H), 1.18 (m, 4H), 1.13 (m, 8H), 0.91 (m, 4H), 0.83 (t, $J = 7.2$ Hz, 6H). $\text{C}_{21}\text{H}_{29}\text{BrS}_2[\text{M}^+]$ Exact Mass = 424.0894, MS (ESI-QTOF) = 424.222.



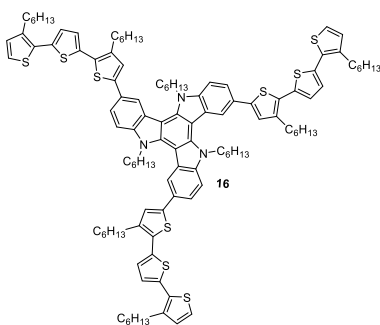
2-(4,4-dihexyl-4H-cyclopenta[2,1-b:3,4-b']dithiophen-2-yl)-4,4,5,5-tetramethyl-1,3,2-dioxaborolane (14). Compound (13) (2.3 g, 5.4 mmol, 1 eq.) was dissolved in 30 mL THF. The solution was cooled to $-78\text{ }^\circ\text{C}$. *n*-Butyllithium (2.5 M in hexane, 2.4 mL, 5.9 mmol, 1.1 eq.) was added dropwise by syringe and the solution was stirred for 1 h at $-78\text{ }^\circ\text{C}$. 2-Isopropoxy-4,4,5,5-tetramethyl-1,3,2-dioxaborolane (1.1 g, 5.9 mmol, 1.1 eq.) was added dropwise by syringe. The solution was allowed to warm to room temperature and stirred overnight. The reaction was quenched by adding 30 mL of water. The organic layer was extracted with DCM (2×40 mL), washed with water (50 mL) and brine (50 mL) and dried over magnesium sulfate. After filtration, the organic layer was concentrated under reduced pressure. The crude product was purified by column chromatography on silica gel using 20-30% DCM in hexane. Yield 1.1 g (43%). ^1H NMR (400 MHz, Chloroform- d) δ 7.43 (m, 1H), 7.17 (m, 1H), 6.92 (m, 1H), 1.85 (m, 4H), 1.35 (s, 12H), 0.85 (m, 16H), 0.74 (m, 6H). ^{13}C NMR (100 MHz, Chloroform- d): δ 160.97, 144.07, 131.87, 83.97, 52.66, 43.20, 35.13, 33.80, 28.31, 24.77, 22.77, 10.57. $\text{C}_{27}\text{H}_{41}\text{BO}_2\text{S}_2[\text{M}^+]$ Exact Mass = 472.2641, MS (ESI-QTOF) = 472.252.

A general method for Suzuki-Miyaura coupling reaction:

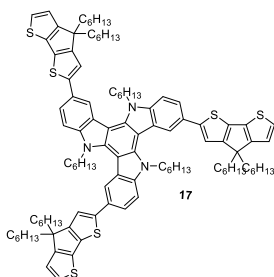
To a degassed mixture of 3,8,13-tribromo-5,10,15-trihexyl-10,15-dihydro-5H-diindolo[3,2- α :3',2'- c]carbazole (0.4 g, 0.48 mmol, 1 eq.), 4,4,5,5-tetramethyl-1,3,2-dioxaborolanes (7, 8 or 14) 3.5 eq. in THF (15 mL) and 2 M aqueous K_2CO_3 (3 mL), $\text{Pd}(\text{PPh}_3)_4$ (20%) was added under N_2 , the resulting solution was heated to $80\text{ }^\circ\text{C}$ overnight. After cooling to room temperature, the mixture was poured into water and extracted with DCM. The organic layer was concentrated and the residue was purified by column chromatography.



5,10,15-trihexyl-3,8,13-tris(3-hexylthiophen-2-yl)-10,15-dihydro-5H-diindolo[3,2-a:3',2'-c]carbazole (15). The pure compound was obtained after column chromatography on silica gel using 20% DCM in hexane. Yield 0.52 g (99%). $^1\text{H NMR}$ (400 MHz, Chloroform- d) δ 8.33 (d, J = 8.7 Hz, 3H), 7.73 (s, 3H), 7.47 (d, J = 8.2 Hz, 3H), 7.11 (d, J = 5.2 Hz, 3H), 6.97 (d, J = 4.9 Hz, 3H), 5.15 – 4.76 (m, 6H), 2.87 (m, 6H), 2.65 (m, 6H), 2.09 (s, 6H), 1.89 – 1.60 (m, 6H), 1.50 – 1.11 (m, 21H), 1.07 – 0.69 (m, 27H). $\text{C}_{72}\text{H}_{93}\text{N}_3\text{S}_3[\text{M}^+]$ Exact Mass = 1095.6532, MS (ESI-QTOF) = 1095.523.



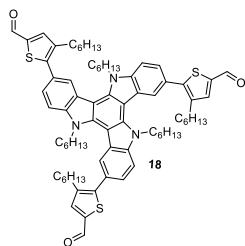
3,8,13-tris(3,3''-dihexyl-[2,2':5,2''-terthiophen]-5-yl)-5,10,15-trihexyl-10,15-dihydro-5H-diindolo[3,2-a:3',2'-c]carbazole (16). The pure compound was obtained after column chromatography on silica gel using 10% acetone in hexane. Yield 0.7 g (80%). $^1\text{H NMR}$ (400 MHz, Methylene Chloride- d_2) δ 8.15 (d, J = 8.5 Hz, 3H), 7.74 (s, 3H), 7.59 (d, J = 7.9 Hz, 3H), 7.36 (s, 3H), 7.28 (d, J = 5.1 Hz, 3H), 7.22 (d, J = 3.8 Hz, 3H), 7.17 (d, J = 3.7 Hz, 3H), 7.05 (d, J = 5.2 Hz, 3H), 4.98 – 4.51 (m, 6H), 3.06 – 2.63 (m, 18H), 2.12 – 1.64 (m, 18H), 1.61 – 1.16 (m, 48H), 1.07 – 0.71 (m, 27H). $\text{C}_{114}\text{H}_{141}\text{N}_3\text{S}_9[\text{M}^+]$ Exact Mass = 1839.8612, MS (ESI-QTOF) = 1839.909.



3,8,13-tris(4,4-dihexyl-4H-cyclopenta[2,1-b:3,4-b']dithiophen-2-yl)-5,10,15-trihexyl-10,15-dihydro-5H-diindolo[3,2-a:3',2'-c]carbazole (17). The pure compound was obtained after column chromatography on silica gel using 10% DCM in hexane. Yield 0.58 g (74%). $^1\text{H NMR}$ (400 MHz, Chloroform- d) δ 8.30 (d, J = 8.8 Hz, 3H), 7.87 (s, 3H), 7.69 (d, J = 8.0 Hz, 3H), 7.38 (s, 3H), 7.24 (d, J = 4.8 Hz, 3H), 7.02 (d, J = 4.7 Hz, 3H), 5.18 – 4.88 (m, 6H), 2.12 – 1.88 (m, 18H), 1.41 – 1.05 (m, 66H), 0.86 (m, 27H). $\text{C}_{105}\text{H}_{135}\text{N}_3\text{S}_6[\text{M}^+]$ Exact Mass = 1629.8980, MS (ESI-QTOF) = 1630.069.

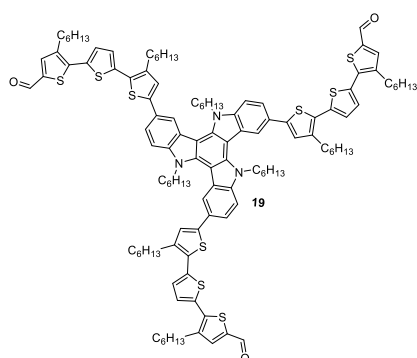
A general method for Vilsmeier–Haack formylation reaction:

Phosphorous oxychloride (5 eq.) was added dropwise to a stirred *N,N*-dimethylformamide (5 eq.) at the temperature of ice water under nitrogen atmosphere. Then the mixture was added to the solution of (15, 16 or 17) 1 eq. in 1,2-dichloroethane (30 mL) dropwise at 0 °C. After addition, the mixture was refluxed overnight. The resulting mixture was neutralized to pH = 7-8 with aqueous NaOH solution (20%), extracted with DCM and the residue was chromatographed on a silica gel column.



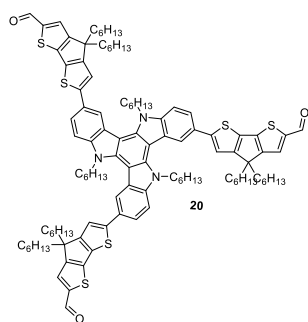
5,5',5''-(5,10,15-trihexyl-10,15-dihydro-5H-diindolo[3,2-a:3',2'-c]carbazole-3,8,13-triyl)tris(4-hexylthiophene-2-carbaldehyde)

(18). The pure compound was obtained after column chromatography on silica gel using DCM, gradually increasing polarity up to 5% THF in DCM. Yield 0.6 g (86%). $^1\text{H NMR}$ (400 MHz, Chloroform- d) δ 9.96 (s, 3H), 8.34 (d, J = 8.4 Hz, 3H), 7.77 (d, J = 7.1 Hz, 6H), 7.51 (d, J = 8.1 Hz, 3H), 2.90 (t, J = 7.9 Hz, 6H), 2.07 (m, 6H), 1.72 (m, 6H), 1.50 – 1.11 (m, 42H), 0.98 – 0.67 (m, 18H). $\text{C}_{75}\text{H}_{93}\text{N}_3\text{O}_3\text{S}_3[\text{M}^+]$ Exact Mass = 1179.6379, MS (ESI-QTOF) = 1179.565.



5'',5''''',5''''''''-(5,10,15-trihexyl-10,15-dihydro-5H-diindolo[3,2-a:3',2'-c]carbazole-3,8,13-triyl)tris(3,3'-dihexyl-[2,2':5',2''-terthiophene]-5-carbaldehyde)

(19). The pure compound was obtained after column chromatography on silica gel using 20-30% acetone in hexane. Yield 0.6 g (95%). $^1\text{H NMR}$ (400 MHz, Methylene Chloride- d_2) δ 9.87 (s, 3H), 8.03 (d, J = 8.7 Hz, 3H), 7.64 (d, J = 5.4 Hz, 6H), 7.51 (d, J = 7.9 Hz, 3H), 7.31 (d, J = 3.7 Hz, 6H), 7.20 (d, J = 3.7 Hz, 3H), 4.79 – 4.51 (m, 6H), 3.00 – 2.74 (m, 6H), 1.85 (m, 18H), 1.66 – 1.14 (m, 60H), 0.97 (t, 27H). $\text{C}_{117}\text{H}_{141}\text{N}_3\text{O}_3\text{S}_9[\text{M}^+]$ Exact Mass = 1923.8459, MS (ESI-QTOF) = 1923.736.



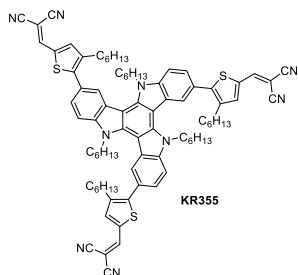
6,6',6''-(5,10,15-trihexyl-10,15-dihydro-5H-diindolo[3,2-a:3',2'-c]carbazole-3,8,13-triyl)tris(4,4-dihexyl-4H-cyclopenta[2,1-b:3,4-b']dithiophene-2-carbaldehyde)

(20). After addition of Vilsmeier complex, the mixture was stirred overnight at room temperature. The pure compound was obtained after column chromatography on silica gel using 15-20% THF in hexane. Yield 0.5 g (73%). $^1\text{H NMR}$ (400 MHz, Chloroform- d) δ 9.90 (s, 3H), 8.32 (d, J = 8.1 Hz, 3H), 7.89 (s, 3H), 7.72 (d, J = 8.0 Hz, 3H), 7.65 (s, 1H), 7.42 (s, 3H), 5.03 (t, 6H), 2.10 – 1.92 (m, 18H), 1.29 (d, J = 18.1 Hz, 66H), 0.96 – 0.67 (m, 27H). $\text{C}_{108}\text{H}_{135}\text{N}_3\text{O}_3\text{S}_6[\text{M}^+]$ Exact Mass = 1713.8828, MS (ESI-QTOF) = 1714.091.

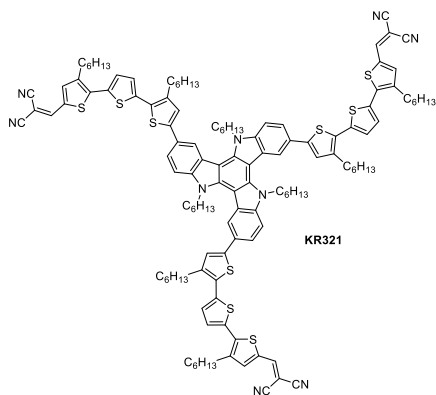
A general method for Knoevenagel condensation reaction:

Aldehyde (18, 19 or 20) 1 eq. and malononitrile (6 eq.) were dissolved in dry DCM (50 mL) and stirred for 1 h with a few drops of triethylamine at room temperature. After completion of the reaction monitored by TLC, the mixture was acidified with few drops of conc. HCl,

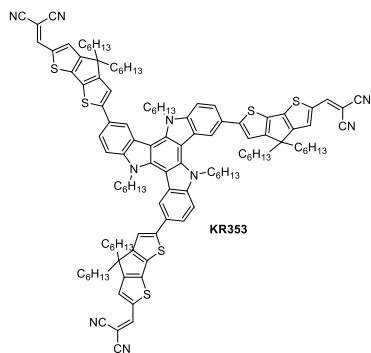
washed with water the organic layer extracted with CH_2Cl_2 , dried over anhydrous magnesium sulfate and filtered. The column chromatography was performed to purify the final compound. Isolated compound was dissolved in THF and dropped into MeOH, precipitate was collected by filtration, washed with MeOH and dried.



2,2',2''-(((5,10,15-trihexyl-10,15-dihydro-5H-diindolo[3,2-a:3',2'-c]carbazole-3,8,13-triyl)tris(4-hexylthiophene-5,2-diyl))tris(methanylylidene))trimalononitrile (KR355). The pure compound was obtained after column chromatography on silica gel using 15-20% THF in hexane. Yield 0.6 g (89%). ^1H NMR (400 MHz, THF-d_8) δ 8.43 (d, J = 8.3 Hz, 3H), 8.30 (s, 3H), 7.90 (d, J = 15.0 Hz, 6H), 7.58 (d, J = 8.3 Hz, 3H), 5.14 – 4.94 (m, 6H), 2.95 (m, 6H), 2.09 – 1.88 (m, 6H), 1.50 – 1.05 (m, 42H), 1.01 – 0.64 (m, 18H). ^{13}C NMR (100 MHz, THF-d_8) δ 151.46, 151.07, 141.66, 140.94, 140.48, 139.94, 133.57, 127.43, 123.73, 121.90, 121.07, 114.18, 113.44, 111.20, 103.24, 75.88, 46.79, 31.65, 31.57, 31.37, 30.58, 29.66, 29.15, 28.96, 28.50, 26.12, 22.54, 22.34, 13.42, 13.28. $\text{C}_{84}\text{H}_{93}\text{N}_9\text{S}_3[\text{M}^+]$ Exact Mass = 1323.6716, MS (ESI-QTOF) = 1323.837.



2,2',2''-(((5,10,15-trihexyl-10,15-dihydro-5H-diindolo[3,2-a:3',2'-c]carbazole-3,8,13-triyl)tris(3,3''-dihexyl-[2,2':5',2''-terthiophene]-5'',5-diyl))tris(methanylylidene))trimalononitrile (KR321). The pure compound was obtained after column chromatography on silica gel starting with pure DCM and switching to 20% hexane in chloroform at the end. Yield 0.4 g (62%). ^1H NMR (400 MHz, THF-d_8) δ 8.29 (d, J = 10.2 Hz, 3H), 8.20 (s, 3H), 7.95 (d, J = 6.3 Hz, 3H), 7.76 (s, 6H), 7.67 (d, J = 8.5 Hz, 3H), 7.50 (d, J = 5.0 Hz, 6H), 7.32 (s, 3H), 5.15 – 4.91 (m, 6H), 2.96 (t, J = 7.3 Hz, 18H), 1.98 (m, 6H), 1.62 – 1.09 (m, 60H), 1.06 – 0.49 (m, 27H). ^{13}C NMR (100 MHz, THF-d_8) δ 153.11, 150.40, 144.78, 144.18, 142.41, 142.01, 141.65, 140.35, 139.92, 139.66, 139.60, 138.26, 133.34, 133.24, 133.02, 132.72, 128.95, 128.85, 128.78, 128.39, 126.03, 125.97, 114.12, 113.38, 76.10, 55.89, 52.70, 31.77, 31.66, 31.33, 30.53, 30.01, 29.80, 29.67, 29.39, 29.17, 29.09, 22.63, 22.58, 22.36, 13.52, 13.48, 13.37. $\text{C}_{126}\text{H}_{141}\text{N}_9\text{S}_9[\text{M}^+]$ Exact Mass = 2067.8796, MS (ESI-QTOF) = 2067.966.



2,2',2''-(((5,10,15-trihexyl-10,15-dihydro-5H-indolo[3,2-a:3',2'-c]carbazole-3,8,13-triyl)tris(4,4-dihexyl-4H-cyclopenta[2,1-b:3,4-b']dithiophene-6,2-diyl))tris(methanylylidene))trimalonitrile (KR353).

The pure compound was obtained after column chromatography on silica gel using 20% THF in hexane. Yield 0.5 g (93%). ^1H NMR (400 MHz, THF- d_8) δ 8.40 (d, J = 8.4 Hz, 3H), 8.19 (s, 3H), 8.10 (s, 3H), 7.80 (d, J = 12.0 Hz, 6H), 7.72 (s,

3H), 5.20 – 5.03 (m, 6H), 2.11 (m, 18H), 1.98 (m, 6H), 1.40 – 1.00 (m, 60H), 0.88 (t, J = 6.6 Hz, 27H). ^{13}C NMR (100 MHz, THF- d_8) δ 165.18, 157.91, 152.98, 151.06, 150.83, 141.62, 139.65, 136.12, 134.03, 131.96, 129.37, 123.45, 122.03, 118.12, 117.52, 114.83, 114.42, 107.44, 103.78, 71.27, 54.17, 37.71, 31.58, 31.33, 29.66, 26.15, 22.53, 22.36, 13.39, 13.30. $\text{C}_{117}\text{H}_{135}\text{N}_9\text{S}_6[\text{M}^+]$ Exact Mass = 1857.9165, MS (ESI-QTOF) = 1858.143.

Chapter 4 Bifluorenylidene-Based Hole Transporting Material

The 4,4'-dimethoxydiphenylamine-substituted 9,9'-bifluorenylidene hole transporting material **KR216** has been synthesized using a straightforward two-step procedure from commercially available and inexpensive starting reagents, mimicking the synthetically challenging 9,9'-spirobifluorene moiety of the well-studied spiro-OMeTAD. A power conversion efficiency of 17.8% has been reached employing a novel HTM in a perovskite solar cells.

This chapter is based on published work: *Rakstys et al. Angew. Chem. Int. Ed. 2016, 55, 7464–7468. DOI: 10.1002/anie.201602545*.¹⁹⁰

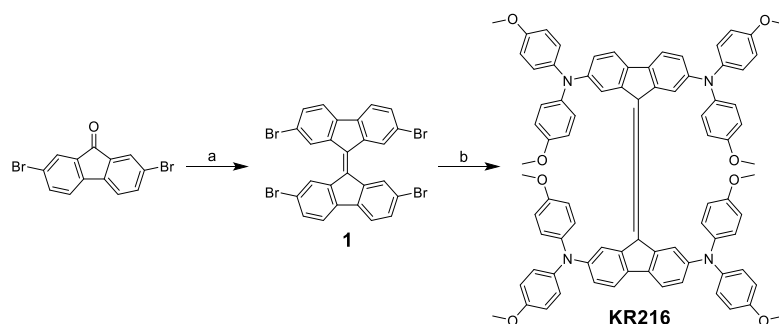
4.1 Introduction

Bifluorenylidene, being known as parent homomeric bistricyclic aromatic ene (BAE), was synthesized in 1875 and started the expansion of BAEs as interesting systems for studies of thermochromic, photochromic, and piezochromic behavior as well as π -extended building blocks for molecular engineering.^{191–194} Here a molecularly engineered HTM 4,4'-dimethoxydiphenylamine-substituted 9,9'-bifluorenylidene **KR216** with performance on par with that of spiro-OMeTAD is presented. In addition, the novel HTM does not require an expensive synthetic procedure and was prepared employing a straightforward two-step strategy. 9-Fluorenylidene moiety is known to facilitate charge carrier migration conveying electrons from donor to acceptor throughout the structure and have never been tested as potential HTM for PSC.¹⁹⁵

4.2 Results and Discussion

4.2.1 Synthesis and Structure Optimization

The general synthesis procedure for the preparation of 2,2',7,7'-tetrakis(*N,N*-di-*p*-methoxyphenylamine)-9,9'-bifluorenylidene **KR216** is shown in Scheme 4.1. Commercially available and inexpensive precursor 2,7-dibromo-9*H*-fluoren-9-one have been reacted with 2,4-bis(4-methoxyphenyl)-1,3,2,4-dithiadiphosphetane-2,4-dithione, well known as Lawesson's reagent, to form 9,9'-ylidene (C=C) double bond. With this the synthesis of 2,2',7,7'-tetrabromo-9,9'-bifluorenylidene **1** by single-step reaction is demonstrated, accelerating the synthetic routes proposed by Wudl and Luh, using dimerization of the substituted 9-bromofluorene in the presence of DBU and desulfurdimerization of dithioketals mediated by $W(CO)_6$, respectively.^{196,197} Furthermore, it is worth noticing that no column chromatography was required in advance for the next step. Then, the symmetrical olefin have been equipped with 4,4'-dimethoxydiphenylamine units using the palladium-catalyzed Buchwald-Hartwig C-N cross-coupling reaction, to release final HTM **KR216** having 9,9'-bifluorenylidene central core, which mimics 9,9'-spirobifluorene moiety of well-studied spiro-OMeTAD.



Scheme 4.1 Straightforward synthetic route for the KR216 HTM. (a) Lawesson's reagent, toluene, 110 °C; (b) 4,4'-dimethoxydiphenylamine, *t*-BuONa, Pd₂dba₃, XPhos, toluene, 110 °C.

It is well known, that both organic impurities and metal residues may present in final raw organic semiconducting materials, and they are known to act as charge carrier traps or photoquenchers significantly affecting their original properties, consequently reducing the photovoltaic performance.^{198,199} Therefore, the lab-grade spiro-OMeTAD was synthesized under the same final cross-coupling step and purified using both flash chromatography and precipitation procedures as for **KR216**, having the same purity grade in order to achieve a more accurate comparison. All synthetic procedures and cost estimation are reported in the section 4.4 Synthetic Methods and Procedures.

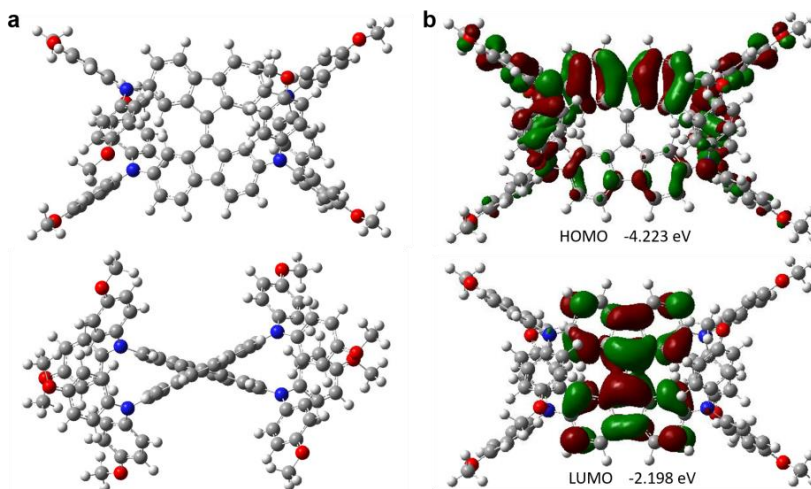


Figure 4.1 a) Geometry optimizations; and b) frontier molecular orbitals of the KR216.

4.2.2 Crystal Structure

The chemical structure of **KR216** is confirmed by X-ray diffraction analysis as displayed in Figure 4.2a. Similar to the ubiquitous spiro-OMeTAD, four diphenyl amine units are attached to the two central fluorene skeletons with four different torsion angles with the minimum of 15.2° and the maximum of 83° . This is an indication of different degree of distortion among the four bulky propeller-shaped diphenyl amine units. This can be understood by Figure 4.2b, in which the crystal structure of **KR216** is found to be distinct from that of spiro-OMeTAD, when the sp^3 carbon atom in the latter is replaced by a double bond between two sp^2 hybridized carbon atoms.²⁰⁰ It is known that the sp^2 hybridized π bond cannot rotate freely and tend to form either *cis*- or *trans*-conformation. So the competition between the planarization and repulsive steric hindrance lead to a pseudo spiro conformation and diversified torsion angles. Therefore, the dihedral angles between the two double-bond connected fluorenes are measured to be either 42.4° (43.7°) or 35.4° (36.5°). These values are much smaller than that of spiro-OMeTAD (89.94°) due to the reason mentioned above (Figure 4.2c).

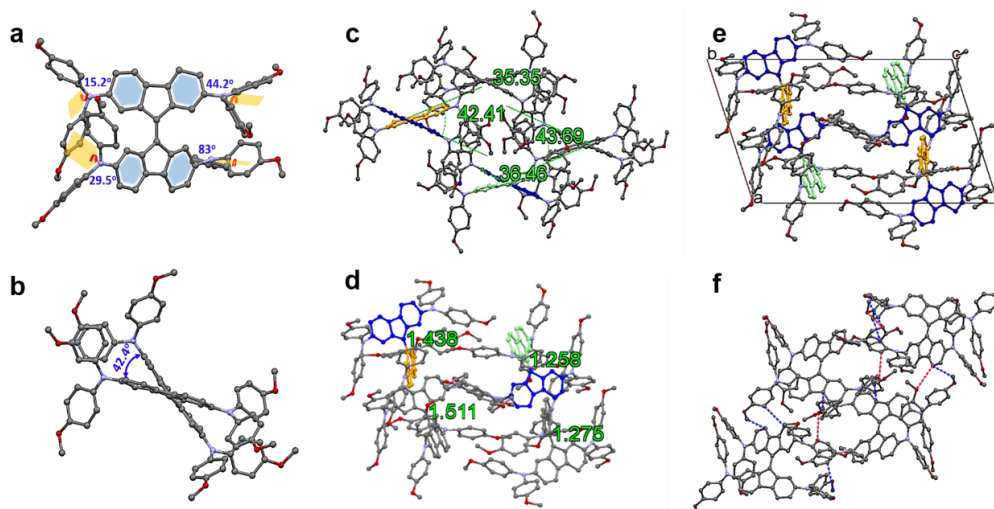


Figure 4.2 a) ORTEP drawings of KR216 determined by X-ray crystallography indicating four different kinds of dihedral angles between the two central fluorenes and four diphenyl amine units (hydrogen atoms omitted for clarity); b) perspective views of KR216 molecule showing one typical dihedral angle between the two fluorene units (42.4°); c) four different dihedral angles between the two planar moieties; d) different length of double bonds of KR216 in one unit cell; e) view down reciprocal cell axis b of the stacking molecules showing three different types of orientation of the eight fluorene units (same orientation with same color); f) non-covalent inter-molecular short contacts of KR216 in one-unit cell. Dashed blue lines illustrate $\pi\cdots\pi$ short contacts (3.378 \AA , and 3.381 \AA) and $C\cdots C$ short contacts (3.254 \AA , 3.313 \AA , 3.336 \AA , 3.340 \AA , 3.350 \AA , and 3.370 \AA). Dashed red lines illustrate $C\cdots O$ short contacts (3.090 \AA , 3.105 \AA , 3.185 \AA and 3.180 \AA).

This effect is also reflected in the length of double bond between two fluorenes, the value of which is also varied according to the degree of distortion (Figure 4.2d). **KR216** was found to crystallize in the triclinic space group $P1$. In one unit cell, four independent molecules the crystal lattice stacked in a highly slipped fashion (Figure 4.2e,f) through $\pi\cdots\pi$, $C\cdots C$, and $C\cdots O$ short contacts as well as CH/π (CH/O) hydrogen bonds. Eight fluorenes are found to have three different types of orientation. As indicated in Figure 4.2e the parallel fluorenes with same orientation is marked with the same color. When scrutinizing the crystal structure of **KR216**, an abundance of non-covalent intermolecular interactions are found with shortest $\pi\cdots\pi$ distance of 3.378 \AA , shortest $C\cdots C$ contacts of 3.254 \AA and shortest $C\cdots O$ contacts of 3.090 \AA . Similar to that of spiro-OMeTAD, due to the highly sterically hindered geometry, no close face to face overlap is observed. However, the small $\pi\cdots\pi$ distance²⁰¹ and short $C\cdots O$ contacts are expected to facilitate the facile establishment of highly efficient charge transport channel.

4.2.3 Thermal, Optical, and Electrochemical Properties

The thermal behavior of HTMs was determined by thermogravimetric analysis (TGA) and differential scanning calorimetry (DSC) measurements (Table 4.1). From TGA, it was found that **KR216** has a similar to spiro-OMeTAD (417 °C) and relatively high decomposition temperature (T_{dec}) of 398 °C, with a weight loss of 5%, indicating good thermal stability, required for photovoltaic devices. The thermal transitions of **KR216** were studied by DSC and compared with spiro-OMeTAD (Figure 4.3b). During the first heating scan, both glass transition (T_g) (157 °C) and melting of the crystals (309 °C) are observed, indicating that the material could exist in both crystalline and amorphous states. Additionally, crystallization process is detected at 228 °C, whereas no crystallization was observed during the cooling and second heating steps, only the glass transition at 157 °C. Similarly to **KR216**, spiro-OMeTAD can also exist in both amorphous and crystalline states.¹⁵⁰ During the first heating, no crystallization and only melting was detected at 234 °C. The glass transition of spiro-OMeTAD was observed only during the second heating cycle at 126 °C and is lower than that of **KR216**, indicating that **KR216** has more stabilized amorphous state.

ID	T_m , (°C) ^a	T_g , (°C) ^a	T_{cr} , (°C) ^a	T_{dec} , (°C) ^b	λ_{abs} , (nm) ^c	E_g , (eV) ^d	E_{HOMO} , (eV) ^e	E_{LUMO} , (eV) ^f
KR216	309	157	228	398	390, 466	2.41	-5.09	-2.68
spiro-OMeTAD	234	126	-	417	390	3.00	-5.04	-2.04

Table 4.1 Thermal, optical and electrochemical properties of KR216 and spiro-OMeTAD. ^aMelting, glass transition, and crystallization temperatures observed from DSC (10 °C/min, Ar atmosphere); ^bdegradation temperature observed from TGA (5% weight loss at 10 °C/min, N₂ atmosphere); ^cabsorption was measured in THF solution; ^ddetermined from the UV-Vis absorption onset; ^emeasured in DCM/tetra-*n*-butylammonium hexafluorophosphate (0.1 M) solution, using glassy carbon working electrode, Pt reference electrode, and Pt counter electrode with Fc/Fc⁺ as an internal standard. Potentials were converted to the normal hydrogen electrode by addition of +0.624 V and -4.44 eV to the vacuum, respectively; ^fcalculated from $E_{LUMO} = E_{HOMO} + E_g$.

The normalized UV-Vis absorption spectra of **KR216** and spiro-OMeTAD in THF are shown in Figure 4.3c. Both exhibit almost identical absorption band in UV region with the absorption maximum at 390 nm, while the **KR216** also shows a broad optical absorption in the visible region centered at 466 nm, revealing enhanced conjugation through 9-ylidene double bond with better π -electron delocalization. Optical bandgaps (E_g) determined from the onset of absorption were 2.41 eV for **KR216** and 3.00 eV for spiro-OMeTAD, respectively. To compare the energy levels of the new HTM with spiro-OMeTAD cyclic voltammetry (CV) measurements were performed. The data derived from the ground-state oxidation potential (E_{HOMO}) estimated

from the cyclic voltammogram shown in Figure 4.3d are summarized in Table 4.1. No reduction potential was observed in the CV measurement. The HOMO value of **KR216** was estimated to be -5.09 eV versus the vacuum, which is slightly destabilized compared with that of spiro-OMeTAD (-5.04 eV). However, the 5 meV difference is small and hardly affects the hole transfer from the perovskite (-5.65 eV)¹⁵² to the **KR216**.

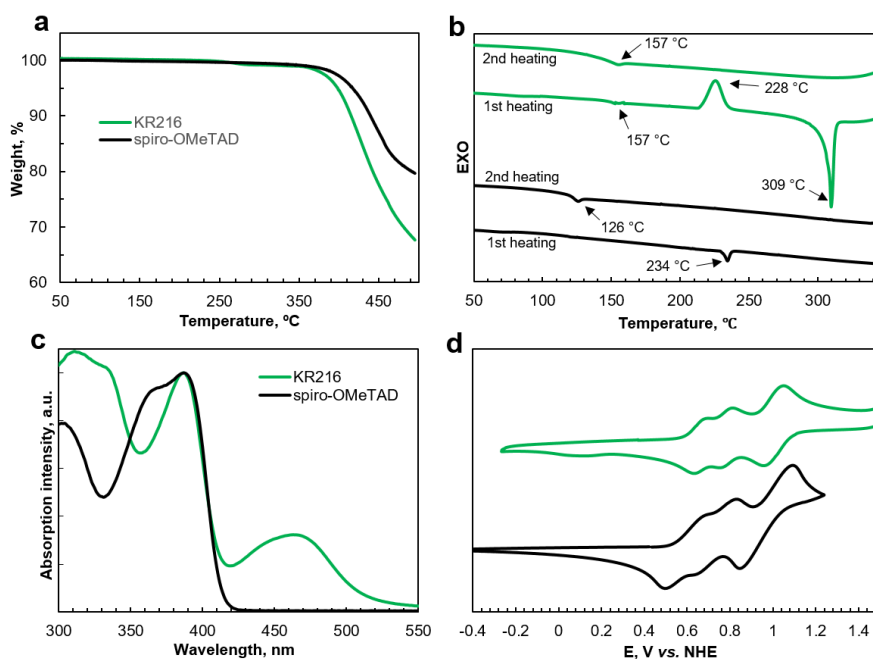


Figure 4.3 a) Thermogravimetric analysis (TGA) data of HTMs, heating rate of 10 °C/min, N₂ atmosphere; b) DSC first and second heating curves of KR216 and spiro-OMeTAD, scan rate 10 °C/min, Ar atmosphere; c) UV-Vis absorption spectra normalized at the peak value; and d) cyclic voltammograms of KR216 and spiro-OMeTAD.

4.2.4 Photoelectric Properties

To elucidate the influence of impurities for energy and electron transfer, electrical properties were determined using both grades of spiro-OMeTAD and compared with the **KR216**. The solid-state ionization potential (I_p) was measured by the electron photoemission in air on the thin films (PESA, Figure 4.4a). **KR216** and spiro-OMeTAD have similar I_p values, 5.01 and 5.10, respectively. The small 0.07 eV difference was noticed to ionize different grade spiro-OMeTAD samples. Lateral thin-film conductivity of HTM layers was measured on OFET substrates (Figure 4.4b). The conductivity of oxidized **KR216** was determined to be $3.40 \times 10^{-5} \text{ S cm}^{-1}$, which is slightly higher of that of lab-grade spiro-OMeTAD ($\sigma = 3.04 \times 10^{-5} \text{ S cm}^{-1}$). More than two

times higher conductivity was obtained for commercial spiro-OMeTAD ($\sigma = 6.89 \times 10^{-5} \text{ S cm}^{-1}$), showing a huge negative influence of remained impurities. Xerographic time of flight (XTOF) measurements were used to characterize charge-transporting properties of the HTMs (Figure 4.4c,d). Gaussian-type hole transport with well-defined transit time was observed in **KR216**. The room-temperature zero-field hole-drift mobility of **KR216** was measured to be $4.6 \times 10^{-5} \text{ cm}^2 \text{ V}^{-1} \text{ s}^{-1}$ and indicates similar charge hopping properties as for spiro-OMeTAD ($\mu_0 = 1 \times 10^{-4} \text{ cm}^2 \text{ V}^{-1} \text{ s}^{-1}$). Similarly to conductivity results, high-purity commercial spiro-OMeTAD has higher hole-drift mobility, reaching $1.3 \times 10^{-4} \text{ cm}^2 \text{ V}^{-1} \text{ s}^{-1}$. All electrical properties are summarized in Table 4.2.

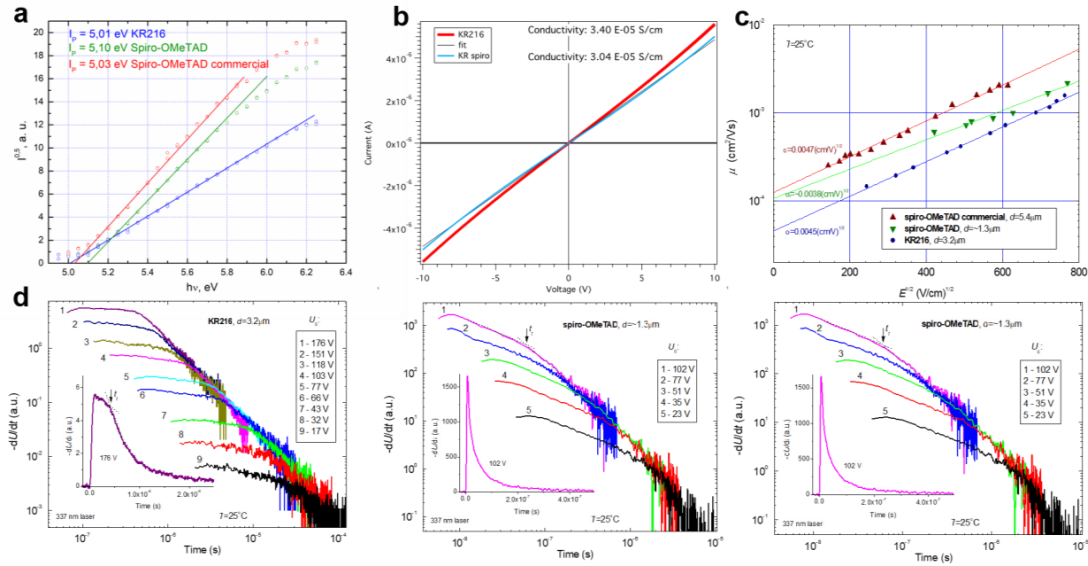


Figure 4.4 a) Photoemission in air spectra; b) conductivity measurements on OFET substrates; c) the dependences of hole-drift mobility on the applied electric field in the amorphous layers of HTMs; and d) transient photocurrents in the layers of the KR216, spiro-OMeTAD synthesized and spiro-OMeTAD commercial at different sample voltages (inserts show the one transient curve in linear plot, arrows on insets indicate a transit time of holes).

ID	I_p , (eV) ^a	μ_0 , ($\text{cm}^2 \text{ V}^{-1} \text{ s}^{-1}$) ^b	μ , ($\text{cm}^2 \text{ V}^{-1} \text{ s}^{-1}$) ^c	σ , (S cm^{-1}) ^d
KR216	5.01	4.6×10^{-5}	7.0×10^{-4}	3.40×10^{-5}
spiro-OMeTAD synthesized	5.10	1×10^{-4}	1×10^{-3}	3.04×10^{-5}
spiro-OMeTAD commercial	5.03	1.3×10^{-4}	2.1×10^{-3}	6.89×10^{-5}

Table 4.2 Comparison of electrical properties. ^aIonization potential was measured by the photoemission in air method from films; ^bhole mobility value at zero field strength; ^chole mobility value at $3.6 \times 10^5 \text{ V cm}^{-1}$ field strength; ^dconductivity was measured using 70mM HTMs solution in chlorobenzene, doped with 3 mol% FK209.

4.2.5 Photovoltaic Performance

To demonstrate the ability of **KR216** act as HTM, PSCs with perovskite as the absorber were prepared and compared with the cells fabricated using the both grades of spiro-OMeTAD under similar conditions. The mixed-perovskite precursor solution contained FAI (1 M), PbI_2 (1.1 M), MABr (0.2 M) and PbBr_2 (0.2 M) dissolved in anhydrous DMF:DMSO 4:1 (volume ratio). The HTM layers were deposited onto the mixed perovskite from a chlorobenzene solution containing 330 mol% tBP, 50 mol% LiTFSI and 3 mol% FK209 as additives. The current density–voltage (J – V) curves of the best devices under 100 mW cm^{-2} AM1.5G solar illumination with reverse and forward scans are shown in Figure 4.5a, and the extracted corresponding parameters are summarized in Table 4.3. Measurements were taken at a slow scan rate of 10 mV s^{-1} , resembling quasi steady-state conditions.^{83,202}

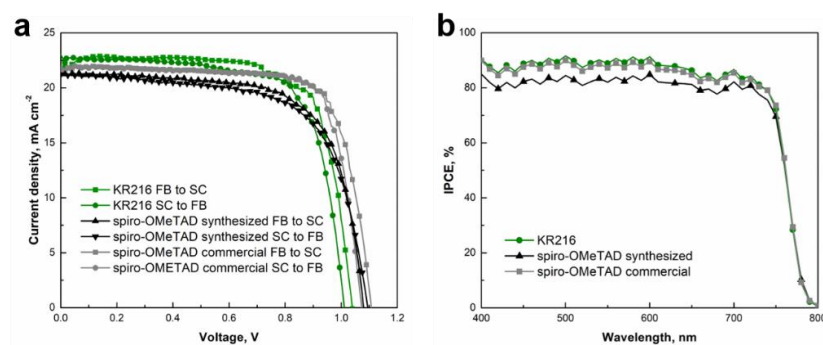


Figure 4.5 a) J - V curves of best performing devices prepared with KR216 and spiro-OMeTAD as the reference. Devices were masked with a black metal aperture of 0.16 cm^2 to define the active area. The curves were recorded scanning at 0.01 V s^{-1} ; and b) IPCE spectra as a function of the wavelength of monochromatic light.

The device with **KR216** as HTM possesses an open-circuit voltage (V_{oc}) of 1023 mV, a short circuit current density (J_{sc}) of 22.3 mA cm^{-2} , and a fill factor (FF) of 0.77, yielding PCE of 17.8% for the forward and 1004 mV, 22.4 mA cm^{-2} , 0.74, 16.8% in backward scan, respectively. In comparison, it is slightly higher than that of device prepared with our lab-grade spiro-OMeTAD, 17.4% for forward and 16.3% in backward scan, respectively. This result clearly shows that **KR216** is an excellent HTM for PSC. Improved photovoltaic performance reaching PCE of 18.4% was observed of the device built on high-purity commercial spiro-OMeTAD under identical conditions. Despite, higher V_{oc} , J_{sc} , and FF yielding higher overall efficiency, there are also less difference obtained between the forward and reverse scans, confirming that high-purity of spiro-OMeTAD is required to obtain high-performance devices. The incident photon-to-current efficiency (IPCE) (Figure 4.5b) of the perovskite devices as a function of wavelength

shows that the device with **KR216** as the HTM exhibits IPCE above 85% from 400 nm covering all the visible region to 700 nm. Photocurrents obtained from the IPCE data are in close agreement with those of current–voltage measurements.

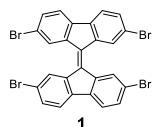
ID	Scan direction	J_{SC} , (mA cm ⁻²)	V_{OC} , (mV)	FF	PCE, (%)
KR216	FB to SC	22.3	1023	0.77	17.8
	SC to FB	22.4	1004	0.74	16.8
spiro-OMeTAD synthesized	FB to SC	20.6	1090	0.75	17.4
	SC to FB	20.7	1080	0.72	16.3
spiro-OMeTAD commercial	FB to SC	21.4	1107	0.76	18.4
	SC to FB	21.7	1073	0.77	18.4

Table 4.3 Solar cell performance parameters, extracted from J - V curves.

4.3 Conclusions

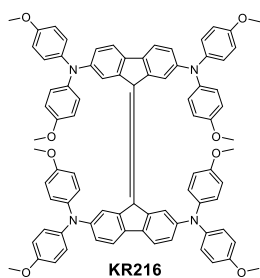
In conclusion, a novel easily attainable 9,9'-bifluorenylidene-based hole transporting material named **KR216**, obtained by a straightforward two-step synthetic route from commercially available and inexpensive starting materials is reported. The estimated price of **KR216** is around 50 times lower than that of commercial spiro-OMeTAD. A remarkable power conversion efficiency of 17.8% was obtained for perovskite solar cells using **KR216**, which is on par with the power conversion efficiency of the high-purity commercial spiro-OMeTAD. The presented result clearly demonstrates that the 9-fluorenylidene moiety is very promising for future molecular engineering of HTMs and **KR216** may have a potential for commercial application in high performance PSC.

4.4 Synthetic Methods and Procedures



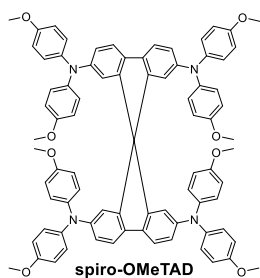
2,2',7,7'-tetrabromo-9,9'-bifluorenylidene (1). A mixture of commercially available 2,7-dibromo-9H-fluorene-9-one (1 g, 3 mmol, 1 eq.) and Lawesson's reagent (0.6 g, 1.5 mmol, 0.5 eq.) with toluene (50 mL) was refluxed overnight.

The resulting reaction mixture was cooled in ice bath, the precipitate was collected by filtration, washed with acetone and dried to give 770 mg of orange solid in 40% yield. ¹H NMR (400 MHz, CDCl₃-d) δ 8.35 (s, 4H), 7.60 (d, J = 8 Hz, 4H), 7.51 (d, J = 8 Hz, 4H). The limited solubility of compound precluded ¹³C NMR characterization. C₂₆H₁₂Br₄[M⁺] exact mass = 639.7673, MS (MALDI-TOF) = 639.800.



2,2',7,7'-tetrakis(*N,N*-di-*p*-methoxyphenylamine)-9,9'-bifluorenylidene (KR216).

In a 50 mL Schlenk-tube, 500 mg of 2,2',7,7'-tetrabromo-9,9'-bifluorenylidene (0.77 mmol, 1 eq.), 890 mg commercially available 4,4'-dimethoxydiphenylamine (3.9 mmol, 5 eq.), and 450 mg *t*-BuONa (4.6 mmol, 6 eq.) were dissolved in 20 mL dry toluene and degassed for 20 min with N₂. After the addition of 100 mg Pd₂dba₃ (0.12 mmol, 15%) and 100 mg Xphos (0.23 mmol, 30%), the reaction was refluxed overnight. The reaction was then diluted with DCM and flashed through a plug of MgSO₄ to remove inorganic salts and metallic palladium. This crude residue was purified by flash chromatography with 35% THF in hexane. Isolated compound was dissolved in THF and dropped into MeOH, precipitate was collected by filtration, washed with MeOH and dried. 800 mg (84% yield) of dark brown solid was obtained. ¹H NMR (400 MHz, THF-*d*₈) δ 8.04 (s, 4H), 7.29 (d, *J* = 8.1 Hz, 4H), 6.83 (d, *J* = 9.2 Hz, 16H), 6.75 (d, *J* = 9.0 Hz, 20H), 3.72 (s, 24H). ¹³C NMR (100 MHz, THF-*d*₈) δ 155.70, 148.12, 142.82, 142.42, 139.98, 136.29, 126.59, 125.65, 121.86, 120.40, 115.55, 55.69. C₈₂H₆₈N₄O₈[M⁺] exact mass = 1236.5037, MS (MALDI-TOF) = 1236.513.



2,2',7,7'-tetrakis(*N,N*-di-*p*-methoxyphenylamine)-9,9'-spirobifluorene (spiro-OMeTAD).

In a 50 mL Schlenk-tube, 500 mg of 2,2',7,7'-tetrabromo-9,9'-spirobifluorene (0.79 mmol, 1 eq.), 900 mg commercially available 4,4'-dimethoxydiphenylamine (4 mmol, 5 eq.), and 450 mg *t*-BuONa (4.6 mmol, 6 eq.) were dissolved in 20 mL dry toluene and degassed for 20 min with N₂. After the addition of 100 mg Pd₂dba₃ (0.12 mmol, 15%) and 100 mg Xphos (0.23 mmol, 30%), the reaction was refluxed overnight. The reaction was then diluted with DCM and flashed through a plug of MgSO₄ to remove inorganic salts and metallic palladium. This crude residue was purified by flash chromatography with 30% THF in hexane. Isolated compound was dissolved in THF and dropped into MeOH, precipitate was collected by filtration, washed with MeOH and dried. 600 mg (73% yield) of pale yellow solid was obtained. ¹H NMR (400 MHz, THF-*d*₈) δ 7.39 (d, *J* = 8.3 Hz, 4H), 6.88 (d, *J* = 8.9 Hz, 16H), 6.76 (d, *J* = 8.6 Hz, 20H), 6.50 (d, *J* = 1.9 Hz, 4H), 3.72 (s, 24H). ¹³C NMR (100 MHz, THF-*d*₈) δ 156.75, 151.21, 148.64, 142.52, 136.41, 126.25, 123.27, 120.69, 118.56, 115.46, 67.13, 55.71. C₈₁H₆₈N₄O₈[M⁺] exact mass = 1224.5037, MS (MALDI-TOF) = 1224.503.

4.4.1 Synthesis Cost Analysis

Rough cost estimation of 1 gram KR216. Prices for 1 kg of each reagent have been collected from major chemical suppliers (Aldrich, TCI, ABCR, MERCK, Fluorochem, and Roth AG). For both synthetic steps quantities of reactants, catalysts and solvents are summarized in Table 4.4, not including materials used for workup, purification, waste treatment and energy consumption. KR216 estimated synthesis cost of 11.3 CHF/1 g is indicative and calculated only for comparison.

Chemical	Weight used, g	Volume used, ml	Price of reagent, CHF for 1 kg	Material cost, CHF	Total cost, CHF
2,7-dibromo-9H-fluoren-9-one	1		430	0.43	
Lawesson's reagent	0.6		342	0.21	1.47
Toluene		50	16.6	0.83	
4,4'-dimethoxydiphenylamine	1.11		5532	6.14	
<i>t</i> -BuONa	0.56		198	0.11	
Pd ₂ dba ₃	0.125		12165	1.52	9.82
Xphos	0.125		7132.5	0.89	
Dry toluene		20	58	1.16	
Table 4.4 Estimated synthesis cost of 1 g KR216.					11.29

Chapter 5 Heteromeric Bistricyclic Aromatic Enes as Hole Transporters

The synthesis, characterization and photovoltaic performance of series of novel molecular hole transport materials based on bistricyclic aromatic enes (BAEs) are presented. The new derivatives were obtained following a simple and straightforward procedure from inexpensive starting reagents mimicking the synthetically challenging 9,9'-spirobifluorene moiety of the well-studied spiro-OMeTAD. The novel HTMs were tested in mixed-perovskite solar cells yielding a power conversion efficiency of 19.2% under standard global 100 mW cm⁻² AM1.5G illumination using 9-{2,7-bis[bis(4-methoxyphenyl)amino]-9H-fluoren-9-ylidene}-N²,N²,N⁷,N⁷-tetrakis(4-methoxyphenyl)-9H-thioxanthene-2,7-diamine coded as **KR374**. The power conversion efficiency data confirms the easily attainable heteromeric fluorenylidene-thioxanthene structure as valuable core for low-cost and highly efficient HTM design and paves the way towards cost-effective PSC technology.

This chapter is based on published work: *Rakstys et al. ChemSusChem* 2017, 10, 3825–3832. DOI: 10.1002/cssc.201700974.²⁰³

5.1 Introduction

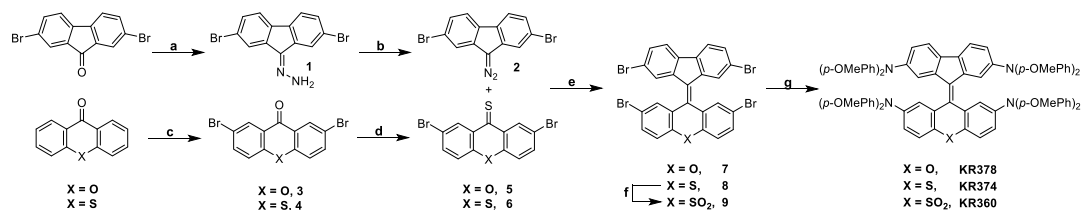
The aforementioned synthetic flexibility and suitability for hole-transport properties sparked to continue exploring this class of compounds (Chapter 4). The synthesis, characterization, and photovoltaic performance of three BAE-based HTMs are presented. In comparison with the previously reported symmetric KR216, here heteromeric BAEs with central five-membered fluorene and six-membered xanthene, thioxanthene, or thioxanthene dioxide as potential scaffolds for novel HTMs are reported. Although dimethoxydiphenylamine-substituted fluorene units were routinely demonstrated to be very efficient in hole transport, six-membered O/S-bridged rings were selected to enhance intramolecularly overcrowded dipolar aromatic “push-pull” system, having a great potential to show high charge-carrier mobility and to reveal the possible additional interaction mediated by O/S atoms with perovskite at the interface.

The new materials were implemented in PSCs as potential HTMs, and the S-bridged analogue **KR374** displayed one of the highest efficiencies so far (19.2 %). Having in mind the synthetic simplicity of the fluorenylidene-thioxanthene core, this result confirms the excellence of **KR374** as low-cost and highly efficient HTM candidate.

5.2 Results and Discussion

5.2.1 Design and Synthesis

The general synthesis procedure for the preparation of 9-{2,7-bis[bis(4-methoxyphenyl)amino]-9H-fluoren-9-ylidene}-*N*²,*N*²,*N*⁷,*N*⁷-tetrakis(4-methoxyphenyl)-9H-xanthene-2,7-diamine **KR378**, 9-{2,7-bis[bis(4-methoxyphenyl)amino]-9H-fluoren-9-ylidene}-*N*²,*N*²,*N*⁷,*N*⁷-tetrakis(4-methoxyphenyl)-9H-thioxanthene-2,7-diamine **KR374**, and 2,7-bis[bis(4-methoxyphenyl)amino]-9-{2,7-bis[bis(4-methoxyphenyl)amino]-9H-fluoren-9-ylidene}-9H-thioxanthene 10,10-dioxide **KR360** is shown in Scheme 5.1. Heteromeric tetra-bromofluorenylidene-chalcogenes **7-8** were synthesized using Barton–Kellogg diazo–thione coupling by a 2-fold extrusion process. Reaction of 2,7-dibromo-9-diazo-9H-fluorene (**2**, prepared from dibromofluorenone by reaction with hydrazine to a hydrazine **1** followed by oxidation) and desired thioketones **5** or **6** (prepared from the respective ketones **3-4** and Lawesson’s reagent) in boiling toluene gave intermediate thianes, which were converted to targeted olefins after elimination of sulfur by treatment with triphenylphosphine in one-pot. Upon cooling to room temperature, the products precipitated and were filtered, requiring no column chromatography in advance for the next step. Separately, compound **8** was oxidized with hydrogen peroxide under acetic acid to yield heteromeric BAE fluorenylidene-thioxanthene-*S,S*-dioxide **9** for the first time. Finally, BAE-based scaffolds **7-9** were equipped with 4,4'-dimethoxydiphenylamine units using the palladium-catalyzed Buchwald–Hartwig C–N cross-coupling reaction, to release the final HTMs **KR378**, **KR374**, and **KR360**, respectively. The final compounds were characterized by nuclear magnetic resonance spectroscopy (NMR) and matrix-assisted laser desorption/ionization-time of flight (MALDI-TOF) mass spectrometry.



Scheme 5.1 Synthesis route for BAE-based HTMs. (a) Hydrazine hydrate, EtOH, 80 °C; (b) HgO, KOH, Na₂SO₄, Et₂O, RT; (c) Br₂, AlCl₃, CS₂, RT for (3) and Br₂, AcOH, 130 °C for (4); (d) Lawesson's reagent, toluene, 80 °C; (e) Δ , PPh₃ toluene, 110 °C; (f) H₂O₂, AcOH, 90 °C; (g) 4,4'-dimethoxydiphenylamine, *t*-BuONa, Pd₂dba₃, XPhos, toluene, 110 °C.

5.2.2 Structure, Optical, and Electrochemical Properties

To gain insight into their electronic structure, the optimized geometries, highest occupied molecular orbitals (HOMOs), and lowest unoccupied molecular orbitals (LUMOs) of the three molecules were investigated with the Gaussian 09 program package and are presented in Figure 5.1a. Here, the MO pictograms were checked to get some clues about the qualitative information on the transfer integral of the molecules. As shown in Figure 5.1a, the MO of all three new HTMs have similar distribution pictures, in which the HOMOs and LUMOs possess π -orbital characteristics. Especially, the LUMOs are mainly localized over the central double-bond-connected cores and the HOMOs are delocalized on the fluorene side and over two adjacent outreaching dimethoxydiphenylamine units. The LUMO electron density is associated with electron transfer, whereas the HOMO electron density is associated with hole transfer. As there are more interorbital overlaps in the HOMO of neighboring molecules, one can expect a larger hole-transport integral. Thus, the distribution character of HOMO electron densities of these HTM is favorable for hole transport.

Figure 5.1c shows the normalized UV-Vis absorption spectra of synthesized HTMs in dichloromethane (CH₂Cl₂) solution. All three molecules showed π - π^* transitions of the absorption band located at around 300 nm, whereas an additional absorption peak was observed at around 390 nm owing to the electron-rich dimethoxydiphenylamine unit. An extra absorption band for **KR360** centered at 345 nm was observed owing to the charge transfer (CT) transitions from the peripheral electron-donating amines to the thioxanthene-*S,S*-dioxide core that contains the electron-withdrawing sulfonyl group. Broad optical absorption in the visible region reveals push-pull communication between two different tricycles through the 9,9'-ylidene double bond, in which the fluorenylidene and the chalcocanthylidene moieties may serve as an acceptor and a donor, respectively.²⁰⁴ Comparing **KR378** ($\lambda_{max} = 610$ nm) to **KR374** ($\lambda_{max} = 540$

nm), a red-shift by 70 nm was noticed. The absorption spectral difference is clearly owed to the difference in electron-donating power between O and S atoms, confirming that oxygen is a stronger electron donor than sulfur. On the other hand, the donating strength of thioxanthene-*S,S*-dioxide in **KR360** is much weaker than that of thioxanthene in **KR374**, but a 50 nm red-shift was observed. One possible explanation for that could be that thioxanthylidene-*S,S*-dioxide unit may act as an acceptor, whereas fluorenylidene is a donor in this intriguing system. Photoluminescence (PL) of the molecules in solution was measured, but no detectable emission was observed. Optical bandgaps (E_g) determined from the onset of absorption were 1.68, 1.97, and 1.84 eV for **KR378**, **KR374**, and **KR360**, respectively.

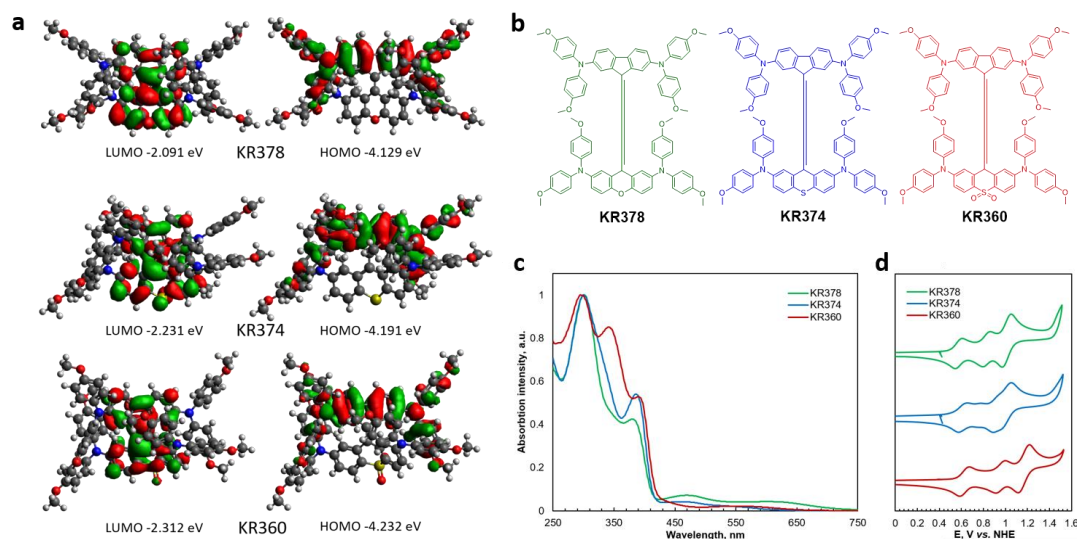


Figure 5.1 a) Isodensity surface plots and energies calculated for the frontier orbitals; b) chemical structures; c) UV-Vis absorption spectra normalized at the peak value; and d) cyclic voltammograms of the HTMs.

ID	λ_{abs} (nm) ^a	E_{HOMO} ([eV]) ^b	E_g (nm) ^c	E_{LUMO} (eV) ^d
KR378	302, 380, 469, 610	-5.03	1.68	-3.35
KR374	300, 386, 465, 540	-5.06	1.97	-3.09
KR360	295, 345, 390, 553	-5.08	1.84	-3.24

Table 5.1 Optical and electrochemical properties of the synthesized HTMs. ^aMeasured in DCM solution; ^bmeasured in DCM/tetra-*n*-butylammonium hexafluorophosphate (0.1 M) solution, using a glassy carbon working electrode, Pt reference electrode and Pt counter electrode with Fc/Fc⁺ as an internal standard. Potentials were converted to the normal hydrogen electrode (NHE) by the addition of +0.624 V and -4.44 eV to the vacuum, respectively; ^cdetermined from the UV-Vis absorption onset; ^dcalculated from $E_{LUMO} = E_{HOMO} + E_g$.

To estimate the relative energy levels of the HTMs, cyclic voltammetry (CV) in CH₂Cl₂ solution in the presence of 0.1 M *n*-Bu₄NPF₆ was performed (Figure 5.1d). The HOMO energies of

KR378, **KR374**, and **KR360** were found to lie at -5.03, -5.06, and -5.08 eV versus vacuum, respectively. The similar HOMO values can be attributed to the same dimethoxydiphenylamine units in all three compounds and are in close agreement with the calculated values. As they are in alignment with that of the photoactive perovskite layer, and the LUMO values are determined to be below -4 eV, energetically facilitated hole extraction and electron blocking from perovskite to HTM should be ensured. All optical and electrochemical properties are summarized in Table 5.1.

5.2.3 Photoelectrical and Photophysical Properties

The solid-state ionization potential (I_p) was measured by electron photoemission in air on the thin films (PESA) and is shown in Figure 5.2b. **KR378**, **KR374**, and **KR360** have similar I_p values of 5.15, 5.12, and 5.05 eV, respectively, which is in very close agreement with E_{HOMO} values for solvated molecules measured by CV. Xerographic time of flight (XTOF) measurements were used to characterize charge-transport properties of the HTMs (Figure 5.2a). The room-temperature zero-field hole-drift mobility of **KR374** was measured to be $1.2 \times 10^{-6} \text{ cm}^2 \text{ V}^{-1} \text{ s}^{-1}$, whereas **KR378** and **KR360** showed one order of magnitude lower hole-drift mobility of 4×10^{-7} and $1.3 \times 10^{-7} \text{ cm}^2 \text{ V}^{-1} \text{ s}^{-1}$, respectively, indicating poor charge-hopping properties and suggesting that the oxidization of the sulfur atom in **KR360** is disadvantageous for charge-transport properties. In comparison, spiro-OMeTAD has a higher hole-drift mobility of $1.3 \times 10^{-4} \text{ cm}^2 \text{ V}^{-1} \text{ s}^{-1}$.¹⁹⁰ To reveal the effect of different atoms and confirm the synthesized compounds as HTMs, we prepared devices with triple-cation perovskite as light absorber using a standard mesoporous configuration device stack of fluorine-doped tin oxide (FTO)/compact-TiO₂/mesoporous-TiO₂/perovskite/HTM/Au. The Cs_{0.1}(MA_{0.15}FA_{0.85})_{0.9}Pb(I_{0.85}Br_{0.15})₃ precursor solution was prepared by mixing CsI (0.11 M), FAI (1.07 M), PbI₂ (1.23 M), MABr (0.19 M), and PbBr₂ (0.19 M) in a mixed solvent of DMF:DMSO = 4:1 (volume ratio). The HTMs were applied from a 20mM solution in chlorobenzene. tBP, FK209, and LiTFSI were added as additives. For comparison, the devices using spiro-OMeTAD as a reference, consisted of 60 mM spiro-OMeTAD solution in chlorobenzene. Equimolar amounts of additives were added for all hole-transporters: 330 mol% tBP, 50 mol% LiTFSI from a 1.8 M stock solution in acetonitrile and 3 mol% FK209 from a 0.25 M stock solution in acetonitrile. Figure 5.2c displays the cross-sectional image of the PSC using **KR374** analyzed with a field-emission scanning electron microscope. The device is made of 400 nm perovskite on top of 200 nm thick mesoporous TiO₂ layer, which was deposited on FTO glass coated with 20 nm compact TiO₂. The device is completed by a 90 nm thick HTM and gold as a back contact on top.

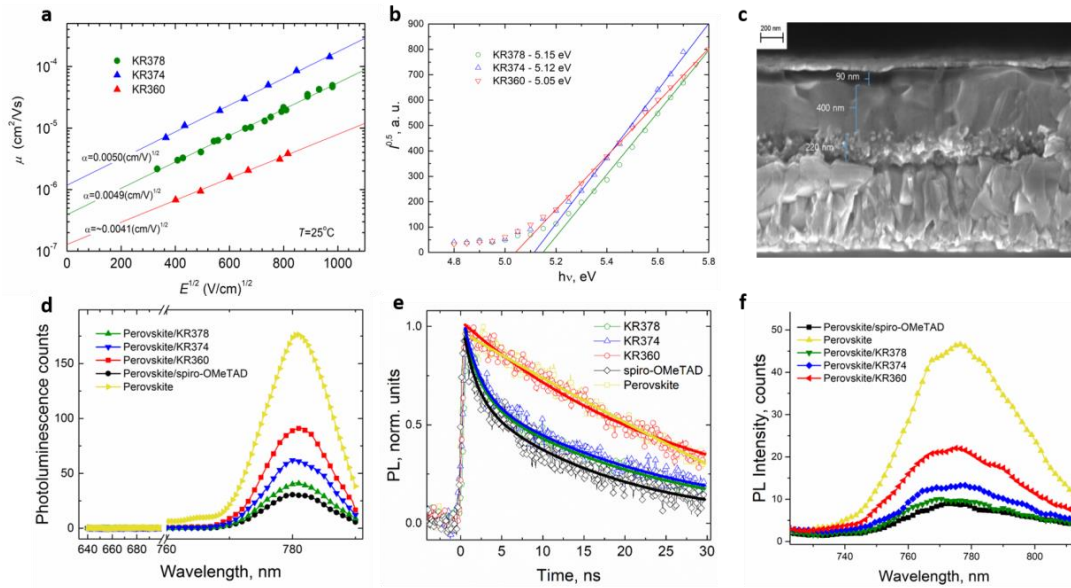


Figure 5.2 a) Electric-field dependencies of the hole drift mobilities in charge-transport layers of HTMs; b) photoemission in air spectra of the HTMs; c) cross-sectional SEM micrograph of the perovskite device containing KR374 as the HTM; d) CWPL spectra of the samples, excitation at 400 nm; e) normalized PL decay in the first 30 ns time window, upon excitation at 460 nm, at excitation density of $<500 \text{ nJ/cm}^2$ corresponding to an average density of absorbed photons of $5 \times 10^{18} \text{ photons/cm}^3$. Solid lines represent the fit from a mono/bi exponential function. The films have been encapsulated with a transparent PMMA layer to prevent degradation or any oxygen/moisture induced effects; f) PL spectra of the perovskite and perovskite/HTM film excited at 700nm. The trend in the PL quenching for the perovskite/HTM interface is similar to what observed exciting at 400nm, indicating that the absorption of the HTM is negligible.

Continuous-wave (CW) and time-resolved (TR) photoluminescence (PL) measurements were performed on the perovskite and perovskite/HTM layers to gain a better understanding on the interface properties. Figure 5.2d shows the CWPL spectra comparing the perovskite emission to the one resulting from the perovskite/HTMs interface. Results show that the perovskite band-edge emission, peaking at around 780 nm, is quenched upon the addition of the HTM, possibly revealing the opening of a new channel related to hole transfer. A different density of surface-trap states might also induce a PL quenching, however, the good match with the PL quenching and device performances points to an improved interfacial charge injection. It is worth noticing that at 400 nm, the HTMs itself absorb light, however, no emission from the HTM (expected below 750 nm) is visible. Note also that the same trend in the PL quenching is observed upon selective excitation of the perovskite layer at 700 nm (Figure 5.2f). TRPL measurements (Figure 5.2e) were performed using time-correlated single photon counting (TCSPC) under pulsed excitation at 460 nm at $5 \times 10^{18} \text{ photons cm}^{-3}$. In this regime, traps are filled and the decay to electron-hole recombination processes can be associated. The pristine perovskite

shows a long-living component extending out of temporal window as already observed.²⁰⁵ A similar behavior is also detected for the perovskite/**KR360** interface. Differently, for the other HTMs, a significant quenching is visible in the first 10 ns. A derived time constant of 1.9 ns was retrieved for the **KR374** and **KR378** and a slightly faster process with $\tau = 1.5$ ns was obtained for the spiro-OMeTAD/perovskite interface. The lifetime analysis, retrieved by a multiexponential fitting procedure, suggests that the PL quenching happens within the first nanosecond, more efficiently for the **KR374** or **KR378**/perovskite interface.

5.2.4 Photovoltaic Properties

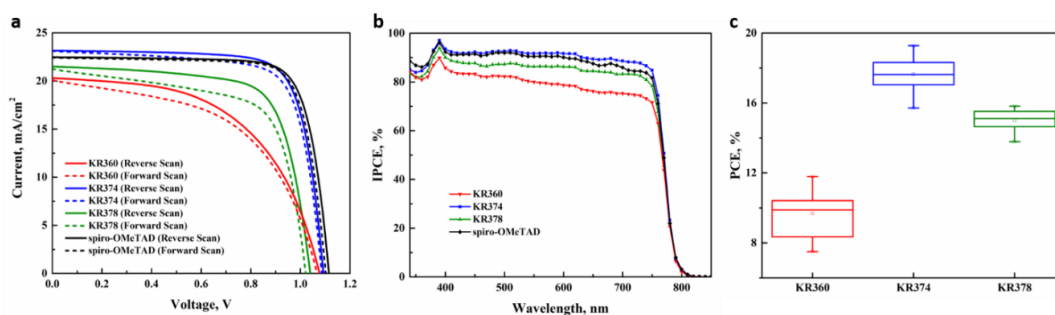


Figure 5.3 a) J - V curves of best performing devices prepared with KR378, KR374, KR360, and spiro-OMeTAD as the reference. Devices were masked with a black metal aperture of 0.16 cm² to define the active area. The curves were recorded scanning at 0.01 V s⁻¹; b) IPCE spectra as a function of the wavelength of monochromatic light; c) statistical distribution of perovskite solar cells performance with new HTMs.

The J - V curves for the champion perovskite solar cells using different HTMs obtained under light illumination (AM1.5G, 100 mW cm⁻²) are shown in Figure 5.3a, spiro-OMeTAD was used as a reference (Reverse HTM in this study). To estimate the impact of the hysteresis on the calculated PCE, the J - V curves were collected by scanning the applied voltage at 0.01 V s⁻¹ from forward bias (FB) to short circuit (SC) and the other way around. The corresponding photovoltaic parameters are summarized in Table 5.2. Different atoms in the heteromeric BAE-based molecules had a noticeable impact on the performance of the semiconductors in the PSC. **KR374**-based device showed an open-circuit voltage (V_{oc}) of 1.09 V, a short-circuit photocurrent density (J_{sc}) of 23.15 mA cm⁻², and a fill factor (FF) of 0.76, yielding a PCE as high as 19.26 %. This is on par with that of the traditionally used spiro-OMeTAD-based solar cells, which showed 19.54% under the same conditions. **KR378** exhibits deterioration on all three parameters simultaneously compared to those of the **KR374**-based device with V_{oc} of 1.04 V, J_{sc} of 21.5 mA cm⁻², and a FF of 0.71, yielding a significantly lower PCE of 15.8 %, most likely because of the

weaker O-Pb²⁺ interaction than that of S-Pb²⁺.²⁰⁶ Furthermore, with improved performance in **KR374**-based devices, it is worth to mention that hysteresis is much smaller than that observed with **KR378**. Expectedly, decreased hole-drift mobility in **KR360** and increased polarity, as well as the hydrophilicity that results from the introduction of the sulfone groups, had a negative effect on the performance of the HTM in the PSC as the PCE was only 11.8 %. The incident photon-to-current efficiency (IPCE) (Figure 5.3b) of the perovskite devices as a function of wavelength shows that the device with **KR374** as the HTM exhibits IPCE above 90% from 400 nm covering the region to 750 nm. The PCE histograms shown in Figure 5.3c reveal good reproducibility of the fabricated devices.

ID	Scan direction	J_{sc} (mA cm ⁻²)	V_{oc} (V)	FF	PCE (%)
KR378	reverse	21.50	1.040	0.708	15.82
	forward	21.27	1.021	0.661	14.35
KR374	reverse	23.15	1.092	0.762	19.26
	forward	23.11	1.086	0.738	18.53
KR360	reverse	20.30	1.077	0.539	11.79
	forward	20.08	1.068	0.526	11.29
spiro-OMeTAD	reverse	22.47	1.115	0.780	19.54
	forward	22.44	1.102	0.779	19.27

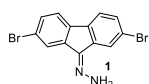
Table 5.2 Photovoltaic performance of the devices based on new HTMs and spiro-OMeTAD as the reference under AM1.5G illumination (100 mW cm⁻²).

5.3 Conclusions

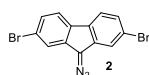
The design, synthesis, and a systematic study of the bistricyclic aromatic ene (BAE)-based dimethoxydiphenylamine-substituted hole transport materials were reported. The impact on different atoms in the heteromeric BAE structure was revealed through the optical, electrochemical, photophysical, and photovoltaic measurements. Novel HTMs are easily attainable by a straightforward synthetic scheme with minimized number of steps and simple purification procedures ensuring cost-effective upscaling. Replacement of the oxygen atom by sulfur showed a significantly improved hole-drift mobility leading to enhanced photovoltaic performance and reduced hysteresis most likely owing to the improved interface between the perovskite and HTM caused by stronger Pb-S interaction, whereas oxidation of sulfur to sulfone has a negative effect on the device performance. S-bridged **KR374** showed a promising power conversion efficiency of up to 19.2% under standard global 100 mW cm⁻² AM1.5G illumination

in mixed-ion perovskite solar cells, which is on par with the widely researched spiro-OMeTAD reference. The results presented here provide a universal feedback for further molecular engineering of HTMs and confirms that pseudo spiro-type structured fluorenylideneethioxanthene may be very attractive alternative towards the cost-effective HTM market.

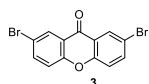
5.4 Synthetic Methods and Procedures



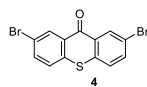
(2,7-dibromo-9H-fluoren-9-ylidene)hydrazine (1). Prepared by procedure adopted from literature.¹⁹³ Hydrazine hydrate (3.5 mL, 66.6 mmol, 5 eq.) was added to 2,7-dibromo-9H-fluoren-9-one (4.5 g, 13.3 mmol, 1 eq.) dissolved in hot ethanol (50 mL), and refluxed for 3 h. The reaction mixture was cooled in an ice bath, and the orange precipitate was filtered off and washed with methanol (4.5 g, 96%). ¹H NMR (400 MHz, Chloroform-d) δ 8.05 (s, 1H), 7.89 (s, 1H), 7.61 (d, J = 8.2 Hz, 2H), 7.50 (d, J = 5.2 Hz, 2H), 6.52 (s, 2H). C₁₃H₈Br₂N₂[M⁺] exact mass = 349.9054, MS (MALDI-TOF) = 349.812.



2,7-dibromo-9-diazo-9H-fluorene (2). Prepared by procedure adopted from literature.¹⁹³ Anhydrous sodium sulfate (3.64 g, 25.6 mmol, 2 eq.), yellow mercury oxide (4.55 g, 21 mmol, 1.65 eq.), and (1) (4.5 g, 12.8 mmol, 1 eq.) were carefully grounded by using a mortar, transferred to a round-bottomed flask equipped with magnetic stirrer and drying tube, and dry diethyl ether (60 mL) was added. Upon dropwise addition of a freshly prepared saturated solution of KOH in ethanol (1.5 mL), the reaction mixture turned deep red. The formation of (2) was monitored by TLC. After 3 h of stirring at RT, the reaction was complete. The solution was filtered, and the residue was washed with diethyl ether. The combined filtrates were evaporated to afford 4 g of final product (89%). ¹H NMR (400 MHz, Chloroform-d) δ 7.33 (dt, J = 7.5, 2H), 7.40 (dt, J = 7.5, 2H), 7.52 (d, J = 7.7, 2H), 7.96 (d, J = 7.6, 2H). ¹³C NMR (100 MHz, Chloroform-d) δ 119.3, 120.9, 124.5, 126.3, 131.4, 132.9. C₁₃H₆Br₂N₂[M⁺] exact mass = 347.8898, MS (MALDI-TOF) = 346.897.



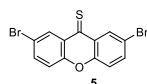
2,7-dibromo-9H-xanthen-9-one (3).²⁰⁷ Xanthone (8.6 g, 50 mmol, 1 eq.) in CS₂ (20 mL) is mixed with AlCl₃ (14.5 g, 108.7 mmol, 2.2 eq.). Bromine (2 mL, 39 mmol, 0.8 eq.) is added dropwise and the mixture is stirred at room temperature for 24 h. The resulting reaction mixture was washed with water, extracted with DCM and purified on silica gel column using 80% DCM in hexane eluent to give 5 g (32%) of white solid. ¹H NMR (400 MHz, Chloroform-d) δ 8.47 (d, J = 2.5 Hz, 2H), 7.85 (dd, J = 8.9, 2.5 Hz, 2H), 7.43 (d, J = 9.1 Hz, 2H). C₁₃H₆Br₂O₂[M⁺] exact mass = 351.8735, MS (MALDI-TOF) = 351.842.



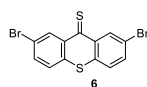
2,7-dibromo-9H-thioxanthone (4).²⁰⁸ Thioxanthone (10 g, 0.048 mol, 1 eq.) was dissolved in 80 mL of acetic acid, and 20 mL of Br₂ was added dropwise at room temperature and heated to 130 °C. After 20 h of reflux, cooled mixture was poured over ice and filtered. The precipitate was washed with water, dried in vacuum and recrystallized from toluene. Resulting bright yellow solid was yielded as 13.5 g (76%). ¹H NMR (400 MHz, Chloroform-*d*) δ: 8.76 (d, *J* = 2.2 Hz, 2H), 7.76 (dd, *J* = 8.6, 2.3 Hz, 2H), 7.49 (d, *J* = 8.6 Hz, 2H). C₁₃H₆Br₂OS[M⁺] exact mass = 367.8506, MS (MALDI-TOF) = 367.851.

A general method for thionation of ketones:

A mixture of commercially available xanthone (3) or thioxanthone (4) (1 eq.) and Lawesson's reagent (0.5 eq.) in toluene (20 mL) was heated at 80 °C for 2 h. The resulting reaction mixture was cooled, filtered and washed with acetone.



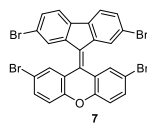
2,7-dibromo-9H-xanthene-9-thione (5). Yield 0.55 g (65%). ¹H NMR (400 MHz, Chloroform-*d*) δ 8.81 (d, *J* = 2.3 Hz, 2H), 7.85 (dd, *J* = 8.8, 2.3 Hz, 2H), 7.41 (d, *J* = 8.8 Hz, 2H). C₁₃H₆Br₂OS[M⁺] exact mass = 367.8506, MS (MALDI-TOF) = 367.854.



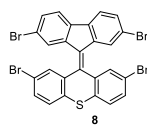
2,7-dibromo-9H-thioxanthene-9-thione (6). Yield 1 g (96%). ¹H NMR (400 MHz, Chloroform-*d*) δ 9.12 (s, 2H), 7.74 (d, *J* = 9.2 Hz, 2H), 7.48 (d, *J* = 8.5 Hz, 2H). C₁₃H₆Br₂S₂[M⁺] exact mass = 383.8277, MS (MALDI-TOF) = 383.842.

A general method for Barton–Kellogg olefination reaction:

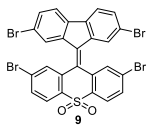
2,7-dibromo-9-diazo-9H-fluorene (2) (1 eq.) and desired thione (1 eq.) were dissolved in toluene (20 mL) and refluxed for 2 h until full nitrogen release and formation of intermediate episulfide derivative, after that triphenylphosphine (1 eq.) was added and the mixture was refluxed for additional 2 h to yield final olefins. The mixture was cooled to room temperature, formed precipitate filtered and washed with acetone.



2,7-dibromo-9-(2,7-dibromo-9H-fluoren-9-ylidene)-9H-xanthene (7). Yield 1.4 g (75%). ¹H NMR (400 MHz, Chloroform-*d*) δ 8.20 (s, 2H), 8.01 (s, 2H), 7.74 (d, *J* = 13.7 Hz, 4H), 7.51 (d, *J* = 32.4 Hz, 4H). C₂₆H₁₂Br₄O[M⁺] Exact Mass = 655.7622, MS (ESI-QTOF) = 655.843.



2,7-dibromo-9-(2,7-dibromo-9H-fluoren-9-ylidene)-9H-thioxanthene (8). Yield 1 g (74%). ¹H NMR (400 MHz, Chloroform-*d*) δ 7.95 (d, *J* = 1.7 Hz, 2H), 7.61 (d, *J* = 8.3 Hz, 2H), 7.56 – 7.51 (m, 4H), 7.49 (d, *J* = 5.3 Hz, 4H). C₂₆H₁₂Br₄S[M⁺] Exact Mass = 671.7393, MS (ESI-QTOF) = 671.719.

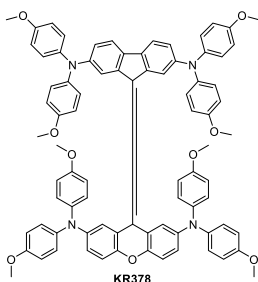


2,7-dibromo-9-(2,7-dibromo-9H-fluoren-9-ylidene)-9H-thioxanthene 10,10-dioxide (9). Hydroperoxide (35%, 5 mL) was added dropwise to a solution of (8) (0.7 g, 1.4 mmol) in acetic acid (15 mL) and was stirred at 90 °C overnight.

After cooled down, the water was added and extracted with ethyl acetate. The separated organic layer was washed with water and brine, then dried over MgSO₄ and removed under reduced pressure. Purified by column chromatography (silica gel, DCM) to afford 0.8 g (78%). ¹H NMR (200 MHz, Chloroform-d) δ 8.09 (d, J = 3.7 Hz, 2H), 8.04 (s, 2H), 7.79 (d, J = 8.3 Hz, 2H), 7.60 (s, 2H), 7.54 (s, 4H). C₂₆H₁₂Br₄O₂S[M⁺] Exact Mass = 703.7292, MS (ESI-QTOF) = 703.712.

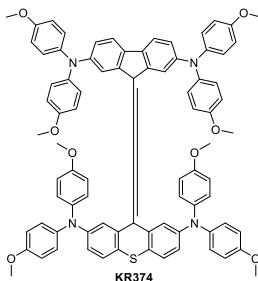
A general method for Buchwald–Hartwig amination reaction:

In a 50 mL Schlenk-tube, desired tetrabromoolefin (1 eq.), commercially available 4,4'-dimethoxydiphenylamine (5 eq.), and *t*-BuONa (6 eq.) were dissolved in 20 mL dry toluene and degassed for 20 min with N₂. After the addition of Pd₂dba₃ (15 mol%) and Xphos (30 mol%), the reaction was refluxed overnight. The reaction was then diluted with DCM and flashed through a plug of MgSO₄ to remove inorganic salts and metallic palladium. This crude residue was purified by flash chromatography.



9-(2,7-bis(bis(4-methoxyphenyl)amino)-9H-fluoren-9-ylidene)-N²,N²,N⁷,N⁷-tetrakis(4-methoxyphenyl)-9H-xanthene-2,7-diamine (KR378). The pure compound was obtained after column chromatography on silica gel using 35% THF in hexane. Yield 0.7 g (51%).

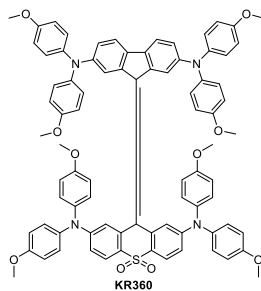
¹H NMR (400 MHz, THF-d₈) δ 7.74 (d, J = 2.0 Hz, 2H), 7.41 (d, J = 8.2 Hz, 2H), 7.27 (d, J = 2.8 Hz, 2H), 6.98 (dd, J = 9.0, 2.5 Hz, 16H), 6.86 (dd, J = 8.1, 2.0 Hz, 2H), 6.84 – 6.73 (m, 18H), 6.69 (dd, J = 8.9, 2.8 Hz, 2H), 3.75 (d, J = 5.0 Hz, 24H). ¹³C NMR (101 MHz, THF-d₈) δ 156.15, 155.39, 148.65, 146.05, 143.80, 141.22, 140.50, 140.02, 135.10, 126.85, 126.09, 124.97, 122.79, 120.99, 119.70, 118.80, 117.62, 116.81, 114.39, 114.29, 54.55. C₈₂H₆₈N₄O₉[M⁺] Exact Mass = 1252.4986, MS (MALDI-TOF) = 1252.553.



9-(2,7-bis(bis(4-methoxyphenyl)amino)-9H-fluoren-9-ylidene)-N²,N²,N⁷,N⁷-tetrakis(4-methoxyphenyl)-9H-thioxanthene-2,7-diamine (KR374). The pure compound was obtained after column chromatography on silica gel using 30-35% THF in hexane. Yield 0.55 g (59%).

¹H NMR (400 MHz, THF-d₈) δ 7.41 – 7.34 (m, 4H), 7.03 (dd, J = 6.4, 2.5 Hz, 16H), 6.98 (d, J = 2.6 Hz, 2H), 6.95 (s, 2H), 6.80 (dd, J = 14.2, 9.0 Hz, 16H), 6.66 (d, J = 9.0 Hz, 2H), 6.35 (dd, J = 8.7, 2.6 Hz, 2H), 3.74 (d, J = 8.6 Hz, 24H). ¹³C NMR (101 MHz, THF-d₈) δ 156.65, 155.54, 146.51, 146.24, 141.00,

140.95, 139.79, 138.27, 137.15, 134.71, 127.84, 126.00, 125.32, 124.92, 121.51, 118.83, 118.42, 116.64, 115.61, 114.39, 54.54. $C_{82}H_{68}N_4O_8S[M^+]$ Exact Mass = 1268.4758, MS (MALDI-TOF) = 1268.388.



2,7-bis(bis(4-methoxyphenyl)amino)-9-(2,7-bis(bis(4-methoxyphenyl)amino)-9H-fluorene-9-ylidene)-9H-thioxanthene 10,10-dioxide (KR360). The pure compound was obtained after column chromatography on silica gel using 40-45% THF in hexane. Yield 0.55 g (60%).

1H NMR (400 MHz, THF- d_8) δ 7.53 (d, J = 2.0 Hz, 2H), 7.43 (d, J = 8.7 Hz, 2H), 7.34 (d, J = 8.2 Hz, 2H), 7.08 (dd, J = 8.9, 2.8 Hz, 18H), 6.93 – 6.77 (m, 18H), 6.35 (dd, J = 8.8, 2.4 Hz, 2H), 3.76 (d, J = 10.3 Hz,

24H). ^{13}C NMR (101 MHz, THF- d_8) δ 157.60, 155.75, 149.26, 146.28, 141.40, 140.62, 138.81, 138.34, 134.86, 129.29, 128.47, 125.56, 125.08, 121.34, 118.61, 118.03, 114.65, 114.53, 114.32, 113.93, 54.61. $C_{82}H_{68}N_4O_{10}S[M^+]$ Exact Mass = 1300.4656, MS (MALDI-TOF) = 1300.114.

5.4.1 Synthesis Cost Analysis

Rough cost estimation of 1 gram KR374 is presented. Prices for 1 kg of each reagent have been collected from major chemical suppliers (Aldrich, TCI, ABCR, MERCK, Fluorochem, and Roth AG). For all synthetic steps quantities of reactants, catalysts and solvents are summarized in Table 5.3, not including materials used for workup, purification, waste treatment and energy consumption. KR374 estimated synthesis cost of 20.2 CHF/1 g is indicative and calculated only for comparison.

Product	Chemicals used	Weight used, g	Volume used, ml	Price of reagent, CHF for 1 kg or 1 L	Material cost, CHF	Total cost, CHF
	2,7-dibromo-9H-fluoren-9-one Hydrazine hydrate Ethanol	0.75 0.55	8	430 87 11.5	0.32 0.05 0.09	0.46
	HgO KOH Na ₂ SO ₄ Diethyl ether	0.79 0.31 0.64	10.5	218 20 16 15	0.17 0.01 0.01 0.16	0.35
	Thioxanthone Br ₂ Acetic acid	0.74	1.5 5.9	1270 207 19	0.94 0.31 0.11	1.36
	Lawesson's reagent Toluene	0.42	40	342 17	0.14 0.68	0.82
	PPh ₃ Toluene	0.5	50	75 17	0.04 0.85	0.89
	4,4'-dimethoxydiphenylamine <i>t</i> -BuONa Pd ₂ dba ₃ Xphos Dry Toluene	1.7 0.8 0.2 0.2	50	5532 198 12165 7132.5 58	9.4 0.16 2.43 1.43 2.9	16.32
Table 5.3 Estimated synthesis cost of 1 g KR374.						20.2

Chapter 6 Dispiro-Oxepine-Based Hole Transporting Material

Dimethoxydiphenylamine-substituted dispiro-oxepine derivative coded **DDOF** has been designed and synthesized using a facile synthetic route. The novel hole transporting material is fully characterized and tested in perovskite solar cells exhibiting a remarkable power conversion efficiency of 19.4%. More importantly, compared with spiro-OMeTAD-based devices, **DDOF** shows significantly improved stability. The comparatively comprehensive solid structure study is attempted to disclose the common features of good performance HTMs. These achievements clearly demonstrated that the highly hindered **DDOF** can be an effective HTM for the fabrication of efficient perovskite solar cells and further enlightened the rule of new HTM design.

This chapter is based on published work: *Rakstys et al. J. Mater. Chem. A, 2016, 4, 18259–18264. DOI: 10.1039/c6ta09028a.*²⁰⁹

6.1 Introduction

Spiro-based organic semiconductor 2,2',7,7'-tetrakis-(*N,N'*-di-4-methoxyphenylamine)-9,9'-spirobifluorene (spiro-OMeTAD) was selected as the benchmark HTM for PSCs.²⁴ In this work, an alternative spiro-annulated HTM 2,2',7,7'-tetrakis-(*N,N'*-di-4-methoxyphenylamine) dispiro[fluorene-9,4'-dithieno[3,2-*c*:2',3'-*e*]oxepine-6',9''-fluorene] **DDOF** is synthesized using a facile 3-step preparation procedure and characterized using various optical, thermal, and electrochemical measurements. The single crystallography study disclosed and visualized the highly hindered nature of **DDOF**. Furthermore, a PCE of 19.4% has been reached employing the titular HTM in a PSC with improved stability, showing potential as a non-sublimed low-cost HTM to replace widely used spiro-OMeTAD.

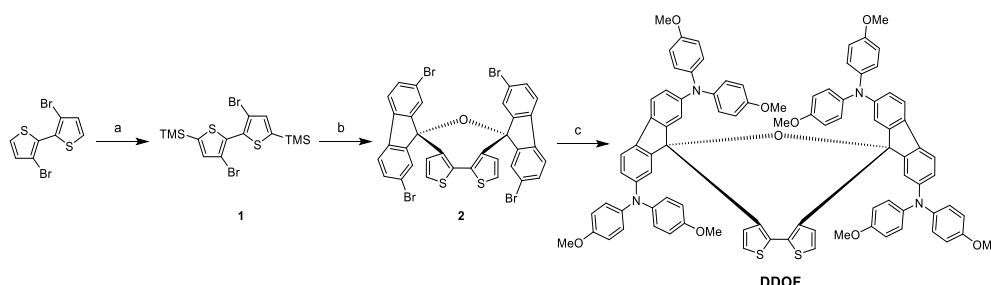
It is well known that lead halide perovskites are extremely soluble in water accelerating device degradation very quickly even under low humidity conditions,²¹⁰ therefore the engineering of

the perovskite/HTM interface is one of the most important goals towards improved moisture resistance. **DDOF** is composed of bithiophene and two dispirodifluorene units incorporated around the oxepine core. While the bithiophene unit has been shown to reveal an additional interaction with perovskite,¹²⁷ the four dimethoxydiphenylamine inherent triangular pyramids formed by sp^3 nitrogen atoms lead to large steric hindrance to further decrease the anisotropic solid structure, which will favor a homogeneous film morphology to effectively block the electron recombination, resist the perovskite surface from moisture and inhibit gold nanoparticle migration from the electrode.^{183,211,212}

6.2 Results and Discussion

6.2.1 Synthesis and Crystal Structure

The general synthesis procedure for the preparation of **DDOF** is shown in Scheme 6.1. Firstly, commercially available precursor 3,3'-dibromo-2,2'-bithiophene has been protected with trimethylsilyl groups obtaining **1**. By adding a stoichiometric amount of *n*-BuLi, 5,5'-ditrimethylsilyl-3,3'-dilithio-2,2'-bithiophene was generated *in situ* and following treatment with an excess of 2,7-dibromo-fluorenone allowed formation of the intermediate carbinol. Condensing in acetic acid in the presence of a catalytic amount of hydrochloric acid, two hydroxyls are involved in intramolecular H-bonding that facilitated an etherification reaction between these groups with closing of the seven membered oxepine ring.²¹³ Finally, dispiro-oxepine derivative **2** was equipped with 4,4'-dimethoxydiphenylamine units via a palladium-catalyzed Buchwald–Hartwig C–N cross-coupling reaction, to release final bithiophene-functionalized **DDOF** with original 3D nodes. All synthetic procedures, ¹H/¹³C NMR, and mass spectra are reported in the section 6.4 Synthetic Methods and Procedures.



Scheme 6.1. Synthetic route for the DDOF HTM. (a) LiN(*Pr*-*i*)₂, TMSCl, THF, -78 °C to RT; (b) *n*-BuLi, 2,7-dibromofluorenone, THF, -78 °C to RT; CH₃COOH/HCl, 110 °C; (c) 4,4'-dimethoxydiphenylamine, *t*-BuONa, Pd₂dba₃, XPhos, toluene, 110 °C.

The chemical structure of **DDOF** is confirmed by X-ray diffraction analysis as displayed in Figure 6.1. Interestingly, in the center of **DDOF**, the distorted oxepine ring chains up the three main cores (two bis(dimethoxyphenylamine)fluorene with bithiophene). The angle of the ether bond is measured to be 130.03° and the angle of the planes of two fluorene cores is 82.4° . Different from the ubiquitous spiro-OMeTAD²⁰⁰ and previously reported KR216,¹⁹⁰ the two fluorene cores of **DDOF** lost their central symmetric configuration and adopted a seesaw type orientation with one side arm (di-*p*-methoxyphenylamine) of each core beneath or above that of the other core (Figure 6.1b,c). Therefore, for the sake of visual clarity, three different colors are introduced to mark the three main cores of this molecule with very irregular geometry.

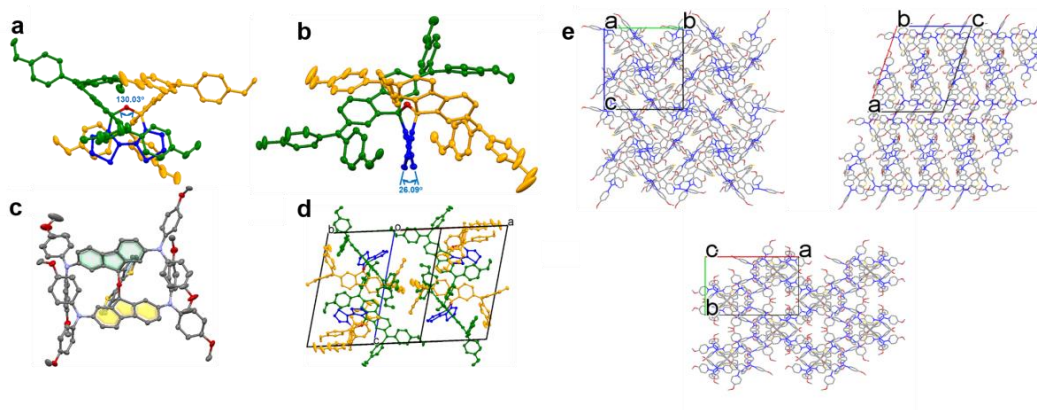


Figure 6.1 a) ORTEP drawings and perspective view along the crossline of two fluorene planes of **DDOF** showing the angle of the ether bonds of 130.03° determined by X-ray crystallography (hydrogen atoms omitted for clarity); b) perspective view along the symmetric center of the bithiophene core of **DDOF** showing dihedral angle between the two thiophene rings (26.09°); c) top view indicating two different kinds of orientation of the fluorene planes filled with green and yellow color; d) perspective view of a unit cell of **DDOF**. No $\pi\cdots\pi$ short contacts can be measured. (Colors are used to identify the three main cores of the molecule: TPA-fluorene in green and orange, bithiophene in blue); e) packing structures of **DDOF** (blue color indicating the self-assembled region of redox active triphenylamine).

Different from the case of **FDT**,¹²⁷ the two thiophene units are not fused by a cyclopentadiene and a torsion angle of 26.09° is measured (Figure 6.2). The two bis(dimethoxyphenylamine)fluorenes are orthogonally connected to the oxepine ring with dihedral angles of 87.65° and 88.92° respectively, which are slightly smaller than that of spiro-OMeTAD (89.94°). **DDOF** was found to crystallize in the monoclinic space group $P121/c$. In one-unit cell, four independent molecules in the crystal lattice stacked in a highly slipped fashion (Figure 6.1d) through only CH/π (CH/O) hydrogen bonds. Similar to that of spiro-OMeTAD, due to the highly sterically hindered geometry, no close face-to-face overlap is observed. As indicated in Figure 6.1e and similar to what was found in other triphenylamine containing HTMs,²¹⁴ the redox active triphenylamine marked with the same color forms channels or networks inside the crystal

lattice, which are expected to facilitate the facile establishment of highly efficient charge transport channels.

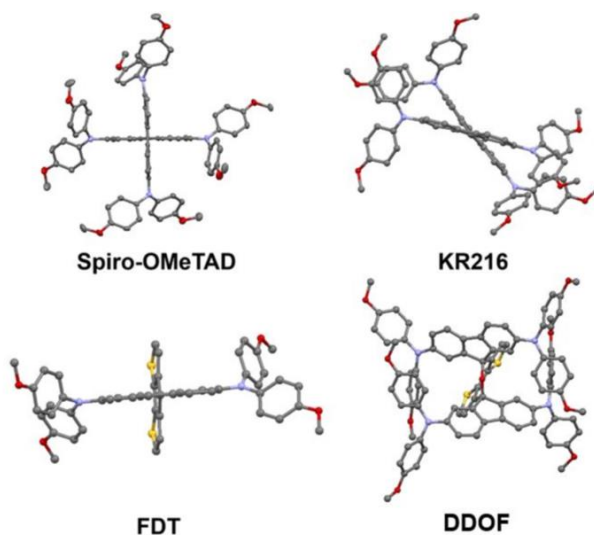


Figure 6.2 A direct comparison of four different HTM showing different space configuration of 2,7-diphenylamine-substituted fluorene.

6.2.2 Structure Optimization

In an attempt to gain more insight into the electronic structure of compound **DDOF**, MO calculations were performed at the TD-DFT and DFT levels of theory, respectively, using the B3LYP functional and 6-31G(d) basis set employing the Gaussian 09 package. The optimized geometry of **DDOF** is shown in Figure 6.3b. The optimized molecular geometry shows that four diphenylamine side arms are extended from the two coplanar fluorene groups forming four redox active centers. The two fluorene planes are roughly orthogonal to each other with an angle of 89.66° . Due to the non-aromatic nature of the oxepine ring, the planes of two thiophene rings are twisted with a dihedral angle of 26.36° . These values are in agreement with what was measured in the single crystallography. Figure 6.3a reveals electron density distributions in the highest occupied molecular orbital (HOMO) and the lowest unoccupied molecular orbital (LUMO). The HOMO of and HOMO-1 **DDOF** are close in energy and spread over the one of the two bis(dimethoxyphenylamine)fluorene groups respectively, resulting from the antibonding interaction of all the aromatic rings. Due to the fact that the oxepine ring breaks the conjugation among the three main conjugated moieties, the interaction between their virtual orbitals

is less pronounced. The LUMO of **DDOF** is a π^* orbital confined on the bithiophene groups, and the LUMO+1 is a π^* orbital that is mainly delocalized over the two fluorene groups.

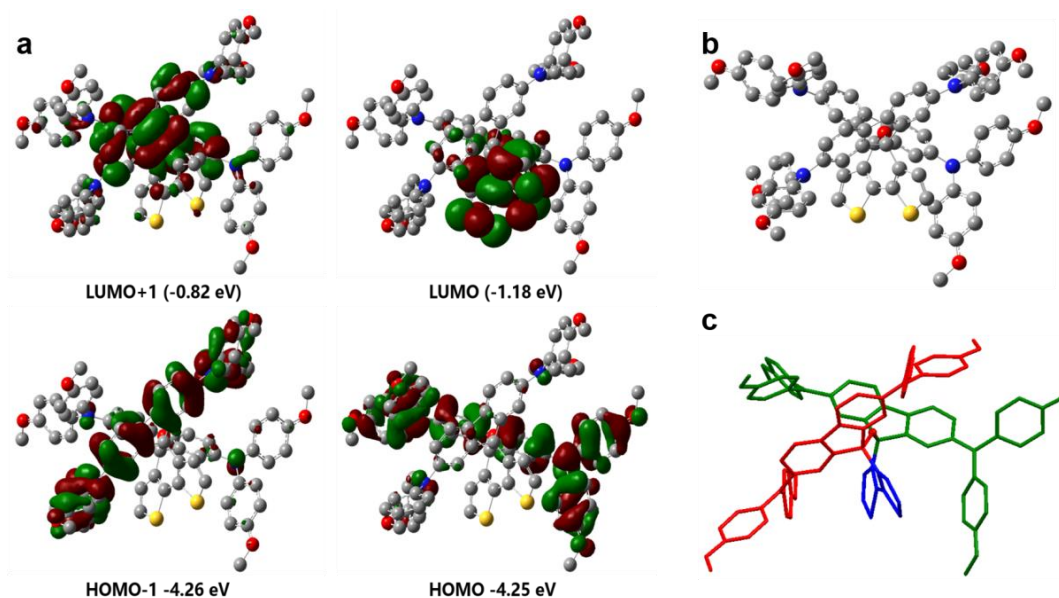


Figure 6.3 a) Isodensity surface plots (isovalue of 0.025) and energies (within parentheses) calculated for the frontier orbitals of DDOF; b) geometry optimization for the ground state of DDOF; c) different color highlighted the three conjugated moieties (hydrogen atoms are omitted for clarity).

6.2.3 Thermal, Optical, and Electrochemical Characterization

The thermal behavior of HTMs was determined by thermogravimetric analysis (TGA) and differential scanning calorimetry (DSC) measurements (Figure 6.4a,b). From TGA, it was found that **DDOF** has a similar to spiro-OMeTAD (417 °C) and relatively high decomposition temperature (T_{dec}) of 412 °C, with a weight loss of 5%, indicating good thermal stability. The thermal transitions of **DDOF** were studied by DSC. Only a glass transition temperature (T_g) of 157 °C was investigated for **DDOF** during the second heating scan, demonstrating that this HTM is fully amorphous. This is desirable to form homogeneous films in PSC devices.

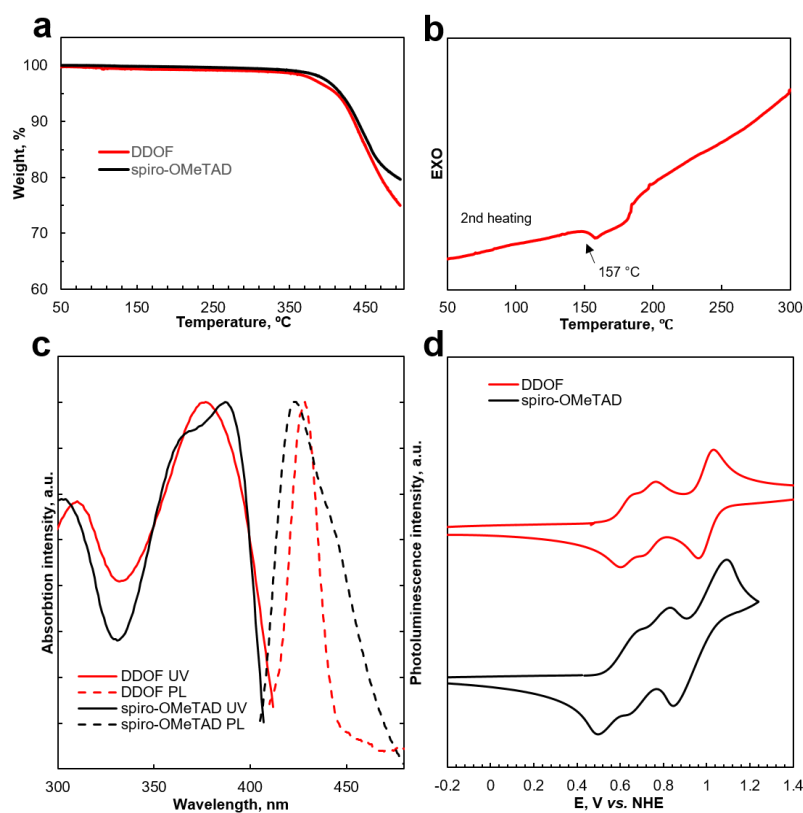


Figure 6.4 a) Thermogravimetric analysis (TGA) data of HTMs, heating rate of $10\text{ }^{\circ}\text{C min}^{-1}$, N_2 atmosphere; b) DSC second heating curve of DDOF, scan rate $10\text{ }^{\circ}\text{C min}^{-1}$, Ar atmosphere; c) UV-Vis absorption spectra normalized at the peak value; and d) cyclic voltammograms of DDOF and spiro-OMeTAD.

The normalized UV-Vis absorption and photoluminescence spectra of **DDOF** and spiro-OMeTAD in THF are shown in Figure 6.4c. Both exhibit an almost identical absorption band in the UV region with the absorption maximum around 385 nm. Compared with spiro-OMeTAD, **DDOF** shows a narrow emission band centered at 426 nm. The optical bandgap (E_g) determined from the onset of absorption was 3.02 eV for **DDOF**, which is almost identical to that of spiro-OMeTAD. To compare the energy levels of the new HTM with spiro-OMeTAD we performed cyclic voltammetry (CV) measurement. The data derived from the ground-state oxidation potential (E_{HOMO}) estimated from the cyclic voltammogram shown in Figure 6.4d are summarized in Table 6.1. The HOMO value of **DDOF** was estimated to be -5.07 eV vs. vacuum, which is slightly destabilized compared with that of spiro-OMeTAD (-5.04 eV). Considering that the valence band of double-mixed perovskite is at -5.65 eV (vs. vacuum),¹⁵² **DDOF** shows enough overpotential leading to efficient photogenerated charge transfer at the interface.

ID	λ_{abs} , (nm) ^a	λ_{em} , (nm) ^a	E_g , (eV) ^b	E_{HOMO} , (eV) ^c	E_{LUMO} , (eV) ^d
DDOF	378	426	3.02	-5.07	-2.05
spiro-OMeTAD	390	424	3.05	-5.04	-1.99

Table 6.1 Optical and electrochemical properties comparison. ^aAbsorption and photoluminescence measured in THF solution; ^bdetermined from the UV-Vis absorption onset; ^cmeasured in DCM/tetra-*n*-butylammonium hexafluorophosphate (0.1 M) solution, using glassy carbon working electrode, Pt reference electrode, and Pt counter electrode with Fc/Fc⁺ as an internal standard. Potentials were converted to the normal hydrogen electrode by addition of +0.624 V and -4.44 eV to the vacuum, respectively; ^dcalculated from $E_{LUMO} = E_{HOMO} + E_g$.

6.2.4 Photophysical Properties

The lateral thin-film conductivity of HTM layers was measured on OFET substrates (Figure 6.5a). The conductivity of oxidized **DDOF** was determined to be $2.5 \times 10^{-5} \text{ S cm}^{-1}$, which is lower than that of spiro-OMeTAD ($\sigma = 4.9 \times 10^{-5} \text{ S cm}^{-1}$). To demonstrate the ability of **DDOF** acting as the HTM, PSCs with $(\text{FAPbI}_3)_{0.85}(\text{MAPbBr}_3)_{0.15}$ perovskite as the absorber were prepared. Figure 6.5b displays the cross-sectional images of the PSCs analyzed with a field-emission scanning electron microscope. The device is made of 400 nm perovskite atop a 200 nm thick m-TiO₂ layer, which was deposited on FTO glass coated with 50 nm compact TiO₂. The device is completed by an 100 nm thick HTM and 80 nm gold as a back contact.

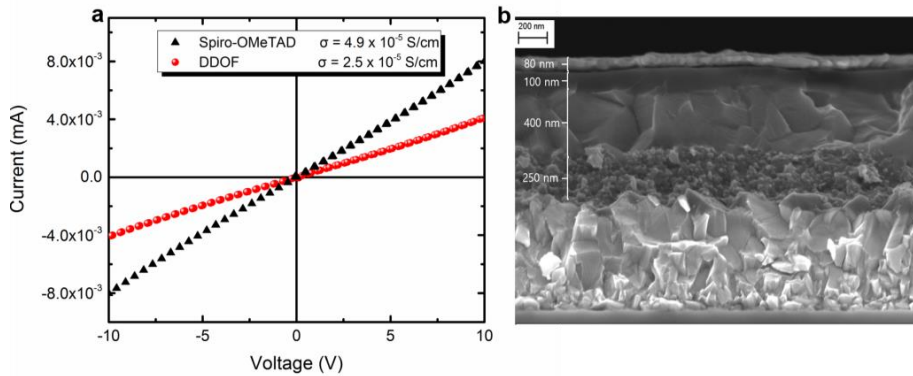


Figure 6.5 a) Conductivity measurements on OFET substrates; and b) cross-sectional SEM micrograph of perovskite device containing DDOF as HTM.

6.2.5 Photovoltaic Properties and Device Stability

Figure 6.6a illustrates the current–voltage (J – V) traces collected under simulated solar illumination (AM1.5G, 100 mW cm^{-2}) for the best PSC among 30 devices. Mixed-perovskite precursor was prepared by mixing 1.15 M PbI_2 , 1.10 M FAI, 0.2 M PbBr_2 , 0.2 M MABr in a mixed solvent of DMF:DMSO = 4:1 (volume ratio). The HTMs were applied from a 20 mM solution in toluene, containing 330 mol% tBP, 50 mol% LiTFSI, and 3 mol% FK209 as additives. Summarized electrical output characteristics are reported in Table 6.2. The device with **DDOF** as the HTM possesses an open-circuit voltage (V_{oc}) of 1101 mV, a short circuit current density (J_{sc}) of 22.37 mA cm^{-2} , and a fill factor (FF) of 0.79, yielding a PCE of 19.4%. The high fill factor may be attributed to the thin HTM layer of 100 nm, causing lower series resistance.

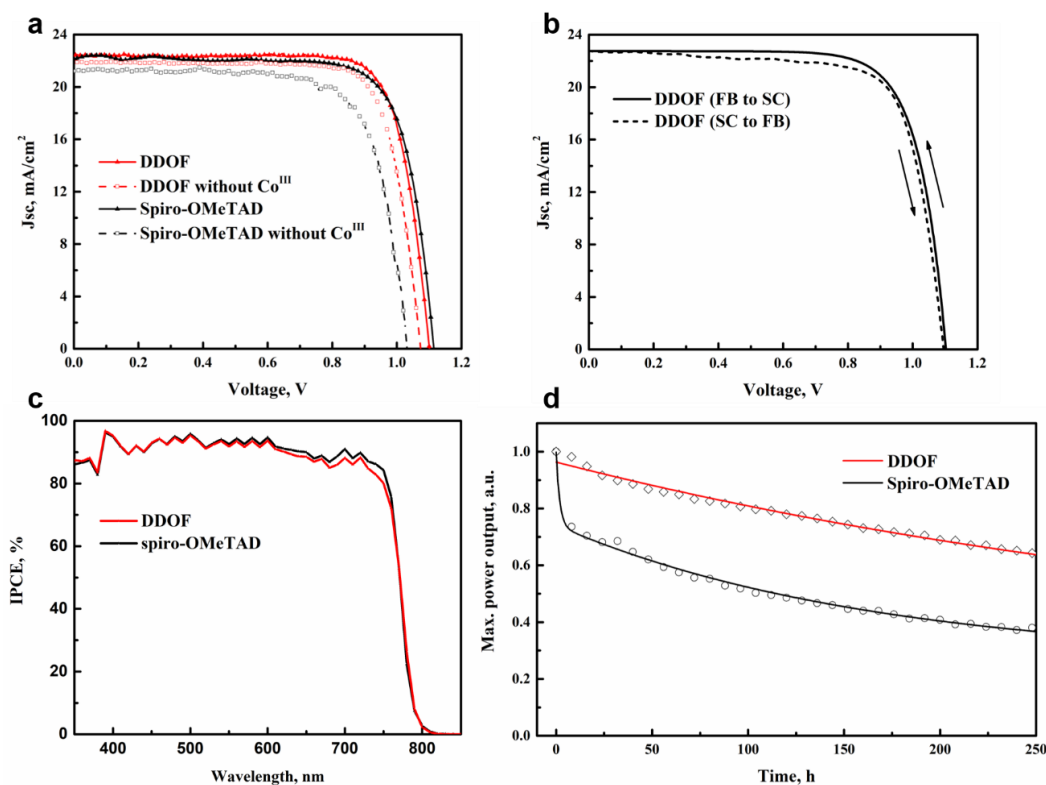


Figure 6.6 a) J – V curves of best performing device prepared with DDOF and Spiro-OMeTAD as reference. Devices were masked with a black metal aperture of 0.16 cm^2 to define the active area. The curves were recorded scanning at 0.01 V s^{-1} ; b) J – V curves were recorded scanning at 0.01 V s^{-1} from forward bias (FB) to short-circuit condition (SC) and the other way round; c) IPCE spectra as a function of the wavelength of monochromatic light; d) normalized maximum power point tracking of perovskite solar cells prepared in a single experiment, using DDOF and Spiro-OMeTAD as HTMs. The measurement was performed under UV-filtered simulated sunlight in an argon atmosphere without any encapsulation for 250 h.

Furthermore, it is worth noticing that the Co^{III} dopant-free **DDOF** employed PSC yields a high PCE of 18.3%. To show the impact of the hysteresis on **DDOF**-based device performance, J - V traces collected by scanning the applied voltage at 0.01 V s⁻¹ from forward bias (FB) to short-circuit (SC) and the other way around are reported (Figure 6.6b). For comparison, the reference device based on spiro-OMeTAD achieved an overall PCE of 18.8%, which is mainly because of a lower FF, despite similar J_{sc} and V_{oc} using a regular procedure and 16.0% excluding the Co^{III} dopant from the hole transporting layer composition, respectively.

The statistical distribution of the PSC parameters employing **DDOF** and spiro-OMeTAD is shown in Figure 6.7a, giving an average **DDOF** PCE value of 18.7% and indicating very high reproducibility. The incident photon-to-current efficiency (IPCE) (Figure 6.6c) of the perovskite devices as a function of wavelength shows that the device with **DDOF** as the HTM exhibits IPCE above 90% from 400 nm covering all the visible region to 700 nm.

ID	J_{sc} (mA/cm ²)	V_{oc} (mV)	FF	PCE (%)
DDOF	22.37	1101	0.79	19.4
DDOF w/o Co ^{III}	21.86	1074	0.78	18.3
spiro-OMeTAD	22.44	1115	0.75	18.8
spiro-OMeTAD w/o Co ^{III}	21.21	1032	0.73	16.0

Table 6.2 Solar cell performance parameters, extracted from J - V curves.

The stability of PSCs is a key factor that plays a major role in their commercialization potential. In Figure 6.6d, we report maximum power point tracking using **DDOF** and spiro-OMeTAD as HTMs. During the measurement, all the unsealed cells were kept in an argon ambience under a constant illumination of 100 mW cm⁻². The devices were maintained at the maximum power point during aging and the current-voltage curve was recorded automatically every 2 h. The efficiency of spiro-OMeTAD dramatically decreased in early time decay. Similar dynamics have been recently observed by Guarnera and co-workers,¹⁸² who demonstrated that a rapid degradation mechanism is activated by metal electrode migration through spiro-OMeTAD and contacting the perovskite layer. **DDOF** has a similar dynamics phenomenon, with a smaller decrease compared with spiro-OMeTAD. At the end of 250 h, the initial values for **DDOF**, and spiro-OMeTAD decay to 65%, and 37%, respectively, confirming that **DDOF** is substantially more stable than the spiro-OMeTAD. In Figure 6.7b, shelf-stability of the devices at a relative humidity of 10% without any encapsulation for 1000 h is reported. The cells with **DDOF** maintained around 95% of their initial PCE, while the PCE of devices with spiro-OMeTAD dropped by 20% under identical conditions. The general tendency indicates better long-term stability of newly developed HTM, demonstrating that such a clear improvement is correlated with the chemical stability of **DDOF** compared to the spiro-OMeTAD.

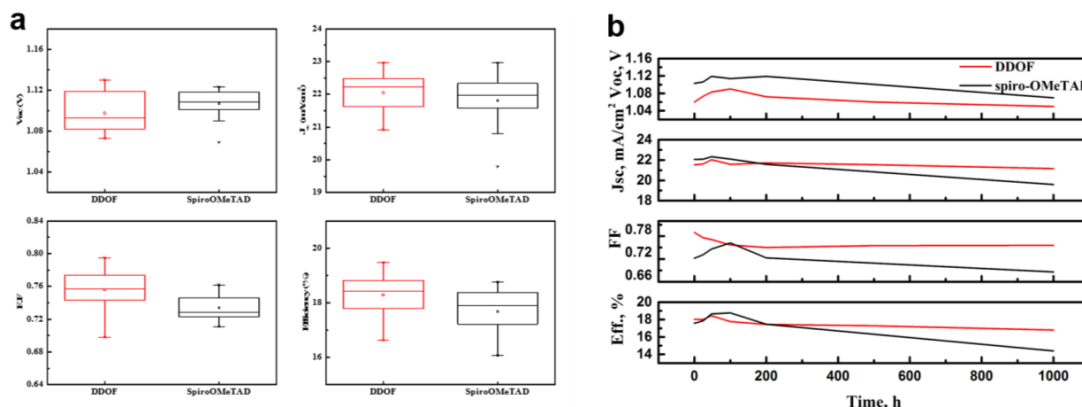
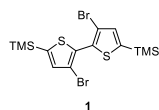


Figure 6.7 a) Statistical distribution of 30 perovskite solar cells performance; b) V_{oc} , J_{sc} , FF and PCE of devices with spiro-OMeTAD and DDOF as HTMs versus time. Stability tests were carried out keeping devices at a relative humidity of 10% without any encapsulation for 1000 h.

6.3 Conclusions

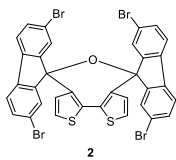
To summarize, a novel dispiro-oxepine derivative as a hole transporting material, obtained by a facile 3-step synthetic route is reported. Perovskite solar cells employing **DDOF** as the HTM showed one of the highest power conversion efficiencies of 19.4% reported to date. The solid structure study by single crystallography indicated again that the π - π interaction is not a prerequisite for designing an effective HTM. Moreover, improved long-term stability over 250 h has been demonstrated, making this HTM a very promising candidate for industrial production. Further modifications of the dispiro-oxepine based HTMs are currently under the progress.

6.4 Synthetic Methods and Procedures



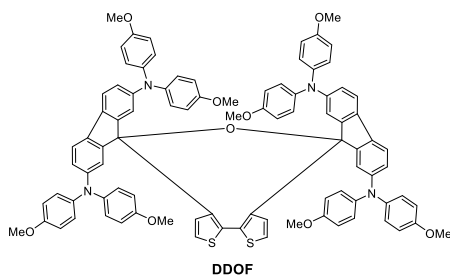
5,5'-Bis(trimethylsilyl)-3,3'-dibromo-2,2'-bithiophene (1).²¹⁵ To a solution of commercially available 3,3'-dibromo-2,2'-bithiophene (5 g, 15.4 mmol, 1 eq.) in dry THF (50 mL), lithium diisopropylamide, 2.0 M (17 mL, 34 mmol, 2.2 eq.) was added dropwise at -78 °C. After stirring for 1 h, trimethylsilyl chloride (4.3 mL, 34 mmol, 2.2 eq.) was added dropwise at -78 °C. The reaction mixture was then allowed to warm to room temperature and stirred overnight. Water was added to quench the reaction. The resulting mixture was extracted with hexane. This crude residue was purified by flash chromatography with pure hexane. Yield: (6.5 g, 90%). Colorless needles. $^1\text{H NMR}$ (400 MHz, CDCl_3) δ

7.18 (s, 2H), 0.37 (s, 18H). ^{13}C NMR (100 MHz, CDCl_3) δ 143.81, 137.44, 134.24, 113.37, -0.36. $\text{C}_{14}\text{H}_{20}\text{Br}_2\text{S}_2\text{Si}_2$ [M^+] exact mass = 465,8912 MS (MALDI-TOF) = 465.880.



2,2'',7,7''-tetrabromodispiro[fluorene-9,4'-dithieno[3,2-c:2',3'-e]oxepine-6',9''-fluorene] (2).²¹³ To a solution of **1** (2 g, 4.3 mmol, 1 eq.) in 50 mL

of dry THF at $-78\text{ }^\circ\text{C}$ under argon atmosphere, *n*-BuLi (2.5 M in hexanes, 3.6 mL, 9 mmol, 2.1 eq.) is dropwise added. After 2 h at the same temperature, 2,7-dibromofluorenone (3.65 g, 10.8 mmol, 2.5 eq.) in THF (50 mL) is added to the mixture dropwise, and the solution was warmed to room temperature and stirred overnight. The mixture was washed with water, extracted with DCM, and the combined organic phases are dried over MgSO_4 . The solvent is evaporated and the crude product is precipitated in ethanol to afford a white solid and is used in the next step without further purification. Obtained solid was dissolved in boiling acetic acid (100 mL), and 1 mL of concentrated hydrochloric acid were added. After refluxing for 2 h, the mixture were washed with water and extracted with DCM, and the combined organic phases are dried over MgSO_4 . This crude residue was purified by flash chromatography with pure 20% DCM in hexane. (1.4 g, 41%). ^1H NMR (400 MHz, CDCl_3) δ 7.49 (dd, $J = 7.9$ Hz, 4H), 7.44 (d, $J = 8.1$ Hz, 4H), 7.18 (d, $J = 5.1$ Hz, 2H), 7.09 (d, $J = 1.5$ Hz, 4H), 6.39 (d, $J = 5.1$ Hz, 2H). ^{13}C NMR (100 MHz, CDCl_3) δ 151.1, 140.8, 137.5, 134.4, 132.4, 129.1, 128.9, 124.8, 122.2, 121.4, 88.1. $\text{C}_{34}\text{H}_{16}\text{Br}_4\text{OS}_2$ [M^+] exact mass = 819,7376 MS (MALDI-TOF) = 819.721.



2,2',7,7'-tetrakis-(*N,N'*-di-4-methoxyphenylamine)dispiro[fluorene-9,4'-dithieno[3,2-c:2',3'-e]oxepine-6',9''-fluorene] (DDOF). In a 50 mL

Schlenk-tube, 400 mg of **2** (0.49 mmol, 1 eq.), 560 mg commercially available 4,4'-dimethoxydiphenylamine (2.5 mmol, 5 eq.), and 280 mg *t*-BuONa (2.9 mmol, 6 eq.) were dissolved in 20 mL dry toluene and degassed for 20 min with N_2 . After the addition of 70 mg Pd_2dba_3 (0.075 mmol, 15%) and 70 mg Xphos (0.15 mmol, 30%), the reaction was refluxed overnight. The reaction was then diluted with DCM and flashed through a plug of MgSO_4 to remove inorganic salts and metallic palladium. This crude residue was purified by flash chromatography with 30% THF in hexane. Isolated compound was dissolved in THF and dropped into MeOH, precipitate was collected by filtration, washed with MeOH and dried. 420 mg (60% yield) of pale yellow solid was obtained. ^1H NMR (400 MHz, THF, 267K) δ 7.28 (d, $J = 8.0$ Hz, 2H), 7.09 (d, $J = 8.1$ Hz, 2H), 7.00 (d, $J = 7.9$ Hz, 8H), 6.90 (s, 2H), 6.80 (d, $J = 8.4$ Hz, 2H), 6.75 (d, $J = 7.8$ Hz, 8H), 6.69 (d, $J = 5.2$ Hz, 2H), 6.65 (s, 16H), 6.56 (d, $J = 7.8$ Hz,

2H), 6.35 (s, 2H), 6.17 (d, J = 5.3 Hz, 2H), 3.73 (s, 12H), 3.70 (s, 12H). ¹³C NMR (100 MHz, THF) δ 155.89, 151.08, 150.15, 148.27, 147.25, 141.77, 141.08, 140.94, 140.92, 133.44, 133.00, 131.40, 129.27, 126.72, 125.53, 122.79, 121.94, 119.77, 118.90, 118.66, 116.72, 114.41, 87.64, 54.58. C₉₀H₇₂N₄O₉S₂ [M⁺] exact mass = 1416,4741 MS (MALDI-TOF) = 1416.304.

Summary

The bulk of the work described in this thesis is focused on the rational design and molecular engineering of a variety of low molecular weight hole transporting materials. The general aim was to investigate the relationship between the molecular structure of the synthesized novel hole transporting materials and performance of perovskite solar cell devices, leading to a fundamental understanding of the requirements of the hole transporting materials and further improvement of the photovoltaic performance. The strategy used throughout the thesis, consists on molecular modifications of different core-based hole transporting materials in order to tune their various properties and enable to function in perovskite solar cells:

- In the second chapter, I have designed a rapid and efficient synthesis of a series of novel triazatruxene-based two-dimensional HTMs comprising electron-rich methoxy-engineered substituents. HTMs are obtained from simple and inexpensive starting materials, offering potentially much lower production costs in comparison with the most widely used spiro-OMeTAD. On the basis of various characterization techniques such as CV, UV-Vis, and PL measurements, it was found that the HOMO and LUMO energy levels of each compound are in good alignment with the energy levels of perovskite material. Moreover, molecularly engineered triazatruxene derivatives exhibit surface interaction with perovskite material resulting efficient hole injection from the valence band of perovskite into the HOMO of HTM. Remarkable power conversion efficiency of 18.3% was realized using KR131, showing a potential of 2D materials like triazatruxene-derivatives as an alternative low-cost HTMs. The trend, showing that deeper HOMO level of the HTM correlates with the higher V_{oc} was indicated.
- In the third chapter, I have further employed triazatruxene scaffold as a planar donor unit for dopant-free hole transporting materials based on D- π -A type architecture, where the π -bridge was modulated with 3-hexylthiophene, 3,3''-dihexyl-2,2':5',2''-terthiophene and 4,4-dihexyl-4*H*-cyclopenta[2,1-*b*:3,4-*b'*]dithiophene, and malononitrile acceptor groups were preserved throughout the series, respectively. The supramolecular organization of the new HTMs was determined by GIWAXS, indicating significant differences in self-assembly between the compounds. The highest order of the series

and a distinct surface arrangement has been found only for KR321, showing an ideally characteristic face-on organization with columnar stacks standing on the surface and benefiting to increased vertical charge carrier transport along the π - π stacking direction within a perovskite solar cell. The calculated vertical hole mobility value of KR321 is $2.6 \times 10^{-4} \text{ cm}^2 \text{ V}^{-1} \text{ s}^{-1}$, which is one order of magnitude higher than that of KR353 and three orders of magnitude higher than that of KR355. Improved charge hopping properties through face-on oriented columnar stacks led to a power conversion efficiency of perovskite devices over 19% with improved stability. This result is marked as the highest so far in the field of a pristine hole transporting materials without any chemical additives or doping.

- In chapter 4, I have designed a straightforward and elegant two-step synthetic route towards an easily attainable KR216 HTM based on 9,9'-bifluorenylidene, which mimics the synthetically challenging 9,9'-spirobifluorene moiety of the well-studied spiro-OMeTAD. Employing commercially available and inexpensive starting materials 2,7-dibromo-9H-fluoren-9-one and Lawesson's reagent reduced the estimated price of KR216 around 50 times compared with that of commercial spiro-OMeTAD. Furthermore, in order to investigate the impact of organic impurities and metal residues in final raw organic semiconducting materials, the lab-grade spiro-OMeTAD was synthesized under the same final cross-coupling step and purified using both flash chromatography and precipitation procedures as for KR216. PCE of 17.8% was obtained for PSC using KR216, which is on par with the PCE of the commercial spiro-OMeTAD reference (PCE 18.4%). It was confirmed that high-purity of spiro-OMeTAD is required to obtain high-performance devices since the lab-grade spiro-OMeTAD exhibited lower hole mobility and conductivity as well as lower PCE and higher hysteresis in perovskite solar cells.
- Chapter 5 follows on from the previous, where I have further explored the bistricyclic aromatic ene (BAE)-based HTMs, obtained using Barton-Kellogg diazo-thione coupling by a 2-fold extrusion process. The impact on different atoms in the heteromeric BAE structure was revealed through the various characterization techniques. Replacement of the oxygen atom by sulfur showed a significantly improved hole-drift mobility leading to enhanced photovoltaic performance and reduced hysteresis, most likely owing to the improved interface between the perovskite and HTM caused by stronger Pb-S interaction, whereas oxidation of sulfur to sulfone has a negative effect on the device performance. S-bridged KR374 exhibited a PCE of 19.2%.

- In chapter 6, dispiro-oxepine derivative, obtained by facile 3-step synthetic route has been reported. The chemical structure of highly-hindered DDOF was confirmed by X-ray diffraction analysis, showing a very irregular geometry. DDOF is composed of bithiophene and two dispirodifluorene units chained up around the distorted oxepine ring. While the bithiophene unit has been shown to reveal an additional interaction with perovskite, the four dimethoxydiphenylamine inherent triangular pyramids formed by sp^3 nitrogen atoms lead to a large steric hindrance to further decrease the anisotropic solid structure, favoring a homogeneous film morphology. PSCs employed DDOF as HTM showed one of the highest power conversion efficiency of 19.4% reported to date. Moreover, improved long-term stability over 250 h has been demonstrated. Further modifications of the dispiro-oxepine based HTMs are currently under the progress.

Summarizing, several examples throughout the thesis demonstrate how small changes in the molecular structure such as different atoms, different electron donors, or the length of the π -conjugated system can result in significant changes in the properties of the materials, leading to improved photovoltaic performance. The strategies of rational design by simple synthetic schemes with a minimized number of steps are presented, enabling to tune plenty of desirable characteristics that are necessary for high performance hole transporting materials in perovskite solar cells such as high hole mobility, well-aligned energy levels, material stability, and hydrophobicity. I hope that well-performing materials presented in the thesis will contribute towards a commercialization of perovskite solar cells and may promote a future research of more efficient materials.

Experimental Part

General Methods for Synthesis

All the chemical reagents used in this thesis were purchased from major commercial suppliers (Aldrich, TCI, ABCR, MERCK, Fluorochem, and Roth AG) and were used without further purification, unless otherwise noted. All moisture and oxygen sensitive reactions were performed under nitrogen atmosphere using glassware that was flame-dried under high-vacuum and backfilled with nitrogen. The course of the reactions were monitored by thin layer chromatography (TLC) on Merck KGaA pre-coated TLC Silica gel 60 F₂₅₄ aluminum sheets and visualized with UV. All extracts were dried over powdered MgSO₄ and solvents removed by rotary evaporation under reduced pressure. Flash chromatography was performed using Silicycle UltraPure SilicaFlash P60, 40-63 μm (230-400 mesh).

Structural Characterization

¹H and ¹³C NMR spectra were recorded on a Bruker Avance-400 (400 MHz), Bruker AvanceIII-400 (400 MHz), Bruker DPX-400 (400 MHz) or Bruker DRX-600 (600 MHz) spectrometer at room temperature, unless otherwise noted. All the data are given as chemical shifts in δ and are reported in ppm using solvent as an internal standard: chloroform-d at 7.26 ppm and 77.16 ppm, tetrahydrofuran-d₈ at 1.72, 3.58 ppm and 25.31, 67.21 ppm, benzene-d₆ at 7.16 ppm and 128.39 ppm, dimethyl sulfoxide-d₆ at 2.50 ppm and 39.51 ppm, acetone-d₆ at 2.05 ppm and 29.84 ppm for ¹H and ¹³C, respectively. Data reported as: s = singlet, d = doublet, t = triplet, q = quartet, p = pentet, m = multiplet, b = broad; coupling constants in Hz; integration.

Mass spectra were recorded on Thermo Fisher Q Exactive HF Hybrid Quadrupole-Orbitrap Mass Spectrometer or Axima-CFR plus (Shimadzu) using matrix-assisted laser desorption/ionization (MALDI) technique, 6530 Accurate-Mass Q-TOF LC/MS (Agilent Technologies) using electrospray ionization (ESI) and atmospheric pressure photoionization (APPI) techniques.

Computational Details

The geometrical and electronic properties of the compound were performed with the Gaussian 09 program package. The calculation was optimized by means of the B3LYP (Becke three parameters hybrid functional with Lee-Yang-Perdew correlation functionals) with the B3LYP/6-31G* atomic basis set. The excitation transitions of HTMs were calculated using time-dependent density functional theory (TD-DFT) calculations with B3LYP/6-31g*. Molecular orbitals were visualized using Avogadro™.

Thermal Measurements

Thermogravimetric analysis (TGA) data were collected using TGA 4000 from PerkinElmer. Degradation temperatures investigated from 5% weight loss at 10 °C/min, N₂ atmosphere. Melting, glass transition, and crystallization temperatures observed from differential scanning calorimetry (DSC), recorded on DSC 8000 from PerkinElmer, 10 °C/min, Ar atmosphere.

Optical Characterization

UV-Vis absorption spectra were recorded on a Hewlett Packard 8453 UV-Vis spectrometer. The fluorescence spectra were recorded on a Fluorolog®-3 - Horiba fluorimeter. All samples were measured using an optical cell with an optical path length of 1 cm at room temperature with a concentration of about 10⁻⁵ M in dichloromethane (DCM) or tetrahydrofuran (THF). Optical bandgaps (E_g) were determined from the onset of absorption, in case of no detectable emission was observed or the intersection of normalized absorption and emission spectra.

Electrochemical Characterization

Cyclic voltammetry (CV) measurements were carried out by a three-electrode assembly cell from Bio-Logic SAS and Autolab Eco Chemie cyclic voltammeter.

Cyclic voltammograms of the HTMs were measured in DCM/tetra-*n*-butylammonium hexafluorophosphate (*n*-Bu₄NPF₆) 0.1 M solution, using glassy carbon working electrode, Pt reference electrode and Pt counter electrode with ferrocene/ferrocenium couple Fc/Fc⁺ as an

internal standard at a scan rate of 50 mV s⁻¹. Potentials were converted to the normal hydrogen electrode (NHE) by addition of +0.624 V and -4.44 eV to the vacuum, respectively.

X-ray Measurements

The diffraction data of HTMs were measured at low temperature [120 K] using Mo K_{α} radiation on a Bruker APEX III CCD diffractometer equipped with a kappa geometry goniometer. The dataset was reduced by *APEX3 suit* and then corrected for absorption. The crystal structure was solved and refined by *Olex 2*. The crystal structure was refined using full-matrix least-squares based on F^2 with all non hydrogen atoms. Hydrogen atoms were placed in calculated positions by means of the “riding” model. A summary of the crystallographic data, the data collection parameters, and the refinement parameters are given in Appendix.

To investigate the molecular ordering, grazing-incidence wide-angle X-ray scattering (GIWAXS) experiments were performed by means of a solid anode X-ray tube (Siemens Kristalloflex X-ray source, copper anode X-ray tube operated at 30 kV and 20 mA), osmic confocal MaxFlux optics, X-ray beam with pinhole collimation, and a MAR345 image plate detector. The beam size was 1.0 mm × 1.0 mm (width × height), and samples were irradiated just below the critical angle for total reflection with respect to the incoming X-ray beam (~0.1°). All X-ray scattering measurements were performed under vacuum (~1 mbar) to reduce air scattering and beam damage to the sample. All GIWAXS data processing and analysis was performed by using the software package Datasqueeze.

Photoelectrical Measurements

The charge carrier mobility was measured by the xerographic time of flight (XTOF) or space-charge limited current (SCLC) methods. In case of former, positive corona charging created electric field inside the HTM layer. The charge carriers were generated at the layer surface by illumination with pulses of nitrogen laser (pulse duration was 2 ns, wavelength 337 nm). The layer surface potential decrease as a result of pulse illumination was up to 1–5% of initial potential before illumination. The capacitance probe that was connected to the wide frequency band electrometer measured the speed of the surface potential decrease dU/dt . The transit time t_t was determined by the kink on the curve of the dU/dt transient in linear or double logarithmic scale. The drift mobility was calculated by the formula $\mu = d^2/U_0t_t$, where d is the layer thickness, U_0 – the surface potential at the moment of illumination. Space-charge limited

current (SCLC) measurement performed using hole only device structure: ITO/PEDOT:PSS/HTM/Au with gold electrode: 7.5mm × 7mm. The data is fitted in the SCLC regime using Mott-Gurney law. The dielectric constant was chosen to be 3 and the built-in potential between PEDOT:PSS and Au to be zero. The films were deposited via spin-coating (2000 rpm) inside a nitrogen filled glovebox at 70 °C from a 50 mM tetrachloroethane solution. The PEDOT:PSS films were spin-coated from a 1:3 (isopropanol/PEDOT:PSS) solution onto ITO substrates and subsequently heated at 110°C for 30 min in air.

The ionisation potential (I_p) was measured by the electron photoemission in air (PESA) method. The samples were illuminated with monochromatic light from the quartz monochromator with deuterium lamp. The power of the incident light beam was $(2-5) \times 10^{-8}$ W. The negative voltage of -300 V was supplied to the sample substrate. The counter-electrode with the 4.5×15 mm² slit for illumination was placed at 8 mm distance from the sample surface. The counter-electrode was connected to the input of the BK2-16 type electrometer, working in the open input regime, for the photocurrent measurement. The 10^{-15} – 10^{-12} A strong photocurrent was flowing in the circuit under illumination. The photocurrent I is strongly dependent on the incident light photon energy $h\nu$. $I^{0.5} = f(h\nu)$ dependence was plotted. Usually the dependence of the photocurrent on incident light quanta energy is well described by linear relationship between $I^{0.5}$ and $h\nu$ near the threshold. The linear part of this dependence was extrapolated to the $h\nu$ axis and I_p value was determined as the photon energy at the interception point.

For the conductivity measurement, solutions of HTMs were doped with 3 mol% FK209. The solution was spin-coated onto the OFET substrate (Fraunhofer IPMS) at 4000 rpm for 20 s. The conductivity measurement was done on a 2.5 µm channel (by length). The channel width was 10 mm and the channel height was 40 nm. The data were recorded with a Keithley 2612A by sweeping from -10 to 10 V (Source-drain voltage) at a scan rate of 1 V s⁻¹. The conductivity was calculated from linear fit (Ohm's law).

Scanning Electron Microscopy

A field-emission scanning electron microscope (FESEM, Merlin) was employed to analyze the morphology of the samples. An electron beam accelerated to 3 kV was used with an in-lens detector. The cross-sectional topography was visualized by SEM images to qualitatively study

the pore filling of HTMs. The thickness of the overstanding layer of HTMs on top of the mesoporous TiO₂ electrode was estimated by zooming into the top-most region of the films.

Photophysical Measurements

Integrated photoluminescence (PL) and time-resolved photoluminescence (TRPL) experiments were performed by exciting the perovskite samples deposited onto non-conducting glass at 420 nm. The collected PL spectra were spectrally and temporally analyzed using a 32-cm-focal length monochromator equipped with a charge-coupled device (CCD), which has a spectral resolution of >1 meV and the streak camera with a temporal resolution of ~5 ps, respectively. For time-resolved photoluminescence studies a picosecond mode-locked Ti:sapphire laser was used. All the samples were excited from the hole transporting materials side under ambient conditions.

Fabrication and Characterization of PSCs

Nippon Sheet Glass 10 Ω /square was cleaned by sonication in 2% Hellmanex water solution for 30 minutes. After rinsing with deionized water and ethanol/isopropanol, the substrates were further cleaned with UV ozone treatment for 15 min. Then, 30 nm TiO₂ compact layer was deposited on FTO via spray pyrolysis at 450 °C from a precursor solution of titanium diisopropoxide bis(acetylacetonate) (TAA) in anhydrous ethanol. After the spraying, the substrates were left at 450 °C for 45 min and left to cool down to RT. Then, m-TiO₂ layer was deposited by spin coating for 20 s at 4000 rpm with a ramp of 2000 rpm s⁻¹, using 30 nm particle paste (Dyesol 30 NR-D) diluted in ethanol to achieve 150-200 nm thick layer. After the spin coating, the substrates were immediately dried at 100 °C for 10 min and then sintered again at 450 °C for 30 min under dry air flow. Then, Li-doping of the mesoporous TiO₂ is done by spin coating a 0.03 M solution of LiTFSI in acetonitrile at 3000 rpm for 20 s, followed by sintering at 500 °C for 20 min before use. After cooling down to 150 °C the substrates were immediately transferred in a nitrogen atmosphere glove box for depositing the perovskite films. The perovskite films were deposited from a precursor solution (compositions specified in each chapter) in anhydrous DMF:DMSO 4:1 (volume ratio). The perovskite solution was spin coated in a two-step program at 1000 and 4000 rpm for 10 and 30 s, respectively. During the second step, 100 μ L of chlorobenzene/toluene was poured on the spinning substrate 15 s prior the end of the program. The substrates were then annealed at 100 °C for 1 h in nitrogen filled glove box. After

the perovskite annealing the substrates were cooled down for few minutes and HTM solution was spin at 4000 rpm for 20 s (concentration and solvent specified in each chapter). All HTMs were doped with bis(trifluoromethylsulfonyl)imide lithium salt (LiTFSI, from Aldrich), tris(2-(1*H*-pyrazol-1-yl)-4-*tert*-butylpyridine)cobalt(III)-tris(bis(trifluoro-methylsulfonyl)imide) (FK209, from dynamo) and 4-*tert*-Butylpyridine (tBP, from Aldrich) with the molar ratio of 0.5, 0.03 and 3.3 for LiTFSI, FK209 and tBP, unless otherwise noted. Finally, 70-80 nm of gold top electrode was thermally evaporated under high vacuum.

The solar cells were measured using a 450 W xenon light source (Oriel). The spectral mismatch between AM1.5G and the simulated illumination was reduced by the use of a Schott K113 Tempax filter (Präzisions Glas & Optik GmbH). The light intensity was calibrated with a Si photodiode equipped with an IR-cutoff filter (KG3, Schott) and it was recorded during each measurement. Current-voltage characteristics of the cells were obtained by applying an external voltage bias while measuring the current response with a digital source meter (Keithley 2400). The voltage scan rate was 10 mV s⁻¹ and no device preconditioning was applied before starting the measurement, such as light soaking or forward voltage bias applied for long time. The starting voltage was determined as the potential at which the cells furnishes 1 mA in forward bias, no equilibration time was used. The cells were masked with a black metal mask (0.16 cm²) to estimate the active area and reduce the influence of the scattered light.

Incident photon-to-current conversion efficiency (IPCE) measurements were made using a 300 W xenon light source (ILC Technology, USA). A double-monochromator spectrometer (Gemini-180, JobinYvon Ltd. UK) was used to select and increment the wavelength of the radiation impinging on the cells. The monochromatic incident light was passed through a chopper running at 1 Hz and the on/off ratio was measured by an operational amplifier. This was superimposed on a white light bias corresponding to an intensity of 10 mW/cm².

Appendix

$^1\text{H}/^{13}\text{C}$ NMR Spectra

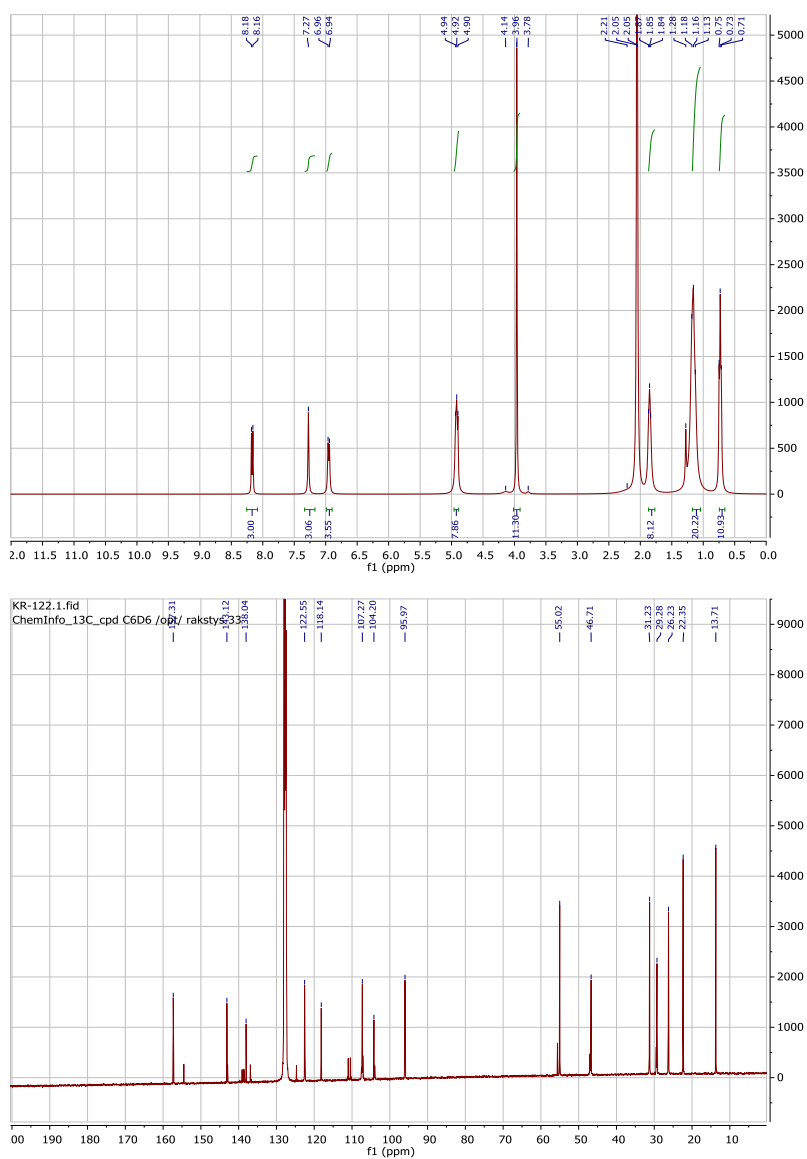


Figure 1. ^1H and ^{13}C NMRs of KR122.

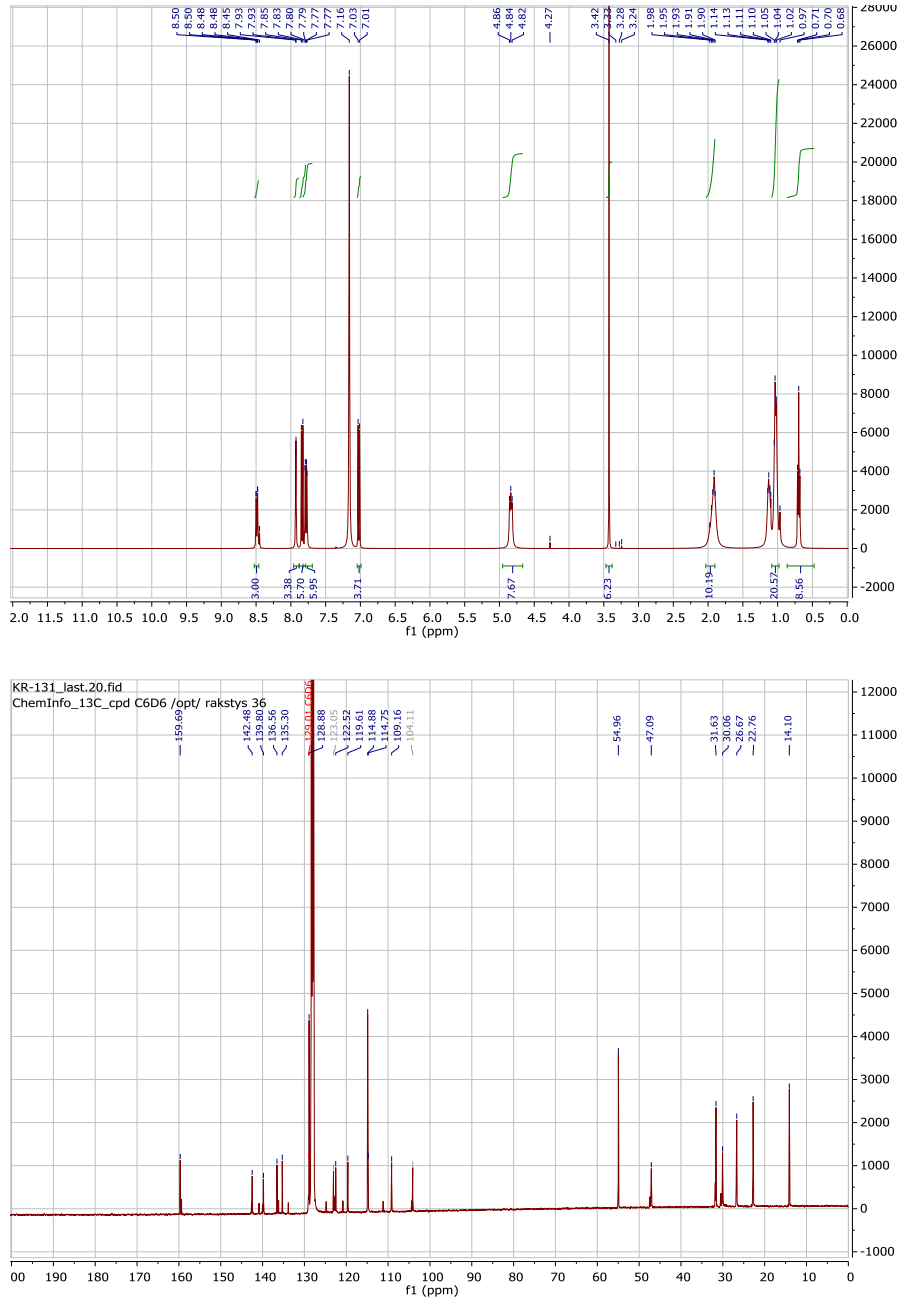


Figure 2. ¹H and ¹³C NMRs of KR131.

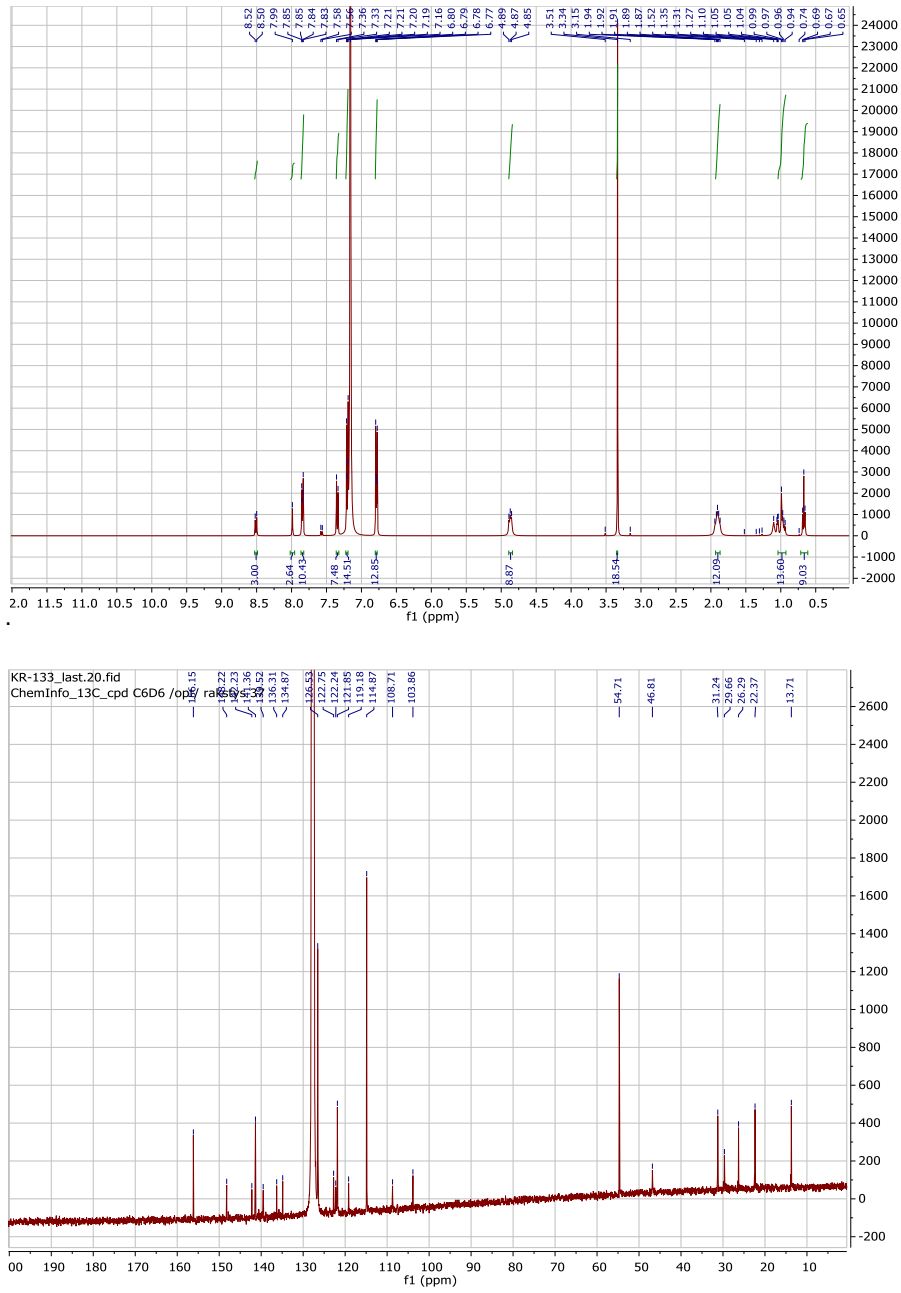
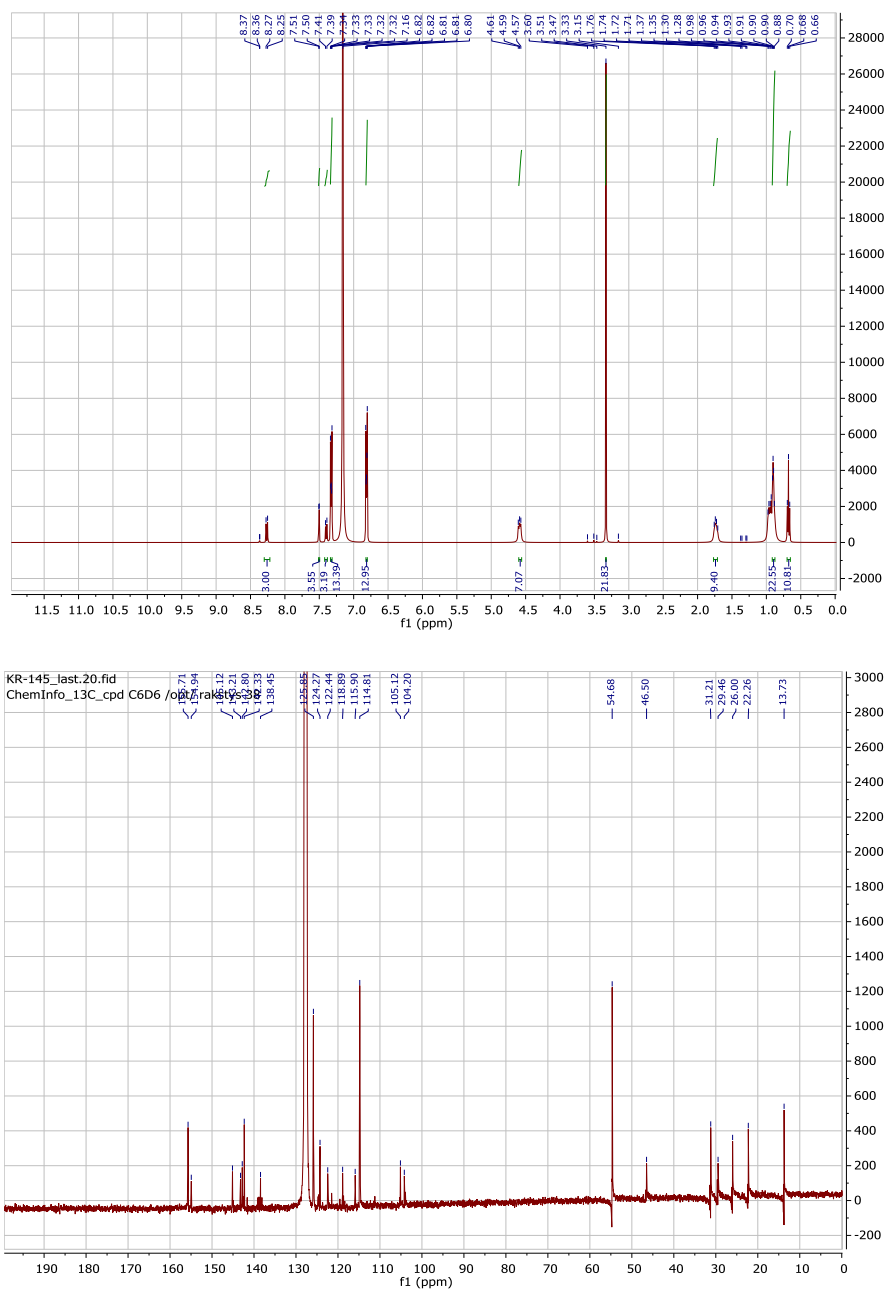


Figure 3. ^1H and ^{13}C NMRs of KR133.

Figure 4. ^1H and ^{13}C NMRs of KR145.

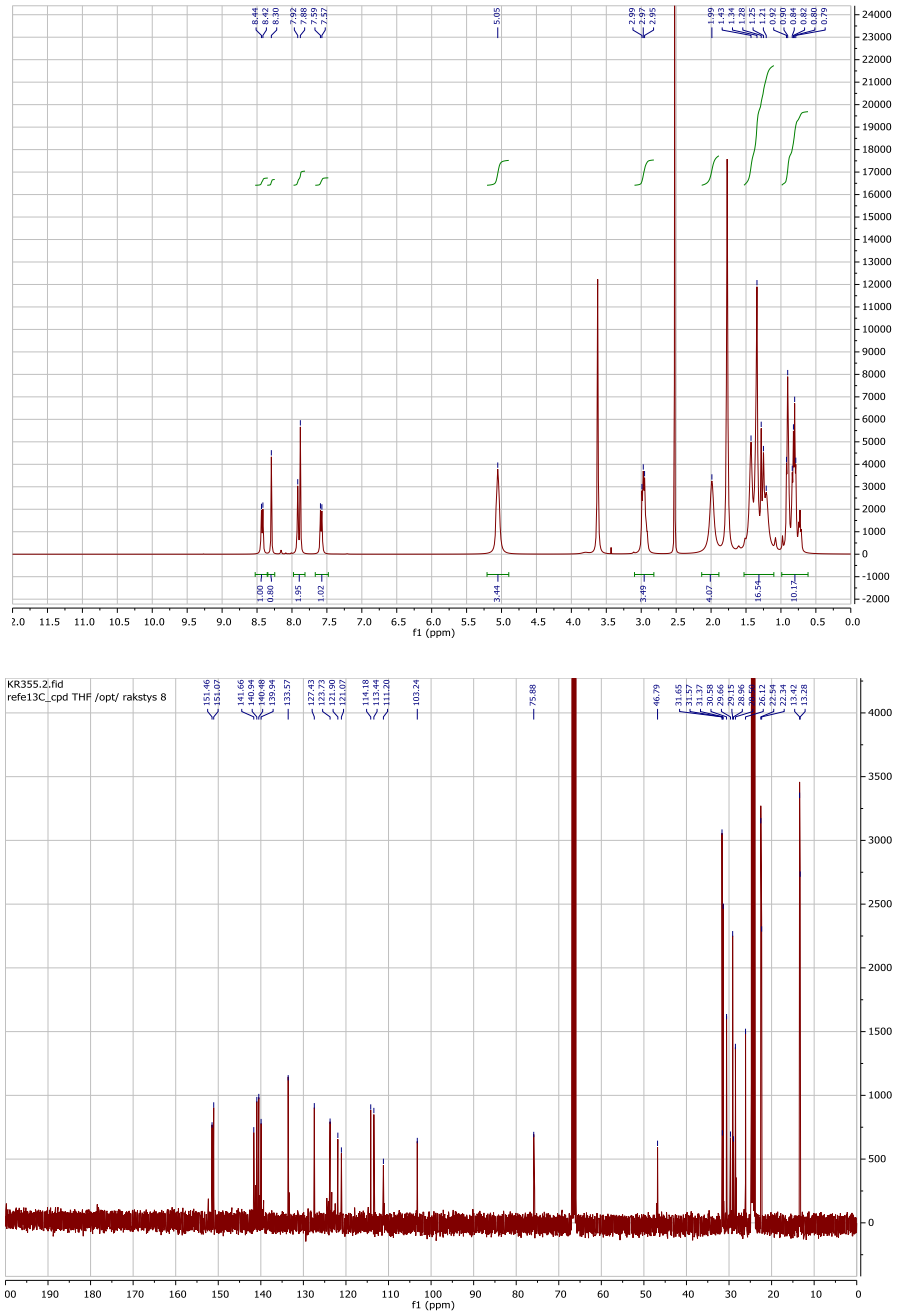


Figure 5. ¹H and ¹³C NMRs of KR355.

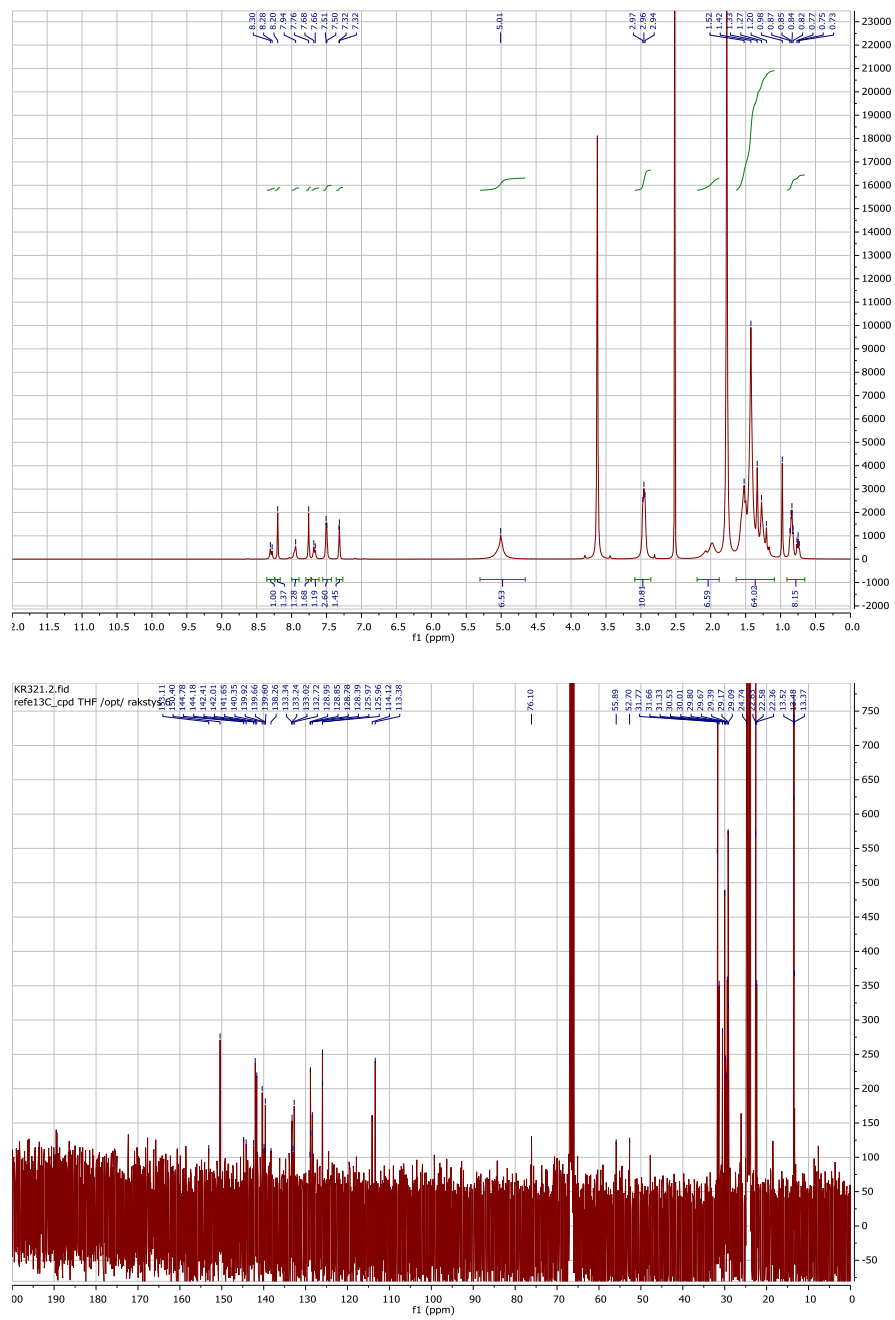


Figure 6. ^1H and ^{13}C NMRs of KR321.

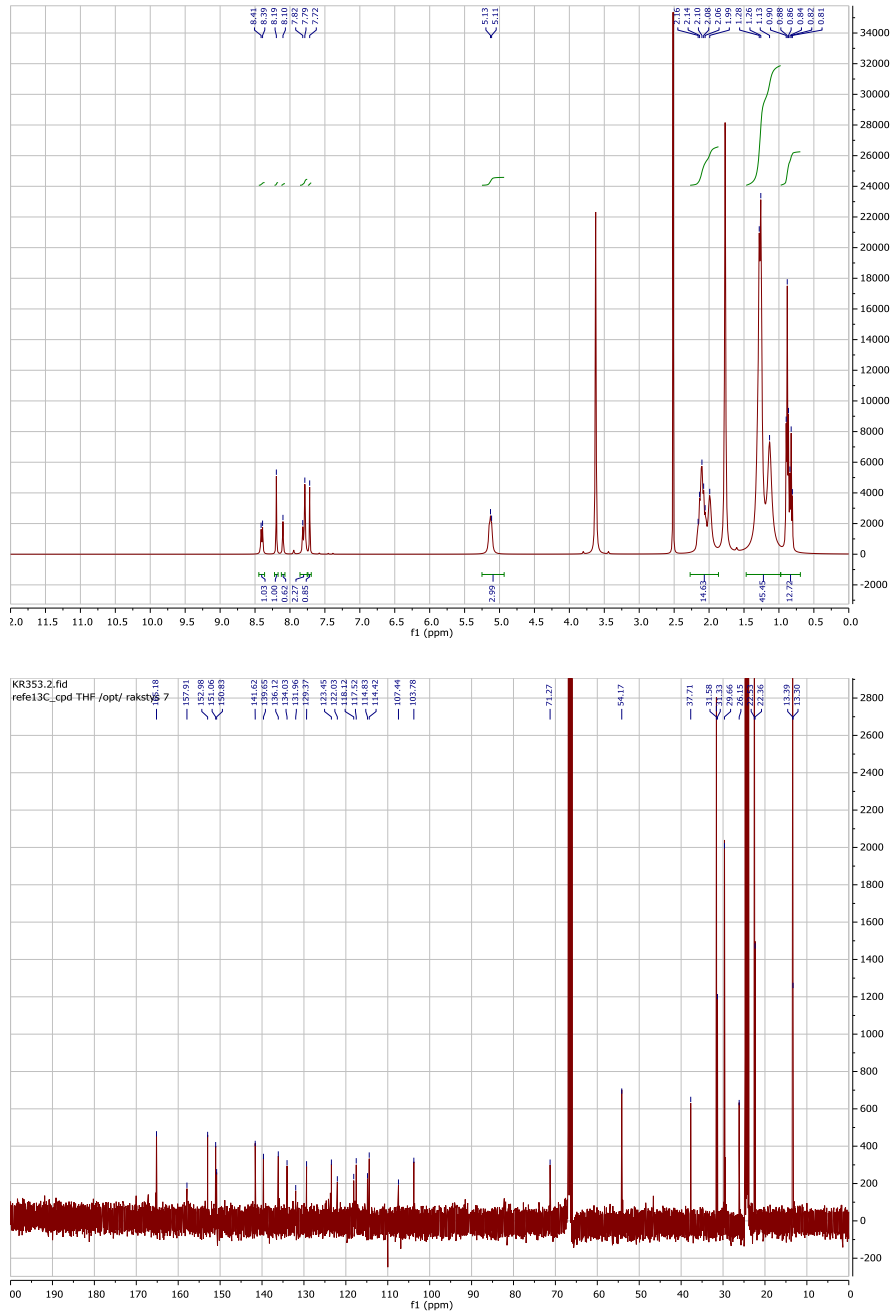


Figure 7. ¹H and ¹³C NMRs of KR353.

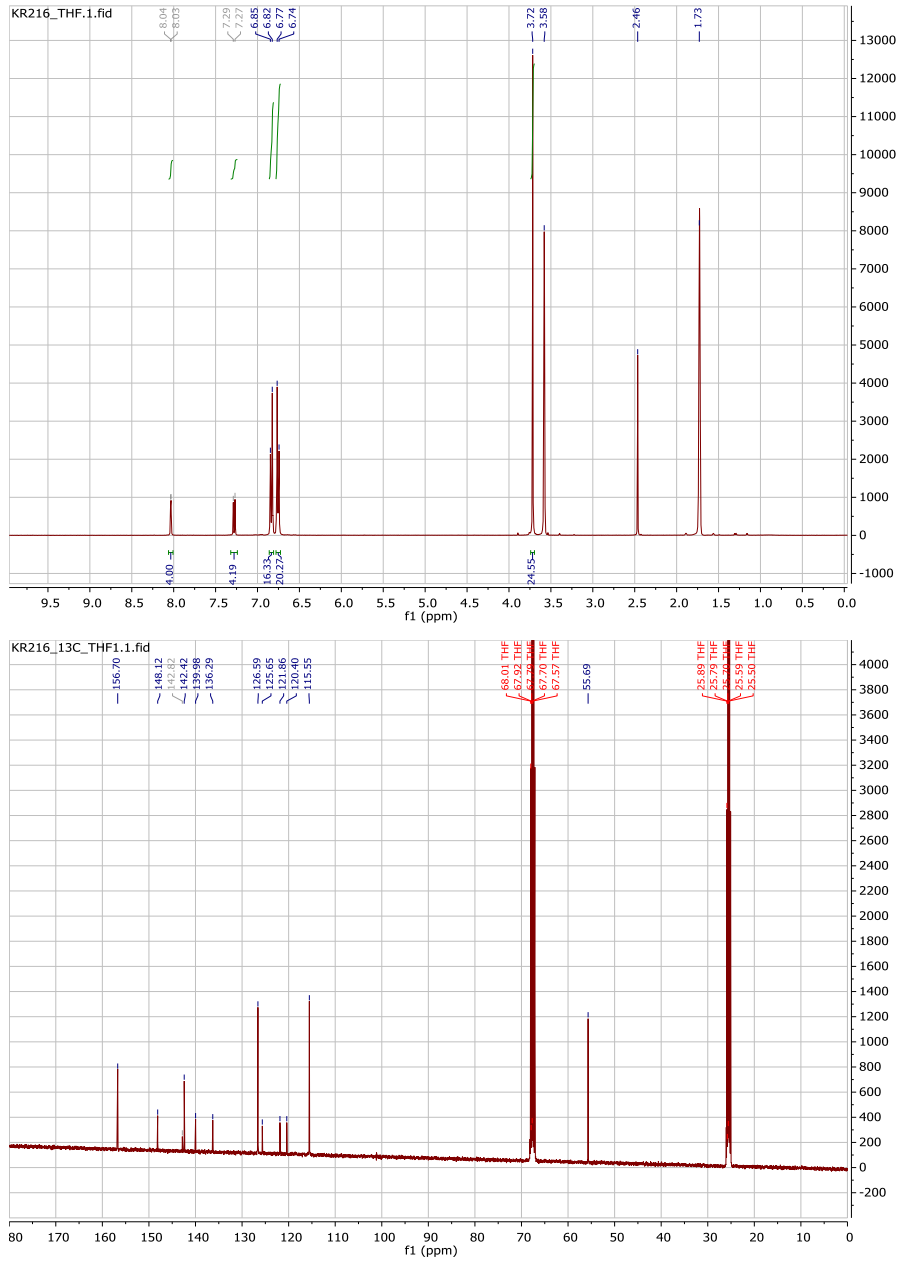


Figure 8. ¹H and ¹³C NMRs of KR216.

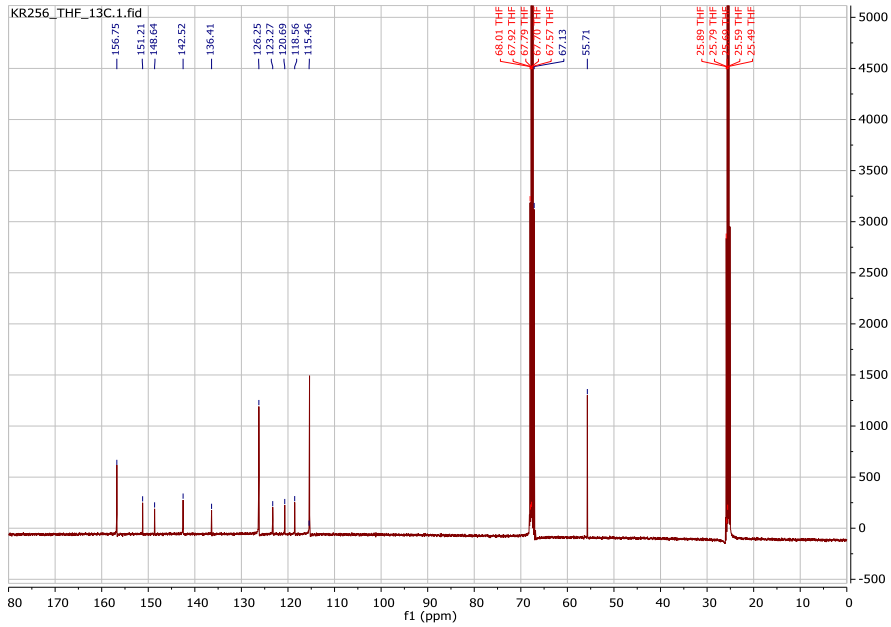
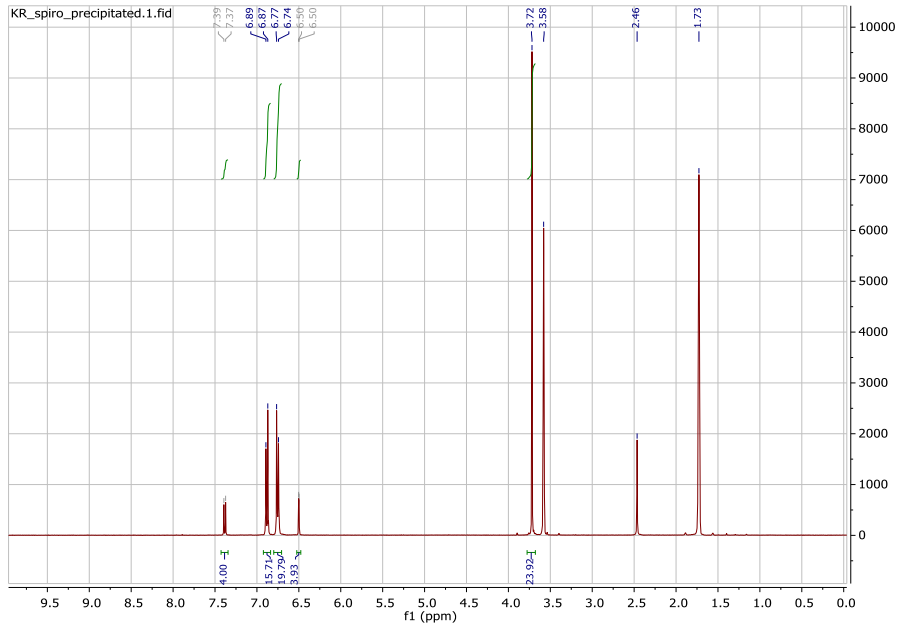
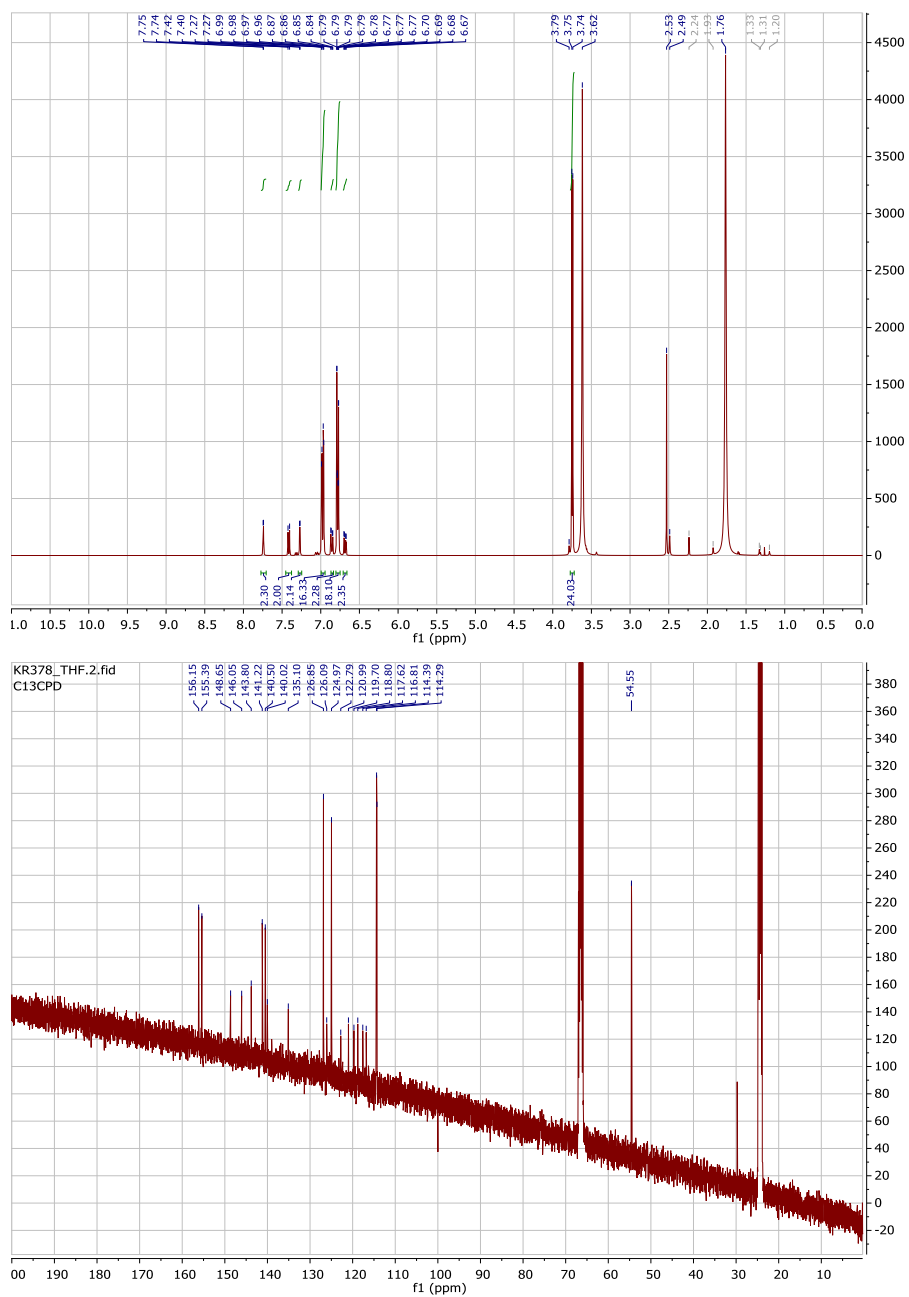


Figure 9. ^1H and ^{13}C NMRs of spiro-OMeTAD.

Figure 10. ^1H and ^{13}C NMRs of KR378.

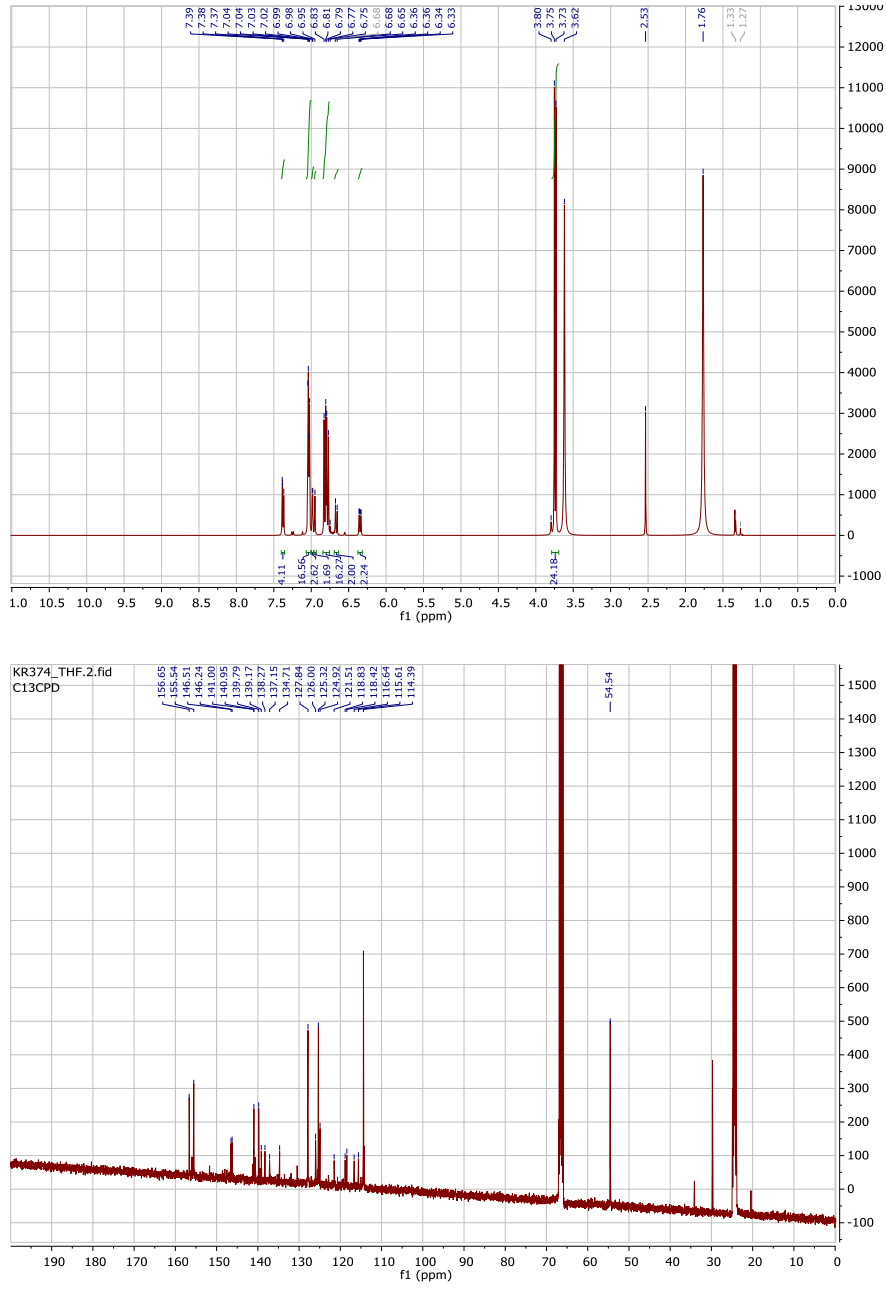


Figure 11. ^1H and ^{13}C NMRs of KR374.

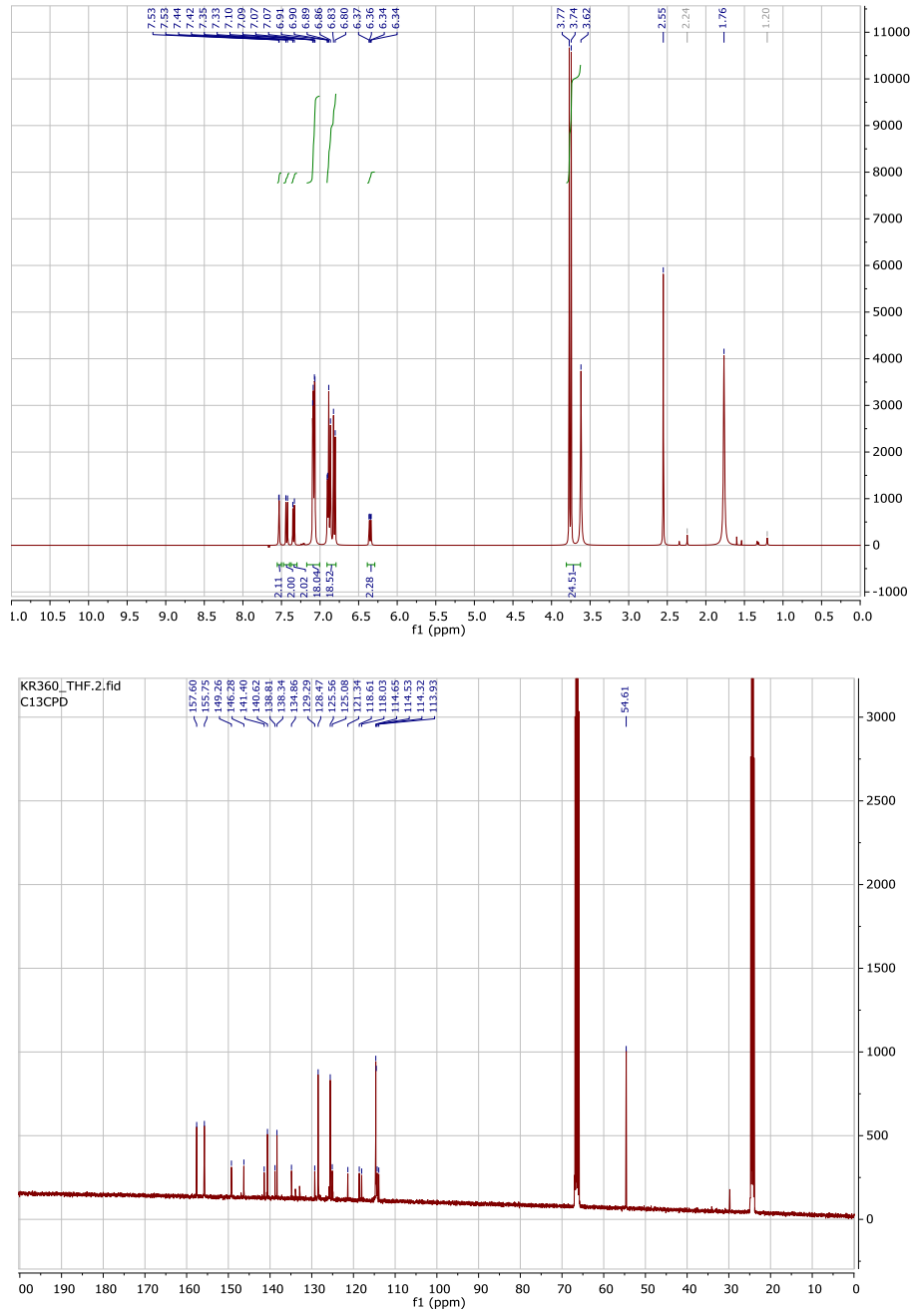


Figure 12. ^1H and ^{13}C NMRs of KR360.

MS Spectra

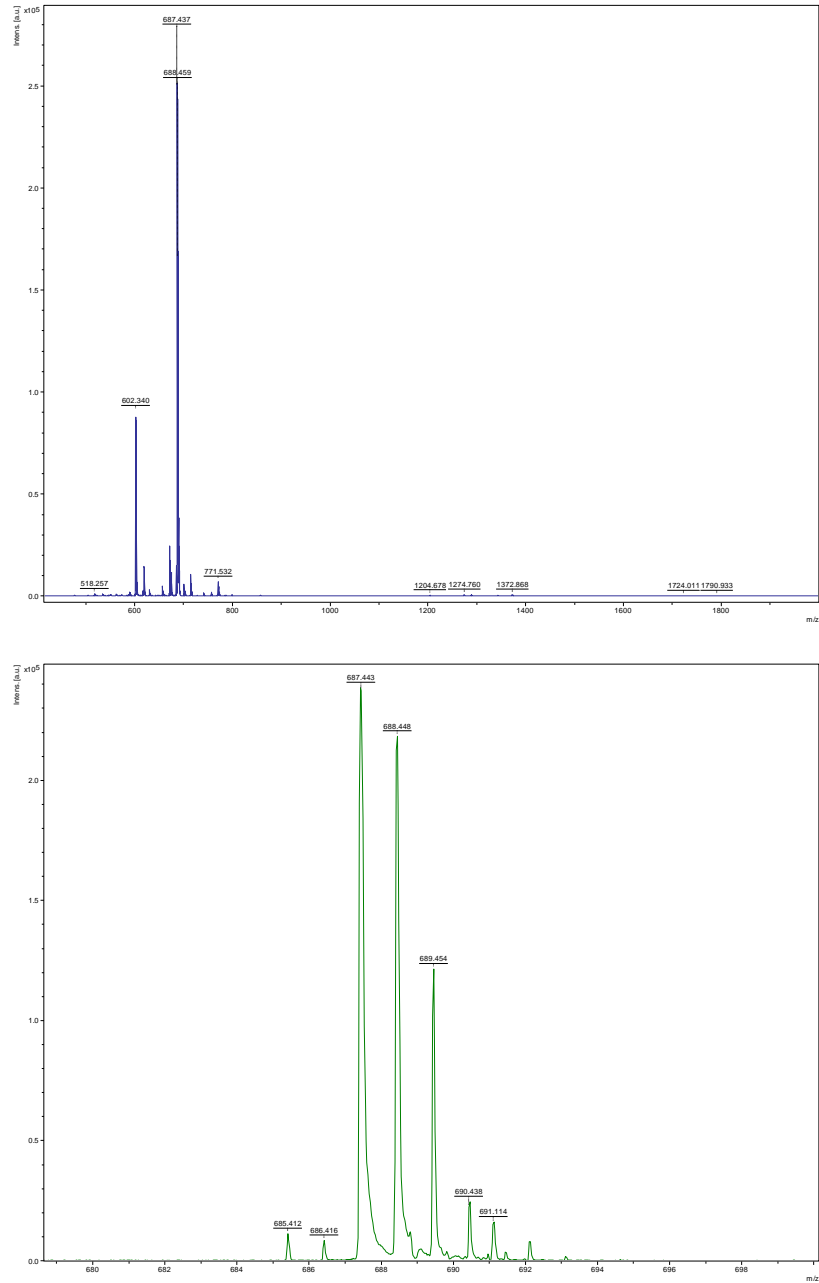


Figure 1. MALDI-TOF-MS spectra in wide and narrow mass ranges of KR122.

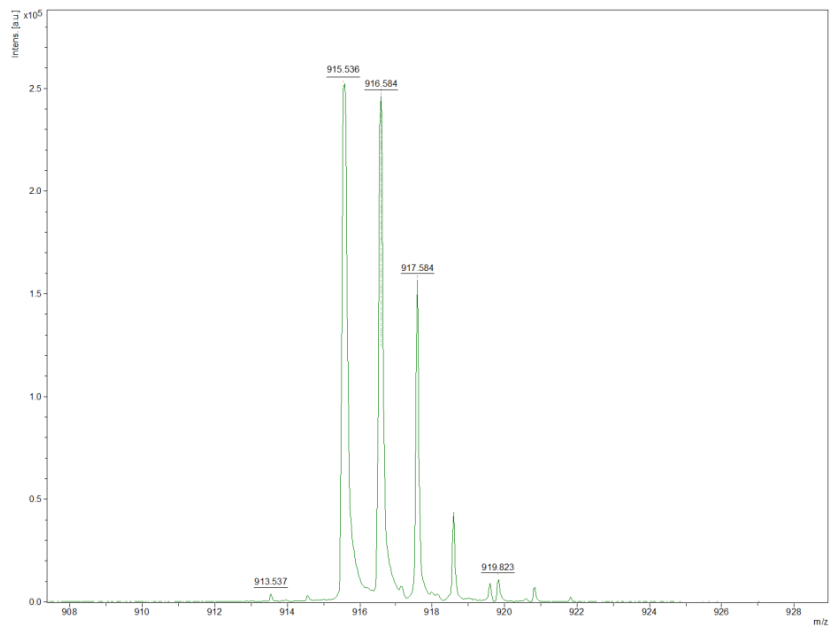
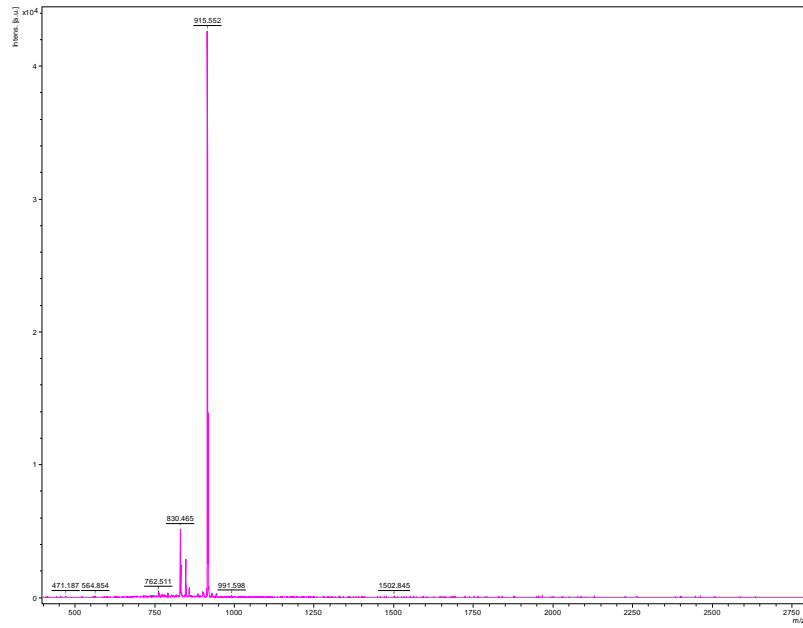


Figure 2. MALDI-TOF-MS spectra in wide and narrow mass ranges of KR131

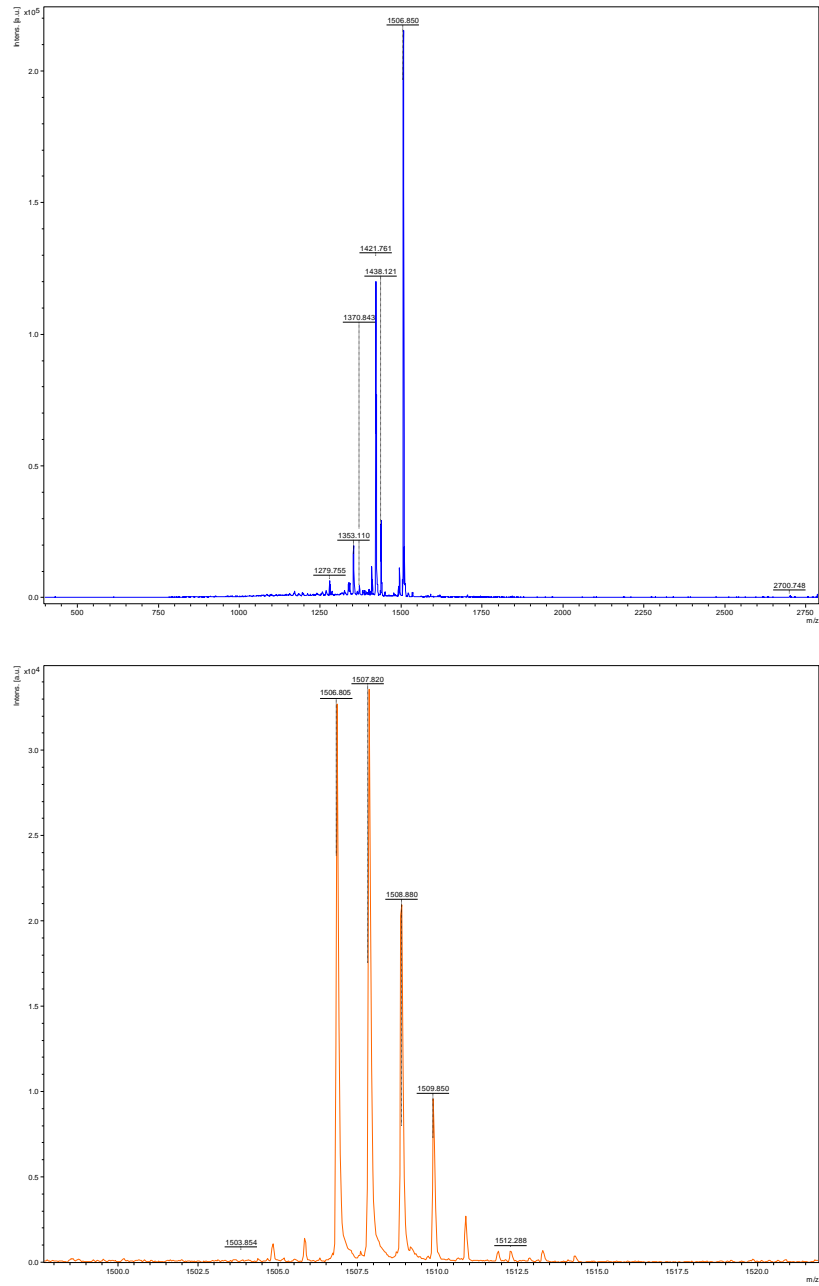


Figure 3. MALDI-TOF-MS spectra in wide and narrow mass ranges of KR133.

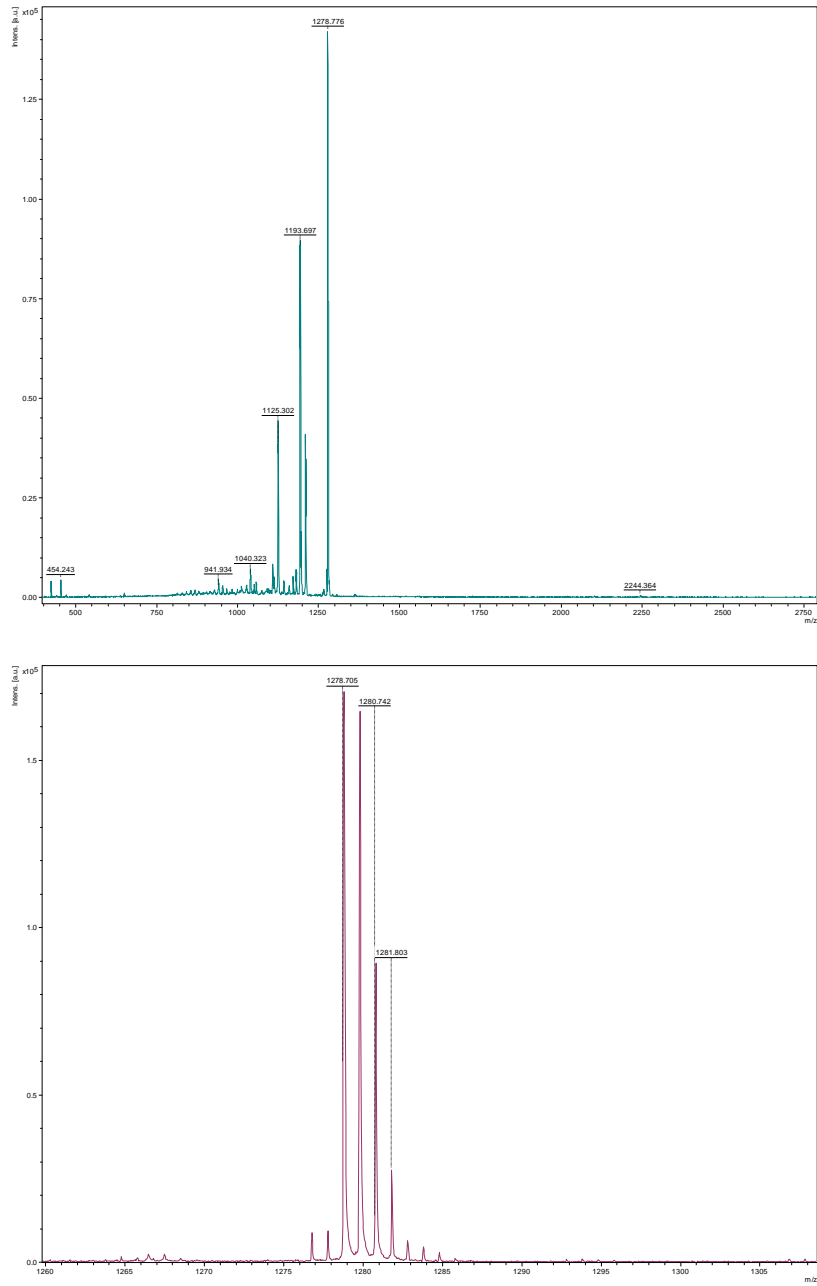


Figure 4. MALDI-TOF-MS spectra in wide and narrow mass ranges of KR145.

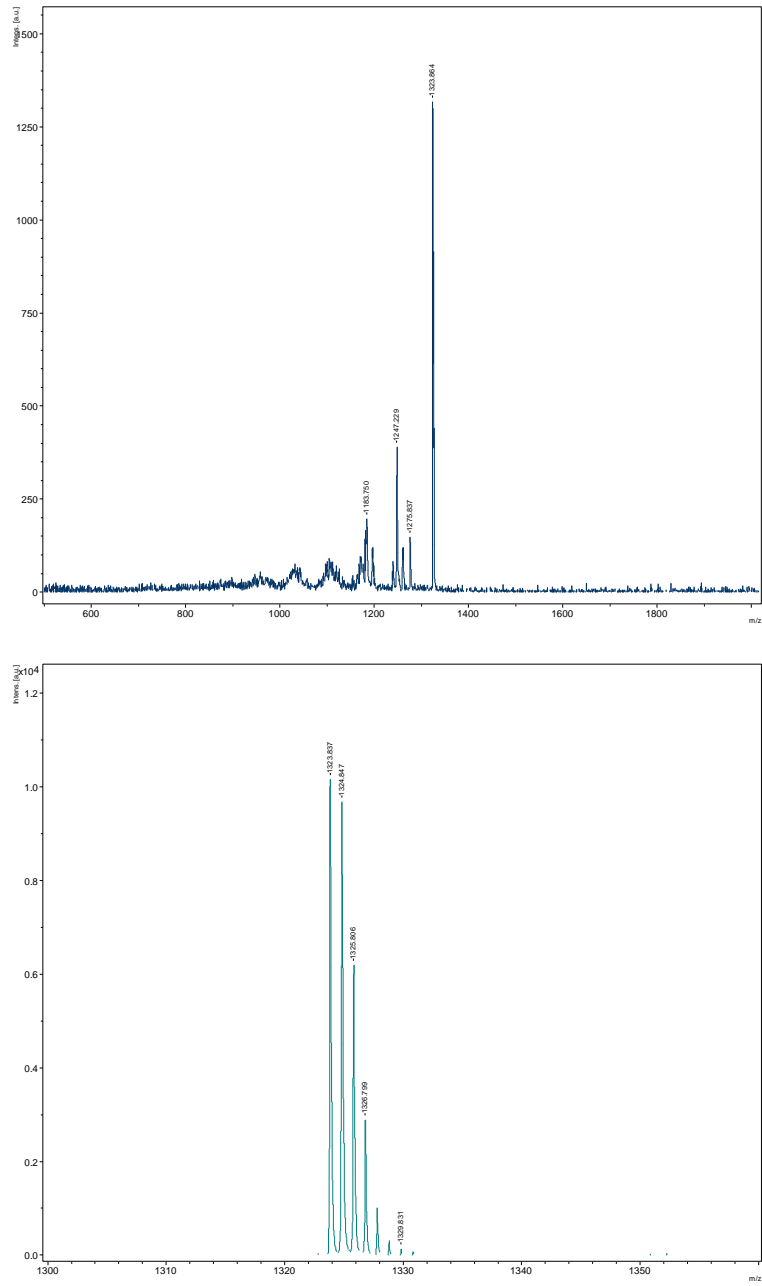


Figure 5. MALDI-TOF-MS spectra in wide and narrow mass ranges of KR355.

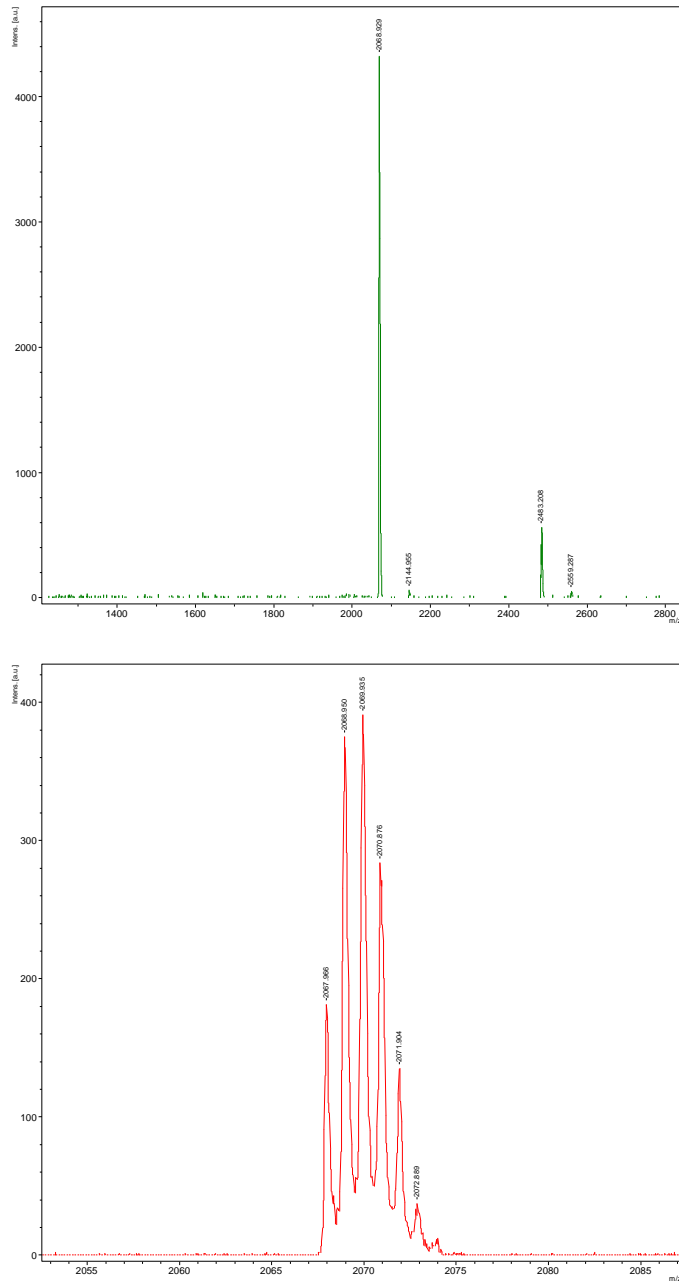


Figure 6. MALDI-TOF-MS spectra in wide and narrow mass ranges of KR321.

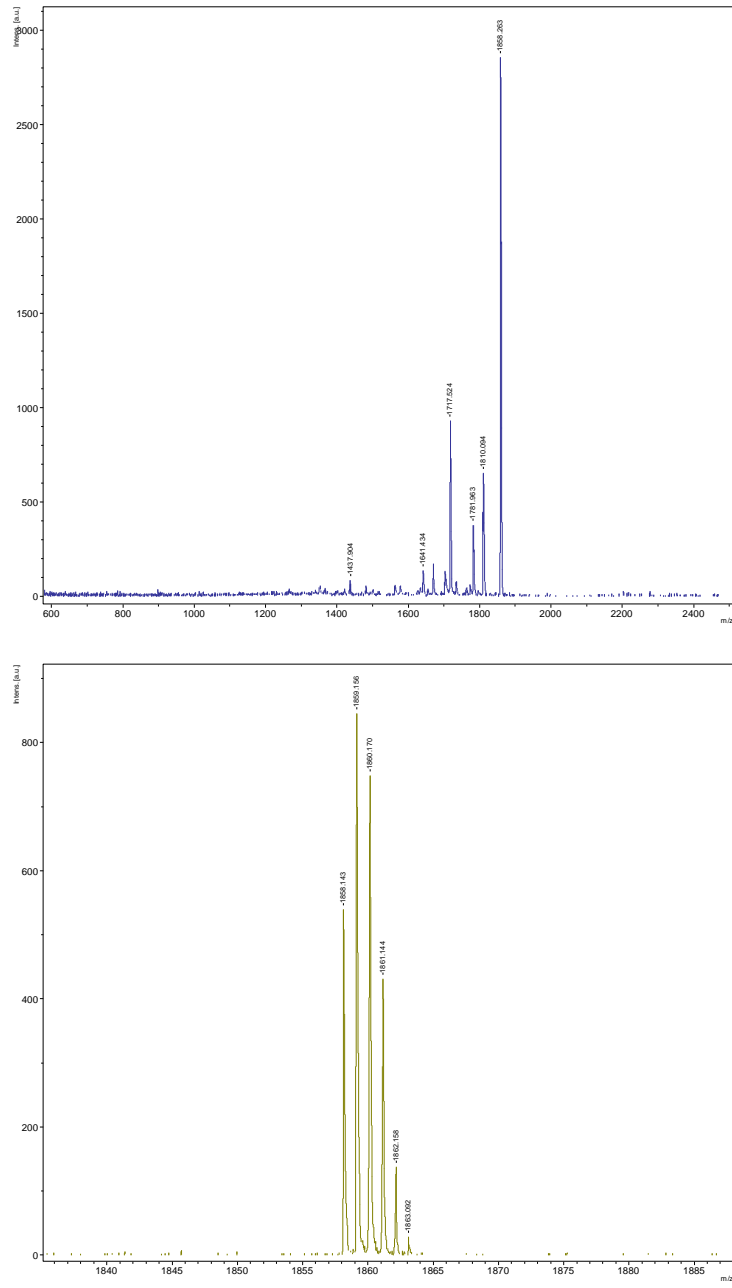


Figure 7. MALDI-TOF-MS spectra in wide and narrow mass ranges of KR353.

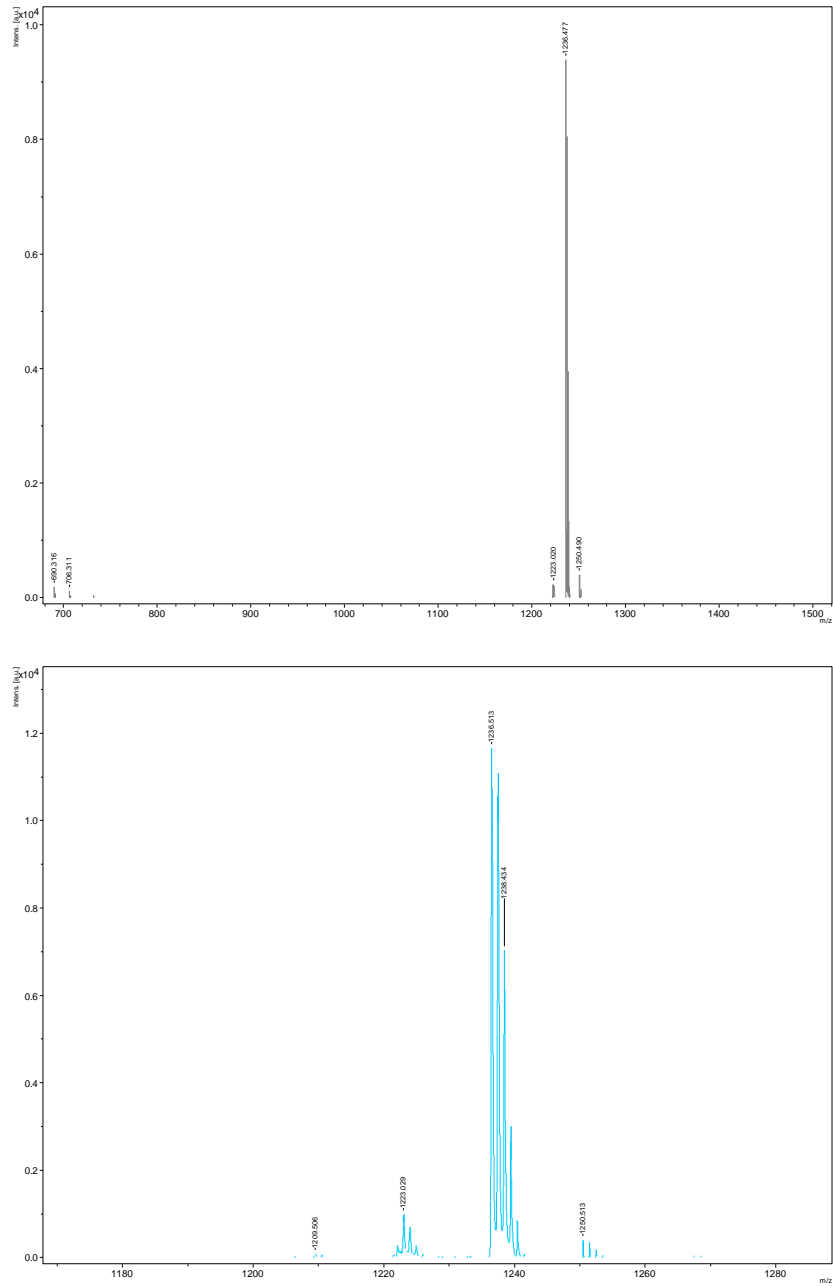


Figure 8. MALDI-TOF-MS spectra in wide and narrow mass ranges of KR216.

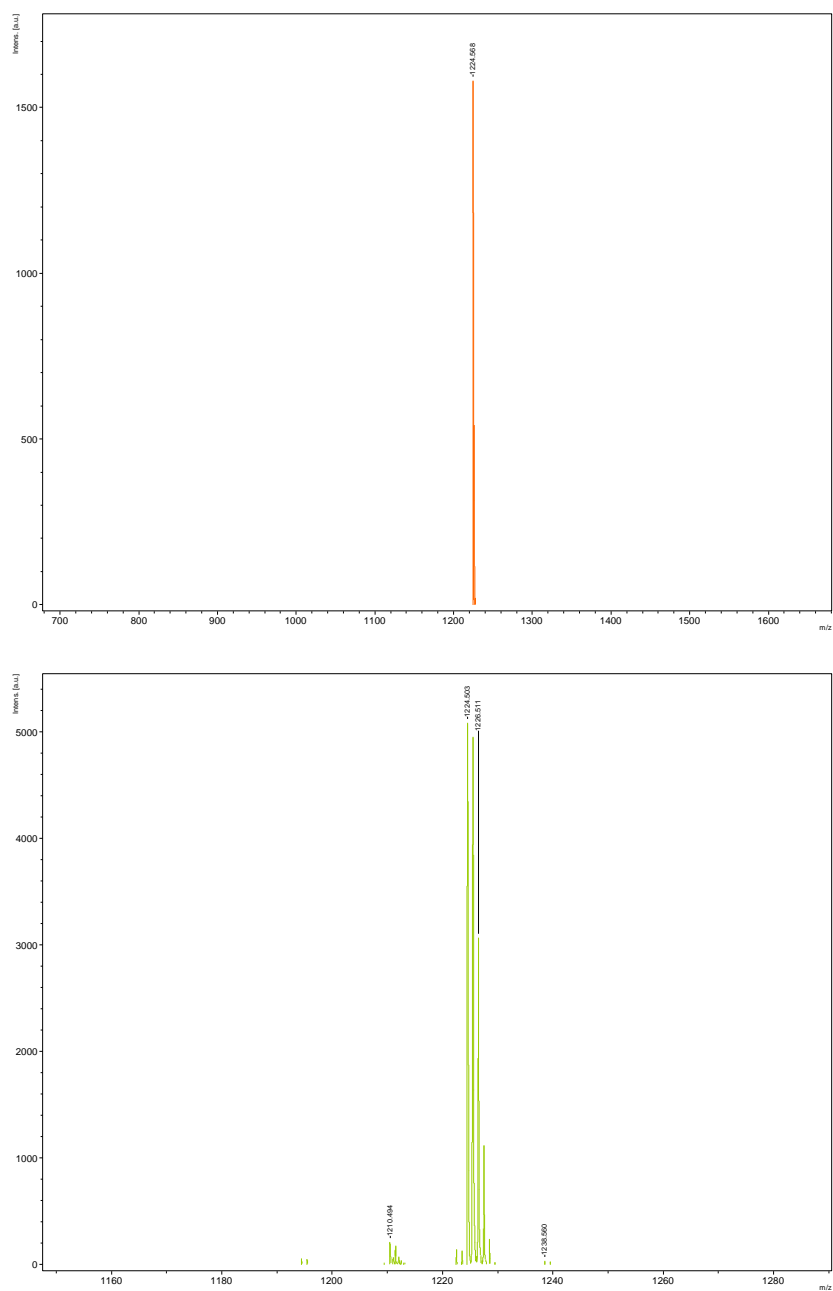


Figure 9. MALDI-TOF-MS spectra in wide and narrow mass ranges of spiro-OMeTAD.

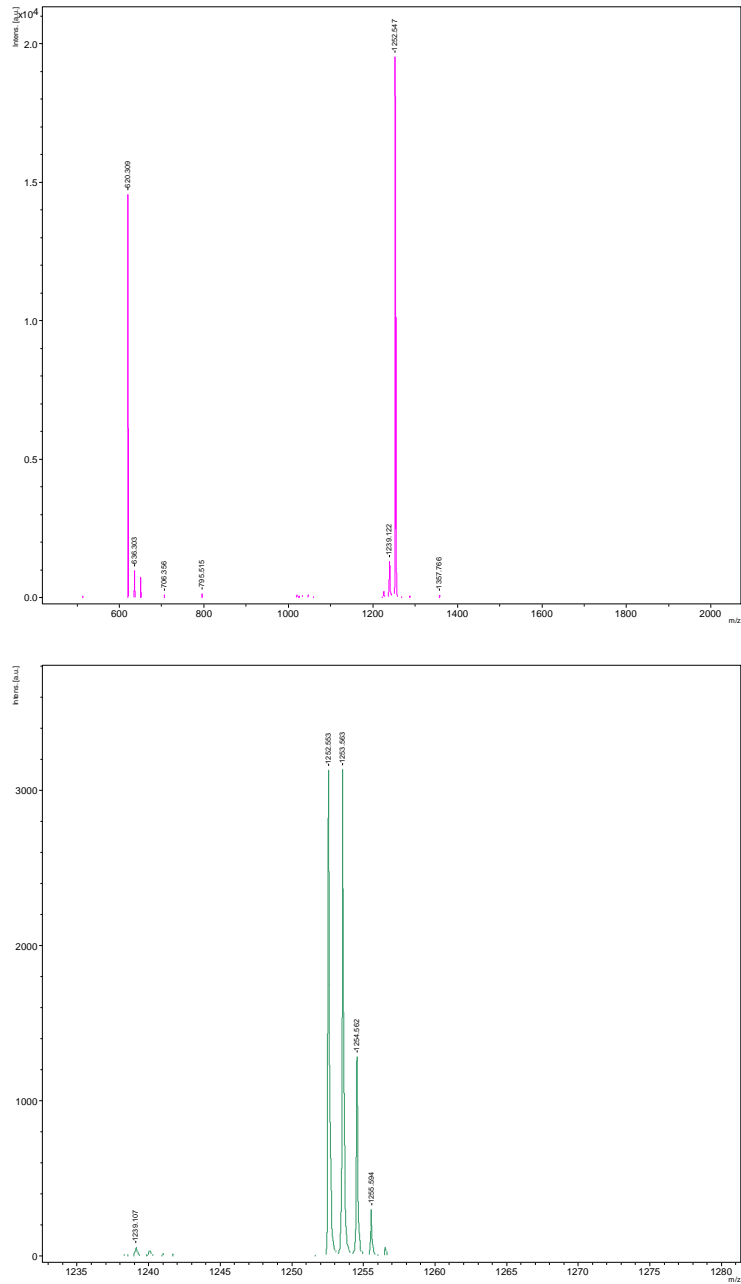


Figure 10. MALDI-TOF-MS spectra in wide and narrow mass ranges of KR378.

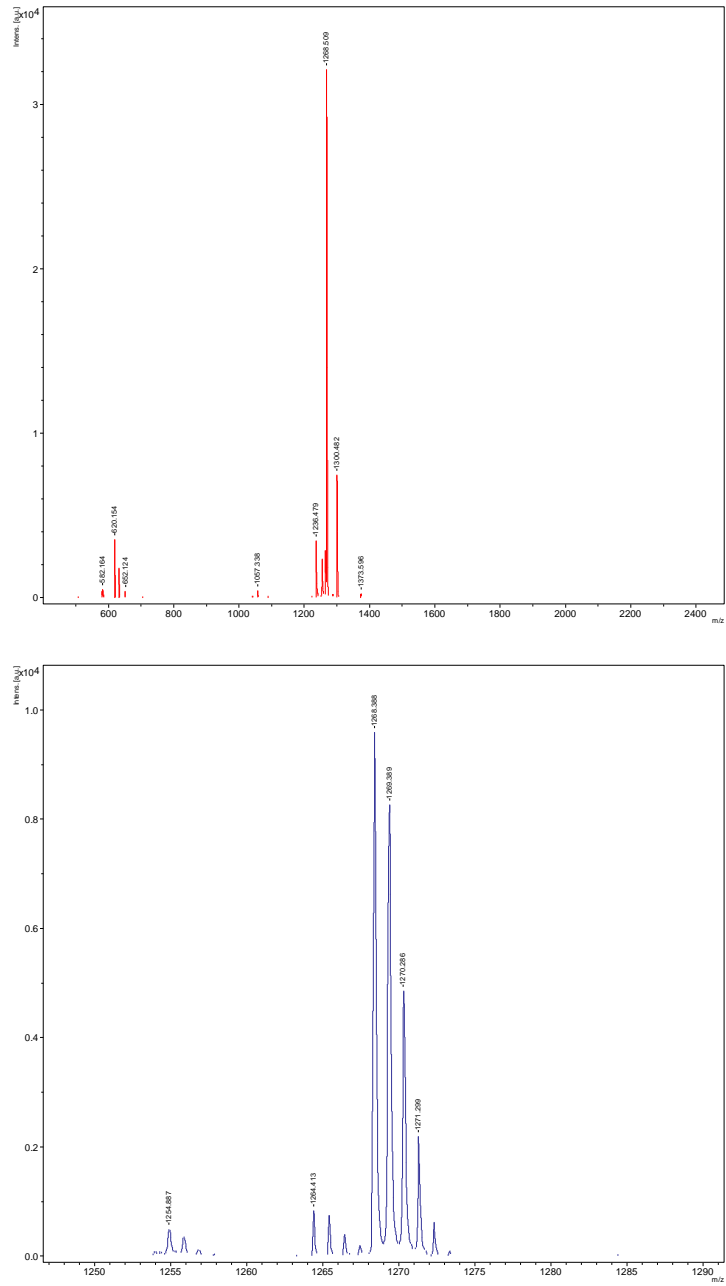


Figure 11. MALDI-TOF-MS spectra in wide and narrow mass ranges of KR374.

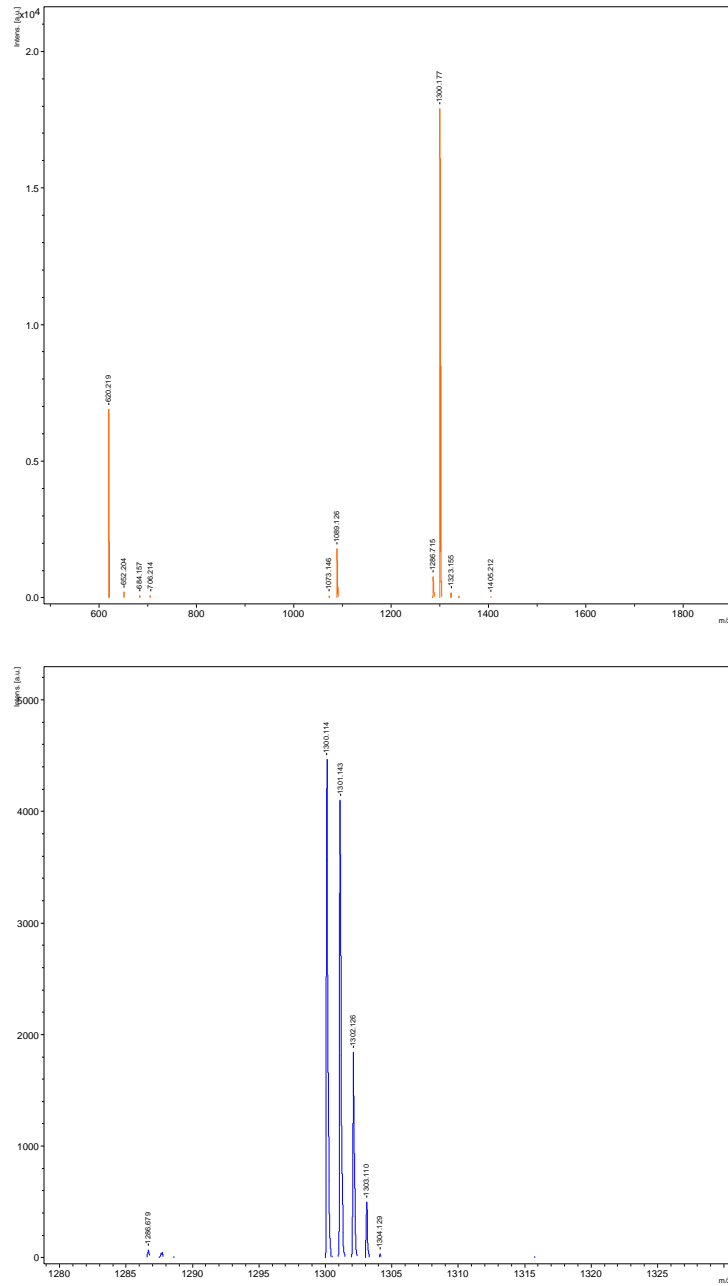


Figure 12. MALDI-TOF-MS spectra in wide and narrow mass ranges of KR360.

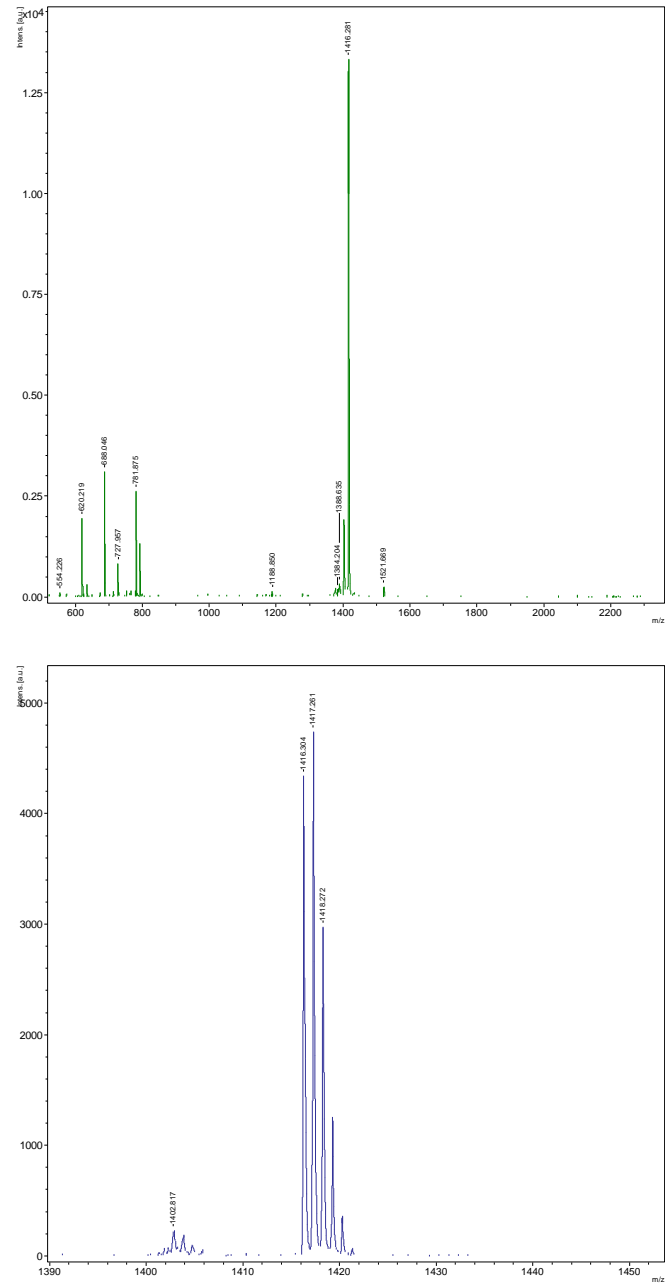


Figure 13. MALDI-TOF-MS spectra in wide and narrow mass ranges of DDOF.

Crystallographic Parameters

CCDC-1458043 contains the supplementary crystallographic data for KR216 and CCDC-1495258 for DDOF, respectively. These data can be obtained free of charge from The Cambridge Crystallographic Data Centre via www.ccdc.cam.ac.uk/data_request/cif.

	KR216	DDOF	spiro-OMeTAD
Empirical formula	C ₈₂ H ₆₈ N ₄ O ₈	C ₉₀ H ₇₂ N ₄ O ₉ S ₂	C ₈₁ H ₆₈ N ₄ O ₈
Formula weight	1237.466	1417.71	1225.455
Crystal color, habit	Black, flake	Colorless, needle	Colorless, needle
Crystal system	triclinic	monoclinic	triclinic
a, Å	15.138(4)	25.4756(19)	13.1111(7)
b, Å	18.448(5)	16.5543(11)	16.1465(7)
c, Å	24.293(6)	19.5340(13)	16.9214(9)
α, deg	72.737(14)	90	75.200(4)
β, deg	73.732(15)	107.428(8)	85.670(4)
γ, deg	89.445(15)	90	75.891(4)
V, Å ³	6199.21(3)	7859.91(1)	3358.57
ρ calc, g/cm ³	1.32574	1.19792	1.267
Space group	P 1	<i>P</i> 1 21/ <i>c</i> 1 (14)	P -1
Z value	4	4	2
Temperature, K	120	293 K	140
no. of reflections measured	20106	16089	23601
no. of variables	1613	1090	909
Residuals: R; wR2	0.1501, 0.3827	0.0891, 0.2758	0.0419, 0.1068

Crystallographic parameters of KR216, DDOF, and spiro-OMeTAD.

Acknowledgements

First of all, I would like to thank my supervisors Prof. Md. K. Nazeeruddin and Prof. M. Grätzel for providing me a chance to come to EPFL and opportunity to work in their multidisciplinary research groups on such booming topic as perovskite solar cells. Special words go to Nazeer for giving me a freedom for the research, but at the same time keeping me continuously busy, putting the pressure and challenging to solve all the problems individually. After 4 years, I can tell that this turned to the very successful results as well as significantly improved my professional and personal development. Thank you for your supervision!

I would like to thank Prof. H. Girault, Prof. A. Hagfeldt, Prof. G. Pozzi, and Prof. T. Torres for being a part of the jury and proofreading the thesis.

Sincere thanks go to all colleagues from GMF team for fruitful collaboration, scientific discussions, and all the help and support over my doctoral stay, I am looking forward to have a good time together in the future.

There are several important people who guided me towards a PhD and have to be thanked here. The first is Prof. V. Getautis, who offered to come to his lab and start the research work at the very early years of my bachelor, this motivated me a lot. I thank him for all helpful advice throughout undergraduate projects and giving the chance to feel the science when I had no clue what it is. My mentors Dr. M. Daskeviciene and Dr. T. W. Holcombe are greatly acknowledged for their unforgettable support and all professional advice. These are the people who showed me all the tricks in the lab and formed my skills and experience doing organic synthesis. Finally, I would like to thank my high school chemistry teacher S. Gustiene, who sparked my interest in organic chemistry. Without her, I would probably have never been turned to study chemistry.

I must thank my family for a level of understanding, encouragement, and support throughout all my life.

Thank you all!

References

- 1 N. S. Lewis and D. G. Nocera, *Proc. Natl. Acad. Sci.*, 2006, **103**, 15729–15735.
- 2 B. Kippelen and J.-L. Brédas, *Energy Environ. Sci.*, 2009, **2**, 251–261.
- 3 Y.-B. Cheng, A. Pascoe, F. Huang and Y. Peng, *Nature*, 2016, **539**, 488–489.
- 4 B. O'Regan and M. Grätzel, *Nature*, 1991, **353**, 737–740.
- 5 C.-Y. Hsu, Y.-C. Chen, R. Y.-Y. Lin, K.-C. Ho and J. T. Lin, *Phys. Chem. Chem. Phys.*, 2012, **14**, 14099.
- 6 S. Mathew, A. Yella, P. Gao, R. Humphry-Baker, B. F. E. Curchod, N. Ashari-Astani, I. Tavernelli, U. Rothlisberger, M. K. Nazeeruddin and M. Grätzel, *Nat. Chem.*, 2014, **6**, 242–247.
- 7 J. Burschka, A. Dualeh, F. Kessler, E. Baranoff, N. L. Cevey-Ha, C. Yi, M. K. Nazeeruddin and M. Grätzel, *J. Am. Chem. Soc.*, 2011, **133**, 18042–18045.
- 8 A. Kojima, K. Teshima, Y. Shirai and T. Miyasaka, *J. Am. Chem. Soc.*, 2009, **131**, 6050–6051.
- 9 J. Burschka, N. Pellet, S.-J. Moon, R. Humphry-Baker, P. Gao, M. K. Nazeeruddin and M. Grätzel, *Nature*, 2013, **499**, 316–319.
- 10 M. Liu, M. B. Johnston and H. J. Snaith, *Nature*, 2013, **501**, 395–398.
- 11 N. J. Jeon, J. H. Noh, Y. C. Kim, W. S. Yang, S. Ryu and S. Il Seok, *Nat. Mater.*, 2014, **13**, 897–903.
- 12 H. Zhou, Q. Chen, G. Li, S. Luo, T. -b. Song, H.-S. Duan, Z. Hong, J. You, Y. Liu and Y. Yang, *Science*, 2014, **345**, 542–546.
- 13 A. R. B. M. Yusoff and M. K. Nazeeruddin, *J. Phys. Chem. Lett.*, 2016, **7**, 851–866.
- 14 D. B. Mitzi, C. A. Feild, W. T. A. Harrison and A. M. Guloy, *Nature*, 1994, **369**, 467–469.
- 15 D. B. Mitzi, S. Wang, C. A. Feild, C. A. Chess and A. M. Guloy, *Science*, 1995, **267**, 1473–1476.
- 16 C. R. Kagan, *Science*, 1999, **286**, 945–947.
- 17 K. Chondroudis and D. B. Mitzi, *Chem. Mater.*, 1999, **11**, 3028–3030.
- 18 S. J. Yoon, K. G. Stamplecoskie and P. V. Kamat, *J. Phys. Chem. Lett.*, 2016, **7**, 1368–1373.
- 19 C. C. Stoumpos and M. G. Kanatzidis, *Adv. Mater.*, 2016, **28**, 5778–5793.
- 20 D. B. Mitzi, in *Progress in Inorganic Chemistry*, John Wiley & Sons, Inc., 1999, pp. 1–121.

- 21 T. Baikie, Y. Fang, J. M. Kadro, M. Schreyer, F. Wei, S. G. Mhaisalkar, M. Graetzel and T. J. White, *J. Mater. Chem. A*, 2013, **1**, 5628.
- 22 N. Pellet, P. Gao, G. Gregori, T. Y. Yang, M. K. Nazeeruddin, J. Maier and M. Gratzel, *Angew. Chemie - Int. Ed.*, 2014, **53**, 3151–3157.
- 23 N. J. Jeon, J. H. Noh, W. S. Yang, Y. C. Kim, S. Ryu, J. Seo and S. Il Seok, *Nature*, 2015, **517**, 476–480.
- 24 M. Saliba, T. Matsui, J.-Y. Seo, K. Domanski, J.-P. Correa-Baena, M. K. Nazeeruddin, S. M. Zakeeruddin, W. Tress, A. Abate, A. Hagfeldt and M. Grätzel, *Energy Environ. Sci.*, 2016, **9**, 1989–1997.
- 25 Q. Ling, W. Huang, A. Baldwin and P. Jarvis, *Science*, 2012, **338**, 655–659.
- 26 L. Etgar, P. Gao, Z. Xue, Q. Peng, A. K. Chandiran, B. Liu, M. K. Nazeeruddin and M. Gratzel, *J. Am. Chem. Soc.*, 2012, **134**, 17396–17399.
- 27 K.-C. Wang, J.-Y. Jeng, P.-S. Shen, Y.-C. Chang, E. W.-G. Diao, C.-H. Tsai, T.-Y. Chao, H.-C. Hsu, P.-Y. Lin, P. Chen, T.-F. Guo and T.-C. Wen, *Sci. Rep.*, 2015, **4**, 4756.
- 28 J. H. Kim, P. W. Liang, S. T. Williams, N. Cho, C. C. Chueh, M. S. Glaz, D. S. Ginger and A. K. Y. Jen, *Adv. Mater.*, 2015, **27**, 695–701.
- 29 S. S. Mali and C. K. Hong, *Nanoscale*, 2016, **8**, 10528–10540.
- 30 C. Momblona, L. Gil-Escrig, E. Bandiello, E. M. Hutter, M. Sessolo, K. Lederer, J. Blochwitz-Nimoth and H. J. Bolink, *Energy Environ. Sci.*, 2016, **9**, 3456–3463.
- 31 Z. Liu, A. Zhu, F. Cai, L. Tao, Y. Zhou, Z. Zhao, Q. Chen, Y.-B. Cheng and H. Zhou, *J. Mater. Chem. A*, 2017, **5**, 6597–6605.
- 32 D. Liu, J. Yang and T. L. Kelly, *J. Am. Chem. Soc.*, 2014, **136**, 17116–17122.
- 33 L. Etgar, in *SpringerBriefs in Applied Sciences and Technology*, Springer, Cham, 2016, pp. 9–24.
- 34 X. Zhou, C. Bao, F. Li, H. Gao, T. Yu, J. Yang, W. Zhu and Z. Zou, *RSC Adv.*, 2015, **5**, 58543–58548.
- 35 G. Grancini, C. Roldán-Carmona, I. Zimmermann, E. Mosconi, X. Lee, D. Martineau, S. Narbey, F. Oswald, F. De Angelis, M. Graetzel and M. K. Nazeeruddin, *Nat. Commun.*, 2017, **8**, 15684.
- 36 W. S. Yang, B.-W. Park, E. H. Jung, N. J. Jeon, Y. C. Kim, D. U. Lee, S. S. Shin, J. Seo, E. K. Kim, J. H. Noh and S. Il Seok, *Science*, 2017, **356**, 1376–1379.
- 37 P. E. Shaw, A. Ruseckas and I. D. W. Samuel, *Adv. Mater.*, 2008, **20**, 3516–3520.
- 38 L. De León and G. Chalar, *Limnetica*, 2003, **22**, 103–113.
- 39 J. H. Noh, S. H. Im, J. H. Heo, T. N. Mandal and S. Il Seok, *Nano Lett.*, 2013, **13**, 1764–1769.
- 40 N. J. Jeon, H. G. Lee, Y. C. Kim, J. Seo, J. H. Noh, J. Lee and S. Il Seok, *J. Am. Chem. Soc.*, 2014, **136**, 7837–7840.

-
- 41 J. C. Mauro, *Am. Ceram. Soc. Bull.*, 2011, **90**, 31–37.
- 42 K. Mahmood, S. Sarwar and M. T. Mehran, *RSC Adv.*, 2017, **7**, 17044–17062.
- 43 G. Yang, H. Tao, P. Qin, W. Ke and G. Fang, *J. Mater. Chem. A*, 2016, **4**, 3970–3990.
- 44 H. Liu, Z. Huang, S. Wei, L. Zheng, L. Xiao and Q. Gong, *Nanoscale*, 2016, **8**, 6209–6221.
- 45 H. Tang, F. Lévy, H. Berger and P. E. Schmid, *Phys. Rev. B*, 1995, **52**, 7771–7774.
- 46 L. Kavan and M. Grätzel, *Electrochim. Acta*, 1995, **40**, 643–652.
- 47 Y. Yang, J. You, Z. Hong, Q. Chen, M. Cai, T. Bin Song, C. C. Chen, S. Lu, Y. Liu and H. Zhou, *ACS Nano*, 2014, **8**, 1674–1680.
- 48 O. Malinkiewicz, A. Yella, Y. H. Lee, G. M. Espallargas, M. Graetzel, M. K. Nazeeruddin and H. J. Bolink, *Nat. Photonics*, 2013, **8**, 128–132.
- 49 C.-H. Chiang, Z.-L. Tseng and C.-G. Wu, *J. Mater. Chem. A*, 2014, **2**, 15897–15903.
- 50 Q. Wang, Y. Shao, Q. Dong, Z. Xiao, Y. Yuan and J. Huang, *Energy Environ. Sci.*, 2014, **7**, 2359–2365.
- 51 Y. Xie, F. Shao, Y. Wang, T. Xu, D. Wang and F. Huang, *ACS Appl. Mater. Interfaces*, 2015, **7**, 12937–12942.
- 52 T. Zhang, M. Yang, Y. Zhao and K. Zhu, *Nano Lett.*, 2015, **15**, 3959–3963.
- 53 G. Longo, L. Gil-Escrig, M. J. Degen, M. Sessolo and H. J. Bolink, *Chem. Commun.*, 2015, **51**, 7376–7378.
- 54 C. Gao, J. Liu, C. Liao, Q. Ye, Y. Zhang, X. He, X. Guo, J. Mei and W. Lau, *RSC Adv.*, 2015, **5**, 26175–26180.
- 55 J. Teuscher, A. Ulianov, O. Mantener, M. Gratzel and N. Tetreault, *ChemSusChem*, 2015, **8**, 3847–3852.
- 56 Q. Chen, H. Zhou, Z. Hong, S. Luo, H. S. Duan, H. H. Wang, Y. Liu, G. Li and Y. Yang, *J. Am. Chem. Soc.*, 2014, **136**, 622–625.
- 57 R. Sheng, A. Ho-Baillie, S. Huang, S. Chen, X. Wen, X. Hao and M. A. Green, *J. Phys. Chem. C*, 2015, **119**, 3545–3549.
- 58 S. Ameen, M. A. Rub, S. A. Kosa, K. A. Alamry, M. S. Akhtar, H. S. Shin, H. K. Seo, A. M. Asiri and M. K. Nazeeruddin, *ChemSusChem*, 2016, **9**, 10–27.
- 59 T. Swetha and S. P. Singh, *J. Mater. Chem. A*, 2015, **3**, 18329–18344.
- 60 Z. Yu and L. Sun, *Adv. Energy Mater.*, 2015, 1500213.
- 61 W. Yan, S. Ye, Y. Li, W. Sun, H. Rao, Z. Liu, Z. Bian and C. Huang, *Adv. Energy Mater.*, 2016, 1600474.
- 62 Z. H. Bakr, Q. Wali, A. Fakharuddin, L. Schmidt-Mende, T. M. Brown and R. Jose, *Nano Energy*, 2017, **34**, 271–305.
- 63 A. Krishna and A. C. Grimsdale, *J. Mater. Chem. A*, 2017, **5**, 16446–16466.

- 64 Y. Yu and P. Gao, *Chinese Chem. Lett.*, 2017, **28**, 1144–1152.
- 65 F. Ullah, H. Chen and C.-Z. Li, *Chinese Chem. Lett.*, 2017, **28**, 503–511.
- 66 C. H. Teh, R. Daik, E. L. Lim, C. C. Yap, M. A. Ibrahim, N. A. Ludin, K. Sopian and M. A. Mat Teridi, *J. Mater. Chem. A*, 2016, **4**, 15788–15822.
- 67 Y. K. Wang, Z. Q. Jiang and L. S. Liao, *Chinese Chem. Lett.*, 2016, **27**, 1293–1303.
- 68 A. Gheno, S. Vedraïne, B. Ratier and J. Bouclé, *Metals*, 2016, **6**, 21.
- 69 L. Dongxue and Y. Liu, *J. Semicond.*, 2017, **38**, 11005.
- 70 P. P. Zhang, Z. J. Zhou, D. X. Kou and S. X. Wu, *Int. J. Photoenergy*, 2017, **2017**, 1–10.
- 71 S. Ito, in *Organic-Inorganic Halide Perovskite Photovoltaics: From Fundamentals to Device Architectures*, Springer International Publishing, Cham, 2016, pp. 343–366.
- 72 R. Rajeswari, M. Mrinalini, S. Prasanthkumar and L. Giribabu, *Chem. Rec.*, 2017, **17**, 681–699.
- 73 U. Bach, D. Lupo, P. Comte, J. E. Moser, F. Weissörtel, J. Salbeck, H. Spreitzer and M. Grätzel, *Nature*, 1998, **395**, 583–585.
- 74 A. Mei, X. Li, L. Liu, Z. Ku, T. Liu, Y. Rong, M. Xu, M. Hu, J. Chen, Y. Yang, M. Gratzel and H. Han, *Science*, 2014, **345**, 295–298.
- 75 W. S. Yang, J. H. Noh, N. J. Jeon, Y. C. Kim, S. Ryu, J. Seo and S. I. Seok, *Science*, 2015, **348**, 1234–1237.
- 76 M. Jung, Y. C. Kim, N. J. Jeon, W. S. Yang, J. Seo, J. H. Noh and S. Il Seok, *ChemSusChem*, 2016, **9**, 2592–2596.
- 77 V. E. Madhavan, I. Zimmermann, C. Roldán-Carmona, G. Grancini, M. Buffiere, A. Belaidi and M. K. Nazeeruddin, *ACS Energy Lett.*, 2016, **1**, 1112–1117.
- 78 P. Qin, S. Tanaka, S. Ito, N. Tetreault, K. Manabe, H. Nishino, M. K. Nazeeruddin and M. Grätzel, *Nat. Commun.*, 2014, **5**, 3834.
- 79 H. Zhang, H. Wang, W. Chen and A. K. Y. Jen, *Adv. Mater.*, 2017, **29**, 1–8.
- 80 S. G. Hashmi, D. Martineau, M. I. Dar, T. T. T. Myllymäki, T. Sarikka, V. Ulla, S. M. Zakeeruddin and M. Grätzel, *J. Mater. Chem. A*, 2017, **5**, 12060–12067.
- 81 F. Behrouznejad, C. M. Tsai, S. Narra, E. W. G. Diau and N. Taghavinia, *ACS Appl. Mater. Interfaces*, 2017, **9**, 25204–25215.
- 82 W. Tress, N. Marinova, T. Moehl, S. M. Zakeeruddin, M. K. Nazeeruddin and M. Grätzel, *Energy Environ. Sci.*, 2015, **8**, 995–1004.
- 83 E. L. Unger, E. T. Hoke, C. D. Bailie, W. H. Nguyen, A. R. Bowring, T. Heumüller, M. G. Christoforo and M. D. McGehee, *Energy Environ. Sci.*, 2014, **7**, 3690–3698.
- 84 J. M. Frost, K. T. Butler and A. Walsh, *APL Mater.*, 2014, **2**, 81506.
- 85 V. W. Bergmann, S. A. L. Weber, F. Javier Ramos, M. K. Nazeeruddin, M. Grätzel, D. Li, A. L. Domanski, I. Lieberwirth, S. Ahmad and R. Berger, *Nat. Commun.*, 2014, **5**, 5001.

-
- 86 C. Eames, J. M. Frost, P. R. F. Barnes, B. C. O'Regan, A. Walsh and M. S. Islam, *Nat. Commun.*, 2015, **6**, 7497.
- 87 A. Mishra and P. Bäuerle, *Angew. Chemie - Int. Ed.*, 2012, **51**, 2020–2067.
- 88 J. D. Myers and J. Xue, *Polym. Rev.*, 2012, **52**, 1–37.
- 89 Y. Yamashita, *Sci. Technol. Adv. Mater.*, 2009, **10**, 24313.
- 90 G. R. Hutchison, M. A. Ratner and T. J. Marks, *J. Am. Chem. Soc.*, 2005, **127**, 16866–16881.
- 91 S. R. Forrest, *Chem. Rev.*, 1997, **97**, 1793–1896.
- 92 V. Coropceanu, J. Cornil, D. A. da Silva Filho, Y. Olivier, R. Silbey and J. L. Brédas, *Chem. Rev.*, 2007, **107**, 926–952.
- 93 F. Wu, Y. Ji, C. Zhong, Y. Liu, L. Tan and L. Zhu, *Chem. Commun.*, 2017, **53**, 8719–8722.
- 94 G. Wu, Y. Zhang, R. Kaneko, Y. Kojima, Q. Shen, A. Islam, K. Sugawa and J. Otsuki, *J. Phys. Chem. C*, 2017, **121**, 17617–17624.
- 95 K. Do, H. Choi, K. Lim, H. Jo, J. W. Cho, M. K. Nazeeruddin and J. Ko, *Chem. Commun.*, 2014, **50**, 10971–10974.
- 96 F. Bureš, *RSC Adv.*, 2014, **4**, 58826–58851.
- 97 I. Salzmann, G. Heimel, M. Oehzelt, S. Winkler and N. Koch, *Acc. Chem. Res.*, 2016, **49**, 370–378.
- 98 J. M. Kim, S. J. Yoo, C. K. Moon, B. Sim, J. H. Lee, H. Lim, J. W. Kim and J. J. Kim, *J. Phys. Chem. C*, 2016, **120**, 9475–9481.
- 99 B. Lüssem, M. Riede and K. Leo, *Phys. Status Solidi Appl. Mater. Sci.*, 2013, **210**, 9–43.
- 100 K. Walzer, B. Maennig, M. Pfeiffer and K. Leo, *Chem. Rev.*, 2007, **107**, 1233–1271.
- 101 M. A. Mahmud, N. K. Elumalai, M. B. Upama, D. Wang, V. R. Gonçalves, M. Wright, C. Xu, F. Haque and A. Uddin, *Phys. Chem. Chem. Phys.*, 2017, **19**, 21033–21045.
- 102 G. Gong, N. Zhao, J. Li, F. Li, J. Chen, Y. Shen, M. Wang and G. Tu, *Org. Electron. physics, Mater. Appl.*, 2016, **35**, 171–175.
- 103 J. Luo, C. Jia, Z. Wan, F. Han, B. Zhao and R. Wang, *J. Power Sources*, 2017, **342**, 886–895.
- 104 Q. Liu, L. Fan, Q. Zhang, A. Zhou, B. Wang, H. Bai, Q. Tian, B. Fan and T. Zhang, *ChemSusChem*, 2017, **10**, 3098–3104.
- 105 C. Chen, W. Zhang, J. Cong, M. Cheng, B. Zhang, H. Chen, P. Liu, R. Li, M. Safdari, L. Kloo and L. Sun, *ACS Energy Lett.*, 2017, **2**, 497–503.
- 106 N. Onozawa-Komatsuzaki, T. Funaki, T. N. Murakami, S. Kazaoui, M. Chikamatsu and K. Sayama, *Electrochemistry*, 2017, **85**, 226–230.
- 107 J. Burschka, F. Kessler, M. K. Nazeeruddin and M. Grätzel, *Chem. Mater.*, 2013, **25**, 2986–2990.
- 108 Z. Hawash, L. K. Ono and Y. Qi, *Adv. Mater. Interfaces*, 2016, **3**, 1600117.

- 109 H. Xi, S. Tang, X. Ma, J. Chang, D. Chen, Z. Lin, P. Zhong, H. Wang and C. Zhang, *ACS Omega*, 2017, **2**, 326–336.
- 110 E. J. Juarez-Perez, M. R. Leyden, S. Wang, L. K. Ono, Z. Hawash and Y. Qi, *Chem. Mater.*, 2016, **28**, 5702–5709.
- 111 A.-N. Cho, H.-S. Kim, T.-T. Bui, X. Sallenave, F. Goubard and N.-G. Park, *RSC Adv.*, 2016, **6**, 68553–68559.
- 112 G. Niu, X. Guo and L. Wang, *J. Mater. Chem. A*, 2015, **3**, 8970–8980.
- 113 T. Leijtens, T. Giovenzana, S. N. Habisreutinger, J. S. Tinkham, N. K. Noel, B. A. Kamino, G. Sadoughi, A. Sellinger and H. J. Snaith, *ACS Appl. Mater. Interfaces*, 2016, **8**, 5981–5989.
- 114 P. Agarwala and D. Kabra, *J. Mater. Chem. A*, 2017, **5**, 1348–1373.
- 115 A. V Vannikov, A. D. Grishina and S. V Novikov, *Russ. Chem. Rev.*, 1994, **63**, 103–123.
- 116 X. Lian, Z. Zhao and D. Cheng, *Mol. Cryst. Liq. Cryst.*, 2017, **648**, 223–235.
- 117 M. Thelakkat, *Macromol. Mater. Eng.*, 2002, **287**, 442–461.
- 118 L. Calió, S. Kazim, M. Grätzel and S. Ahmad, *Angew. Chemie - Int. Ed.*, 2016, **55**, 14522–14545.
- 119 J. Londenberg, T. P. I. Saragi, I. Suske and J. Salbeck, *Adv. Mater.*, 2007, **19**, 4049–4053.
- 120 L. H. Xie, F. Liu, C. Tang, X. Y. Hou, Y. R. Hua, Q. L. Fan and W. Huang, *Org. Lett.*, 2006, **8**, 2787–2790.
- 121 R. G. Clarkson and M. Gomberg, *J. Am. Chem. Soc.*, 1930, **52**, 2881–2891.
- 122 T. P. I. Saragi, T. Spehr, A. Siebert, T. Fuhrmann-Lieker and J. Salbeck, *Chem. Rev.*, 2007, **107**, 1011–1065.
- 123 B. Xu, D. Bi, Y. Hua, P. Liu, M. Cheng, M. Grätzel, L. Kloo, A. Hagfeldt and L. Sun, *Energy Environ. Sci.*, 2016, **9**, 873–877.
- 124 J. Zhang, Y. Hua, B. Xu, L. Yang, P. Liu, M. B. Johansson, N. Vlachopoulos, L. Kloo, G. Boschloo, E. M. J. Johansson, L. Sun and A. Hagfeldt, *Adv. Energy Mater.*, 2016, **6**, 1–9.
- 125 Y. Hua, J. Zhang, B. Xu, P. Liu, M. Cheng, L. Kloo, E. M. J. Johansson, K. Sveinbjörnsson, K. Aitola, G. Boschloo and L. Sun, *Nano Energy*, 2016, **26**, 108–113.
- 126 B. Xu, Z. Zhu, J. Zhang, H. Liu, C. C. Chueh, X. Li and A. K. Y. Jen, *Adv. Energy Mater.*, 2017, **7**, 1700683.
- 127 M. Saliba, S. Orlandi, T. Matsui, S. Aghazada, M. Cavazzini, J.-P. Correa-Baena, P. Gao, R. Scopelliti, E. Mosconi, K.-H. Dahmen, F. De Angelis, A. Abate, A. Hagfeldt, G. Pozzi, M. Graetzel and M. K. Nazeeruddin, *Nat. Energy*, 2016, **1**, 15017.
- 128 Y. Wang, Z. Zhu, C. C. Chueh, A. K. Y. Jen and Y. Chi, *Adv. Energy Mater.*, 2017, **7**, 1700823.
- 129 J. Zhang, B. Xu, L. Yang, C. Ruan, L. Wang, P. Liu, W. Zhang, N. Vlachopoulos, L. Kloo, G. Boschloo, L. Sun, A. Hagfeldt and E. M. J. Johansson, *Adv. Energy Mater.*, 2017, 1701209.

- 130 B. Xu, J. Zhang, Y. Hua, P. Liu, L. Wang, C. Ruan, Y. Li, G. Boschloo, E. M. J. Johansson, L. Kloo, A. Hagfeldt, A. K. Y. Jen and L. Sun, *Chem*, 2017, **2**, 676–687.
- 131 M. S. Kang, S. Do Sung, I. T. Choi, H. Kim, M. Hong, J. Kim, W. I. Lee and H. K. Kim, *ACS Appl. Mater. Interfaces*, 2015, **7**, 22213–22217.
- 132 F. Wu, Y. Shan, J. Qiao, C. Zhong, R. Wang, Q. Song and L. Zhu, *ChemSusChem*, 2017, **10**, 3833–3838.
- 133 C. Lu, I. T. Choi, J. Kim and H. K. Kim, *J. Mater. Chem. A*, 2017, **5**, 20263–20276.
- 134 X. Yin, L. Guan, J. Yu, D. Zhao, C. Wang, N. Shrestha, Y. Han, Q. An, J. Zhou, B. Zhou, Y. Yu, C. R. Grice, R. A. Awni, F. Zhang, J. Wang, R. J. Ellingson, Y. Yan and W. Tang, *Nano Energy*, 2017, **40**, 163–169.
- 135 X. Li, M. Cai, Z. Zhou, K. Yun, F. Xie, Z. Lan, J. Hua and L. Han, *J. Mater. Chem. A*, 2017, **5**, 10480–10485.
- 136 A. Molina-Ontoria, I. Zimmermann, I. Garcia-Benito, P. Gratia, C. Roldan-Carmona, S. Aghazada, M. Graetzel, M. K. Nazeeruddin and N. Martin, *Angew. Chemie - Int. Ed.*, 2016, **55**, 6270–6274.
- 137 I. García-Benito, I. Zimmermann, J. Urieta-Mora, J. Aragón, A. Molina-Ontoria, E. Ortí, N. Martín and M. K. Nazeeruddin, *J. Mater. Chem. A*, 2017, **5**, 8317–8324.
- 138 I. Zimmermann, J. Urieta-Mora, P. Gratia, J. Aragón, G. Grancini, A. Molina-Ontoria, E. Ortí, N. Martín and M. K. Nazeeruddin, *Adv. Energy Mater.*, 2017, **7**, 1–8.
- 139 F. Zhang, Z. Wang, H. Zhu, N. Pellet, J. Luo, C. Yi, X. Liu, H. Liu, S. Wang, X. Li, Y. Xiao, S. M. Zakeeruddin, D. Bi and M. Grätzel, *Nano Energy*, 2017, **41**, 469–475.
- 140 T. Malinauskas, M. Saliba, T. Matsui, M. Daskeviciene, S. Urnikaite, P. Gratia, R. Send, H. Wonneberger, I. Bruder, M. Graetzel, V. Getautis and M. K. Nazeeruddin, *Energy Environ. Sci.*, 2016, **9**, 1681–1686.
- 141 I. Cho, N. J. Jeon, O. K. Kwon, D. W. Kim, E. H. Jung, J. H. Noh, J. Seo, S. Il Seok and S. Y. Park, *Chem. Sci.*, 2017, **8**, 734–741.
- 142 Y. C. Kim, T.-Y. Yang, N. J. Jeon, J. Im, S. Jang, T. J. Shin, H.-W. Shin, S. Kim, E. Lee, S. Kim, J. H. Noh, S. Il Seok and J. Seo, *Energy Environ. Sci.*, 2017, **10**, 2109–2116.
- 143 C. Huang, W. Fu, C. Z. Li, Z. Zhang, W. Qiu, M. Shi, P. Heremans, A. K. Y. Jen and H. Chen, *J. Am. Chem. Soc.*, 2016, **138**, 2528–2531.
- 144 S. Paek, P. Qin, Y. Lee, K. T. Cho, P. Gao, G. Grancini, E. Oveisi, P. Gratia, K. Rakstys, S. A. Al-Muhtaseb, C. Ludwig, J. Ko and M. K. Nazeeruddin, *Adv. Mater.*, 2017, **29**, 1606555.
- 145 K. Rakstys, A. Abate, M. I. Dar, P. Gao, V. Jankauskas, G. Jacopin, E. Kamarauskas, S. Kazim, S. Ahmad, M. Gratzel and M. K. Nazeeruddin, *J. Am. Chem. Soc.*, 2015, **137**, 16172–16178.
- 146 S. W. Shelton, T. L. Chen, D. E. Barclay and B. Ma, *ACS Appl. Mater. Interfaces*, 2012, **4**, 2534–2540.
- 147 A. Benito-Hernández, U. K. Pandey, E. Caverio, R. Termine, E. M. García-Frutos, J. L. Serrano, A. Golemme and B. Gómez-Lor, *Chem. Mater.*, 2013, **25**, 117–121.
- 148 F. J. Ramos, K. Rakstys, S. Kazim, M. Grätzel, M. K. Nazeeruddin and S. Ahmad, *RSC Adv.*,

- 2015, **5**, 53426–53432.
- 149 J. Zhang, Z. Hu, L. Huang, G. Yue, J. Liu, X. Lu, Z. Hu, M. Shang, L. Han and Y. Zhu, *Chem. Commun.*, 2015, **51**, 7047–7050.
- 150 T. Malinauskas, D. Tomkute-Luksiene, R. Sens, M. Daskeviciene, R. Send, H. Wonneberger, V. Jankauskas, I. Bruder and V. Getautis, *ACS Appl. Mater. Interfaces*, 2015, **7**, 11107–11116.
- 151 A. Torres and L. G. C. Rego, *J. Phys. Chem. C*, 2014, **118**, 26947–26954.
- 152 J. P. Correa Baena, L. Steier, W. Tress, M. Saliba, S. Neutzner, T. Matsui, F. Giordano, T. J. Jacobsson, A. R. Srimath Kandada, S. M. Zakeeruddin, A. Petrozza, A. Abate, M. K. Nazeeruddin, M. Grätzel and A. Hagfeldt, *Energy Environ. Sci.*, 2015, **8**, 2928–2934.
- 153 S. Kazim, M. K. Nazeeruddin, M. Grätzel and S. Ahmad, *Angew. Chemie - Int. Ed.*, 2014, **53**, 2812–2824.
- 154 A. Abate, T. Leijtens, S. Pathak, J. Teuscher, R. Avolio, M. E. Errico, J. Kirkpatrick, J. M. Ball, P. Docampo, I. McPherson and H. J. Snaith, *Phys. Chem. Chem. Phys.*, 2013, **15**, 2572.
- 155 A. Abate, D. R. Staff, D. J. Hollman, H. J. Snaith and A. B. Walker, *Phys. Chem. Chem. Phys.*, 2014, **16**, 1132–1138.
- 156 G. Xing, N. Mathews, S. Sun, S. S. Lim, Y. M. Lam, M. Gratzel, S. Mhaisalkar and T. C. Sum, *Science*, 2013, **342**, 344–347.
- 157 H. J. Snaith, A. Abate, J. M. Ball, G. E. Eperon, T. Leijtens, N. K. Noel, S. D. Stranks, J. T. W. Wang, K. Wojciechowski and W. Zhang, *J. Phys. Chem. Lett.*, 2014, **5**, 1511–1515.
- 158 M. Planells, A. Abate, D. J. Hollman, S. D. Stranks, V. Bharti, J. Gaur, D. Mohanty, S. Chand, H. J. Snaith and N. Robertson, *J. Mater. Chem. A*, 2013, **1**, 6949.
- 159 M. Franceschin, L. Ginnari-Satriani, A. Alvino, G. Ortaggi and A. Bianco, *European J. Org. Chem.*, 2010, **2010**, 134–141.
- 160 L. Rong, Q. Liu, Y. Shi and J. Tang, *Chem. Commun.*, 2011, **47**, 2155.
- 161 W. Y. Lai, Q. Y. He, R. Zhu, Q. Q. Chen and W. Huang, *Adv. Funct. Mater.*, 2008, **18**, 265–276.
- 162 Y. Li, H. Zhou, W. Chen, G. Sun, L. Sun and J. Su, *Tetrahedron*, 2016, **72**, 5620–5625.
- 163 Q. Y. Yu, J. Y. Liao, S. M. Zhou, Y. Shen, J. M. Liu, D. Bin Kuang and C. Y. Su, *J. Phys. Chem. C*, 2011, **115**, 22002–22008.
- 164 A. Dessì, G. Barozzino Consiglio, M. Calamante, G. Reginato, A. Mordini, M. Peruzzini, M. Taddei, A. Sinicropi, M. L. Parisi, F. Fabrizi De Biani, R. Basosi, R. Mori, M. Spatola, M. Bruzzi and L. Zani, *European J. Org. Chem.*, 2013, **2013**, 1916–1928.
- 165 K. Rakstys, S. Paek, P. Gao, P. Gratia, T. Marszalek, G. Grancini, K. T. Cho, K. Genevicius, V. Jankauskas, W. Pisula and M. K. Nazeeruddin, *J. Mater. Chem. A*, 2017, **5**, 7811–7815.
- 166 S. Wang, M. Sina, P. Parikh, T. Uekert, B. Shahbazian, A. Devaraj and Y. S. Meng, *Nano Lett.*, 2016, **16**, 5594–5600.

- 167 S. Jeon, U. K. Thakur, D. Lee, Y. Wenping, D. Kim, S. Lee, T. K. Ahn, H. J. Park and B. G. Kim, *Org. Electron. physics, Mater. Appl.*, 2016, **37**, 134–140.
- 168 M. Franckevičius, A. Mishra, F. Kreuzer, J. Luo, S. M. Zakeeruddin and M. Grätzel, *Mater. Horiz.*, 2015, **2**, 613–618.
- 169 X. Zhao, F. Zhang, C. Yi, D. Bi, X. Bi, P. Wei, J. Luo, X. Liu, S. Wang, X. Li, S. M. Zakeeruddin and M. Grätzel, *J. Mater. Chem. A*, 2016, **4**, 16330–16334.
- 170 Y. Yang, Y. Liu, Z. Hong, Q. Chen, H. Chen, W. H. Chang and T. Bin Song, *Adv. Mater.*, 2016, **28**, 440–446.
- 171 Z. Li, Z. Zhu, C. C. Chueh, S. B. Jo, J. Luo, S. H. Jang and A. K. Y. Jen, *J. Am. Chem. Soc.*, 2016, **138**, 11833–11839.
- 172 F. Zhang, X. Zhao, C. Yi, D. Bi, X. Bi, P. Wei, X. Liu, S. Wang, X. Li, S. M. Zakeeruddin and M. Grätzel, *Dyes and Pigments*, 2017, **136**, 273–277.
- 173 F. Zhang, X. Liu, C. Yi, D. Bi, J. Luo, S. Wang, X. Li, Y. Xiao, S. M. Zakeeruddin and M. Graetzel, *ChemSusChem*, 2016, **9**, 2578–2585.
- 174 A. L. Kanibolotsky, I. F. Perepichka and P. J. Skabara, *Chem. Soc. Rev.*, 2010, **39**, 2695.
- 175 J. Roncali, *Chem. Rev.*, 1997, **97**, 173–206.
- 176 C. Piliago, T. W. Holcombe, J. D. Douglas, C. H. Woo, P. M. Beaujuge and J. M. J. Fréchet, *J. Am. Chem. Soc.*, 2010, **132**, 7595–7597.
- 177 M. S. Chen, O. P. Lee, J. R. Niskala, A. T. Yiu, C. J. Tassone, K. Schmidt, P. M. Beaujuge, S. S. Onishi, M. F. Toney, A. Zettl and J. M. J. Fréchet, *J. Am. Chem. Soc.*, 2013, **135**, 19229–19236.
- 178 M. Li, C. An, T. Marszalek, M. Baumgarten, H. Yan, K. Müllen and W. Pisula, *Adv. Mater.*, 2016, **28**, 9430–9438.
- 179 G. Schweicher, G. Gbabode, F. Quist, O. Debever, N. Dumont, S. Sergeev and Y. H. Geerts, *Chem. Mater.*, 2009, **21**, 5867–5874.
- 180 W. Pisula, Ž. Tomović, B. El Hamaoui, M. D. Watson, T. Pakula and K. Müllen, *Adv. Funct. Mater.*, 2005, **15**, 893–904.
- 181 O. Thiebaut, H. Bock and E. Grelet, *J. Am. Chem. Soc.*, 2010, **132**, 6886–6887.
- 182 S. Guarnera, A. Abate, W. Zhang, J. M. Foster, G. Richardson, A. Petrozza and H. J. Snaith, *J. Phys. Chem. Lett.*, 2015, **6**, 432–437.
- 183 K. Domanski, J. P. Correa-Baena, N. Mine, M. K. Nazeeruddin, A. Abate, M. Saliba, W. Tress, A. Hagfeldt and M. Grätzel, *ACS Nano*, 2016, **10**, 6306–6314.
- 184 D. J. Turner, R. Anémian, P. R. Mackie, D. C. Cupertino, S. G. Yeates, M. L. Turner and A. C. Spivey, *Org. Biomol. Chem.*, 2007, **5**, 1752–63.
- 185 D. E. Janzen, M. W. Burand, P. C. Ewbank, T. M. Pappenfus, H. Higuchi, D. A. Da Silva Filho, V. G. Young, J. L. Brédas and K. R. Mann, *J. Am. Chem. Soc.*, 2004, **126**, 15295–15308.
- 186 S. J. Evenson and S. C. Rasmussen, *Org. Lett.*, 2010, **12**, 4054–4057.

- 187 J. Shi, W. Zhao, L. Xu, Y. Kan, C. Li, J. Song and H. Wang, *J. Phys. Chem. C*, 2014, **118**, 7844–7855.
- 188 F. V. Drozdov, E. N. Myshkovskaya, D. K. Susarova, P. A. Troshin, O. D. Fominykh, M. Y. Balakina, A. V. Bakirov, M. A. Shcherbina, J. Choi, D. Tondelier, M. I. Buzin, S. N. Chvalun, A. Yassar and S. A. Ponomarenko, *Macromol. Chem. Phys.*, 2013, **214**, 2144–2156.
- 189 P. Gao, D. Cho, X. Yang, V. Enkelmann, M. Baumgarten and K. Müllen, *Chem. - A Eur. J.*, 2010, **16**, 5119–5128.
- 190 K. Rakstys, M. Saliba, P. Gao, P. Gratia, E. Kamarauskas, S. Paek, V. Jankauskas and M. K. Nazeeruddin, *Angew. Chemie - Int. Ed.*, 2016, **55**, 7464–7468.
- 191 C. de la Harpe and W. A. van Dorp, *Berichte der Dtsch. Chem. Gesellschaft*, 1875, **8**, 1048–1050.
- 192 P. U. Biedermann and I. Agranat, in *Topics in Current Chemistry*, Springer, Cham, 2014, vol. 350, pp. 177–278.
- 193 P. U. Biedermann, J. J. Stezowski and I. Agranat, *Chem. - A Eur. J.*, 2006, **12**, 3345–3354.
- 194 A. Levy, S. Pogodin, S. Cohen and I. Agranat, *European J. Org. Chem.*, 2007, **2007**, 5198–5211.
- 195 G. L. Eakins, M. W. Cooper, N. N. Gerasimchuk, T. J. Phillips, B. E. Breyfogle and C. J. Stearman, *Can. J. Chem.*, 2013, **91**, 1059–1071.
- 196 F. G. Brunetti, X. Gong, M. Tong, A. J. Heeger and F. Wudl, *Angew. Chemie - Int. Ed.*, 2010, **49**, 532–536.
- 197 L. L. Yeung, Y. C. Yip and T. Y. Luh, *J. Org. Chem.*, 1990, **55**, 1874–1881.
- 198 M. Degbia, M. Ben Manaa, B. Schmaltz, N. Berton, J. Bouclé, R. Antony and F. Tran Van, *Mater. Sci. Semicond. Process.*, 2016, **43**, 90–95.
- 199 Ö. Usluer, M. Abbas, G. Wantz, L. Vignau, L. Hirsch, E. Grana, C. Brochon, E. Cloutet and G. Hadziioannou, *ACS Macro Lett.*, 2014, **3**, 1134–1138.
- 200 P. Ganesan, K. Fu, P. Gao, I. Raabe, K. Schenk, R. Scopelliti, J. Luo, L. H. Wong, M. Grätzel and M. K. Nazeeruddin, *Energy Environ. Sci.*, 2015, **8**, 1986–1991.
- 201 K. Avasthi, L. Shukla, R. Kant and K. Ravikumar, *Acta Crystallogr. Sect. C Struct. Chem.*, 2014, **70**, 555–561.
- 202 J. A. Christians, J. S. Manser and P. V. Kamat, *J. Phys. Chem. Lett.*, 2015, **6**, 852–857.
- 203 K. Rakstys, S. Paek, G. Grancini, P. Gao, V. Jankauskas, A. M. Asiri and M. K. Nazeeruddin, *ChemSusChem*, 2017, **10**, 3825–3832.
- 204 A. Levy, P. U. Biedermann and I. Agranat, *Org. Lett.*, 2000, **2**, 1811–1814.
- 205 Y. Zhang, G. Grancini, Y. Feng, A. M. Asiri and M. K. Nazeeruddin, *ACS Energy Lett.*, 2017, **2**, 802–806.
- 206 H. Chen, W. Fu, C. Huang, Z. Zhang, S. Li, F. Ding, M. Shi, C. Z. Li, A. K. Y. Jen and H. Chen, *Adv. Energy Mater.*, 2017, 1700012.

-
- 207 Y. Gardikis, P. G. Tsoungas, C. Potamitis, M. Zervou and P. Cordopatis, *Heterocycles*, 2011, **83**, 1077–1091.
- 208 S. Dadashi-Silab, H. Bildirir, R. Dawson, A. Thomas and Y. Yagci, *Macromolecules*, 2014, **47**, 4607–4614.
- 209 K. Rakstys, S. Paek, M. Sohail, P. Gao, K. T. Cho, P. Gratia, Y. Lee, K. H. Dahmen and M. K. Nazeeruddin, *J. Mater. Chem. A*, 2016, **4**, 18259–18264.
- 210 M. Grätzel, *Nat. Mater.*, 2014, **13**, 838–842.
- 211 I. C. Smith, E. T. Hoke, D. Solis-Ibarra, M. D. McGehee and H. I. Karunadasa, *Angew. Chemie - Int. Ed.*, 2014, **53**, 11232–11235.
- 212 Y.-F. Chen, J.-M. Liu, J.-F. Huang, L.-L. Tan, Y. Shen, L.-M. Xiao, D.-B. Kuang and C.-Y. Su, *J. Mater. Chem. A*, 2015, **3**, 8083–8090.
- 213 V. Jeux, C. Dalinot, M. Allain, L. Sanguinet and P. Leriche, *Tetrahedron Lett.*, 2015, **56**, 1383–1387.
- 214 S. Paek, I. Zimmermann, P. Gao, P. Gratia, K. Rakstys, G. Grancini, M. K. Nazeeruddin, M. A. Rub, S. A. Kosa, K. A. Alamry and A. M. Asiri, *Chem. Sci.*, 2016, **7**, 6068–6075.
- 215 X. Guo, S. R. Puniredd, M. Baumgarten, W. Pisula and K. Müllen, *J. Am. Chem. Soc.*, 2012, **134**, 8404–8407.

Curriculum Vitae

Kasparas Rakstys

kasparas.rakstys@epfl.ch; riklandas@gmail.com

Date of birth: 01 01 1989

Nationality: Lithuanian

EDUCATION

PhD Candidate in Chemistry and Chemical Engineering, September 2013 – November 2017

École Polytechnique Fédérale de Lausanne, Group for Molecular Engineering of Functional Materials, Switzerland

Final degree project: Molecularly Engineered Hole Transporting Materials for High Performance Perovskite Solar Cells

Master of Chemistry, Applied Organic Chemistry, September 2011 – June 2013

Kaunas University of Technology, Faculty of Chemical Engineering, Lithuania

Overall GPA: 9.95/10

Final degree project: Synthesis and Photovoltaic Properties of Diketopyrrolopyrrole-based Organic Dyes

Erasmus mixed mobility programme, February 2012 – September 2012

École Polytechnique Fédérale de Lausanne, Laboratory of Photonics and Interfaces, Switzerland
Project in Molecular Sciences

Bachelor of Chemistry, Applied Chemistry, September 2007 – June 2011

Kaunas University of Technology, Faculty of Chemical Engineering, Lithuania

Overall GPA: 8.56/10

Final degree project: Synthesis of 1-phenyl-1,2,3,4-tetrahydroquinoline-based Rhodanine Dyes for Solar Cells

AWARDS

- WILEY best poster award in 2nd International Conference on Perovskite Solar Cells and Optoelectronics (PSCO-2016)
- Lithuanian Academy of Sciences prize for best Master thesis in Chemistry (2014)
- Rector's promoting grant (2013)
- J. P. Kazickas patron scholarship (2012)
- Students Scientific Conference "Chemistry and Chemical Technology 2011" first-prize winner
- Youth Scientists exhibition "KTU Technorama 2009" first-prize winner
- Bank "Snoras" patron scholarship (2009)
- Students Scientific Conference "Chemistry and Chemical Technology 2009" third-place winner

PUBLICATIONS

1. S. Paek, P. Qin, Y. Lee, K. T. Cho, P. Gao, G. Grancini, E. Oveisi, P. Gratia, K. Rakstys, S. A. Al-Muhtaseb, C. Ludwig, J. Ko, Md. K. Nazeeruddin. Dopant-Free Hole-Transporting Materials for Stable and Efficient Perovskite Solar Cells. *Adv. Mat.* **2017**, *29*, 1606555.
2. K. Rakstys, S. Paek, G. Grancini, P. Gao, V. Jankauskas, A. M. Asiri, Md. K. Nazeeruddin. Low-cost Perovskite Solar Cells Employing Dimethoxydiphenylamine-Substituted Bistricyclic Aromatic Enes as Hole Transporting Materials. *ChemSusChem* **2017**, *10*, 3825–3832.
3. K. Rakstys, S. Paek, P. Gao, P. Gratia, T. Marszalek, G. Grancini, K. T. Cho, K. Genevicius, V. Jankauskas, W. Pisula, Md. K. Nazeeruddin. Molecular Engineering of Face-On Oriented Dopant-free Hole Transporting Material for Perovskite Solar Cells with 19% PCE. *J. Mater. Chem. A* **2017**, *5*, 7811–7815.
4. M. Daskeviciene, S. Paek, Z. Wang, T. Malinauskas, G. Jokubauskaite, K. Rakstys, K. T. Cho, A. Magomedov, V. Jankauskas, S. Ahmad, H. J. Snaith, V. Getautis, Md. K. Nazeeruddin. Carbazole-based Enamine: Low-cost and Efficient Hole Transporting Material for Perovskite Solar Cells. *Nano Energy* **2017**, *32*, 551–557.
5. K. Rakstys, S. Paek, M. Sohail, P. Gao, K. T. Cho, P. Gratia, Y. H. Lee, K. H. Dahmen, Md. K. Nazeeruddin. A Highly Hindered Bithiophene-functionalized Dispiro-oxepine Derivative as an Efficient Hole Transporting Material for Perovskite Solar Cells. *J. Mater. Chem. A* **2016**, *4*, 18259–18264.
6. K. T. Cho, K. Rakstys, M. Cavazzini, S. Orlandi, G. Pozzi, Md. K. Nazeeruddin. Perovskite Solar Cells Employing Molecularly Engineered Zn(II) Phthalocyanines as Hole-transporting Materials. *Nano Energy* **2016**, *30*, 853–857.
7. P. Qin, S. Paek, M. I. Dar, K. Rakstys, H. ElBatal, S. A. Al-Muhtaseb, C. Ludwig, Md. K. Nazeeruddin. Weakly Conjugated Hybrid Zinc Porphyrin Sensitizers for Solid-State Dye-Sensitized Solar Cells. *Adv. Funct. Mater.* **2016**, *26*, 5550–5559.
8. S. Paek, I. Zimmermann, P. Gao, P. Gratia, K. Rakstys, G. Grancini, Md. K. Nazeeruddin, M. A. Rub, S. A. Kosa, K. A. Alamry, A. M. Asiri. Donor- π -Donor Type Hole Transporting Materials: Marked π -Bridge Effects on Optoelectronic Properties, Solid-state Structure, and Perovskite Solar Cell Efficiency. *Chem. Sci.* **2016**, *7*, 6068–6075.
9. K. Rakstys, M. Saliba, P. Gao, P. Gratia, E. Kamarauskas, S. Paek, V. Jankauskas, Md. K. Nazeeruddin. Highly Efficient Perovskite Solar Cells Employing an Easily Attainable Bifluorenylidene-based Hole-transporting Material. *Angew. Chem. Int. Ed.* **2016**, *55*, 7464–7468.
10. I. Petrikyte, I. Zimmermann, K. Rakstys, M. Daskeviciene, T. Malinauskas, V. Jankauskas, V. Getautis, Md. K. Nazeeruddin. Efficiency Enhancement of Perovskite Solar Cells *via* Incorporation of Phenylethenyl Side Arms into Indolocarbazole-based Hole Transporting Materials. *Nanoscale* **2016**, *8*, 8530–8535.
11. K. Rakstys, A. Abate, M. I. Dar, P. Gao, V. Jankauskas, G. Jacopin, E. Kamarauskas, S. Kazim, S. Ahmad, M. Graetzel, Md. K. Nazeeruddin. Triazatruxene-Based Hole Transporting Materials for Highly Efficient Perovskite Solar Cells. *J. Am. Chem. Soc.* **2015**, *137*, 16172–16178.
12. F. J. Ramos, K. Rakstys, S. Kazim, M. Graetzel, Md. K. Nazeeruddin, S. Ahmad. Rational Design of Triazatruxene-based Hole Conductors for Perovskite Solar Cells. *RSC Adv.* **2015**, *5*, 53426–53432.
13. P. Gao, K. Domanski, S. Aghazada, K. Rakstys, S. Paek, Md. K. Nazeeruddin. Molecular Engineering of Functional Materials for Energy and Opto-Electronic Applications. *Chimia*, **2015**, *69*, 253–263.
14. K. Rakstys, J. Solovjova, T. Malinauskas, I. Bruder, R. Send, A. Sackus, R. Sens, V. Getautis. A Structural Study of 1-phenyl-1,2,3,4-tetrahydroquinoline-based Dyes for Solid-state DSSC Applications. *Dyes and Pigments*, **2014**, *104*, 211–219.
15. T. W. Holcombe, J.-H. Yum, Y. Kim, K. Rakstys, M. Graetzel. Diketopyrrolopyrrole-based Sensitizers for Dye-sensitized Solar Cell Applications: Anchor Engineering. *J. Mater. Chem. A* **2013**, *1*, 13978–13983.
16. J.-H. Yum, T. W. Holcombe, Y. Kim, K. Rakstys, T. Moehl, J. Teuscher, J. H. Delcamp, Md. K.

- Nazeeruddin, M. Graetzel. Blue-coloured Highly Efficient Dye-sensitized Solar Cells by Implementing the Diketopyrrolopyrrole Chromophore. *Sci. Rep.* 2013, 3, 2446.
17. J.-H. Yum, T. W. Holcombe, Y. Kim, J. Yoon, K. Rakstys, Md. K. Nazeeruddin, M. Graetzel. Towards High-performance DPP-based Sensitizers for DSC Applications. *Chem. Commun.* 2012, 48, 10727-10729.
18. T. W. Holcombe, J.-H. Yum, J. Yoon, P. Gao, M. Marszalek, D. Di Censo, K. Rakstys, Md. K. Nazeeruddin, M. Graetzel. A Structural Study of DPP-based Sensitizers for DSC Applications. *Chem. Commun.* 2012, 48, 10724-10726.

PATENTS

1. K. Rakstys, S. Paek, M. Sohail, K. H. Dahmen, M. K. Nazeeruddin. Dispiro-Oxepine/Thiapine Derivatives for Optoelectronic Semiconductors. PCT/US2017/041060.
2. S. Ahmad, F. J. Ramos, S. Kazim, C. M. Doblare, M. K. Nazeeruddin, M. Graetzel, K. Rakstys. Novel Compound and Use Thereof as a Hole-Transport Material. WO2016083655.
3. H. Yamato, S. Nakamichi, R. Takahashi, H. Yamamoto, R. Send, H. Wonneberger, I. Bruder, V. Getautis, K. Rakstys, T. Malinauskas. Methine Dyes with Large Organic Counter Anion for Dye Sensitized Solar Cells. WO2015011638.

PRESENTATIONS

- Oral talk "Molecularly Engineered Hole Transporting Materials for High Performance Perovskite Solar Cells" at 9th International Conference on Materials for Advanced Technologies (ICMAT2017), Singapore.
- Poster "Molecular Engineering of Face-on Oriented Dopant-free Hole Transporting Material for 19% Perovskite Solar Cells" at International Conference on Hybrid and Organic Photovoltaics (HOPV17), Lausanne, Switzerland.
- Oral talk "Face-on Oriented Dopant-Free Hole Transporting Material for 19% Perovskite Solar Cells" at International Conference for Students of Physics and Natural Sciences (Open Readings 2017), Vilnius, Lithuania.
- Poster "19.4% Perovskite Solar Cells Employing Highly Hindered Bithiophene-functionalized Hole Transporting Material" at 2nd International Conference on Perovskite Solar Cells and Optoelectronics (PSCO-2016), Genova, Italy.
- Poster "18.3% Perovskite Solar Cells Employing Triazatruxene Derivatives as Hole Transporting Materials" at 1st International Conference on Perovskite Solar Cells and Optoelectronics (PSCO-2015), Lausanne, Switzerland.
- Poster "Triazatruxene-based Hole Transporting Materials for Efficient CH₃NH₃PbI₃ Perovskite Solar Cells" at International Conference on Solution Processed Innovative Solar Cells (SPINS15), Santiago de Compostela, Spain.
- Oral presentation in NanoMatCell 4th Project Meeting, 2015, London, United Kingdom.
- Oral presentation in 6th Consortium Meeting of Powerweave Project, 2014, Turin, Italy.
- Oral presentation in 5th Project Steering Committee Meeting of Powerweave Project, 2014, Aarhus, Denmark.
- Oral talk "Nauji Rodanino Dažikliai, Turintys 1-fenil-1,2,3,4-tetrahydrochinolino Fragmentą" at Students Scientific Conference (Chemistry and Chemical Technology 2011), Kaunas, Lithuania.
- Oral talk "Rodanino bei 1-fenil-3-hidroksi-1,2,3,4-tetrahydrochinolino Chromoforų Turinčio Dažiklio Sintezė" at Students Scientific Conference (Chemistry and Chemical Technology 2010), Vilnius, Lithuania.
- Oral talk "Aktyvių Dažiklių Saulės Elementams Sintezė" at Students Scientific Conference (Chemistry and Chemical Technology 2009), Klaipėda, Lithuania.

